

INSTITUT FRANCO-ALLEMAND DE RECHERCHES DE SAINT-LOUIS  
DEUTSCH-FRANZÖSISCHES FORSCHUNGSINSTITUT SAINT-LOUIS



**Aerodynamic characteristic of the A3 DRDC-ISL  
reference projectile: Missile with lattice fins**

DUPUIS A.\*, BERNER C., BERNIER A.\*

# REPORT DOCUMENTATION PAGE

Form Approved OMB No. 0704-0188

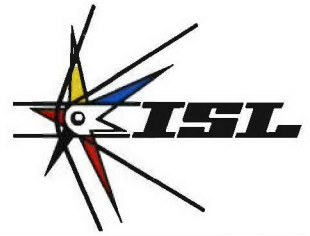
Public reporting burden for this collection of information is estimated to average 1 hour per response, including the time for reviewing instructions, searching existing data sources, gathering and maintaining the data needed, and completing and reviewing the collection of information. Send comments regarding this burden estimate or any other aspect of this collection of information, including suggestions for reducing this burden to Washington Headquarters Services, Directorate for Information Operations and Reports, 1215 Jefferson Davis Highway, Suite 1204, Arlington, VA 22202-4302, and to the Office of Management and Budget, Paperwork Reduction Project (0704-0188), Washington, DC 20503.

1. AGENCY USE ONLY (Leave blank)		2. REPORT DATE 12 December 2005	3. REPORT TYPE AND DATES COVERED Report	
4. TITLE AND SUBTITLE Aerodynamic characteristic of the A3 DRDC-ISL reference projectile: Missile with lattice fins			5. FUNDING NUMBERS	
6. AUTHOR(S) A. Dupuis, C. Berner, A. Bernier				
7. PERFORMING ORGANIZATION NAME(S) AND ADDRESS(ES)				
9. SPONSORING/MONITORING AGENCY NAME(S) AND ADDRESS(ES) ISL, 5 rue du General Cassagnau – BP 70034, 68301 Saint Louis Cedex, France			10. SPONSORING/MONITORING AGENCY REPORT NUMBER R 138/2005	
11. SUPPLEMENTARY NOTES Text in English,, 277 pages.				
12a. DISTRIBUTION/AVAILABILITY STATEMENT Public release. Copyrighted. (1 and 21)			12b. DISTRIBUTION CODE	
<b>ABSTRACT (Maximum 200 words)</b>  Free-flight tests were conducted in the Defence R&D Canada (DRDC) Valcartier aeroballistic range and at the ISL open range test site and wind tunnel experiments in the DRDC Valcartier Indraft Trisonic and the French German Research Institute wind tunnels as well as numerical computations on the A3 DRDC-ISL reference projectile at subsonic and supersonic velocities. The projectile consisted of an ogive-cylinder body with a length-to-diameter ratio of 10 with four lattice control surfaces. The reference grid fin consisted of nine thick cells in a vertical orientation and located at 0.7 cal from the base. The wind tunnel tests were conducted for various fin deflection angles at a range of angles of attack and roll orientations to determine the static aerodynamic coefficients. Very thin walls, an open base concept as well as a cruciform cell orientation were also investigated in the wind tunnels. Flow visualizations were obtained from wind tunnel as well as free-flight tests. The wind tunnel tests were conducted in the Mach number range of 0.6 to 4.0, while the free-flight tests were conducted in the Mach number range of 1.4 to 3.3. The stability derivatives and static aerodynamic coefficients were very well determined. Numerical investigations were carried out on the reference configuration to visualize the flow features and obtain predictions of the aerodynamic coefficients. The aerodynamic coefficients and stability derivatives are presented individually and then compared where warranted. Finally, the results are compared with a classical fin design.				
14. SUBJECT TERMS FIZBW, German, Aeroballistic, Wind tunnel, Projectile, Subsonic velocities, Supersonic velocities, Aerodynamic coefficients, Flow visualizations			15. NUMBER OF PAGES	
			16. PRICE CODE	
17. SECURITY CLASSIFICATION OF REPORT UNCLASSIFIED	18. SECURITY CLASSIFICATION OF THIS PAGE UNCLASSIFIED	19. SECURITY CLASSIFICATION OF ABSTRACT UNCLASSIFIED	20. LIMITATION OF ABSTRACT UL	

NSN 7540-01-280-5500

Standard Form 298 (Rev. 2-89)  
Prescribed by ANSI Std. Z39-18  
298-102





---

## **Aerodynamic characteristic of the A3 DRDC-ISL reference projectile: Missile with lattice fins**

DUPUIS A.\*, BERNER C., BERNIER A.\*\*

\* DRDC, Valcartier

\*\* SNC-TEC

---

Date du document 12.12.2005  
*Berichtsdatum*

Axe de recherches  
*Schwerpunkt*

**2.14**

Pilotage des projectiles  
*Steuerung von Geschossen*

---

*AQ F07-01-0198*

**R 138/2005**



#### **Éditeur / Herausgeber**

---

Institut franco-allemand de recherches de Saint-Louis  
5 rue du Général Cassagnou - BP 70034  
68301 SAINT LOUIS CEDEX  
France  
<http://www.isl.tm.fr>

*Deutsch-Französisches Forschungsinstitut Saint-Louis*  
*Postfach 1260*  
*79574 Weil am Rhein*  
*Deutschland*  
<http://www.isl.tm.fr>

**Création graphique - Mise en page - Impression / Layout - Druck**  
Service / Abt. ED - ISL

**Commande de publications / Bestellung von Publikationen**  
Service / Abt. BB - ISL  
Tel. : +33 (0)3 89 69 51 36  
Fax : +33 (0)3 89 69 53 35  
E-mail : [dar@isl.tm.fr](mailto:dar@isl.tm.fr)

**Relations externes / Presse- und Öffentlichkeitsarbeit**  
Service / Abt. COM - ISL  
Tel. : +33 (0)3 89 69 51 43  
Fax : +33 (0)3 89 69 58 58  
E-mail : [com@isl.tm.fr](mailto:com@isl.tm.fr)

Reproduction et diffusion des rapports interdites sans accord préalable de l'ISL  
© Institut franco-allemand de recherches de Saint-Louis (ISL)

*Vervielfältigung und Weitergabe von Berichten ist ohne die schriftliche Genehmigung des ISL untersagt*  
*© Deutsch-Französisches Forschungsinstitut Saint-Louis (ISL)*

## Abstract

Free-flight tests were conducted in the Defence R&D Canada (DRDC) Valcartier aeroballistic range and at the ISL open range test site and wind tunnel experiments in the DRDC Valcartier Indraft Trisonic and the French German Research Institute wind tunnels as well as numerical computations on the A3 DRDC-ISL reference projectile at subsonic and supersonic velocities. The projectile consisted of an ogive-cylinder body with a length-to-diameter ratio of 10 with four lattice control surfaces. The reference grid fin consisted of nine thick cells in a vertical orientation and located at 0.7 cal from the base. The wind tunnel tests were conducted for various fin deflection angles at a range of angles of attack and roll orientations to determine the static aerodynamic coefficients. Very thin walls, an open base concept as well as a cruciform cell orientation were also investigated in the wind tunnels. Flow visualizations were obtained from wind tunnel as well as free-flight tests. The wind tunnel tests were conducted in the Mach number range of 0.6 to 4.0, while the free-flight tests were conducted in the Mach number range of 1.4 to 3.3. The stability derivatives and static aerodynamic coefficients were very well determined. Numerical investigations were carried out on the reference configuration to visualize the flow features and obtain predictions of the aerodynamic coefficients. The aerodynamic coefficients and stability derivatives are presented individually and then compared where warranted. Finally, the results are compared with a classical fin design.

## Résumé

Des essais en vol libre ont été effectués dans le corridor aérobalistique du Centre de Recherche et développement pour la défense Canada (RDDC) Valcartier et au champ de tir de l'ISL ainsi que des essais dans la soufflerie à rafales trisonique de RDDC Valcartier et la soufflerie supersonique à rafales de l'Institut franco-allemand de recherches (ISL) sur le projectile de référence DRDC-ISL A3. Des simulations numériques ont également été effectuées sur la même configuration à des vitesses subsoniques et supersoniques. Le projectile de référence consistait en un corps ogive-cylindre d'un allongement de 10 calibres équipé de quatre surfaces de contrôle en forme de treillis. L'ailette en treillis de référence consistait en neuf cellules d'orientation verticale et située à 0,7 cal de la base du projectile. Les essais en soufflerie ont été effectués à différents angles d'assiette, angles d'attaque et de roulis afin de déterminer les coefficients aérodynamiques statiques. Des essais en soufflerie ont aussi été effectués sur des ailettes dont l'épaisseur des murs était très mince, une dont la base était ouverte et sur une dernière où les cellules étaient orientées en croix. Des visualisations d'écoulement ont été obtenues en soufflerie ainsi qu'en vol libre. Les essais en soufflerie ont été effectués à des nombres de Mach compris entre 0,6 et 4,0 et les essais en vol libre dans la gamme de nombre de Mach entre 1,4 à 3,3. Des simulations numériques ont également été effectuées sur la configuration de référence afin de visualiser la structure des écoulements et permettre la prédiction des coefficients aérodynamiques. Les résultats sont présentés individuellement et des comparaisons sont effectuées lorsque nécessaire. Finalement, les résultats sont comparés à des ailettes classiques.

## Table of contents

Abstract.....	3
Executive summary .....	3
Sommaire.....	3
Table of contents .....	5
List of figures .....	9
Acknowledgements .....	13
1. Introduction .....	15
2. Model Configurations.....	17
2.1 Wind Tunnel Models.....	17
2.1.1 Reference Lattice Fins with Thick Walls .....	17
2.1.2 Various Lattice Fins Geometries .....	18
2.2 Aeroballistic and Open Range Model .....	18
3. Wind Tunnel Tests .....	21
3.1 Wind Tunnel Facilities and Instrumentation .....	21
3.1.1 DRDC Trisonic Indraft Wind Tunnel.....	21
3.1.2 ISL Blow Down Wind Tunnel .....	22
3.1.3 Reynolds Number Comparison .....	22
3.2 Data Acquisitioning and Reduction.....	22
3.3 Flow Visualization.....	25
3.4 Wind Tunnel Results – Group 1 (fins canted for roll).....	26
3.4.1 Comparison of ISL and DRDC Results.....	27
3.4.2 Aerodynamic Coefficients versus Incidence .....	28
3.4.2.1 Mach 0.6 Comparison .....	29
3.4.2.2 Mach 1.5 Comparison .....	30
3.4.2.3 Mach 3.0 Comparison .....	31
3.4.3 Aerodynamic Coefficients versus Mach Number .....	32

3.4.3.1	Roll Moment Coefficient – Group 2 .....	34
3.4.4	Main Conclusions for Group 1 results.....	34
3.5	Wind Tunnel Results – Group 3 (fins deflected for trim) .....	35
3.5.1	Aerodynamic Coefficients versus Incidence .....	35
3.5.1.1	Mach 0.6 Comparison .....	35
3.5.1.2	Mach 1.5 Comparison .....	36
3.5.1.3	Mach 2.5 Comparison .....	37
3.5.2	Aerodynamic Coefficients versus Mach number .....	37
3.5.3	Main Conclusions for Group 3 Results .....	38
3.6	Wind Tunnel Results – Various Fin Geometries.....	38
3.6.1	Aerodynamic Coefficients versus Incidence .....	39
3.6.1.1	Mach 0.6 Comparison .....	39
3.6.1.2	Mach 1.5 Comparison .....	39
3.6.1.3	Mach 3.0 Comparison .....	40
3.6.2	Aerodynamic Coefficients versus Mach Number .....	41
3.6.3	Main Conclusions for Various Fin Geometries Results .....	43
3.7	Discussion of Results .....	43
4.	Free-Flight Tests.....	45
4.1	Aeroballistic Range .....	45
4.1.1	Facility Description .....	45
4.1.2	Models and Test Conditions.....	45
4.1.2.1	Projectile Configuration .....	45
4.1.2.2	Sabot Design .....	46
4.1.2.3	Test Conditions and Particularities .....	46
4.1.3	Free-Flight Data Reduction .....	47
4.2	Open Range Test Site .....	48
4.2.1	Experimental Site, Instrumentation and Test Conditions.....	48
4.2.2	Models .....	49
4.2.2.1	Projectile configuration.....	49
4.2.2.2	Sabot Design .....	49
4.3	Free-Flight Results and Discussions .....	49
4.3.1	Flow Visualization .....	49

4.3.2	Linear Theory Results .....	50
4.3.3	Six-Degree-of-Freedom Results .....	51
4.3.4	Comparison of 6DOF Single- and Multiple-Fit Results.....	53
5.	Computational Fluid Dynamic Analysis .....	55
5.1	Computational Fluid Dynamic Code .....	55
5.1.1	Code Description .....	55
5.1.2	Computational Mesh .....	56
5.1.3	Boundary Conditions .....	57
5.2	Aerodynamic Coefficients Predictions .....	57
5.2.1	Wind Tunnel Model .....	57
5.2.2	Aeroballistic Range Model .....	58
5.2.3	Comparison of Predictions for the two Models .....	59
5.3	Pressure Distribution inside Central Cell .....	60
5.4	CFD Flow Field Visualization.....	61
6.	Comparison of Experimental and Predicted Results .....	63
6.1	Aerodynamic Coefficients vs. Angle of Attack.....	63
6.2	Aerodynamic Coefficients vs. Mach Number .....	64
6.2.1	Wind Tunnel Aerodynamic Coefficient Slopes for Comparison .....	64
6.2.2	Comparison of Results vs. Mach Number.....	64
7.	Comparison of Lattice and Classical Fin Aerodynamic Coefficients.....	67
8.	Conclusions .....	69
9.	References .....	73
	Annexe A – Plotted Wind Tunnel Aerodynamic Coefficients for A3 Configurations.....	175
	Annexe B – Tabulated Wind Tunnel Aerodynamic Coefficients vs. Mach Number for A3 .....	229
	Annexe C – Theoretical Choking Mach Number .....	235
	Annexe D – Tabulated Wind Tunnel Aerodynamic Coefficients for Various Lattice Fin Geometries.....	237

Annexe E – Plotted Wind Tunnel Aerodynamic Coefficients for Various Geometries (M = 0.8, 2.0, 2.5 and 4.0) ..... 239

Annexe F – Free-Fligth Motion Plots ..... 249

List of symbols ..... 273



## List of figures

Figure 1. Wind tunnel configuration A3_1– Projectile Geometry (all dimensions in caliber, 1 cal = 20.0 mm).....	89
Figure 2 - Wind tunnel configurations – various lattice fin types (all dimensions in calibers, 1 cal = 20.0 mm) .....	90
Figure 3. Photographs of wind tunnel model.....	91
Figure 4. Aeroballistic range configuration - Projectile Geometry (all dimensions in caliber, 1 cal = 30.0 mm).....	92
Figure 5. Photograph of aeroballistic range model.....	93
Figure 6 - Wind tunnel facilities.....	93
Figure 7. Dimensions and characteristics of the 12.70 mm MK-LX-B balance.....	94
Figure 8. Model shown in DRDC wind tunnel facility .....	94
Figure 9. Wind tunnel shadowgraph for $\alpha = 0^\circ$ at Mach = 3.0 .....	95
Figure 10. Wind tunnel shadowgraph for $\alpha=12^\circ$ at Mach=3.0 .....	95
Figure 11. Angle of attack effects for A3_1 (4 fins at $\delta=0^\circ$ ) at Mach =3.0.....	96
Figure 12. Angle of attack effects for A3_4 (4 fins at $\delta=15^\circ$ ) at Mach =3.0.....	96
Figure 13. Schematic of the flow structure.....	97
Figure 14. Comparison of DRDC and ISL wind tunnel results for A3_4, M = 3.0 .....	98
Figure 15. Comparison of wind tunnel results for Group 1, Mach = 0.6; $\phi = 0.0^\circ$ .....	101
Figure 16. Comparison of wind tunnel results for Group 1, Mach = 1.5; $\phi = 0.0^\circ$ .....	104
Figure 17. Comparison of wind tunnel results for Group 1, Mach = 3.0; $\phi = 0.0^\circ$ .....	107
Figure 18. Comparison of wind tunnel results for Group 1 vs. Mach number; $\phi = 0.0^\circ$ .....	110
Figure 19. Comparison of wind tunnel $C_{l\delta}$ results for Group 2 vs. Mach number; $\phi = 0.0^\circ$ .....	112
Figure 20. Comparison of wind tunnel results for Group 3, Mach = 0.6; $\phi = 0.0^\circ$ .....	113
Figure 21. Comparison of wind tunnel results for Group 3, Mach = 1.5; $\phi = 0.0^\circ$ .....	116

Figure 22. Comparison of wind tunnel results for Group 3, Mach = 2.5; $\phi = 0.0^\circ$ .....	119
Figure 23. Comparison of wind tunnel results for Group 3 vs. Mach number; $\phi = 0.0^\circ$ .....	122
Figure 24. Comparison of wind tunnel results for various fin geometries, Mach = 0.6; $\phi = 0.0^\circ$ .....	124
Figure 25. Comparison of wind tunnel results for various fin geometries, Mach = 1.5; $\phi = 0.0^\circ$ .....	126
Figure 26. Comparison of wind tunnel results for various fin geometries, Mach = 3.0; $\phi = 0.0^\circ$ .....	128
Figure 27. Comparison of wind tunnel results for various fin geometries vs. Mach number; $\phi = 0.0^\circ$ .....	130
Figure 28. Photograph of aeroballistic range complex .....	132
Figure 29. Aeroballistic Range photographic station spacing .....	132
Figure 30. Schematic of sabot design .....	133
Figure 31. Photograph model-sabot package.....	133
Figure 32. Typical sabot separation.....	135
Figure 33. Free-flight Schlieren photographs.....	135
Figure 34. Free-flight shadowgraphs for shot K01.....	136
Figure 35. DRDC Aeroballistic Range Facility Data Analysis System .....	137
Figure 36. ISL Open Range Test Site Setup.....	138
Figure 37. ISL Sabot Design .....	139
Figure 38. ISL Free-flight shadowgraphs.....	140
Figure 39. Comparison of free-flight 6DOF reduced aerodynamic coefficients vs. Mach number.....	144
Figure 40. Computational mesh for wind tunnel model .....	148
Figure 41. CFD predictions (SST, BF0.75) for wind tunnel model vs. angle of attack .....	149
Figure 42. Comparison of CFD aerodynamic coefficients vs. Mach number for both models .....	151
Figure 43. Pressure taps location in central cell. ....	153

Figure 44. Comparison of computed and measured pressures in central cell ( $\kappa$ - $\epsilon$ , BF-0.75).....	154
Figure 45. Flow field for Mach = 0.6, $\alpha$ = 0.0° .....	155
Figure 46. Flow field for Mach = 1.5, $\alpha$ = 0.0° .....	156
Figure 47. Flow field for Mach = 3.0, $\alpha$ = 0.0° .....	158
Figure 48. Flow field for Mach = 3.0, $\alpha$ = 10.0° .....	160
Figure 49. Comparison of numerical and wind tunnel experimental results vs. incidence for model A3 .....	162
Figure 50. Pitch moment coefficient vs. incidence for model A3_1 at Mach 3.0 .....	163
Figure 51. Comparison of wind tunnel aerodynamic coefficient slopes vs. Mach number for model A3_1 .....	164
Figure 52. Comparison of predicted and experimental aerodynamic coefficients vs. Mach number .....	166
Figure 53. Drawings of Air Force Finner reference projectile (all dimensions in caliber) .....	169
Figure 54. Comparison of aerodynamic coefficients for grid and classical fins vs. Mach number .....	170

## List of tables

Table 1. Grid fin panel deflections for reference thick fin and wind tunnel tests.....	77
Table 2. Reynolds number comparison .....	77
Table 3. $C_{X0}$ relative variation for one fin w.r.t thick fin model.....	78
Table 4. Nominal physical properties of free-flight models .....	78
Table 5. Physical properties of free-flight test projectiles .....	78
Table 6. Range conditions .....	79
Table 7. Muzzle velocities.....	79
Table 8. Linear theory analysis parameters.....	80

Table 9. Linear theory aerodynamic coefficients .....	80
Table 10. Six-degree-of-freedom aerodynamic coefficients – Single fits .....	81
Table 11. Six-degree-of-freedom aerodynamic coefficients – Multiple fits.....	83
Table 12. Roll moment coefficient due to fin cant .....	85
Table 13. CFD predictions for wind tunnel model (A3_1) vs. incidence.....	86
Table 14. $C_{X0}$ CFD predictions for wind tunnel model (A3_1) vs. Mach number .....	86
Table 15. CFD predicted slopes for wind tunnel model (A3_1) vs. Mach number.....	87
Table 16. CFD predictions for aeroballistic range model at $\alpha = 2.5^\circ$ .....	87
Table 17. $C_{X0}$ CFD predictions for aeroballistic range model vs. Mach number .....	87
Table 18. $C_{lp}$ CFD predictions for aeroballistic range model vs. Mach number.....	88
Table 19. CFD predicted slopes for aeroballistic range model vs. Mach number.....	88
Table 20. Wind tunnel aerodynamic data used for Mach number comparison .....	88

## Acknowledgements

With a program of this size, there are many people who were involved from both research centers and some contractors. It is difficult to name everybody since we will definitely miss some who were critical for the program success, and if we do, we apologize. At DRDC, Mr. R. Bélanger is thanked for the wind tunnel tests that were conducted; Mr. M. Normand of MAETEC for the initial design of the sabots and the assistance of Mr. Marco Boivin, from DRDC Valcartier, for the sabot design and modifications as well as his active participation during the tests were very much appreciated; Mr. Jean Beaupré, from the METC, for operating the aeroballistic range during the trials, Mr. D. Dubuc who sorted and scanned the films and to the whole METC trials team for their dedication in making these tests a success. We are also grateful to the DRDC staff from the Prototype Section who manufactured the free-flight models. The assistance of Mr. W. Hathaway of Arrow Tech Associates in the final analysis of the free-flight data is very much appreciated. At ISL thanks are due to Mr. C. Hartmann and the workshop employees who respectively designed and manufactured all the wind tunnel models, to Mr. P. Duffner and C. Demeautis for the wind tunnels tests and to the staff of the open range test site for conducting the free-flight tests at ISL.

# 1. Introduction

Defence Research and Development Canada (DRDC) - Valcartier and the French-German Research Institute (ISL) in Saint-Louis, France, agreed, under the auspices of AS N°14 of the Franco-Canadian Accord, to conduct an extensive experimental and computational investigation on three projectile configurations. Both research establishments have wind tunnels, aeroballistic range facilities, open ranges and Computational Fluid Dynamic (CFD) means to determine the aerodynamic characteristics and the stability of any projectile configuration. The aim was to use a triangular exploration (wind tunnel, free-flight and predictions) to reduce as much as possible the number of required aerodynamic tests, which tend to be quite expensive. Every effort was made to use the available tools at both establishments, in a complementary fashion rather than duplicative, to maximize the efficiency.

Many options are being examined by both research establishments to improve the performance of existing weapons platforms or by investigating novel technologies that could be used with present systems by increasing their current capabilities. One example consists in increasing the range of artillery shells beyond 40 km by using deployable wings during the flight, and by providing them with some maneuverability on the battlefield. This would enhance the hit probability on selected high threat targets, or if a type of visual system could be mounted in the shell, it could also be used as an observing stage. The use of lattice, or grid, fins could increase the performance of missiles over classical aerodynamic control surfaces to improve maneuvering capability at high angles of attack. The available information on how such modifications would improve the aerodynamic performance over the classical projectile or missile shapes is rather limited. Before characterizing any enhancements, it is necessary to provide detailed and reliable information on reference test cases so as to be able to quantify any improvements over the classical projectile.

The use of grid fins as a stabilization and control device on projectiles and missiles offers an interesting alternative to the classical fin design. Grid fins consist of an outer frame that supports a unique internal grid of lifting surfaces. One advantage of this type of control surface (Refs. 1-11) is very high angle of attack lift performance at high Mach numbers, which is a requirement for a high-g missile. The data shows that this type of fin does not stall at very high angles of attack and control deflections. They also have linear aerodynamic characteristics with angle of attack, even to very large incidences. They also produce a very low hinge moment that permits smaller mechanical actuators. The main shortcoming of the grid fins is that they have a very high drag as compared to the planar ones.

The grid fins studied in Refs. 1-11 were very thin walled, had approximately 30 cells and were oriented in a cruciform fashion. For this project, it was decided to study a simpler design with fewer cells (nine) and oriented in a vertical direction, with very thick walls to allow pressure measurements inside the central cell and to be able to conduct free-flight tests at high supersonic velocities with a structurally-sound fin.

The objective of this investigation was to obtain the aerodynamic characteristic of a missile body with lattice fins from wind tunnel and free-flight tests as well as from numerical predictions. The main aerodynamic coefficients and stability derivatives as well as the nonlinear ones were determined experimentally and numerically. Flow visualizations from shadowgraphs were obtained and the flow structure is explained. A comparison of the results from the different methodologies is given and, finally, a comparison of the results with a classical fin design is conducted.

This study was conducted as part of a cooperative research program between DRDC and ISL under the auspices of AS N°14 entitled "Projectiles et missiles pilotés par ailettes en treillis" of the Franco-Canadian Accord. This work was performed at DRDC Valcartier between October 1999 and May 2003 under Work Unit 3eb12, Flight Dynamics for Missile Performance Studies.



## 2. Model Configurations

### 2.1 Wind Tunnel Models

Wind tunnel tests were conducted in two test series. The first series consisted of the reference grid fin with thick walls with the fins canted and deflected in various combinations. Based on the results obtained during the first series, it was decided during the project to conduct a further series of wind tunnel experiments on different fin shapes, orientation and wall thickness. The wind tunnel models all had a diameter of 20.0 mm.

#### 2.1.1 Reference Lattice Fins with Thick Walls

The projectile configuration that was retained for this joint project is shown in Fig. 1. The reference configuration was the Air Force Finner (Refs. 12 and 13) body equipped with four grid fins, as shown in Fig. 1a. The body consisted of a 2.5 caliber tangent-ogive followed by a 7.5 caliber cylinder. The fins were placed at 0.7 calibers from the base. The total span is 2.4 calibers with a chord of 0.08 calibers. These last dimensions and placements were typical of missiles systems that were studied based on a literature survey on the data that was available at that time. The reference center of gravity position was located at 4.05 cal from the nose of the projectile. The reference diameter for the wind models was 20.0 mm.

The grid fin, presented in Fig. 1b, has nine cells with thick walls. Thick walls were chosen to allow wind tunnel static wall pressure measurements on the central cell. This grid fin geometry, contrary to many other papers (Refs. 1-11), has a vertical cell orientation instead of a cruciform one. This was done to simplify the geometry and to be able to understand basic aerodynamic phenomena of simple cells. Each cell is rectangular with a width of 0.124 caliber and a height of 0.161 caliber. In order to avoid possible structure deficiencies during free-flight tests, a solid base was designed to mount the fins on the body.

Nine combinations of panel deflections were looked at and these are provide in Table 1 and the Mach number where they were tested in the wind tunnels are indicated. The sign convention of the deflections of the fins and the roll orientation of the model in the wind tunnels are shown in Fig. 1c.

The first model, defined as the reference configuration was labeled A3\_1, and, often call the thick finned model, had zero fin deflection angles on all four fins. To produce a pure roll motion, a second group was defined, (A3\_2 to A3\_4) and they had all four fins canted at 5.0°, 10.0° and 15.0°, respectively. A third group, A3\_5 to A3\_7, had one pair of devices kept at 0.0°, while the other pair were canted again at 5.0°, 10.0° and 15.0°,

respectively, to produce a pure roll motion. The last group, A3\_8 and A3\_10, had one pair of panels at  $0.0^\circ$  while the other two fins were deflected at  $5.0^\circ$  and  $15.0^\circ$ , respectively, in such a fashion to produce lift and moment trims a zero angle of attack.

### 2.1.2 Various Lattice Fins Geometries

Three other fin types (Fig. 2) were tested in the DRDC wind tunnel at Mach numbers of 0.6, 0.8, 1.5, 2.0, 2.5, 3.0 and 4.0 at zero roll orientation only. They had no deflection angles. The location of these fins on the missile body was the same as the tick fin one with the same span and chord.

The first variation consisted of the same geometry and cell structure as the thick fin model except that a hole, with dimensions of  $0.158 \times 0.15$  cal, was placed at the base of the support structure as shown in Fig. 2a.

The second modification consisted of a set of fins with the traditional hexagonal shape (Fig. 2b) found on most grid fin projectiles and missiles. In this case, the cells were square with a width of 0.135 cal. The wall thickness was 0.017 cal, the same as the other two types, and the base support was less obstructive than the thick fin projectile with the solid base.

The last set of fins tested consisted of very thin walls (Fig. 2c) as compared to the thick fin model. The shape is exactly the same as model A3\_1 (Fig. 1b) except that the wall thickness was decreased to 0.005 cal. The cell height and width for this case was 0.163 cal and 0.149 cal, respectively. The same base support as the thick fin projectile was utilized.

Photographs of the wind tunnel model and enlargements in the fin regions of the various fin types are provided in Fig. 3.

During the second series of wind tunnel tests, it was decided to test the projectile with no fins attached.

## 2.2 Aeroballistic and Open Range Model

The model configuration that was used for the aeroballistic range trials was very similar to the wind tunnel model with the thick fin (A3\_1) and the sketches are shown in Fig. 4. The only difference with the wind tunnel model (A3\_1, Fig. 1a) is that the base width is 0.13 cal instead of 0.22 cal. For the free-flight trials, one pair of panels were canted at  $2.0^\circ$  to produce a pure roll motion while the opposite pair was deflected at  $0.5^\circ$  to produce lift and moment trims a zero angle of attack. For the ISL open range trials, the configuration was identical to the DRDC but the fins had no deflection.

The aft portion of the projectile was made of aluminum and the nose section was made of a tungsten alloy so as to obtain a forward center of gravity position at roughly 4.05 cal from the nose. A photograph of the model can be seen in Fig. 5. The roll pin to

measure the roll orientation in the aeroballistic range can be seen at the base of the projectile. The free-flight models has a diameter of 30.0 mm.

### 3. Wind Tunnel Tests

All the models were fabricated at ISL for the wind tunnels tests and they had a reference diameter of 20.0 mm.

#### 3.1 Wind Tunnel Facilities and Instrumentation

The experimental data gathered for this investigation were collected at two facilities: the ISL and DRDC wind tunnels. The following describes these facilities in detail.

##### 3.1.1 DRDC Trisonic Indraft Wind Tunnel

The DRDC-Valcartier trisonic wind tunnel (Fig. 6a) is fully described in Ref. 14. It is an indraft-type wind tunnel with a test section of 60 cm x 60 cm and a useful run time of about 6 s. Air is drawn in an evacuated tank from an atmospheric pressure reservoir. Supersonic flow is achieved by using seven interchangeable nozzle blocks for the supersonic regime for nominal Mach numbers of 1.5, 1.75, 2.0, 2.5, 3.0, 3.5, and 4.0. Transonic flow is obtained by using of a perforated chamber with boundary layer control through suction. Subsonic flow is obtained with one nozzle block and a downstream choke valve.

Standard instrumentation (Pitot tubes, wall pressure taps and temperature probes) located in the plenum chamber and in the test section was used to monitor the tunnel free stream conditions. Forces and moments are measured with 12.7 mm and 19.05 mm six component strain gauge balances. In this case, a 12.7 mm MK-LX-B ABLE balance was utilized and its characteristics are provided in Fig. 7. The balance was calibrated before the experiments were conducted.

The wind tunnel aerodynamic results obtained ( $C_X$ ,  $C_N$ ,  $C_M$ ,  $C_{l\delta\delta}$  and  $X_{Cp}$ ) for the first series of tests were obtained from a combination of model sweeps between  $-10.0^\circ$  to  $+10.0^\circ$  incidences at roll orientations of  $0.0^\circ$  and  $45.0^\circ$ . The first series of tests were conducted at Mach 0.6, 1.5, 2.5 and 3.0. For the second series of tests with the different fin geometries, Mach numbers of 0.8, 2.0 and 4.0 were added and the angle of attack was swept between  $-5.0^\circ$  and  $15.0^\circ$ . The roll orientation was kept at  $0.0^\circ$ .

A photograph of the model mounted in the DRDC wind tunnel is shown in Fig. 8.

### 3.1.2 ISL Blow Down Wind Tunnel

The wind tunnel that was used at the French-German Research Institute of Saint-Louis (ISL) is a blow down type facility (Fig. 6b) capable of Mach numbers from 1.7 to 4.38 and it has a test section of 20 cm x 20 cm. The run time for this wind tunnel is approximately 50 seconds with a 25-minute recharge time. Pitot tubes and temperature probes mounted in the settling chamber allow for the determination of the free stream conditions. A 12.7 mm MK-XIII-A ABLE balance was utilized at ISL and it is identical to the DRDC one, as shown in Fig.7.

Shadowgraph flow visualizations, force and moment measurements at a nominal Mach number of 3.0 were obtained for the first series of tests. For the second series of tests with the different geometries, force and moment measurements were also obtained for a Mach number of 4.0. Models were swept between  $-12.0^\circ$  to  $+5.0^\circ$  and positioned at  $0.0^\circ$  and  $45.0^\circ$  roll orientation.

### 3.1.3 Reynolds Number Comparison

Since the DRDC wind tunnel facility is an indraft type, the Reynolds number ( $Re_l$ ) drops to very low values at high Mach numbers. The Reynolds numbers based on the length of the projectile for these tests are given in Table 2 and they are compared with those of the ISL wind tunnel. In those two cases  $Re_l$  is based on a total length of 0.2 m. The aeroballistic range Reynolds numbers are also provided for comparison purposes, and those are based on a length of 0.3 m.

At Mach 3.0, the ISL Reynolds number is a factor of 4 higher than the DRDC value. The free-flight Reynolds number (Section 4.2.3) at the same Mach number is 13 and 3.0 times the DRDC and ISL wind tunnel values, respectively. At the other Mach numbers, the free-flight Reynolds numbers are a factor of 3.3 to 25.0 higher than the DRDC wind tunnel, at the low and high Mach numbers, respectively.

## 3.2 Data Acquisition and Reduction

The data acquisition and the data reduction are very similar at DRDC and ISL. The procedure at DRDC will be provided and where there are big differences with ISL, those will be noted.

For each run, the analog output signals from both the balance and the pressure transducers were digitized and then fed into a microcomputer for storage and later analysis. A separate tare run was done at  $M = 0.0$  to allow for correction of the balance outputs due to model weight. Resulting data were reduced and processed according to the following equations:

$$M_i = \left[ \left( \left( \frac{P_{ti}}{P_{vi}} \right)^{\frac{\gamma-1}{\gamma}} - 1 \right) \frac{2}{\gamma-1} \right]^{\frac{1}{2}}$$

$$P_t = \frac{\sum P_{ti}}{n} \quad n = \text{number of readings}$$

The free stream Mach number ( $M_\infty$ ), used in the following formulations in the wind tunnel data reduction, was based on the average of Tap 8 located on the side wall of the wind tunnel. Therefore,

$$M_\infty = \overline{M}_8$$

The other parameters are given as:

$$P_s = P_t \left[ 1 + \frac{\gamma-1}{2} M_\infty^2 \right]^{\frac{-\gamma}{\gamma-1}}$$

$$Q = \frac{\gamma}{2} M_\infty^2 P_s$$

$$S = \frac{\pi d^2}{4}$$

$$N = N_1 + N_2$$

$$C_N = \frac{N}{QS}$$

$$C_X = \frac{A}{QS}$$

$$C_{RM} = \frac{R}{QSd}$$

The moment about the BRC of the projectile is given by:

$$M^{BRC} = N_1 a - N_2 b$$

$$C_M^{\text{BRC}} = \frac{M^{\text{BRC}}}{Q S d}$$

The aerodynamic moment about the base of the projectile is given by:

$C_M^b = C_M^{\text{BRC}} - C_N \frac{c}{d}$ , where  $c$  is the distance between the BRC and the base of the projectile.

The center of pressure about the base is then given by:

$$X_{\text{CP}} = -\frac{C_M^b}{C_N}$$

$$T_v = T_a \left( 1.0 + \frac{\gamma-1}{2} M_\infty^2 \right)^{-1}$$

$$\mu = b \frac{T_v^{1.5}}{T_v + S}$$

with:  $b=1.458 \cdot 10^{-6} \text{ kg/msK}^{1/2}$  and  $S=110.4 \text{ K}$

$$\rho = \frac{P_t}{R T_a} \left( \frac{T_v}{T_a} \right)^{2.5}$$

with:  $R=287.05$

$$\text{Re} = \frac{\rho U_\infty}{\mu}, \quad (\text{m}^{-1})$$

$$\text{Re}_l = \frac{\rho U_\infty l}{\mu}$$

The static aerodynamic coefficients ( $C_N, C_M, C_A$ ) were obtained by best least-square fitted polynomials through the measured experimental data as follows:

Parameter	Polynomial
$C_N$	$B_0 + B_1 \alpha + B_3 \alpha^3 + B_5 \alpha^5 + B_7 \alpha^7 \quad (-10^\circ \text{ to } 10^\circ)$
$C_M^b$	$B_0 + B_1 \alpha + B_3 \alpha^3 + B_5 \alpha^5 + B_7 \alpha^7 \quad (-10^\circ \text{ to } 10^\circ)$



$$C_X = B_0 + B_2 \alpha^2 + B_4 \alpha^4 + B_6 \alpha^6 + B_8 \alpha^8 \quad (-10^\circ \text{ to } 10^\circ)$$

The sweeps for the second series of tests were from  $-5.0^\circ$  to  $+15.0^\circ$ . At ISL, the sweeps were from  $-12.0^\circ$  to  $+5.0^\circ$ .

$C_{N\alpha}$  and  $C_{M\alpha}^b$  at zero angle of attack were calculated as the slopes of a best least-square straight line fitted to the data over the range of  $-5^\circ$  to  $+5^\circ$ .

$$C_{N\alpha} = B_1 \text{ of polynomial } "B_0 + B_1 \alpha"$$

$$C_{M\alpha}^b = B_1 \text{ of polynomial } "B_0 + B_1 \alpha"$$

The axial force coefficient at zero angle of attack ( $C_{X0}$ ) is given by the first coefficient of a polynomial fitted to the  $C_X$  data ( $B_0$  above). The pressure at the base of the projectile was not measured in this test program.

$$\text{The center of pressure at zero angle of attack is given by } X_{CP0} = \frac{C_{M\alpha}^b}{C_{N\alpha}}.$$

No polynomial fits were conducted for the roll moment due to the fin cant since it is difficult to predict its behavior. The value at zero angle of attack was found by inspection of the graphs of  $C_{RM}$  with angle of attack.

By inspection of the coefficients as a function of angle of attack, it was obvious that in some cases, the data in  $C_N$  and, especially  $C_M$ , were not quite linear between  $-5^\circ$  to  $+5^\circ$ . Nevertheless, the slopes were still computed over that range and the main conclusions when comparing the wind tunnel data remain the same. Some tests were conducted in calculating the slopes in a narrower range of angle of attack, and the small number of data points in this cases caused large variations in the slopes due to a bad point, in most cases. When the wind tunnel data will be compared to the free-flight data and the CFD results, a comparison between two different ranges in angles of attack will be conducted.

### 3.3 Flow Visualization

The flow visualizations were conducted in the ISL wind tunnel. Figures 9 and 10 show some typical shadowgraph examples of three configurations (A3\_1, A3\_4 and A3\_7) for a Mach number of 3.0 at  $0.0^\circ$  and  $12^\circ$  angle of attack and at zero roll orientation. All figures show how the flow field is highly complicated due to the interaction between grid cells as well as the interaction between the grid fins and the body. This is especially true since the shadowgraphs are made by integrating the flow thru the entire test section and therefore it is difficult to dissociate the different phenomena..

A schematic of the flow structure in the vicinity of a single fin at  $\alpha=0^\circ$  is presented in Fig. 13. At zero angle of attack the flow structure between the three configurations is quite similar. After the attached nose shock, clearly seen in Fig. 9a, the boundary layer increases and the flow along the body separates. This separation generates a recompression shock (1) in front of the grid fin triggered by the recirculating region (2) generated by, in our case, the solid fin attachment. Due to this region, the flow is deviated and collapses with the grid fin under an incidence close to the angle of shock (1). At high Mach numbers, flow through the cells is started (swallowed) and the normal bow shock (3') observed in front of the fins is generated by the different webs and not by a unique choked flow located in front of the grid fin. Shock (3'') is the upper part of the bow shock generated by the top web. Behind the fin, one can see a first shock (4) generated by the base of the top web followed by multiple shock waves (5) and expansions whose origin are due to the front recompression and web bow shocks passing through each single grid cell or by the shocks generated by the small near-wakes (6) behind each web. Close to the body, a near-wake recompression shock (7) is triggered by the base recirculating region (8) behind the fin attachment. Shock generated by the fins located at a  $90^\circ$  roll angle, not represented in Fig. 13, can also be observed.

Figures 10a to 10c show the same configurations at an angle of attack of  $12^\circ$ . As shown in Fig. 10, the attached shock is, as expected, more intense on the windward side and the shock system in front and behind the grid fins is asymmetric and even more complicated than for zero angle of attack. Along the body, the flow is also separated and interacts with the upper fin and therefore decreases the efficiency of that fin. Figs. 11 and 12 show sequences of the flow evolution taken every  $1^\circ$  up to  $\alpha=12^\circ$ , respectively for configuration A3\_1 and A3\_4. In both sequences and for angle of attacks between  $5$  and  $10^\circ$ , it is interesting to see how the leeward shock system ahead of the fins are divided into two recompression shocks. This is due to the increase of the boundary thickness that interacts with the different cells as the angle of attack increases. No particular phenomena are observed on the windward side of the fins. The aerodynamics of grid fins are so complex that it is very difficult to draw definite conclusions from the flow visualization. The CFD predictions and experimental wind tunnel tests to be carried out on an up-scaled (x9) single grid fin mounted in the test section on a partially cylindrical splitter plate might help to better understand the flow features around this type of fin configurations. These will be provided in a separate report.

### 3.4 Wind Tunnel Results – Group 1 (fins canted for roll)

The test matrix for this group is provided in Table 1. All tests were conducted at roll orientation of  $0.0^\circ$  and  $45.0^\circ$  and a limited number at  $90.0^\circ$  (not provided here). As mentioned previously, ISL only conducted tests at Mach 3.0. Some runs were repeated at random to make sure that the data repeated itself.

The wind tunnel data for group 1, 2 and 3 are provided in Annex A (Table 1 test matrix) graphically for every configuration that was tested and at both roll orientation angles. The repeated runs are not included. For each configuration, the aerodynamic

coefficients are provided as function of angle of attack for all Mach number tested. Some of those results were published (Refs. 15 and 16) at a slight different center of gravity position.

In some cases, run were conducted at Mach 3.0 at DRDC to have a basis of comparison with ISL. The DRDC results will be presented over the ISL ones in those cases. This is done to be able to provide trends as there were differences in the results of ISL and DRDC as provided below. The cases where the ISL data will be presented are easily discernable since the angles of attack varied from  $-12^\circ$  to  $+5.0^\circ$ .

The basic static aerodynamic coefficients ( $C_{X0}$ ,  $C_{N\alpha}$ ,  $C_{M\alpha}^b$ ,  $C_{M\alpha}^{cg}$  and  $C_{RM}$ ) are tabulated in Annex B as a function of Mach number. They will be compared in a further section below.

The reference center of gravity position for the pitch moment is 4.05 cal from the nose of the projectile, the same as the free-flight testes projectiles.

### 3.4.1 Comparison of ISL and DRDC Results

The first comparison will consist of comparing the wind tunnel results from ISL and DRDC for one configuration A3\_4 (all four fins canted at  $15.0^\circ$  to produce a roll motion) at roll orientations of  $0.0^\circ$  and  $45.0^\circ$  at Mach 3.0.

The axial force as a function of angle of attack is shown in Fig. 14a.  $C_X$  is of the order 1.0 as expected due to the very thick wall of the webs. At a roll orientation of  $0.0^\circ$ , the DRDC data shows a small drag bucket, which is often seen in the DRDC tunnel due to the very low Reynolds number. The ISL  $Re_1$  is a factor 4 higher than the DRDC value at this Mach number (Table 2). The ISL data is basically flat with incidence and the data between  $-5.0$  and  $+5.0^\circ$  is the same at  $0.0^\circ$  and  $45.0^\circ$  orientation, as with the DRDC data. At angles higher than  $5.0^\circ$ , there is a small difference between the two roll orientations as the angle of attack increases. At zero angle of attack the values are the same, as expected on both data sets. The  $C_{X0}$  values at ISL and DRDC are 1.14 and 0.99, respectively. The ISL results are about 15% higher than the DRDC measured value. The boundary layer in the DRDC wind tunnel is laminar while it is turbulent in the ISL one. Previous wind tunnel tests at Mach 2.5 on a clipped delta fin projectile (Ref. 17) did not show large differences as this one. Therefore, it is believed that the differences shown here are due to the particular grid fin and its sensitivity to the boundary layer type.

The normal force comparison is provided in Fig. 14b. The first observation is that there are no differences between the results due to the roll orientations at both facilities. The  $C_N$  data between  $-5^\circ$  and  $+5.0^\circ$  agree extremely well and the ISL  $C_N$  data has a slight higher magnitude at the higher angles of attack compared to the DRDC values.

The pitching moment coefficients are compared about the base and the center of gravity position in Fig. 14c and Fig. 14d, respectively. Even though there is very good correlation between the results about the base, one can notice some differences when the data is transferred about the center of gravity position. This happens often when comparing the pitch moment coefficient and a particular attention to this has to be kept in mind. Providing a large moment arm tends to compress the values. The ISL  $C_M^{cg}$  data are basically the same at the lower angles of attack and the  $45.0^\circ$  values are higher in magnitude than the  $0.0^\circ$  data. The same trend is seen in the DRDC data, but the magnitude at the higher angles is slightly less except that the shift in the data is the same.

The center of pressure location determined wind tunnel values are compared in Fig. 14e. The large variation about zero angle of attack is expected since the normal force is 0.0 at  $0.0^\circ$  angle of attack. Overall the agreement is very good.

The roll producing moment ( $C_{RM}$ ) data from the canted fins are shown in Fig. 14f. The first comment is that the maximum  $C_{RM}$  occurs at zero angle of attack and the magnitude decreases as the angle of attack increases. Also, the influence of the roll orientation on  $C_{RM}$  is well observed particularly as the angle of attack increases, that is, as the incidence increases, there is more roll moment in the + configuration than the X one, and the difference increases with incidence also.

The DRDC  $C_{RM}$  data has a pure V shape while the ISL data is more parabolic in nature. This is also probably due to the boundary layer type in both facilities. There is very good agreement between the data sets at angles of attack higher than  $2.0^\circ$  with the same shift in the data between the two roll orientations.

### 3.4.2 Aerodynamic Coefficients versus Incidence

The results for the first group of projectile where the fins were all canted to produce a roll motion will be provided at  $M=0.6$ , 1.5 and 3.0 as a function of angle of attack for the four tested cant angles. The scales were expanded in some cases so as to be able to discriminate the slight differences in the data. The data is presented only for a roll orientation of  $0.0^\circ$ . The effect of the Mach number for one particular cant angle as a function of angle of attack are given in Annex A. The fin cants will be mentioned in a positive way to simplify matters.

### 3.4.2.1 Mach 0.6 Comparison

The effect of the cant angle on  $C_X$  as a function of angle of attack at Mach 0.6 is shown in Fig. 15a. The axial force coefficient is the same for fin cants of  $0.0^\circ$  and  $5.0^\circ$  and it increases in magnitude by 6.3% and 16.1% for the  $10.0^\circ$  and  $15.0^\circ$  fin cants, respectively. There are hardly any effects of the angles of attack on  $C_X$ .

The normal force comparison is provided in Fig. 15b. In this case, as the angle of attack increases, the magnitude of  $C_N$  increases with increasing fin cant angle. For example at  $10.0^\circ$  incidence, the  $15.0^\circ$  cant model has 75% more  $C_N$  than the model with no fin cant.

The pitching moment coefficient about the base and the center of gravity are provided in Fig. 15c and 15d, respectively. Again the data about the base shows no major differences but this is not the case about the center of gravity. From now on, the data about the base will be shown for information purposes and will not be commented upon. The first fact, from the results, is that this projectile is statically stable at Mach 0.6 at all angles of attack for the  $15.0^\circ$  canted model and marginally stable for the  $10.0^\circ$  fin cant model. For the other fin cant models, they are statically unstable in the angle of attack region between  $-4.0^\circ$  and  $+4.0^\circ$ , marginally or neutrally stable between  $4.0^\circ$  and  $8.0^\circ$ , and statically stable at the higher angles of attack. In other words, as the cant angle increases, the static stability increases.

Since the normal force was basically the same over the whole angle of attack region and fin cants, this implies that there is an immense shift in the center of pressure as a function of fin cant angle, and this is shown in Fig. 15e. The data shows in some cases that the  $X_{CP}$  is even in front of the projectile at the lower angles of attack, as for example for the  $0.0^\circ$  fin cant model. In that case, at  $10.0^\circ$  angle of attack, the  $X_{CP}$  is at 7.3 cal from the base and as the angle of attack decreases,  $X_{CP}$  moves towards the nose of the projectile and at values below  $4.0^\circ$  incidence it is in front of the projectile. The theoretical choking Mach number for this configuration at zero incidences, based on similar calculations to Ref. 1, is Mach 0.548. These calculations are provided in Annex C for this configuration and the other ones studied in this report. The results of Ref. 1 showed an instability at a critical Mach number with a similar large shift in the center of pressure. The measured critical Mach numbers of Ref. 1 were slightly higher

than the calculated values. This does not imply that this is an explanation for the instability in our case.

The roll producing moment comparison is shown in Fig. 15f. The zero fin cant model shows a slight positive roll moment but it should be theoretically zero. It is possible that they are not exactly zero due to manufacturing tolerances. For the other three cases,  $C_{RM}$  increases with fin cant angle and angle of attack. The 5.0° fin cant model has a positive roll moment at zero angle of attack and then decreases to negative values past 4.0° in angle of attack, signifying a roll reversal.

### 3.4.2.2 *Mach 1.5 Comparison*

The axial force coefficient comparison at Mach 1.5 is provided in Fig. 16a.  $C_X$  as a function of angle of attack is parabolic in nature and it increases with angle of attack.  $C_X$  for the 5.0° canted fin model is just slightly above the projectile with no fin cant.  $C_{X0}$ , for the 10.0° and 15.0° canted fin models, is roughly 10.0% and 14% higher, respectively, than the model with no fin cant.

$C_N$  as a function of angle of attack is shown in Fig. 16b. At this Mach number, the normal force coefficient is exactly the same for all the fin cants tested.

$C_M^b$  and  $C_M^{cg}$  are compared in Fig. 16c and Fig. 16d, respectively. There is a bit of scatter in the data with  $C_M^{cg}$ . At the negatives angles of attack, the data is the same for the four fin cants and there are slight variations at the positive angles of attack. The projectile is statically stable.

The variation in the center of pressure location with angle of attack is shown in Fig. 16e.  $X_{Cp}$  is basically the same for all four configurations and is just slightly behind the reference center of gravity. It should be mentioned that during the planning of the project, the initial reference center of gravity was located at 4.8 cal from the nose of the projectile (Ref. 18), the same as the Air Force Reference model (Refs. 12 and 13). The present wind tunnel results showed that the projectile was statically unstable at Mach numbers below 2.5 at that center of gravity position. It was then decided to displace the center of gravity position forward to the present position so as to be able to free-flight test them as close as possible to Mach 1.5. Two projectiles were fired in the



sabot integrity trials (Ref. 18) with a center of gravity position at 4.8 cal from the nose at Mach 2.49 and 2.00, and both projectiles were statically unstable, confirming the wind tunnel results.

The roll moment as a function of angle of attack for the four configurations is provided in Fig. 16f. The variation of  $C_{RM}$  with incidence is very minor for all four configurations, and  $C_{RM}$  increases in magnitude with increasing angle of cant.

#### **3.4.2.3 Mach 3.0 Comparison**

The results at Mach 3.0 for the axial force coefficient are shown in Fig. 17a. The results for the 5.0° and 10.0 ° fin cant models are from the ISL wind tunnel. As mentioned previously, it is suspected that there are Reynolds number effects and it is therefore difficult to provide a good comparison. Nevertheless, the shapes of the curves as a function of angle of attack at the two different facilities are consistent with each other, but differ in shape between the two facilities. More comments will be provided in the next section concerning this.

The normal force coefficient is displayed in fig. 17b. At the low angles of attack,  $C_N$  for the four cases are basically the same and small differences start to occur at roughly 4.0°, especially for the 15.0° canted fin model.

The pitching moment coefficient at the two reference positions is provided in Fig. 17c and Fig. 17d. The  $C_M^{CG}$  data is symmetric about zero angle of attack, and the stability decreases with increasing fin cant angle.

$X_{CP}$  as a function of angle of attack is shown in Fig. 17e. The overall trend in  $X_{CP}$  at this Mach number is that it moves forward as the fin cant increases, and more so at the lower angles of attack.

The roll producing moment is compared in Fig. 17f. At this Mach number, again,  $C_{RM}$  increases in magnitude with increasing fin cant angle. The shapes of the curves are parabolic with angle of attack, with the highest magnitude at zero incidence and  $C_{RM}$  decreasing in magnitude as the angle of attack increases.



### 3.4.3 Aerodynamic Coefficients versus Mach Number

In this section, the main aerodynamic coefficients ( $C_{X0}$ ,  $C_{N\alpha}$ ,  $C_{M\alpha}^{cg}$  and  $C_{l\delta}$ ) will be compared for a roll orientation of  $0.0^\circ$  for all four fin cants. The differences in the ISL and DRDC results are also included and will be commented upon when necessary. Repeated runs are also included.

The axial force coefficient at zero angle of attack vs. Mach number is shown in Fig. 18a.  $C_{X0}$  is of the order of 0.8 to 1.4, and these magnitudes were expected (Refs. 1-11). This is one of the principal concerns of using grid fins. However, altering the cross section shape on the outer frame and the web design (see section 3.6) can reduce this high drag coefficient. In general, the trend of  $C_{X0}$  with Mach number is that of conventional planar fins (Ref. 12 and 13). The results also show an increase of  $C_{X0}$  of 20% when the fins are deflected at  $15.0^\circ$  as compared to no deflection. This increase is observed over the whole Mach number range. The data also indicates that  $C_{X0}$  for the models with  $0.0^\circ$  and  $5.0^\circ$  fin cants are the same. The ISL data also confirms these results at Mach 3.0.

The ISL data at Mach 3.0 is encircled in the figures and if any DRDC data is enclosed within this circle, it is identified. There is a difference in the measured  $C_{X0}$  values between DRDC and ISL at Mach 3.0. The ISL results are roughly 15.0 % higher than the DRDC measured value for both fin cants ( $\delta = 0.0^\circ$  and  $15.0^\circ$ ). As mentioned and explained previously, it is believed that the difference shown here is due to the particular grid fin and its sensitivity to the boundary layer type.

Fig. 18b presents the normal force coefficient slope,  $C_{N\alpha}$ , as a function of Mach number. In this case, there was only a difference of about 11% between the DRDC and ISL measured values at Mach 3.0. The first trend to observe is that  $C_{N\alpha}$  increases as the Mach number increases. This implies that the fins become more effective as the Mach number increases while standard planar fins (Ref. 12 and 13) usually have the opposite trend. At Mach 1.5, all four configurations have the same  $C_{N\alpha}$  value. Supersonically, the fin effectiveness decreases as the fin deflection increases and this difference increases with Mach number. Subsonically, the trend is the opposite of the supersonic one. That is, the fins are more effective at  $15.0^\circ$  deflection than at  $0.0^\circ$ . Also, subsonically, there is almost a factor of 2.0 in  $C_{N\alpha}$  between fins not deflected and those deflected at  $15^\circ$ .

The Mach number effects on the pitching moment coefficient slope about the center of gravity ( $C_{M\alpha}^{cg}$ ) are presented in Fig. 18c. In this case, there was a 20.0% difference in the measured values between DRDC and ISL at Mach 3.0 for the  $0.0^\circ$  fin cant model and only 6.0% for the model with the fins

canted at  $15.0^\circ$ . As for  $C_{N\alpha}$  at Mach 1.5,  $C_{M\alpha}^{cg}$  is the same for all four fin deflections. Supersonically, the static stability increases with increasing Mach number. This trend is also opposite of the behavior of a planar fin. Supersonically, the static stability decreases as the fin deflection increases and this difference increases with Mach number. At Mach 3.0, there is a factor of 2.0 in  $C_{M\alpha}^{cg}$  when the fins are deflected at  $15.0^\circ$  and when they are not. An unexpected result was seen at Mach 0.6. The projectile is statically unstable when the fins are deflected at  $0.0^\circ$  and  $5.0^\circ$ , marginally stable at  $10^\circ$  and statically stable when all four fins are deflected at  $15^\circ$ . As for  $C_{N\alpha}$ , the trend is again opposite of the supersonic one.

The center of pressure locations (about the base of the projectile) from the wind tunnel experimental tests are compared vs. Mach number in Fig. 18d. Supersonically,  $X_{CP0}$  is again the same at Mach 1.5 for all four fin deflections, and just aft of the center of gravity.  $X_{CP0}$  moves to the back of the projectile towards the fins, which implies that the projectile becomes more stable, with increasing Mach number. The static stability, defined as the difference between the center of pressure and the center of gravity, is decreasing with increasing fin deflection and this difference increases with Mach number. For example at Mach 3.0, there is a one-caliber difference in  $X_{CP0}$  when the fins are fully deflected and when they are not. For the same Mach number, the ISL  $X_{CP0}$  is located at 0.4 calibers more towards the nose of the projectile than the DRDC measured value.

The most interesting results in this case occur subsonically. When the fins are not deflected, the center of pressure is located in front of the projectile. As the fin deflection increases,  $X_{CP0}$  moves backward along the projectile, and it is behind the center of gravity only when all four fins are fully deflected at  $15.0^\circ$ . There is almost a five caliber displacement of the center of pressure with fin deflection. This means, with no doubt, that subsonically, the static stability of this grid fin configuration is very sensitive to the fin deflection.

The evolution of the roll moment coefficient,  $C_{l\delta}$ , at zero angle of attack (basically,  $C_{RM}$  at  $\alpha = 0.0^\circ$ ) due to the fin deflection is shown in Fig. 18e versus Mach number. The configuration with no deflections, of course, produced no roll moment or very small values. There is just a slight difference in the DRDC and ISL results in this case. Supersonically,  $C_{l\delta}$  increases linearly with Mach number and this was expected since the normal coefficient slope  $C_{N\alpha}$  increases also with Mach number. Again this trend is opposite of planar fins. In addition,  $C_{l\delta}$  is not linear with the fin deflection angle. More so, the roll producing moment is less effective as the fin deflection increases.

Once more, subsonically, an interesting result is observed. When the fins are deflected at  $10.0^\circ$  and  $15.0^\circ$ ,  $C_{l\delta}$  is negative and it is positive when the fins are deflected at  $5.0^\circ$ , indicating a roll reversal. This result, Annex A, was also seen when the model was oriented at a roll angle of  $45^\circ$ .

#### **3.4.3.1 Roll Moment Coefficient – Group 2**

The only comparison conducted for the second group (only two fins canted to produce roll) was the roll producing moment and this is provided in Fig. 19. The results provided are  $C_{l\delta}$  over the number of canted fins. If, the fins were as effective by cant angle and number of fins, this coefficient would be the same at each Mach number. As clearly seen in the figure, this is not necessarily the case. Supersonically, with the fins deflected at  $15.0^\circ$ , there are hardly any differences, but the difference increases as the cant angle decreases. Subsonically, there is a large variation only with the model with the fin canted at  $5.0^\circ$ . There is no doubt that small manufacturing errors could be the source for some of the disparities.

#### **3.4.4 Main Conclusions for Group 1 results**

Overall, the trend of  $C_{N\alpha}$  and  $C_{M\alpha}^{cg}$  for the grid finned projectile is opposite of a standard planar finned projectile. That is, for a constant fin deflection, the effectiveness of the fins and the static stability increases as the Mach number increases, supersonically. On the other hand, subsonically (at Mach 0.6), the projectile is statically unstable, while for a planar fin it is statically stable. Also,  $C_{N\alpha}$  and  $C_{M\alpha}^{cg}$  are the same for all the various configurations at Mach 1.5.

The results showed that all the aerodynamic coefficients were very sensitive to the deflection angle of the fins, and at the same Mach number, there were large differences in the results. As well, the trend with Mach number was reversed when going from subsonic to supersonic.

One very interesting result was observed subsonically. When the fins were not deflected, the center of pressure was located in front of the projectile, and when the fins were deflected, it shifted towards the back of the model.

A roll reversal was detected at Mach 0.6 that was dependent on the fin deflection

### 3.5 Wind Tunnel Results – Group 3 (fins deflected for trim)

In this group, one pair of fins was deflected in such a way as to produce a trim and no roll motion. The results are presented in same fashion as for the previous group and they will be compared with the reference projectile where the fins are deflected. The effects of the Mach number for one particular fin deflections are presented in Annex A. Some of those results were published (Ref. 15) at a slight different center of gravity position.

#### 3.5.1 Aerodynamic Coefficients versus Incidence

The results will be provided at  $M = 0.6$ , 1.5 and 2.5 as a function of angle of attack for the three tested deflection angles. The scales were expanded in some cases to be able to discriminate the slight differences in the data. The data is presented only for a roll orientation of  $0.0^\circ$ . The fin cants will be mentioned in a positive way to simplify matters. The roll moment was negligible and will not be compared in this section but the results are provided in Annex A.

##### 3.5.1.1 *Mach 0.6 Comparison*

The effect of the cant angle on  $C_X$  as a function of angle of attack at Mach 0.6 is shown in Fig. 20a. The first remark concerning the data for the canted fins is the lack of symmetry about zero angle of attack, as expected. The  $5.0^\circ$  model has less axial force than the model with no fin cant for all the angles of attack.  $C_X$  for both those models have similar values for angles of attack from  $-10.0^\circ$  to roughly  $-4.0^\circ$  and  $C_X$  for the  $5.0^\circ$  model continues to decrease to a value of about 0.91 and flattens out as the angle of attack increases. The  $15.0^\circ$  canted fin model has a totally different behavior. The maximum  $C_X$  value occurs at  $\alpha = -10.0^\circ$ , keeps flat to that value up to  $\alpha = -5.0^\circ$ , and then decreases linearly to 0.95 at  $\alpha = +5.0^\circ$ , and then increases again to reach 0.98 at  $\alpha = +10.0^\circ$ . This type of behavior is somewhat expected, since, when the fins are canted, at say  $10.0^\circ$ , those fins will be at zero angle of attack when the model's angle of attack is  $-10.0^\circ$ .

The normal force coefficient comparison is provided in Fig. 20b. The results for the  $5.0^\circ$  canted fin model are shifted slightly in a positive way. The  $15.0^\circ$  model has basically no trim at  $\alpha = 0.0^\circ$ . These are surprising results. One would expect that the trim normal force would increase with increasing fin deflection. At this Mach number, the  $15.0^\circ$  fin deflected model has basically no trim normal force while the  $5.0^\circ$  model exhibits a small value. A possible explanation is the fact that for  $5.0^\circ$ , there is some flow

inside the cells that create lift whereas at  $15.0^\circ$  the flow is blocked (no or less lift) and the flow deviates around the fin.

The static pitch moment coefficient about the base and the center of gravity are provided in Fig. 20c and 20d, respectively. The data about the base shows no major differences for all three models, no trim moments and a linear variation with angle of attack. When the data is shifted to the reference center of gravity, Fig. 20d, a different pattern emerges. There is quite a bit of scatter in the wind tunnel data. The only substantial trim moment measured occurred with the  $5.0^\circ$  model. The  $5.0^\circ$  and  $15.0^\circ$  fin deflected models have basically the same trend but different magnitudes. The  $5.0^\circ$  fin deflected model is statically stable from  $\alpha = -10.0^\circ$  to  $-4.0^\circ$ , and then the slope is positive as  $\alpha$  increases, indicating a static instability when  $\alpha$  is greater than  $-4.0^\circ$ . For all instances, the three projectile configurations are statically unstable in the range of angle of attack between roughly  $-5.0^\circ$  and  $+5.0^\circ$ .

The center of pressure location is provided in Fig. 20e. The data is not symmetric about zero as expected. At the higher angles of attack, only a few data points are behind the center of gravity.

### 3.5.1.2 *Mach 1.5 Comparison*

The axial force coefficient comparison at Mach 1.5 is provided in Fig. 21a. At this Mach number,  $C_{X0}$  is lowest for the model with no fin cant and it increases with increasing fin deflection angle. The results are skewed about  $\alpha = 0.0^\circ$ .

$C_N$  as a function of angle of attack is shown in Fig. 21b. At this Mach number, the normal force coefficient has the same behavior with angle of attack for all the fin deflections tested, except that they are shifted due to the trim force produced by the deflected fins.

$C_M^b$  and  $C_M^{cg}$  are compared in Fig. 21c and Fig. 21d, respectively. The trend versus angle of attack for  $C_M^{cg}$  is the same for all three models except that they are shifted by the trim moment due to the deflected fins. As expected, the negative trim force produces a positive trim moment. All the projectiles are statically stable.

The variation in the center of pressure location with angle of attack is shown in Fig. 21e.



### 3.5.1.3 Mach 2.5 Comparison

The results at Mach 2.5 for the axial force coefficient are shown in Fig. 22a.  $C_X$  for the projectile with no fin cant and the  $5.0^\circ$  one have basically the same pattern and magnitude as a function of angle of attack. The  $15.0^\circ$  model has the same pattern with incidence but is shifted upwards by roughly 10%. There is some symmetry about  $0.0^\circ$ .

The normal force coefficient has a similar trend as at Mach 1.5 (Fig. 22b), except that the trims are higher in magnitudes, as would be expected.

The pitch moment about the base and center of gravity are provided in Fig. 22c and 22d, respectively. The  $C_M^{cg}$  trim values at for the  $5.0^\circ$  and  $15^\circ$  models at zero angle of attack are 0.5 and 1.1, correspondingly, indicating a non-linear relationship with fin deflection.

$X_{CP}$  as a function of angle of attack for the three models are compared in Fig 21d.

## 3.5.2 Aerodynamic Coefficients versus Mach number

In this section, the main aerodynamic coefficients ( $C_{X0}$ ,  $C_{N\alpha}$ ,  $C_{M\alpha}^{cg}$  and  $C_{l\delta}$ ) will be compared for a roll orientation of  $0.0^\circ$  for the three fin deflections. The differences in the ISL and DRDC results are also included and will be commented upon. Repeated runs are also included.

The axial force coefficient at zero angle of attack vs. Mach number is shown in Fig. 23a. The pair of fins deflected at  $0.0^\circ$  and  $5.0$  basically have the same  $C_{X0}$  values over the whole Mach number range. The model with the pair of fins deflected at  $15^\circ$  has a  $C_{X0}$  higher by roughly 5.0% than the other two configurations and over the whole Mach number range. The ISL data at Mach 3.0 is encircled in the figures and if any DRDC data is enclosed within this circle, it is identified. There is a difference in the measured  $C_{X0}$  values between DRDC and ISL at Mach 3.0. The ISL results are roughly 15.0 % higher than the DRDC measured value. These are similar results as before with the same explanations.

Fig. 23b presents the normal force coefficient slope,  $C_{N\alpha}$ , as a function of Mach number for the same configurations. Similar trends as the previous group can be observed but the spread in the results for a particular Mach

number is less than the previous group. At Mach 1.5, the results are the same for the three configurations.

The Mach number effects on the pitching moment coefficient slope about the center of gravity ( $C_{M\alpha}^{cg}$ ) are presented in Fig. 23c. Similar trends as for the previous group can be observed but the spread in the results for a particular Mach number is slightly less. Yet again, the results for the pair of fin deflections at 15° stand out from the other two cases. One interesting fact in this case, is that, subsonically, the projectile is statically unstable for all fin deflections.

The center of pressure locations (about the base of the projectile) from the experimental tests are compared vs. Mach number in Fig. 23d for the three grid fin configurations. In this case,  $X_{CP0}$  is located in front of the center of gravity at Mach 0.6 for all the fin deflections. Similar comments hold as for the previous group of results at the other Mach numbers.

### 3.5.3 Main Conclusions for Group 3 Results

The main observations for the fins deflected to obtain trim were as expected supersonically, that is, the amount of trim increases with the fin deflection, but not linearly, and it increases as the Mach number increases. Subsonically, the projectile is unstable for three fin deflections and the results as a function of angle of attack are highly skewed about zero angle of attack.

## 3.6 Wind Tunnel Results – Various Fin Geometries

In this second series of wind tunnel tests, as mentioned previously, three other different fin geometries were investigated as shown in Fig. 2. They were only tested at DRDC and at 0.0° roll orientation and the angle of attack sweeps were from -5.0° to +15.0°. The Mach number range was also increased, by adding Mach 0.8 and Mach 4.0. There were no fin deflections on the models and the location of these fins on the missile body was the same as the thick fin one (A3\_1) with the same span and chord. The model with no fins attached was also tested. Some of the results presented here were previously published (Ref. 19) at a different center of gravity position.

The Mach number variations of the aerodynamic coefficients as a function of angle of attack for each configuration are provided in Annex D.

### 3.6.1 Aerodynamic Coefficients versus Incidence

In this section, the aerodynamic coefficients of each configuration are compared as a function of angle of attack at three Mach numbers, 0.6, 1.5 and 3.0. The comparisons at the other Mach numbers are furnished in Annex E. The results for the models with no fins are also included.

#### 3.6.1.1 Mach 0.6 Comparison

The axial force coefficient for the various configurations with angle of attack is provided in Fig. 24a for  $M = 0.6$ . The variation with angle of attack is mostly constant. The thick fin and the hexagonal shape fins have the same axial force coefficient, with the open base fin  $C_X$  slightly lower. The thin fin model has the lowest axial force coefficient, as expected.

The normal force coefficient for the different configurations is shown in Fig. 24b. Between  $-5.0^\circ$  and  $+5.0^\circ$ , only the thin fin model has a higher slope than the other models. At angles of attack higher than  $7.0^\circ$ , there are slight differences in the slopes of  $C_N$  for the other fins, and at  $15.0^\circ$  incidence they converge again.

Fig. 24c presents the static pitch moment coefficient about the center of gravity for all the configurations as a function of the angle of attack. The first observation is that the only model that is statically stable over the angle of attack range is the thin fin model, due to its negative slope. The other three finned projectiles are statically unstable between  $-5.0^\circ$  and  $+5.0^\circ$ . The open base, hexagonal and thick fin models become statically stable at  $5.8^\circ$ ,  $7.5^\circ$  and  $8.0^\circ$ , respectively.

The center of pressure as a function of angle of attack is compared for different models in Fig. 24d. The only model that has a center of pressure behind the  $X_{cg}$  is the thin fin model and the  $X_{Cp}$  of other models, at the lower incidences, are forward the  $X_{cg}$  and even in front of the model.

#### 3.6.1.2 Mach 1.5 Comparison

The Mach 1.5 results for the axial force coefficient for the various configurations with angle of attack are provided in Fig. 25a. The variation with angle of attack is constant for the thin and hexagonal shape finned models. The thick and thin fin models have a parabolic nature of  $C_X$  with incidence. The thin model has



the lowest  $C_X$  while the other three projectiles have a  $C_X$  of the same order of magnitude.

$C_N$  at this Mach number is compared in Fig. 25b.  $C_N$  for all the models, except the open base model, is the same for the whole range angle of attack tested. The open base has a slightly lower slope than the other three projectiles.

The static pitch moment coefficient about the  $X_{CG}$  is compared in Fig. 25c. The open base model is neutrally stable up to  $\alpha = 10.0^\circ$  and then turns statically stable at the higher incidences. All the other cases are basically statically stable. The thin fin model has a zero slope, or very small negative one, between  $\alpha = 3.0^\circ$  and  $7.0^\circ$  (indication of a marginal stability in this region), and a highly negative slope at the higher angles of attack. The hexagonal shape fins have a similar behavior but at a different angle of attack range.

$X_{CP}$  as a function of angle of attack is given in Fig. 25d. It can be noticed that the  $X_{CP}$  of the open base model is exactly at the  $X_{CG}$  location.

### 3.6.1.3 *Mach 3.0 Comparison*

At Mach 3.0, Fig 26a, the usual parabolic shape of  $C_X$  with angle of attack is observed. In this case,  $C_X$ , except for the thin fin model, have the same order of magnitude. The thick fin model has a higher variation with angle of attack than the open base and hexagonal fins.  $C_X$  for the thin model is roughly 35% lower than the other models.

Only  $C_N$  for the thin fin model (Fig. 26b) is slightly different than the other three fins for the angles of attack tested. The thick fin model has a slightly higher slope at the negative angles of attack.

The results for  $C_M^{cg}$  at Mach 3.0 are compared in Fig. 26c. In this case, all the models, except of course the model with no fins, are statically stable. The thin fin model has quite a different trend than the other three finned models. There appears to be three different slopes for the thin fin projectile depending on the angle of attack.

Between  $-1.3^\circ$  and  $+1.3^\circ$  degrees, the slope of  $C_M^{cg}$  is quite high (seems to correspond to the other models), then, between  $1.3^\circ$  and

7.0°, the slope is slightly negative (indicating marginal stability) and then the slope becomes highly negative at incidences higher than 7.0°. The trends of  $C_M^{cg}$  for the open base and hexagonal finned models are the same whereas the one for the thick finned model is slightly different.

$X_{CP}$ , for the five models is compared in Fig. 26d.

### 3.6.2 Aerodynamic Coefficients versus Mach Number

The tabulated data for the aerodynamic coefficients ( $C_{X0}$ ,  $C_{N\alpha}$ ,  $C_{M\alpha}^b$ ,  $C_{M\alpha}^{cg}$  and  $X_{CP0}$ ) as a function of Mach number are provided in Annex D for the thin fin, open base model, hexagonal shape fins and with the projectile with no fins.

The variation of the axial force coefficient at zero angle of attack,  $C_{X0}$ , with Mach number is given in Fig. 27a for all the configurations. The trend with Mach number for all the models is of the classical type planar fin. Overall,  $C_{X0}$  for the thick fin, the open base and the hexagonal shape fins are roughly the same, of the order of 1.0, with the open base model being slightly lower by 12% subsonically.  $C_{X0}$  for the thin fin model is about 30% lower than the other models for the whole Mach number range tested.

The difference in  $C_{X0}$ , relative to the thick fin model, for one fin alone is provided in Table 3. The hexagonal shape fin has relatively the same axial force, just slightly higher than the thick fin one by about 2%, and the variation increases to about 10% at the higher Mach numbers. The open base fin  $C_{X0}$  is similar to the thick fin one at the higher supersonic Mach numbers and it gets lower as the Mach number decreases, up to 13% at Mach 0.6. There is no doubt that the thin fin represents the best axial force alternative. It is less than the other projectiles by roughly 50% over the whole Mach number range. One interesting combination that would further decrease  $C_{X0}$  of the thin fin model subsonically would be to add an open base. This combination would decrease the total axial force very close to a plane fin model.

The normal force coefficient slope,  $C_{N\alpha}$ , is provided in Fig. 27b for all the concepts. Subsonically,  $C_{N\alpha}$  for the thin fin model is higher by about a factor of 2.0 than the other models. Strangely at Mach 0.6, the other fin types have the same  $C_{N\alpha}$  as the model with no fins. This implies that the fins for the thick fin, the open base and hexagonal shape models are totally useless at Mach 0.6 and to a certain extent at Mach 0.8. Supersonically, the trend of

$C_{N\alpha}$  with Mach number is opposite of a planar fin, that is  $C_{N\alpha}$  increases with Mach number while for a planar fin, it decreases with Mach number. At Mach 2.0 and above,  $C_{N\alpha}$  for the open base and the hexagonal shapes are the same, and the thick fin model has about 10% more  $C_{N\alpha}$ . There is a sudden loss of  $C_{N\alpha}$  at Mach 4.0 for these two models. At Mach numbers of 1.5 and 2.0,  $C_{N\alpha}$  for the thin fin model is slightly higher than the other models with the same trend with Mach number, then the slopes changes abruptly at Mach 2.5 to remain relative constant for the higher Mach numbers. There is a sudden loss of fin effectiveness for the thin fin model between Mach 2.0 and 2.5, for unknown reasons, while this occurred between Mach 3.0 and 4.0 for the other two configurations.

Fig. 27c presents the Mach number effects on the pitching moment coefficient slope,  $C_{M\alpha}^{cg}$ . Subsonically, only the thin finned model is statically stable. At Mach 1.5 the open base model is statically unstable while the other finned configurations are stable, with the thin finned model having more stability. Between Mach 2.0 and 4.0, the  $C_{M\alpha}^{cg}$  trend with Mach number for the open base, hexagonal shape and thick finned models are the same, that is, the static stability increases with Mach number, except at Mach 4.0 where there is a sudden loss of fin effectiveness. It should be noted that this trend is opposite of a classical planar finned projectile. The thick finned model has more static stability than the other two models and the difference increases as the Mach number increases. As with the  $C_{N\alpha}$  results, the trend of  $C_{M\alpha}^{cg}$  with Mach number for thin finned model is peculiar. At Mach 1.5 and Mach 2.0, it shows more static stability then the other models by 70%, and then there is a sudden loss of static stability between Mach 2.0 and Mach 2.5.  $C_{M\alpha}^{cg}$  for the thin finned model between Mach 2.5 and 4.0 is below the other models by a factor of 2 to 3, and this difference increases with Mach number.

The center of pressure at zero angle of attack ( $X_{CP0}$ ) is provided in Fig. 27d. Subsonically, only the thin finned model has the center of pressure located aft of the center of gravity and it is constant at those two Mach numbers tested. At Mach 0.6,  $X_{CP0}$  for the thick finned model is even in front of the model, while it is just at the nose tip for the hexagonal shape finned one. At Mach 0.8, the center of pressure moves backwards on the models for the open base and the hexagonal configurations. At Mach 1.5,  $X_{CP0}$  for the open based finned model is just ahead of the center of gravity, while it is behind the center of gravity for the other models. At the higher Mach numbers, all the models have the center of pressure behind the center of gravity, indicating good static stability. There is again a change in the trend in the results between Mach number 2.0 and 2.5 for the thin finned model. At Mach 1.5 and 2.0,  $X_{CP0}$  is aft of the other models and at Mach 2.5 and above, it is

ahead. Also,  $X_{CP0}$  for the thin finned model remains relatively constant with Mach number, while it moves further back on the model for the other projectiles, indicating more stability as the Mach number increases.

### 3.6.3 Main Conclusions for Various Fin Geometries Results

Overall, the trend of  $C_{N\alpha}$  and  $C_{M\alpha}^{cg}$  for the thick finned, open base and hexagonal shaped finned projectiles were opposite of a standard planar finned projectile. That is, the effectiveness of the fins and the static stability increases as the Mach number increases, supersonically. On the other hand, subsonically, they were statically unstable while for a planar fin it is statically stable.

This was not the case for the thin finned model. In this instance, the projectile was stable subsonically and supersonically, but there was an abrupt change in the trends of  $C_{N\alpha}$ ,  $C_{M\alpha}^{cg}$  and  $X_{CP0}$  between Mach 2.0 and 2.5. There was also a change in these two coefficients for the other models but at a higher Mach number.

It was also shown that the drag coefficient could be reduced to acceptable levels, especially with very thin fins.

## 3.7 Discussion of Results

As mentioned previously, a possible explanation for the results seen here, was that some fins choke. This was seen on another fin type (Refs. 1 and 4), and occurred only in a very narrow band of Mach number and not over a whole range of Mach number as seen here. Calculations similar to Ref. 1 were conducted on the different fin types tested here and these are provided in Annex C. The critical Mach numbers in our cases were 0.548, 0.744 and 0.542 for the thick, thin and hexagonal fin concepts. The area ratios and cell width in our cases are similar to those of Ref. 1. The only differences is the web thickness for the thick and hexagonal fins which are a factor of 3 higher than those of Ref. 1, and the thin fin model, in our case. They postulate that a choking occurs, close to the critical choking Mach number, which causes a sudden loss of normal force, and a forward movement of the center of pressure, causing a static instability if the center of gravity is not forward enough. This is exactly what is observed here for the thick and hexagonal fin shapes but over a much wider range in Mach number. It is possible that the flow is not stated, i.e. it is always choked. The thin model seems to behave like the results of Ref. 1 but the choking was not witnessed in the wind tunnel since it was tested at discrete Mach numbers, and the critical Mach number was definitely missed. In the free-flight tests there are possible transient effects as a function of Mach number and angle of attack which could have some cells choked and not others.

Another possibility they bring forward is that the choking produces a reduced pressure field acting on the missile body aft of the fins causing the center of pressure to move forward.

## **4. Free-Flight Tests**

### **4.1 Aeroballistic Range**

#### **4.1.1 Facility Description**

The DRDC-Valcartier aeroballistic range (Refs. 20 and 21) is an insulated steel-clad concrete structure used to study the exterior ballistics of various free-flight configurations. The range complex consists of a gun bay, control room and the instrumented range (Fig. 28). A massive blast wall is located in front of the building to stop sabot pieces and minimize vibrations transmitted to the range structure and instrumentation. Projectiles of calibers ranging from 5.56 to 155 mm, including tracer types, may be launched. Large caliber models have been fired up to Mach 7.

The 230-meter instrumented length of the range has a 6.1-m square cross section with a possibility of 54-instrumented sites along the range (Fig. 29). All the stations were used for these trials. These sites house fully instrumented orthogonal shadowgraph stations that yield photographs of the shadow of the projectile as it flies down the range. The maximum shadowgraph window, an imaginary circle within which a projectile will cast a shadow on both reflective screens, is 1.6 meters in diameter. There are also four Schlieren stations (two operational for these tests) at the beginning of the range that yield high quality flow photographs. The range is also air conditioned to maintain a constant relative humidity of approximately 25%. The nominal operational conditions of the range are 20° C at standard atmospheric conditions. The spark source and reference point locations that were used were deduced from a standard survey. A dynamic calibration (Ref. 22) was conducted in the X, Y, X,  $\theta$  and  $\psi$  coordinates

#### **4.1.2 Models and Test Conditions**

##### **4.1.2.1 *Projectile Configuration***

The free-flight projectiles were ballasted to obtain a center of gravity at approximately 4.05 calibers from the nose of the projectiles to assure static stability at all the tested Mach numbers. The ogive of the model was made of a high-density alloy and the fins and the cylindrical portion of the projectile were made of an aluminum alloy. The nominal physical properties of the models tested are given in Table 4 and the physical properties of each test projectile are listed in Table 5.

The free-flight models were modified by the addition of a roll pin to measure the projectile's roll orientation in the aeroballistic range (Fig. 31).

#### **4.1.2.2 Sabot Design**

Since the model configuration in this case is fin stabilized, a smooth bore gun was utilized. The standard gun employed at DRDC to fire fin-stabilized projectiles of these dimensions in the aeroballistic range is a 110-mm smooth bore gun.

A schematic of the sabot design for the A3 projectile is shown in Fig. 30. It is a two-petal sabot design made of aluminum. It had four projectile centering screws at the front of the sabot. The lengths of the saw cuts on each side were adjusted to obtain adequate petal separation for the expected velocities. A sabot base seal pad was also used to prevent gas leakage past the sabot body.

A pivot pin, which is in line with the saw cuts, was added to force the sabot opening at that point. A polycarbonate ring with a 5° angle is positioned at the aft end of the sabot. There are two reasons for this. The first one, is to have a good pressure seal between the sabot and the gun tube so as to be able to have a known shot start pressure which helps in having consistent muzzle velocities at the same propellant charge mass. The second reason is that, as the sabot leaves the gun tube, the high radial pressure acting on the rear ring relative to the front part, causes the pivoting action at the pivot point of the sabot petals. The mass of the combined sabot-projectile was approximately 2.8 kg.

A photograph of the sabot-model package is shown in Fig. 31. The details of the sabot design as well as the tests that were conducted to verify the sabot-model integrity at launch are supplied in Ref. 18.

#### **4.1.2.3 Test Conditions and Particularities**

Eleven projectiles were fired in the aeroballistic range program with the 110 mm smooth bore gun. The range conditions for each test projectile at time of firing are indicated in Table 6. The muzzle velocities ranged (Table 7) from a low of 531 m/s (Mach 1.5) to a maximum of 1215 m/s (Mach 3.5) which yielded Reynolds number, based on the length of projectile, between  $9.7 \times 10^6$  and  $22.7 \times 10^6$ , respectively. The initial angles of attack were from a low of 2.3° to a maximum of 10.5°.



Typical sabot separation photographs taken at 9.2 m from the muzzle for shot K02 and K10, fired at muzzle velocities of 541.2 m/s and 1136.9 m/s, respectively, are shown in Figs. 32a and 32b, respectively. Schlieren photographs and shadowgraphs are provided in Figs. 33 and 34.

The numbering scheme to refer to the shots is as follows. The shot numbers are identified by one letter followed by 6 digits, as for example K030501. The letter corresponds to a particular configuration. The first four numbers (0305) indicate the date (year and month) that the projectile was fired in the range. The last two digits correspond to the shot number for that particular configuration. For the example given above, the shot number corresponds to the first shot that was fired in the range in May 2003. For convenience, the shot numbers are usually referred to by the letter and the shot number, K01.

#### **4.1.3 Free-Flight Data Reduction**

The first part of the data analysis process is to calculate the trajectories of the projectiles in the aeroballistic range facility coordinate system. The developed films are scanned and read with the CADRA system (Ref. 23). CADRA is a user-friendly, turnkey system for reducing shadowgraphs to aerodynamic data. The CADRA system hardware includes an Apple PowerPC CPU, monitor, keyboard, pointing device, digitizing device, and mass storage devices; the software components include CADRA1. CADRA1 has tools that identify images of the model's shadow and fiducial system in each shadowgraph, measure the positions of these images, and transform these measurements to three dimensional trajectory coordinates. CADRA1 uses measurement techniques that give sub pixel accuracy and it can automatically read a sequence of digitized photographs.

Extraction of the aerodynamic coefficients and stability derivatives is the primary goal in analyzing the trajectories measured in the aeroballistic range. This was done by means of the Aeroballistic Range Facility Data Analysis System (ARFDAS, Ref. 24) described in Fig. 35. These programs incorporate a standard linear theory and a six-degree-of-freedom (6DOF) numerical integration technique. The 6DOF routine incorporates the Maximum Likelihood Method (MLM) to match the theoretical trajectory with the experimentally measured trajectory. The MLM is an iterative procedure that adjusts the aerodynamic coefficients to maximize a likelihood function. The application of this likelihood function eliminates the inherent assumption in least square theory that the magnitude of the measurement noise must be consistent between parameters (irrespective of units). In general, the aerodynamic coefficients are nonlinear functions of angle of attack, Mach number and roll angle.



ARFDAS represents a complete ballistic range data reduction system capable of analyzing both symmetric and asymmetric models. The essential steps of the data reduction system are to (1) assemble the dynamic data (time, position, and angles) from the CADRA system, model measured physical properties and atmospheric conditions, (2) perform linear theory analysis, and (3) perform 6DOF analysis.

These three steps have been integrated into the data analysis system to provide the test scientist with a convenient and efficient means of interaction. At each step in the analysis, permanent records for each shot are maintained so that subsequent analyses with data modification are much faster.

The 6DOF data reduction system can also simultaneously fit multiple data sets (up to five) to a common set of aerodynamics. Using this multiple-fit approach, a more complete range of angle of attack and roll orientation combinations is available for analysis than would be available from a single flight. This increases the accuracy of the determined aerodynamic coefficients over the entire range of angles of attack and roll orientations.

The aerodynamic data presented in this report were obtained using the fixed-plane 6DOF analysis (MLMFXPL) with both the single- and multiple-fit data correlation techniques. The equations of motion have been derived in a fixed-plane coordinate system with Coriolis effects included. The formal derivation of the fixed-plane model is given in Ref. 25.

All the results given here were reduced after the dynamic calibration biases were accounted for in the  $X$ ,  $Y$ ,  $X$ ,  $\theta$  and  $\psi$  coordinates. The methodology of the dynamic calibration for the aeroballistic range is explained in (Ref. 22).

## **4.2 Open Range Test Site**

### **4.2.1 Experimental Site, Instrumentation and Test Conditions**

The trials were conducted during nighttime at the ISL open range test site only to improve the resolution of the photographs obtained in the DRDC aeroballistic range facility. Flow visualization was obtained by means of two orthogonal shadowgraph stations located inside a shelter as shown in Figs. 36a and 36b.

All the models were fired from a 90 mm powder smooth bore gun. Velocities were measured and the sparks were triggered by means of two optical gates. The sabot pieces were stopped by two separate walls made of wood and concrete blocks. The projectiles were recovered after the shelter in a recovery system filled up with sand.

A schematic of the test setup is shown in Fig. 36c.

Five projectiles were fired at muzzle velocities ranging from 545.7m/s (Mach 1.59) to a maximum of 1028.3m/s (Mach 3.01). Four firings were successful and one was missed due to spark defects.

## **4.2.2 Models**

### **4.2.2.1 Projectile configuration**

The dimensions of the tested free-flight projectiles were identical to the projectiles fired at the aeroballistic range facility. In this case, the ogive of the model was made of brass, the cylindrical portion of the projectile was made of a Zicral aluminum alloy and the fins were made of steel. The grid fins had zero fin deflection angle.

### **4.2.2.2 Sabot Design**

A schematic of the sabot design for the projectiles is shown in Fig. 37a. It is a four-petal sabot design made of “polyoxyméthylène” and followed by an aluminum pusher plate. A sabot base seal pad was also used to prevent gas leakage past the sabot body. The projectile was centered on the pusher plate by grooves located at the projectile base. The lengths of the saw cuts on each side were adjusted to obtain adequate petal separation for the expected velocities. The mass of the combined sabot-projectile was approximately 2.0 kg. A photograph of the sabot-model package is shown in Fig. 37b.

## **4.3 Free-Flight Results and Discussions**

The aerodynamic coefficients and stability derivatives that were reduced from the free-flight trajectories measured in the aeroballistic range are presented in tabular form for the linear theory analysis and in both tabular and plotted format for the 6DOF reductions. All of the determined aerodynamic coefficients are given at the mid range measured Mach number.

### **4.3.1 Flow Visualization**

For completeness, free-flight Schlieren photographs of the A3\_1 configuration are provided in Fig. 33 at Mach 1.53 and 2.12 as well as a series of shadowgraphs for shot K01 at Mach numbers of 1.53, 1.46 and 1.36 in Fig. 34. It is clearly seen that the web bow shock in Fig. 34 is very close to the fins at Mach 1.53 and as the projectile decelerates it distances itself from the fin. The recompression shock in front of the fins is as high as the fin in that Mach number range.

To increase the resolution of these photographs, another series of flow visualization were made at the ISL open range test site. They consist of direct orthogonal shadowgraphs (Fig. 38) conducted at Mach numbers of 1.6, 2.4 and 3.0. Figs 38a to 38g show some examples of the results. As mentioned previously, models had zero fin deflection angles. Figures 38a and 38b show the base flow details for  $M=1.59$  at  $\alpha = 0.2$  and  $4.8^\circ$ , respectively. As shown previously, one can see that the three-dimensional flow field is as complicated as the one observed from the wind tunnel visualization. For both angles of attack, one can see the strong recompression and the detached web bow shock generated ahead of the fin. Behind the fin, one can see the interaction of multiple shock waves generated by the top edge of the fins and each grid cell. Also observed are shock systems that result from the grid fins located in the span wise direction. As the Mach number increases (Figs. 38c, 38e and 38g), the web bow shock moves closer to the fin and the separation region ahead of the fin becomes smaller and can be compared to the schematic of Fig. 13. Behind the fin, the multiple shocks waves emanating from each grid cell seem to merge and their intensity becomes stronger. Again, only CFD predictions can help to better understand such highly complicated flow fields.

#### 4.3.2 Linear Theory Results

The linear theory parameters deduced from the decoupled motion are provided in Table 8. The magnitudes of the angles of attack varied from a low of  $2.3^\circ$  to a maximum of  $10.5^\circ$ . The amplitude of the initial nutation and precession arms, KF and KS, and the mean squared yaw (Dbsq) provides an indication of these angles of attack.

In all the cases the shots were dynamically stable as observed by the negative nutation and precession damping modes (LF and LS). The frequencies (WF and WS) are consistent. The trims are quite evident (KT) and these are due to the  $0.5^\circ$  deflected fins.

The aerodynamic coefficients deduced from the linear theory parameters are presented in Table 9. The methodology to obtain the aerodynamic coefficients is explained in Ref. 24. The aerodynamic coefficients ( $C_{X0}$ ,  $C_{M\alpha}^{cg}$ ,  $C_{Mq}$ ,  $C_{lp}$  and  $C_{l\delta}$ ) are consistent. There are some variations in  $C_{Mq}$  and  $C_{N\alpha}$  and this is due, in most cases, to the low angles of attack. This scatter is expected in these cases. All the models were statically and dynamically stable.

The standard deviation errors in the angular motion (E-ANG) from the linear theory analysis (Table 9) are of the order of  $0.3^\circ$ . This suggests that the linear theory analysis does an adequate job in reducing the coefficients, as would be expected at low angles of attacks. The 6DOF reduction technique of the next section and especially the multiple fit processes will allow a better

determination of the aerodynamic coefficients. The standard deviation errors in the downrange and in the swerve directions are a bit high, of the order of 2.0 mm and 1.5 mm, respectively.

### 4.3.3 Six-Degree-of-Freedom Results

The determined aerodynamic coefficients, their standard deviation errors, and the standard deviation errors between the theoretical and experimental trajectories for the axial, angular and roll motions are given in Table 10 and Table 11 for the single- and multiple-fit data reduction techniques, respectively. The moment reference centre for the moment coefficients was at 40.5% of the length from the nose of the projectile (4.05 cal). All the results are given at the mid-range Mach number for the single-fit data reductions and at the average mid-range Mach numbers for the multiple-fit data reductions

A coefficient that appears with a value and a (\*) in parentheses directly below, indicates that this coefficient was held constant and one that has a (-) in parentheses indicates that this coefficient was solved for and that the standard deviation error for this coefficient was higher than 100%, that is, it does not influence the fit and it is considered undetermined. Those with numbers in parentheses represent the standard deviation error for that particular coefficient

The multiple fit groups were chosen by Mach number and four groups of multiple fit data reductions were conducted, as given in Table 11. Shot K12 was not included in a multiple fit since the results did not follow the main trend of the other results. This was also seen in the wind tunnel results for this configuration.

Appendix F presents, for every test shot, the total angle of attack history with the observed angular motion and the theoretically determined one with the reduced aerodynamic coefficients. The experimental data points (closed circles) and the calculated trajectory (continuous line) from the determined coefficients are compared. This allows verification that the reduced aerodynamic coefficients do fit the experimental trajectory satisfactorily. For every shot, the total angle of attack and the angular motion plots in pitch and yaw are given as a function of the downrange coordinate.

The spin rates obtained downrange, for the two-degree nominal fin cant angle, were of the order of  $-20.0^\circ$ /m. Some cases showed a traverse in resonance.

As seen from the Tables 10 and 11, all of the main aerodynamic coefficients were well determined as indicated by the low standard deviation of fits on the coefficients. The aerodynamic force and moment trims were solved for all the shots.

In some instances, the results showed more variation in  $C_{lp}$  than would be expected at the same Mach number for all the configurations. This might be due to the tolerances in the canted angles for roll, and those deflected for trim for these particular fins, which was  $\pm 0.1^\circ$ . It would be expected that just a small deflection from the reference canted value, that the wetted area to the cross flow increases significantly, as compared to classical fins. Therefore, for some configurations, the multiple-fit data reductions were conducted as follows. For a multiple shot grouping, the values  $C_{lp}$  were held constant at the average of the single-fit results and the variations from this value were then uniquely solved for each shot. These variations are also given in the multiple-fit result tables as well as their standard deviations. This was conducted for the multiple fit data reductions at Mach 2.218 and 2.604. The probable errors of fits improved significantly in those two cases.

For shot K01 and K02, the roll data was limited to only the first 20 stations and the single fit  $C_{lp}$  values were held constant at the multiple fit values and  $C_{l\delta}$  was solved for.

In the high angle of attack shots, the non-linear terms,  $C_{N\alpha^3}$  and  $C_{M\alpha^3}$  were well deduced in the multiple fit data reductions as well as induced in-plane and induced side moments in some cases. The single fit data reductions were kept constant at the multiple fit values for these coefficients for the low angle of attack shots.

The data reduction process solves for a total roll moment coefficient due to fin cant  $C_{l\delta}$ . This coefficient produces the required moment to impose a roll motion or desired spin rate on the projectile. It is solved individually when conducting multiple fits since it is unique for a particular projectile or fin cant. The coefficient that is usually published is  $C_{l\delta}$  and in this case, per radian. The combined values  $C_{l\delta}$  and the computed  $C_{l\delta}$  based on the nominal fin cant of  $2.0^\circ$  are given in Table 12 for each individual shot number. The values of  $C_{l\delta}$  are consistent.

The standard deviation errors of the single and multiple fits are of the order of 1.0 mm in the downrange coordinate, 1.4 mm in the swerve motion,  $0.12^\circ$  in pitch and yaw and of the order of  $6.0^\circ$  in roll. These errors of the fits are consistent when compared with other test programs conducted in the DRDC-Valcartier aeroballistic range. The 6DOF probable errors of fits are smaller than those of the linear theory because of the better mathematical modeling of the motion, such as the inclusion of aerodynamic trims, angle of attack dependent terms and variations with Mach number.

#### 4.3.4 Comparison of 6DOF Single- and Multiple-Fit Results

Comparisons of the reduced aerodynamic coefficients from the 6DOF data reduction techniques with the single- and multiple-fit results are given in Figure 39. The single fit data points (AB - SF) are shown as open circles while the multiple fit data reduction results (AB - MF) are given as solid circles.

The axial force coefficient at zero angle of attack ( $C_{X0}$ ) as a function of Mach number is shown in Fig. 39a.  $C_{X0}$  is about 1.25 at Mach 1.5 and then reduces linearly with Mach number to roughly 0.8 at Mach 3.1. The last data point at Mach 3.3 is 0.95. The agreement is excellent between the single and the multiple fits.

$C_{N\alpha}$ , the normal coefficient slope, versus Mach number is displayed in Fig. 39b. There is a little bit of scatter in the single fit results due to some low angle of attack cases.  $C_{N\alpha}$  is 4.6 at Mach 1.5 increases linearly to 6.3 at Mach 3.1 and then decreases to 5.9 at Mach 3.3. The trend with Mach number is similar to the wind tunnel results for the thick fin configuration. Again the agreement is very good between the single and multiple fits.

The variation of the pitching moment coefficient slope,  $C_{M\alpha}^{cg}$ , with Mach number are shown in Fig. 39c. The scatter in the single fit results for  $C_{M\alpha}$  is higher than would be expected for this coefficient.  $C_{M\alpha}^{cg}$  is of the order of -4.0 at Mach 1.5 and 2.5, and then increases in magnitude to -6.5 at Mach 2.6 and -7.6 at Mach 3.1. There is sudden change in the trend of static stability between Mach 3.1 to 3.3, that is, there is a sudden loss of roughly 13%. Again, a similar trend was observed in the thick and thin fins configurations in the wind tunnel results.

The center of pressure location as a function of Mach number is presented in Fig. 39d. It varies from 5.2 cal from the base at Mach 1.5 to 4.76 cal at Mach 3.3.

The determined pitch damping moment coefficient,  $C_{Mq}$ , as a function of Mach number, is presented in Fig. 39e.  $C_{Mq}$  is of the order of -270 from Mach 1.5 to 2.6 and then there is a sudden increase in magnitude to -550 at Mach 3.1 to decrease again to -290 at Mach 3.3. There is a bit of scatter in the single fit results for this coefficient probably due to the low angle of attack cases.

$C_{lp}$ , the roll damping coefficient, is demonstrated versus Mach number in Fig. 39f. It is of the order of -4.8 over the whole Mach number range. The scatter in the two middle groups was explained in the last section.

The trend of  $C_{l\delta}$  with Mach number is offered in Fig. 39g. There is some scatter, and the nominal value is of the order of -0.72 for all the Mach number range tested with a slight increase in magnitude as the Mach number increases.

The trim moments were very well determined and to a lesser extent for the trim force, as seen in Table 10 and they improved the fits noticeably when they were included in the fitting process. These trims are due to any manufacturing tolerances and, in this case, mostly to the deflected fins at  $0.5^\circ$ . A trim angle can be calculated separately from the force and the moment terms. The total moment trim is:

$$C_{M\delta} \delta_T = \sqrt{(C_{M\delta} \delta_A)^2 + (C_{M\delta} \delta_B)^2}$$

with the total trim angle calculated as:

$$\delta_T = \arcsin\left(\frac{C_{M\delta} \delta_T}{C_{M\alpha}}\right)$$

The force trims are calculated in the same manner. The trend of the total trims angle from the force and moment calculations is shown in Fig. 39h and the magnitudes are not the same from the two different methods at the same Mach number. Usually, the trim moments are better resolved than the normal force trims. The trim angle varies from roughly  $0.3^\circ$  to a high  $1.7^\circ$ . The scatter in the results is also expected.



## 5. Computational Fluid Dynamic Analysis

A Computational Fluid Dynamic (CFD) analysis was conducted, under contract to SNC-TEC (Ref. 26) for predicting the aerodynamic coefficients of these novel control surfaces. The wind tunnel configuration A3\_1 as well as the aeroballistic range model with the thick fin without deflections were investigated.

The computations for the wind tunnel model were conducted at Mach numbers of 0.6, 1.5, 2.5 and 3.0, and at angles of attack of 0.0°, 2.5°, 5.0°, 7.5°, 10.0° and 15.0°. The static aerodynamic coefficients ( $C_{X0}$ ,  $C_N$ , and  $C_M$ ) and the center of pressure locations were calculated for each condition. Also, the static pressures in the middle cell for the wind tunnel model were extracted and compared with those obtained from an oversized fin (Ref. 27).

For the aeroballistic range model, the computations were only conducted at the supersonic velocities ( $M = 1.5, 2.5$  and  $3.5$ ) at an angle of attack of 2.5° for the same aerodynamic coefficients. The roll damping coefficient at zero incidence was also computed at the three Mach numbers.

The slopes were then calculated for each model at 2.5° and these will be compared. The comparison with the experimental data will be conducted in the next section.

Mach number distributions as well as velocity vector fields will be presented at the various Mach numbers and angles of attack. These will be compared with shadowgraphs and/or Schlieren photographs obtained from the wind tunnel or the aeroballistic range.

### 5.1 Computational Fluid Dynamic Code

The CFD simulations to predict the flowfield and static aerodynamic coefficients were conducted with the Navier-Stokes CFX 5.6 (Ref. 28) developed by AEA Technology now owned by ANSYS Inc. The simulations were performed in parallel on a PC Pentium III – 1Ghz with 2 processors and 2 G bytes of RAM memory.

#### 5.1.1 Code Description

CFX 5.6 was developed by AEA technology when this company purchased ASC that had developed the TASCFlow3D code. ANSYS Inc. has recently acquired the CFX package from AEA Technology. Fundamentally, the CFX 5.6 code uses the same method as the TASCFlow3D. The pre-processor now incorporates a new CAD import and mesh generating tool that is the result of a team effort between the CFX and ANSYS development teams. More details on the theory can be found in Ref. 28. The code has three advection schemes: a first order low resolution (LR) advection scheme that is mainly used to generate a better initial guess as it is only first order accurate, a high



resolution (HR) scheme and a scheme for which a blend factor is specified. The blend factor blends between first and second order advection schemes to calculate the advection terms in the discrete finite volume equations. A value of 0.0 is equivalent to using the first order advection scheme and it is the most robust option. A value of 1.0 uses second order differencing for the advection terms. This setting is more accurate but less robust. With the high-resolution setting, the blend factor values vary throughout the domain based on the local solution field in order to enforce a boundedness criterion. In flow regions with low variable gradients, the blend factor will be close to 1.0 for accuracy. In areas where the gradients change sharply, the blend factor will be closer to 0.0 to prevent overshoots and undershoots and maintain robustness. For most simulation runs, a specified blend factor of 0.75 (BF 0.75) was used and this gave good convergence characteristics.

Various turbulence models are available in the code. In the past, the  $\kappa$ - $\epsilon$  model was principally used. However, the Shear Stress Transport (SST) model is now available in the code and it was identified as the best model to use for simulation of separated flows of grid-finned configurations.

### 5.1.2 Computational Mesh

The projectile geometry and the exterior domain were generated with Solid Works. An all-hexahedral mesh was used for this mesh that was generated with ICEM CFD – Hexa. In generating the meshes, boundary layer mesh spacing was used near the missile body and grid fin surfaces. The exterior domain dimensions were extended at lower Mach numbers. The domain dimensions were modified in Solid Works and new meshes could be easily generated for a different geometry and Mach numbers. Sloped far-field surfaces were used for all supersonic simulations to ensure that the flow is out of the domain when a supersonic outlet boundary condition is applied.

Various types of mesh were utilized for the simulations. In fact, the results to obtain the normal force and static moment coefficients at the various angles of attack were performed with a rectangular hexahedral mesh covering a  $180^\circ$  domain. For the supersonic speeds, the computational domain did not include the base flow. Even though there was flow separation behind the fins, the flow did eventually return to supersonic conditions at the back and did not cause any convergence problems. This can be made for supersonic flows but the base flow had to be included for the subsonic regime.

To determine the axial force coefficient at zero angle of attack, a  $90^\circ$  domain was employed and the base flow was taken into account. In this case, the external domain was in a circular form with a sloped far-field surface as for the other cases.

The mesh contained 1,079,000 nodes for the supersonic speeds without the base flow and 1,709,000 nodes when the base flow was included. On both domains, the node distribution was similar on the body of the missile, and all

the additional nodes were added at the base to simulate the base flow. Many nodes were added near the fins where shock interactions were anticipated (Fig. 40).

### 5.1.3 Boundary Conditions

For the supersonic cases, the inlet condition was defined as a “supersonic inlet”. The static pressures and temperatures were those of the wind tunnel conditions. For the subsonic case, the total pressure was specified at the inlet. Since the total pressure is constant upstream of the body, and all the flow is into the domain, the inlet boundary can be relatively closer to the body, as compared to using a velocity and temperature specification as a way to set the Mach number. The subsonic flow upstream of the body feels the presence of the object downstream. The outlet condition “supersonic outlet” was used for the supersonic cases while the static pressure was utilized for the subsonic case.

At all the speed regimes, a “symmetry” condition was defined on the surface where the model was cut.

The projectile represents a wall condition. The log-law model was used as an adiabatic wall and the SST and the  $\kappa$ - $\epsilon$  models were used in most of the cases for comparison between both models in the prediction of the flow and the aerodynamic coefficients.

## 5.2 Aerodynamic Coefficients Predictions

Only the results of the projectile with the grid fins with the highest resolution schemes (BF 0.75 or HR) and the SST turbulence model will be presented. Computations (Ref. 26) were also conducted with the  $\kappa$ - $\epsilon$  and a BF of 0.75 at the same angles of attack and Mach number as the SST calculations. Also, a comprehensive analysis was done with the projectile without the fins at higher angles of attack and at more Mach numbers

### 5.2.1 Wind Tunnel Model

The reference diameter for the computations was 20.0 mm, as with the wind tunnel test model. The computations were conducted at Mach numbers of 0.6, 1.5, 2.5 and 3.0, and at angles of attack of 0.0°, 2.5°, 5.0°, 7.5°, 10.0° and 15.0°. The static aerodynamic coefficients ( $C_N$  and  $C_M$ ) and the center of pressure location were calculated at each condition and these are provided in Table 13. The axial force coefficient at zero angle of attack is given in Table 14. All the computations were done with the SST turbulence model and at the highest resolution scheme with BF 0.75. The mesh size that was used for the computations is also indicated.

The computed normal force coefficient, as a function of angle of attack, is shown in Fig. 41a at the four Mach numbers. The computations indicate a nonlinear variation with angle of attack at the four Mach numbers.  $C_N$  at Mach 2.5 and 3.0 are very similar.

The predicted pitch moment coefficient about the base and the center of gravity position are presented in Fig. 41b and 41c, respectively. At Mach 0.6, the computed  $C_M^{cg}$  indicate a marginal stability between  $0.0^\circ$  and  $5.0^\circ$  incidence and static stability at the higher angles of attack. At Mach 2.5 and 3.0, the projectile is statically stable over the whole angle of attack range. At Mach 1.5, there is a sudden change in the trend of  $C_M^{cg}$  past  $\alpha = 10.0^\circ$ .

The estimated center pressure is provided in Fig. 41d. As the pitch data indicated, the center of pressure is forward of the center of gravity at Mach 0.6.  $X_{CP}$  for the other Mach numbers are basically constant with angle of attack, except for a slight shift forward for  $\alpha = 15.0^\circ$  at Mach 1.5.

The computed slopes for  $C_{N\alpha}$ ,  $C_{M\alpha}^b$  and  $C_{M\alpha}^{cg}$  were taken at  $2.5^\circ$ , and  $X_{CP0}$  was calculated from the ratio of the first two. These results are provided in Table 15.

## 5.2.2 Aeroballistic Range Model

The reference diameter for the computations was 30.0 mm, as with the test models fired in the aeroballistic range. The computations were conducted with the atmospheric conditions of the aeroballistic range at Mach numbers of 1.5, 2.5 and 3.5, and at an angle of attack of  $2.5^\circ$ . The static aerodynamic coefficients ( $C_N$  and  $C_M$ ) and the center of pressure location were calculated for each condition and these are provided in Table 16. Some convergence problems were encountered at Mach 1.5 and 3.5 with the SST turbulence model, without any viable reasons.

The axial force at zero angle of attack is given in Table 17. Convergence problems were also experienced with the SST turbulence model with the second order scheme, and therefore the Low Resolution (LR) scheme was utilized with the  $\kappa$ - $\epsilon$  turbulence model in this case. Even with these changes, convergence was not achieved at Mach 2.5.

The roll damping coefficient was also calculated at zero angle of attack. In this case, the computational domain was defined as a rotating spinning frame at the spin rate of the projectile (30.0 °/m) and the inlet condition was stationary. The  $\kappa$ - $\epsilon$  turbulence model was employed and the results are provided in Table 18. It should be noticed that results could only be obtained with a BF of 0.50 at Mach 3.5.

The computed slopes for  $C_{N\alpha}$ ,  $C_{M\alpha}^b$  and  $C_{M\alpha}^{cg}$ , taken at  $2.5^\circ$ , and  $X_{CP0}$  was calculated from the ratio of the first two are provided in Table 19.

No graphical presentations will be provided for the predicted data for this model since the computations were very limited in angle of attack. The slopes and the other computed coefficients at zero angle of attack will be compared against the wind tunnel and free-flight test data in the forthcoming sections.

### 5.2.3 Comparison of Predictions for the two Models

The computed results for  $C_{X0}$ ,  $C_{N\alpha}$ ,  $C_{M\alpha}^{cg}$  and  $X_{CP0}$  for the wind tunnel and aeroballistic range models are compared in Fig. 42 and at the supersonic velocities only. Again as a reminder, the only difference in the models was that the base support of the grid fin for the aeroballistic range model was a bit smaller than the wind tunnel one, and that this represented only a 3% reduction in total wetted area in calibers. The diameters were also different, 20.0 mm and 30.0 mm, respectively. The  $Re_l$  were of course different, as provided in Table 2.

The predicted axial force coefficient at zero angle of attack ( $C_{X0}$ ) as a function of Mach number is shown in Fig. 42a.  $C_{X0}$  is predicted to be about 1.2 for both models at Mach 1.5. At the higher Mach numbers, the wind tunnel model predicted values are just slightly below those of the aeroballistic range model.

The estimated  $C_{N\alpha}$  versus Mach number is displayed in Fig. 42b. The agreement between the two sets of data in this case is very good. The wind tunnel predicted results lie just above the aeroballistic range model and the Mach number trends are on the whole, the same.

The differences in the calculated pitching moment coefficient slope,  $C_{M\alpha}^{cg}$ , with Mach number are shown in Fig. 42c. The wind tunnel computed values predict more stability than the aeroballistic range determined ones and by 34% and 75%, at Mach 1.5 and 2.5, respectively. By inspection of the trends with Mach number, this difference accentuates as the Mach number increases.

The CFD center of pressure location as a function of Mach number is presented in Fig. 42d. At Mach 1.5,  $X_{CP0}$  is basically the same for the two models and the wind tunnel calculated  $X_{CP0}$  are a bit further back on the model than the aeroballistic range model.

### 5.3 Pressure Distribution inside Central Cell

Wind tunnel tests were conducted at DRDC and at ISL on an oversized A3\_1 fin so as to measure the pressure distribution inside the central cell walls. The details of those experiments and all the results can be found in Ref. 27. Shadowgraphs and surface oil flow visualizations were conducted as well as flow velocity measurements by Doppler laser velocimetry. The fin size was 9x the wind tunnel one and they were not put, of course, on a full size model. The mounting systems were different at the two facilities, as explained in Ref. 27. A comparison of the results at Mach 3.0 showed very good agreement of the measured static pressures inside the central cell. The different bases that were used to hold the fins accounted for the slight differences.

The opportunity was taken during the CFD calculations to extract the pressure distributions in the central cell for the same positions as the pressure taps on the oversized fin. The computations were conducted with the DRDC wind tunnel conditions and therefore only those results will be used to compare the predictions. The calculations were conducted with the standard reference diameter of 20.0 mm at Mach 0.6 and Mach 3.0, and one calculation was done with a reference diameter of 120.0 mm. The estimates and the wind tunnel tests were conducted at zero angle of attack.

The pressure tap locations were located at mid height and mid width on the inside walls of the central cell as shown in Fig. 43. The first tap was located at 0.0133 cal from the leading edge and the other four on the same surface were spaced 0.0133 cal apart.

The CFD computations are compared in Fig. 44. At Mach 3.0 and  $\delta=0^\circ$ , two CFD cases are shown (Fig. 44a) for reference diameters of 20.0 mm and 120.0 mm. The  $\kappa$ - $\epsilon$  turbulence model was used with a BF of 0.75. The first observation is that the computed results are exactly the same for the two lengths, indicating minor, or no Reynolds number effects, for a factor of 6, at least. Due to symmetry, the computed results for taps 17 to 20 (not provided) are exactly the same as those taps 6 to 10. The CFD pressure ratio results along the inside of the top surface (Fig. 44a) of the central cell has the general trend of the experimental results but overestimates at the first tap point and underestimates it for the remaining top taps. The pressure rise is basically missed. The CFD results agree relatively well on the side surface, except for the first tap position. On the lower surface, the predicted pressure ratio is overestimated and the trend is not the same, but agrees relatively well for the last two taps.

The comparison for Mach 0.6 is shown in Fig. 44b. The trend of the calculated pressure ratio with tap number is similar to the experimental data on the upper and side surfaces, but it under predicts the test data by roughly 10%-15%, and again the pressure rise is not well characterized. The lower surface predictions underestimate the wind tunnel data by about 20%.

## 5.4 CFD Flow Field Visualization

Some of the computed flow field along the centerline of the projectile will be presented at Mach 0.6, 1.5 and 3.0, and compared with shadowgraphs from either the ISL wind tunnel or those obtained from the free-flight experiments. The velocity vectors and the Mach number contours will be provided with special attention to the fin area.

The CFD Mach number contours and velocity vectors in the fin area at Mach 0.6 and zero angle of attack are provided in Fig. 45. No shadowgraphs exist at this Mach number. The nominal wind tunnel velocity at this Mach number is 203.0 m/s. The flow aft of the fins, in the base area shows a large recirculating region that extends past the base. The recirculating region in front of the fin base is rather small at this velocity. Just in front of the fins, the flow velocity reduces and then increases rapidly as it flows through the cell. The top two cells have very similar velocity profiles aft of the fins, whereas the bottom cell flow field is influenced by the base of the supporting fins.

An overall view of the Mach number contours at Mach 1.5 is provided in Fig. 46a and it is compared with a free-flight shadowgraph (Fig. 46b) at the same Mach number at zero angle of attack. The bow shock wave is well captured, as well as the separation shock in front of the fins and its curvature just in front of the fins. The Mach number contours and the velocity vectors details in the fin area are provided in Fig. 46c and 46d, respectively, as well as an enlargement of the shadowgraph in the same region (Fig. 46e, see also Fig. 38a from ISL). At this Mach number, the wind tunnel nominal velocity is 431.0 m/s. The boundary layer separation point, the recirculating area as well as the fin base base-recirculating region and reattachment point aft of the fins are well depicted. The flow decelerates as it approaches the grid fins, the flow is subsonic inside the cells and it accelerates again to supersonic velocities aft of the fins. The influence of the redirected flow field from the bottom cell and the recirculating region on the aft flow field is well described.

Similar comparisons of the Mach 3.0 flow fields are provided at in Fig. 47 and 48 at angles of attack of  $0.0^\circ$  and  $10.0^\circ$ , respectively. The bow shock in front of the fins is closer to the webs and again the flow is decelerated as it flows through the cells. The asymmetry of the flow at  $10.0^\circ$  is well qualified.

Recently published results on the CFD analysis (Ref. 29) show more detailed flow visualization of the A3\_1 configuration and the thin fin model. A more refined mesh was used in the fin area. Those results indicate that, for low angles of attack, the flow for the thick fin model is more or less choked at all velocities.

A comprehensive numerical analysis was also carried out (Ref. 30 and 31) on the wind tunnel thin fin model to specifically investigate local choking phenomena in the subsonic region and the sudden change in some aerodynamic coefficients (Fig. 27) in the supersonic region. The CFD predicted aerodynamic coefficients agree quite well with the wind tunnel data and the sudden change in the coefficients with Mach number was explained by the un-choking of some upper cells.

## 6. Comparison of Experimental and Predicted Results

The aerodynamic results ( $C_N$ ,  $C_M^b$  and  $C_M^{cg}$ ) will first be compared as a function of angle of attack. In this case, only the wind tunnel model (A3\_1) will be used. Then, the static aerodynamic coefficients ( $C_{X0}$ ,  $C_{N\alpha}$ ,  $C_{M\alpha}^{cg}$ ,  $X_{CP0}$ ,  $C_{l\delta}$  and  $C_{lp}$ ) from the aeroballistic range, wind tunnel and the numerical predictions of both models will be compared as a function of Mach number.

### 6.1 Aerodynamic Coefficients vs. Angle of Attack

The wind tunnel  $C_N$  and  $C_M$  results were shifted so that they pass through zero at 0.0 angle of attack.

$C_N$  as a function of attack (Fig. 49a) is very well predicted at all the angles of attack at Mach 1.5 and at 2.5° incidence at the other Mach numbers, except at 0.6. At Mach 2.5 and 3.0, the computed  $C_N$  underestimates the wind tunnel results at the higher angles of attack by less than 10% at Mach 2.5 and 3.0. At Mach 0.6, the computed  $C_N$  overestimates the wind tunnel results by a factor of 2 over the whole angle of attack range.

The static pitch moment coefficient about the base is compared in Fig. 49b. At all Mach numbers, at this reference position, the agreement is very good.

This same coefficient is compared at a center-of-gravity location located at 4.05 cal from the nose in Fig. 49c. At this cg position, the predicted stability is quite underestimated at Mach 2.5 and Mach 3.0 and at all angles of attack. At Mach 1.5,  $C_M^{cg}$  is well predicted at  $\alpha = 2.5^\circ$  and the predicted  $C_M^{cg}$  overestimates the stability at the higher angles, by roughly 30%. The predicted  $C_M^{cg}$  at Mach 0.6 underestimates the test data by quite a margin. At this Mach number, the wind tunnel results show that the projectile is unstable at the low angles of attack and marginally stable at angles attack between 6.0° to 8.0°, and somewhat statically stable past 8.0°. On the other hand, the computed results predict neutral stability up to 5.0° and stability past that point.



## 6.2 Aerodynamic Coefficients vs. Mach Number

### 6.2.1 Wind Tunnel Aerodynamic Coefficient Slopes for Comparison

As mentioned in the wind tunnel section, the slopes of the aerodynamic coefficients that were presented so far were taken to be the best fit line through the experimental between  $-5.0^\circ$  to  $+5.0^\circ$ . By inspection of the data in the annexes as a function of angle of attack for A3\_1, it is quite evident that in some cases that this was not the case, especially for  $C_M^{cg}$ . To compare the wind tunnel values with the other data, it is imperative that the right slopes be taken.

The  $C_M^{cg}$  wind tunnel results for the A3\_1 model from the ISL and the DRDC wind tunnel are provided in Fig. 50 between  $-10.0^\circ$  to  $+10.0^\circ$  at Mach 3.0. It is quite evident that the DRDC wind tunnel data is not linear between  $-5.0^\circ$  to  $+5.0^\circ$  and to some extent, the ISL data. If the slope is taken in between  $-2.0^\circ$  to  $+2.0^\circ$ , the DRDC  $C_{M\alpha}^{cg}$  is  $-11.42$ , 25% steeper than those taken between  $-5.0^\circ$  to  $+5.0^\circ$ . For the ISL case, the difference is only 7% steeper. The same exercise was done for  $C_{N\alpha}$ . In this case, at Mach 3.0, the DRDC  $C_{N\alpha}$  for the reduced range of angle of attack was 3% higher than the previous values. For the ISL case, it was 2% lower.

All the DRDC values for  $C_{N\alpha}$  and  $C_{M\alpha}^{cg}$  were recalculated at the other Mach numbers in the same fashion as mentioned in the previous paragraph. Those values and the recalculated  $X_{CP0}$  are provided in Table 20. It should be noted that in some cases the range of angle of attack was further reduced to make sure that the data was linear. These slopes are compared with the ones used previously in Fig. 51. The  $C_{N\alpha}$  for the two ranges of angles of attack (Fig 51a) are very close with the maximum difference being at Mach 3.0. The slope of the pitch moment coefficient about the centre of gravity is compared in Fig. 51b. The worst case was at Mach 1.5 since the data was rather flat in the reduced angle of attack range (Annex A) and the scatter in the data was extremely high. The centers of pressure were recalculated from the two previous values and these are compared in Fig. 51c. Again the largest difference is at Mach 1.5.

### 6.2.2 Comparison of Results vs. Mach Number

The aerodynamic coefficients obtained from the aeroballistic range and wind tunnel tests as well as the predicted results for the wind tunnel and aeroballistic range models will be compared at the supersonic velocities. The



ISL values at Mach 3.0 are also included. Again, it is reminded that there were slight differences in the models.

The axial force coefficient at zero angle of attack was computed with the base flow simulated and the results are compared in Fig. 52a. The wind tunnel axial force coefficient provided is as measured by the balance with no corrections for the base flow. All the results at Mach 1.5 are in excellent agreement with a value of 1.25. The DRDC wind tunnel  $C_{X0}$  values are about 10% below the free-flight values at Mach 2.0 and 18% below at Mach 3.0. The ISL data point at Mach 3.0 agrees extremely well with the free-flight data. The CFD predictions for the aeroballistic range model agrees exceptionally well with the free-flight data over the whole Mach number range. The predicted values for the wind tunnel model at Mach 2.5 and 3.0 lie in between the DRDC experimental data. As noted before, the differences in the predicted  $C_{X0}$  for the two models were very small.

$C_{N\alpha}$ , the normal coefficient slope, is compared in Fig. 52b. The predicted and wind tunnel values are the same at Mach 1.5 and they lie just below the free-flight data by 8%. The trend with Mach number for all the results show that the fins become more effective as the Mach number increases, but at different rates. The wind tunnel values indicate a higher slope than the free flight test data and the numerical predictions a lower one when compared with the free-flight case. The ISL and DRDC wind tunnel data agree very well at Mach 3.0, and they are about 13% higher than the aeroballistic range data. The predictions for the wind tunnel model are just slightly above the free-flight model and below the free-flight data by roughly 15% at Mach 3.0. When compared with the wind tunnel data, the CFD computations for the wind tunnel model are under predicted by 20% at Mach 2.5 and 3.0. The predictions for the aeroballistic range model underestimate the free-flight data by the same margin at those Mach numbers.

The comparison for the pitch static moment coefficient slope about the center of gravity is shown in Fig. 52c. Again there is good agreement at Mach 1.5 except for the wind tunnel data, which predicts 45% more stability. As with the normal force data, the experimental and predicted  $C_{M\alpha}^{cg}$  indicate an increase in stability with increasing Mach number but at different rates. The DRDC wind tunnel data indicates more static stability than the free-flight data as the Mach number increases, and by a factor of about 2.0 at Mach 2.5 and at Mach 3.0. The ISL data point at Mach 3.0 also specifies 50% more static stability than the aeroballistic range data. There is a difference of 50% between the wind tunnel values at Mach 3.0. Differences like this were never seen between the two wind tunnels with classical type fins (clipped delta and wrapped around fins). Since the  $C_{N\alpha}$  values were basically the same at Mach 3.0, this implies that there is a large difference in the location of the centre of pressure as measured from the two facilities. It is suspected that the base flow is severely disturbed by the thick grid fins and that the sting mount

might have an effect. The predicted values for the wind tunnel model tend to agree more with the aeroballistic determined coefficient than with the wind tunnel data, while the numerical data for the free-flight model underestimates the aeroballistic range data by about 40% at Mach 2.5 and the predicted value at Mach 3.5 tends to match the trend of the free-flight data.

The estimated locations of the center of pressure and the experimentally determined ones at zero angle of attack are supplied in Fig. 52d. At Mach 1.5, beside the DRDC wind tunnel data point, all the other data agree very well. As the Mach number increases, the DRDC wind tunnel  $X_{CP0}$  is more towards the base than the free flight data, from 0.4 cal at Mach 1.5 to 1.1 cal at Mach 3.0. The ISL wind tunnel  $X_{CP0}$  is 0.50 cal aft the free-flight data.

As with the  $C_{M\alpha}^{cg}$  results, the predicted CFD  $X_{CP0}$  for the wind tunnel model agrees relatively well with the free-flight data than the wind tunnel results. For the aeroballistic range model, the predicted values for  $X_{CP0}$  are more towards the nose of the projectile by about 0.4 cal when compared with the free-flight one at Mach 2.5 and agrees with the free-flight data trend at Mach 3.5.

The predicted values for the roll damping coefficient for the aeroballistic range model are compared with the free-flight data values in Fig. 52e. The CFD computations were conducted with the fins not deflected while for the free-flight trials one pair on fins were canted at  $2.0^\circ$  to obtain roll motion and the other set was deflected at  $0.5^\circ$  to produce a trim. The CFD predictions agree very well with the free-flight data and they under predict it by about 15% over the whole Mach number range tested. But, for these type of fins, it would be expected that when the fins are deflected, the surface area to the cross flow increases very rapidly when compared to a classical fin, and therefore, it would be anticipated that  $C_{lp}$  would be higher in those cases.

The predicted values for  $C_{lp}$  tend to agree.

The roll producing moment due to fin cant determined from the wind tunnel and the free-flight results are compared in Fig. 52f for two fins canted at  $2.0^\circ$ . The results from the wind tunnel were recalculated for this. The wind tunnel results did show a nonlinear relationship of  $C_{l\delta}$  with the cant angle. The spread in the free-flight data was explained previously and is probably due for the same reasons as those exposed in the last paragraph. The wind tunnel and free-flight values are within the scatter of both sets of results.

## 7. Comparison of Lattice and Classical Fin Aerodynamic Coefficients

In this section the aerodynamic results for the grid-finned projectile will be compared with those of the Air Force Finner Reference projectile with classical fins. The Air Force Finner projectile was extensively tested in the DRDC aeroballistic range (Ref. 13) and the Eglin aeroballistic range (Ref. 12). Therefore, only the free-flight results will be compared. A sketch of the Air Force Finner projectile is provided in Fig. 53.

The Air Force Finner reference model (Refs. 12 and 13) consists of a 2.5 caliber tangent ogive nose cone on a 7.5 caliber cylindrical body with four-clipped delta fins, as shown in Fig. 53a. These are the same body dimensions as the one for the lattice fin (Fig. 1a). The classical fin has a span of 2.0 caliber and the details of the fin are provided in Fig. 53b. The fins have leading and trailing edges with a nominal mid-thickness of 0.047 calibers. The ogive of the model was made of a brass alloy and the fins and the cylindrical portion of the projectile were made of aluminum. The projectiles tested in the DRDC aeroballistic range had a diameter of 30.0 mm while those tested at Eglin had a diameter of 25.4 mm. In both cases, the models were ballasted to obtain a center of gravity at approximately 4.8 calibers from the nose of the projectiles to assure static stability at all tested Mach numbers. For the DRDC test program, the fins were deliberately canted to produce roll motion. Nominal fin cants of 0.0°, 2.0° and 4.0° were applied. All the fins were canted at the same nominal cant angle on one model to produce a clockwise roll motion when the projectile is viewed from the rear. The projectile for the Eglin aeroballistic program had no fin cant.

The moment reference center of gravity is the one for the grid fin projectile (4.05 cal from the nose of the projectile) and the appropriate transfers were carried out for the Air Force Finner.

A comparison of the reduced aerodynamic coefficients from the 6DOF data reductions techniques with the single- and multiple-fit results for the grid finned projectile and the classical fins from Eglin Air Force Base and DRDC are given in Fig. 54. Only the supersonic results are compared.

The axial force coefficient at zero angle of attack ( $C_{X0}$ ) as a function of Mach number is shown in Fig. 54a. The grid fin axial force coefficient is about a factor of 2.5 higher than the planar fin results for the whole Mach number range. The wind tunnel results for the thin fin model indicated that the axial force coefficient could be reduced by 30% from the thick fin model. This would imply that the thin model  $C_{X0}$  would be about 1.6 times higher than the planar fin results.

$C_{N\alpha}$ , the normal coefficient slope, versus Mach number is displayed in Fig. 54b. There is quite a bit of scatter in the data sets for the planar fin, but the main trends are clear, especially with the multiple results. As mentioned, previously,  $C_{N\alpha}$  for the grid fin increases with Mach number while it is opposite for the planar fin. At Mach 1.5,

$C_{N\alpha}$  for the grid finned projectile is 50% of the planar fin, relatively the same at Mach 2.5, and if the planar fin data is extrapolated, the grid fin value is higher by roughly 20% at Mach 3.5.

The variation of the pitching moment coefficient slope,  $C_{M\alpha}^{cg}$ , with Mach number is shown in Fig. 54c. The lattice fin  $C_{M\alpha}^{cg}$  results are basically constant with Mach number between Mach 1.5 and 2.2 and then the static stability increases at the higher Mach numbers. For the planar fin, the static stability is extremely high at Mach 1.5 and decreases very quickly as the Mach number increase. At Mach 1.5, the static stability of the grid fin model is a factor of 4 less than the planar fin model, and they are relatively the same at Mach 3.0. Yet again, if the planar fin data is extrapolated to the higher Mach numbers, the grid fin will have more static stability than the planar fin one. For a maneuvering missile, in this particular case, it would be easier to control the grid fin projectile than the planar one at the low Mach number, since there is less of the overturning moment to compensate for.

The location of the center of pressure from the base of the projectile is provided in Fig. 54d. At Mach 1.5,  $X_{CP0}$  for the grid fins is 1.42 cal further towards the front of the projectile than the planar fin results and the difference diminishes to zero at Mach 2.6.

The determined pitch damping coefficients,  $C_{Mq}$ , as a function of Mach number are presented in Fig. 54e. The scatter in the results of both planar fin data sets is extremely high. The scatter in the DRDC planar data is a bit higher than the Eglin data due to the low angles of attack obtained at DRDC. Nevertheless the main trends can be distinguished. First of all, between Mach 1.5 to 2.5,  $C_{Mq}$  for both projectiles are more or less constant with Mach number with the lattices finned results being approximately 30% below the classical fin type values. Extrapolating again to the higher Mach numbers,  $C_{Mq}$  for the grid-finned projectile would be roughly the same or slightly higher than the standard fin type at Mach 3.5. It is believed to be one of the first times that a reliable  $C_{Mq}$  has been determined for a grid finned projectile.

$C_{lp}$ , the roll damping coefficient, is compared versus Mach number in Fig. 54f. The DRDC planar fin data in this case should be more accurate than the Eglin data since the DRDC projectiles had various fin cants while the Eglin projectiles were all fired with no fin cant. This explains the low scatter in the DRDC results when compared with the Eglin data.  $C_{lp}$  for the grid fin model is more or less constant as a function of Mach number at  $-5.6$  while the planar fin data is at a maximum of  $-4.0$  at Mach 1.5 and then decreases to around  $-2.0$  at Mach 2.5. This is a very interesting result. The grid fin projectile has more roll damping than the planar fin. The opposite was expected since the surface area of the planar fin is much higher than the lattice fin one when subjected to the cross flow. The wetted surface area to the cross flow of the planar fin is  $0.50 \text{ cal}^2$  while it is  $0.056 \text{ cal}^2$  if only the outside surface area is taken into account and it is  $0.172 \text{ cal}^2$  when the inside surface areas to the cross flow are also taken into consideration.

The trend of  $C_{l\delta}$  with Mach number is offered in Fig. 54g. Only the planar fin data from DRDC are presented since there was no deliberate fin cant on the Eglin models. The planar  $C_{l\delta}$  data was deduced from four fins canted at  $2.0^\circ$  and  $4.0^\circ$  and for the grid fin it was calculated for two fins canted at  $2.0^\circ$ . Both sets of data are more or less constant with Mach number. When the planar data is divided by two to compare with the grid fin data,  $C_{l\delta}$  is about 1.0, just slightly above the lattice fin data. Again this is a surprising result, for the same reason as the last paragraph.

## 8. Conclusions

An extensive study, that included wind tunnels and free-flight aeroballistic range determined coefficients as well as a computational study, was conducted on a missile projectile body equipped with four lattice fins. The reference fin that was utilized consisted of nine cells oriented in a vertical direction with very thick webs. During the program, variations on this reference fin, such as the cell orientation and web thickness were also studied mostly in the wind tunnel test program. Also, the fins were deflected in various combinations to explore their effectiveness at the various velocity regimes. The wind tunnel tests were conducted at subsonic and supersonic velocities, the free-flight tests were conducted from Mach 1.5 to 3.0, and the CFD computations were conducted over the whole Mach number range.

The wind tunnel results for the thick reference fin were compared as a function of angle of attack, Mach number and fin deflections. The types of fins studied (thick fin, open base, hexagonal orientation and thin fin) were compared as a function of angle of attack and Mach number with no fin deflection. The computed aerodynamic coefficients obtained from the CFD predictions and those from the wind tunnel for the reference fin were then compared with the aerodynamic coefficients and stability derivatives that were determined from free-flight tests conducted in the aeroballistic range. Also, the flow fields from the CFD calculations are compared with shadowgraphs obtained from the wind tunnel and the free-flight tests.

Overall, the wind tunnel and free-flight as well as the CFD results showed that:

- a. Except for the thin finned model, all the thick finned projectiles were unstable at Mach 0.6, at least at low angles of attack. The wind tunnel data and CFD predictions indicate that they are statically stable at higher incidences. The aerodynamic coefficients were very sensitive to fin deflection.
- b. At supersonic velocities, the fins become more effective and static stability increases as the Mach number increases. At a critical Mach number, there is a sudden loss of fin effectiveness and static stability and this critical Mach number is different for the thin and thick webs. The aerodynamic coefficients were very sensitive to the fin deflection. All the results for  $C_{N\alpha}$  and  $C_{M\alpha}^{cg}$  converge at Mach 1.5.
- c. In all cases, the axial force coefficient was very high for Mach numbers above 0.8. Using very thin webbed fins decreased the axial force coefficient significantly by about 35 to 40%.

The conclusions drawn in a, b and c concern essentially the thick finned models (Fig. 1b, 2a and 2b). By reducing the thickness of the fin web, not only the axial force was reduced but also the evolution of  $C_{N\alpha}$  and  $C_{M\alpha}^{cg}$  became different. The observed differences between the configurations can be explained by a drastic modification of the flow structure inside the fin cells. Indeed, for thick walls, the internal mass flow is,



as a function of Mach number, more or less choked. In the subsonic regime, the loss of mass flow rate inside the cells due to the thickening of the boundary layers generates a lift decrease and, as a consequence, the static stability. By reducing the wall thickness, the mass flow rate remains higher because of a smaller decrease of the cells cross-area (thinner boundary layers) that generates higher lift. For the supersonic regime and for thick finned models, one can see in front of each grid a shock system which is, a function of the Mach number, more or less detached and reflecting on the inner walls of each cell. In this case, the lift forces are smaller than the drag forces and the projectile is rather drag stabilized. With decreasing the wall thickness, shocks become attached and are not reflecting on the inner cell walls which mean that lift is increased and drag reduced. In this case, the projectile is stabilized by the lift forces and the grid fins behave more like conventional planar fins, but still preserving some of the advantages described previously.

The static aerodynamic coefficients  $C_{X0}$  and  $C_{N\alpha}$  obtained from the wind tunnel tests and the predicted results for the projectile with the thick webbed finned compared somewhat to the free-flight results. The wind tunnel data indicated more fin effectiveness and the CFD predictions less than the free-flight data. The static stability obtained from the wind tunnels at the higher Mach numbers are well above the free-flight data, by a factor of 3.0 for the DRDC wind tunnel data and by a factor of 2.0 for the ISL data. The CFD data predicts less static stability than the free-flight data.

It is also believed to be one the first times than reliable pitch damping and roll damping aerodynamic coefficients were obtained experimentally for a latticed fin projectile.

The CFD flow field computations provided insight in the flow regime compared very well with shadowgraphs of the flow field and help understand some of the unexpected results for this lattice fin configuration.

The results of the lattice-finned missile were compared with those of a classical fin design to provide some insight on the advantages and disadvantages of using this type of control surfaces. Comparison between the two configurations showed that the trend of  $C_{N\alpha}$  and  $C_{M\alpha}^{cg}$  for the grid finned projectile is opposite of a standard planar finned projectile.

In conclusion, one can say that grid fins with thick walls are totally unsuited for the subsonic flight domain but show some interesting aerodynamic characteristics for the supersonic and hypersonic flow regimes. The command and control of the lift as a function of the incidence and Mach number is certainly possible by optimizing the fin geometry. However, the choice between grid and conventional planar fins always be a compromise between the different aerodynamic coefficients, especially drag and lift.



## 9. References

1. Abate, G., Winchenbach, G. and Hathaway, W., "Transonic Aerodynamic and Scaling Issues for Lattice Projectiles Tested in Ballistic Ranges", 19<sup>th</sup> International Symposium on Ballistics, 7-11 May, 2001, Interlaken, Switzerland.
2. Washington, W.D., Miller, M.S., "Experimental Investigations on Grid Fin Aerodynamics: A Synopsis of Nine Wind Tunnel and Three Flight Tests", RTO-MP-5 AC/323(AVT)TP/3, November 1998
3. Simpson, G.M., Saddler, A.J., "Lattice Controls: A Comparison with Conventional Planar Fins", RTO-MP-5 AC/323(AVT)TP/3, November 1998
4. Abate, G.L., Duckerschein, R.P., Hathaway, W., "Subsonic/Transonic Free-Flight Tests of a generic Missile with Grid Fins", AIAA Paper 2000-0937, 38<sup>th</sup> AIAA Aerospace Sciences Meeting and Exhibit, Reno, NV, USA, Jan. 2000
5. Fournier, E., "Aerodynamic Coefficients Measurements of a High L/D Projectile with Grid Fins", DREV TM 2001-035, April 2001, UNCLASSIFIED
6. DeSpirito, J., Edge, H., Weinacht, P., Sahu, J. and Dinavahi, S., "Computational Fluid Dynamics (CFD) Analysis of a Generic Missile with Grid Fins", ARL-TR-2318, September 2000
7. Fournier, E., "Aerodynamic Coefficient Measurements of a Canard-Controlled Missile with Planar and Lattice Tail Surfaces", DREV TM 2002-007, March 2002, UNCLASSIFIED.
8. Dupuis, A., Boivin, M., and Normand, M., "Model, Sabot Design and Free-Flight Tests of the KTA 2-16 Grid Finned Missile at Supersonic Velocities", DRDC Valcartier TM 2003-078, July 2003, UNCLASSIFIED
9. Fournier, E., "Validation of Grid Fin Data in the DREV Trisonic Wind Tunnel", DREV TN 2001-092, July 2001, UNCLASSIFIED
10. DeSpirito, J., Vaughn, M. and Washington, D., "Numerical Investigation of Aerodynamics of Canard-Controlled Missile Using Planar and Grid Tail fins, Part I: Supersonic Flow", ARL-TR-2848, September 2848.
11. DeSpirito, J., and Sahu, J., "Viscous CFD Calculations of Grid Fin Missile Aerodynamics in the Supersonic Flow Regime", ARL-RP-19, April 2001.
12. West, K. O., "Comparison of Free-flight Spark Range and Wind Tunnel Test Data for a Generic Missile Configuration at Mach Numbers From 0.6 to 2.5", AFATL-TR-81-87

13. Dupuis, A., "Aeroballistic Range Tests of the Air Force Finner Reference Projectile", DRDC Valcartier TM 2002-008, May 2002, UNCLASSIFIED.
14. "Commissioning Report of the DREV 2 ft. Indraft Tunnel", Dilworth, Secord, Meagher and Associated Ltd., Report No. 695/912, March 1977
15. Berner, C., and Dupuis, A., "Wind Tunnel Tests of a Grid Finned Projectile Configuration", AIAA 2001-0105, 39<sup>th</sup> Aerospace Sciences Meeting and Exhibit, 8-11 January 2001, Reno, Nevada (also published as ISL PU346/2000)
16. Dupuis, A., Berner, C., "Aerodynamic Aspects of a Grid Finned Projectile at Subsonic and Supersonic Velocities", 19<sup>th</sup> International Symposium on Ballistics, Interlaken, Switzerland, 7-11 May 2001, (also published as ISL PU623/2002)
17. Berner C. and Dupuis, A. "Wind Tunnel Investigation and Analysis of the DREV-ISL Reference Projectiles", DREV-R-9520, June 1996, UNCLASSIFIED.
18. Dupuis, A., Boivin, M. and Normand, M., "Model, Sabot Design and Free-Flight Tests of the DRDC-ISL A1, A2, and A3 Models", DRDC Valcartier TM 2003-077, July 2003, UNCLASSIFIED
19. Dupuis, A., Berner, C., "Aerodynamic Aspects of Fin Geometries on a Latticed Finned Projectile" 20<sup>th</sup> International Symposium on Ballistics, Orlando, FL, 23-27 September 2002, (also published as ISL PU635/2002)
20. Drouin, G., Dupuis, A. and Côté, F., "Instrumentation Development and Data Analysis for the DREV Aeroballistic Range", DREV M-2800/87, March 1987, UNCLASSIFIED
21. Dupuis, A. and Drouin, G., "The DREV Aeroballistic Range and Data Analysis System", AIAA Paper No. 88-2017, AIAA 15th Aerodynamic Testing Conference, San Diego, California, 18-20 May, 1988.
22. Whyte, R. and Hathaway, W., "Dynamic Calibration of Spark Aeroballistic Ranges", 44<sup>th</sup> Aeroballistic Range Association Meeting, 13-17 September, 1993, Munich.
23. "CADRA System", AerospaceComputing, Inc., 2000
24. "ARFDAS", Version 4.30, Arrow Tech Associates Inc, August 2003.
25. Hathaway, W. H. and Whyte, R., "Aeroballistic Research Facility Free-Flight Data Analysis using the Maximum Likelihood function", AFATL-TR-79-98, December 1979, UNCLASSIFIED.
26. Bernier A., "Calcul de CFD de Configurations d'Ailettes en Treillis", SNC-TEC 682-265, Octobre 2003.

27. Berner, C. and Fournier, E., "Wind Tunnel Tests of the A4 DRDC-ISL Reference Oversized Grid Fin", ISL TR-XXXX, to be published
28. "Documentation CFX 5.6", AEA Technology, 2002.
29. Bernier, A. and Dupuis, A., "Numerical Computations of Subsonic and Supersonic Flow for a Grid Finned Projectile", 21<sup>st</sup> International Symposium on Ballistics, Adelaide, Australia, April 19-23, 2004.
30. Parisé, N., "Numerical Computations of Subsonic and Supersonic Flow Choking Phenomena in Grid Finned Projectiles", SNC-TEC 723-265, March 2005
31. Parisé, N. and Dupuis, A., "Numerical Computations of Subsonic and Supersonic Flow Choking Phenomena in Grid Finned Projectiles", 22<sup>nd</sup> International Symposium on Ballistics, Vancouver, B.C., Canada,

**Table 1. Grid fin panel deflections for reference thick fin and wind tunnel tests**

Model		Cant angle $\delta$ (°)				Mach number				
		P1	P2	P3	P4	0.6	1.5	2.0	2.5	3.0
A3_1		0	0	0	0	X	X	X	X	X
GROUP 1	A3_2	-5	-5	-5	-5	X	X			X
	A3_3	-10	-10	-10	-10	X	X			X
	A3_4	-15	-15	-15	-15	X	X	X	X	X
GROUP 2	A3_5	0	-5	0	-5	X	X			X
	A3_6	0	-10	0	-10	X	X			X
	A3_7	0	-15	0	-15	X	X	X	X	X
GROUP 3	A3_8	0	+5	0	-5	X	X	X	X	X
	A3_10	0	+15	0	-15	X	X	X	X	X

**Table 2. Reynolds number comparison**

Wind tunnel DRDC (l = 0.2 m)		Wind Tunnel ISL (l = 0.2 m)		Free-Flight DRDC Aeroballistic Range (l = 0.3 m)	
Mach	Re <sub>l</sub>	Mach	Re <sub>l</sub>	Mach	Re <sub>l</sub>
0.6	1.90x10 <sup>6</sup>	-	-	-	-
0.8	2.60 x10 <sup>6</sup>	-	-	-	-
1.5	3.04 x10 <sup>6</sup>	-	-	1.5	10.17 x10 <sup>6</sup>
2.0	2.56 x10 <sup>6</sup>	-	-	2.0	13.56 x10 <sup>6</sup>
2.5	2.02 x10 <sup>6</sup>	-	-	2.5	16.96 x10 <sup>6</sup>
3.0	1.56 x10 <sup>6</sup>	3.0	6.60 x10 <sup>6</sup>	3.0	20.35 x10 <sup>6</sup>
4.0	0.94 x10 <sup>6</sup>	-	-	3.5	23.74 x10 <sup>6</sup>

**Table 3.  $C_{X0}$  relative variation for one fin w.r.t thick fin model**

Mach Number	THIN FIN (%)	OPEN BASE (%)	HEXAGONAL (%)
0.6	-47.9	-13.5	1.3
1.5	-43.2	-6.7	2.1
2.0	-45.8	-7.8	-1.0
2.5	-48.8	-0.8	4.6
3.0	-54.6	0.5	9.3

**Table 4. Nominal physical properties of free-flight models**

d (mm)	m (g)	$I_x$ (g-cm <sup>2</sup> )	$I_y$ (g-cm <sup>2</sup> )	l (mm)	CG from nose ( $X_{CG}/l$ )
30.0	881.2	954.55	64517.07	300.0	0.405

**Table 5. Physical properties of free-flight test projectiles**

Model #	d (mm)	$I_x$ (g cm <sup>2</sup> )	$I_y, I_z$ (g cm <sup>2</sup> )	m (g)	CG from nose/l (-)	CG from nose (mm)	CG from nose (cal)	l (mm)
K01	29.98	950.17	64403.71	879.5	0.40520	121.528	4.053	299.924
K02	29.98	951.93	64457.82	880.6	0.40504	121.501	4.052	299.975
K04	29.98	953.56	64428.18	880.6	0.40499	121.475	4.056	299.949
K05	29.98	954.19	64484.18	881.1	0.40497	121.430	4.051	299.848
K06	29.99	954.06	64512.42	880.9	0.40503	121.510	4.050	300.000
K07	29.98	954.88	64474.76	880.7	0.40506	121.487	4.052	299.924
K08	29.98	954.38	64438.53	879.8	0.40528	121.563	4.052	299.949
K09	29.99	959.79	64815.49	884.7	0.40574	121.692	4.054	299.924
K10	29.98	954.50	64454.06	880.0	0.40460	121.268	4.058	299.721
K11	29.98	955.45	64564.22	881.5	0.40496	121.528	4.044	300.102
K12	30.00	952.68	64454.06	879.9	0.40516	121.549	4.053	300.000

**Table 6. Range conditions**

Shot Number	No. Of Stations	Observed distance (m)	P <sub>R</sub> (mbar)	T <sub>R</sub> (° C)	Relative Humidity (%)	ρ (kg/m <sup>3</sup> )	a <sub>R</sub> (m/s)	Re <sub>1</sub>
K030501	36	210.0	1001.70	19.84	35.26	1.1910	343.141	0.972x10 <sup>7</sup>
K030502	35	110.0	1001.70	19.71	34.96	1.1915	343.066	1.018 x10 <sup>7</sup>
K030504	47	207.5	1003.52	19.77	40.96	1.1935	343.099	1.352 x10 <sup>7</sup>
K030505	49	205.0	1003.52	19.77	42.10	1.1935	343.098	1.439 x10 <sup>7</sup>
K030506	52	207.5	1003.52	19.76	42.84	1.1935	343.091	1.533 x10 <sup>7</sup>
K030507	46	210.0	980.26	20.63	35.20	1.1624	343.604	1.620 x10 <sup>7</sup>
K030508	51	210.0	980.26	20.96	34.64	1.1611	343.796	1.739 x10 <sup>7</sup>
K030509	47	210.0	987.78	20.08	36.46	1.1735	343.282	1.804 x10 <sup>7</sup>
K030510	44	210.0	989.33	20.05	38.76	1.1755	343.265	2.081 x10 <sup>7</sup>
K030511	47	190.0	989.70	19.63	42.26	1.1776	343.018	2.137 x10 <sup>7</sup>
K030512	51	210.0	1003.52	19.63	42.46	1.1941	343.016	2.266 x10 <sup>7</sup>

**Table 7. Muzzle velocities**

M<sub>Sabot + modèle</sub> = 2.8 kg; Propellant type NQM 044

Model Number	Propellant mass (kg)	V <sub>muz</sub> (m/s)
K01	1.45	531.7
K02	1.45	541.2
K04	2.25	734.3
K05	2.40	780.5
K06	2.55	830.3
K07	3.00	896.0
K08	3.20	964.4
K09	3.35	987.6
K10	3.90	1136.9
K11	4.00	1157.9
K12	4.20	1216.3

Table 8. Linear theory analysis parameters

Shot No.	Mach No.	Dbsq deg <sup>2</sup>	KF deg	KS deg	LF 1/m	LS 1/m	WF deg/m	WS deg/m	KT deg	E-ANG deg
K030501	1.437	6.67	3.27	2.44	-0.0060	-0.0024	5.12	-5.27	0.105	0.152
K030502	1.504	47.21	4.73	6.60	-0.0043	-0.0025	5.88	-5.71	0.643	0.201
K030504	1.994	0.54	1.00	1.00	-0.0064	-0.0064	4.92	-4.87	0.263	0.485
K030505	2.123	6.40	0.96	3.03	-0.0091	-0.0019	5.26	-5.29	0.474	0.289
K030506	2.260	8.46	3.79	3.14	-0.0053	-0.0047	5.26	-5.45	0.187	0.276
K030507	2.456	3.28	2.64	2.11	-0.0048	-0.0085	6.28	-6.94	0.231	0.290
K030508	2.640	1.79	1.78	1.45	-0.0038	-0.0088	6.64	-6.74	0.142	0.129
K030509	2.708	2.57	2.11	1.04	-0.0056	0.0005	6.21	-6.57	0.335	0.306
K030510	3.120	13.29	5.57	3.37	-0.0059	-0.0045	7.38	-7.46	0.225	0.290
K030511	3.193	14.84	4.78	4.48	-0.0057	-0.0055	7.46	-7.46	0.141	0.432
K030512	3.341	4.86	2.50	2.50	-0.0056	-0.0036	6.61	-6.72	0.159	0.174

Table 9. Linear theory aerodynamic coefficients

Shot No.	Mach No.	Dbsq deg <sup>2</sup>	CX0	CX2	CNa	Cma	Cmq	Cld	Clp	E-X m	E-SWR m	E-ANG deg	E-PHI deg
K030501	1.437	6.7	1.223	7.40	4.41	-4.20	-212.5	-0.0259	-4.6252	0.0011	0.0023	0.152	5.99
K030502	1.504	47.2	1.128	7.12	5.12	-5.23	-145.5	-0.0170	-4.5473	0.0029	0.0064	0.201	5.58
K030504	1.994	0.5	1.137	5.87	8.42	-3.73	-299.7	-0.0254	-4.3409	0.0013	0.0018	0.485	5.70
K030505	2.123	6.4	1.089	5.69	4.90	-4.34	-293.3	-0.0223	-5.1796	0.0023	0.0019	0.289	6.27
K030506	2.260	8.5	1.076	5.51	5.31	-4.47	-256.1	-0.0211	-5.4944	0.0021	0.0015	0.276	6.34
K030507	2.456	3.3	1.027	5.24	5.35	-6.92	-377.0	-0.0242	-4.3901	0.0021	0.0013	0.290	7.70
K030508	2.640	1.8	1.007	4.94	5.45	-7.16	-350.9	-0.0337	-5.4656	0.0009	0.0010	0.129	5.67
K030509	2.708	2.6	1.008	4.83	6.60	-6.48	-69.5	-0.0270	-5.2000	0.0008	0.0014	0.306	6.87
K030510	3.120	13.3	0.935	4.27	6.26	-8.70	-260.3	-0.0252	-4.5012	0.0032	0.0013	0.290	7.13
K030511	3.193	14.8	0.921	4.21	6.33	-8.67	-278.6	-0.0243	-4.3584	0.0032	0.0019	0.432	8.61
K030512	3.341	4.9	0.956	4.11	6.07	-6.91	-214.9	-0.0281	-5.0198	0.0012	0.0013	0.174	7.05



Table 10. Six-degree-of-freedom aerodynamic coefficients – Single fits

Shot Number	Mach Number	DBSQ ABARM	CX CX2	CNa CNa3	CYpa Cnpa	Cma Cma3	Cmq Cmq2	CZga3 Cmga3	CYga3 Cnga3	Clga2 Cnsm	Clp Cld	CNda CNdB	Cmδα CmδB	Standard Error	
														X(m) Y-Z(m)	Angle(deg) Roll(deg)
K030501	1.438	7.0	1.237 ( 0.%) ( 3.%)	4.52 (*) ( 3.%)	0.00 (*) ( 1.%)	-3.892 (*) ( 1.%)	-284.9 (*) ( 7.%)	0.0 (*) ( 1.%)	0.0 (*) ( 1.%)	0.00 (*) ( 0.%)	-5.200 (*) ( 0.%)	0.017 (*) ( 0.%)	-0.028 (*) ( 0.%)	0.0011	0.183
			5.1 (*) ( 0.5%)	48.0 (*) ( 4.8%)	0.0 (*) ( 0.0%)	-71.0 (*) ( 1.0%)	0.0 (*) ( 0.0%)	0.0 (*) ( 0.0%)	-75.0 (*) ( 1.0%)	0.00 (*) ( 0.0%)	-0.028 (*) ( 0.0%)	-0.033 (*) ( 0.0%)	0.001 (*) ( 0.0%)	0.0025	6.645
K030502	1.505	38.6	1.225 ( 0.%) ( 9.%)	4.41 (*) ( 1.%)	0.00 (*) ( 1.%)	-3.303 (*) ( 1.%)	-224.8 (*) ( 11.%)	0.0 (*) ( 1.%)	0.0 (*) ( 1.%)	0.00 (*) ( 1.%)	-5.200 (*) ( 1.%)	-0.013 (*) ( 1.%)	0.053 (*) ( 1.%)	0.0016	0.216
			10.5 (*) ( 56.%)	33.3 (*) ( 56.%)	0.0 (*) ( 56.%)	-71.0 (*) ( 56.%)	0.0 (*) ( 56.%)	0.0 (*) ( 56.%)	-137.1 (*) ( 11.%)	0.00 (*) ( 1.%)	-0.018 (*) ( 1.%)	0.001 (*) ( 1.%)	0.083 (*) ( 9.%)	0.0021	8.233
K030504	1.996	1.5	1.138 ( 0.%) ( 3.%)	4.78 (*) ( 3.%)	0.00 (*) ( 1.%)	-3.167 (*) ( 1.%)	-273.8 (*) ( 7.%)	0.0 (*) ( 1.%)	0.0 (*) ( 1.%)	0.00 (*) ( 1.%)	-4.259 (*) ( 5.%)	-0.002 (*) ( 1.%)	-0.007 (*) ( 45.%)	0.0010	0.099
			2.3 (*) ( 0.5%)	0.0 (*) ( 0.5%)	0.0 (*) ( 0.5%)	-35.0 (*) ( 1.0%)	0.0 (*) ( 0.5%)	0.0 (*) ( 1.0%)	0.0 (*) ( 1.0%)	0.00 (*) ( 0.0%)	-0.025 (*) ( 0.0%)	-0.004 (*) ( 0.0%)	0.048 (*) ( 6.%)	0.0014	5.880
K030505	2.125	6.1	1.101 ( 0.%) ( 2.%)	4.76 (*) ( 2.%)	0.00 (*) ( 1.%)	-4.143 (*) ( 0.%)	-246.3 (*) ( 3.%)	0.0 (*) ( 1.%)	0.0 (*) ( 1.%)	0.00 (*) ( 0.0%)	-4.736 (*) ( 6.%)	0.019 (*) ( 20.%)	-0.075 (*) ( 2.%)	0.0008	0.088
			3.8 (*) ( 0.5%)	0.0 (*) ( 0.5%)	0.0 (*) ( 0.5%)	-35.0 (*) ( 1.0%)	0.0 (*) ( 0.5%)	0.0 (*) ( 1.0%)	0.0 (*) ( 1.0%)	0.00 (*) ( 0.0%)	-0.021 (*) ( 4.%)	-0.009 (*) ( 50.%)	-0.016 (*) ( 12.%)	0.0015	6.328
K030506	2.263	9.1	1.091 ( 0.%) ( 1.%)	5.42 (*) ( 1.%)	0.00 (*) ( 1.%)	-4.110 (*) ( 0.%)	-294.6 (*) ( 3.%)	0.0 (*) ( 1.%)	0.0 (*) ( 1.%)	0.00 (*) ( 0.0%)	-5.528 (*) ( 6.%)	-0.006 (*) ( 79.%)	-0.015 (*) ( 12.%)	0.0009	0.129
			6.3 (*) ( 0.5%)	0.0 (*) ( 0.5%)	0.0 (*) ( 0.5%)	-35.0 (*) ( 1.0%)	0.0 (*) ( 0.5%)	0.0 (*) ( 1.0%)	0.0 (*) ( 1.0%)	0.00 (*) ( 0.0%)	-0.021 (*) ( 4.%)	0.007 (*) ( 71.%)	-0.012 (*) ( 15.%)	0.0012	6.526
K030507	2.459	3.8	1.034 ( 0.%) ( 2.%)	5.14 (*) ( 2.%)	0.00 (*) ( 1.%)	-6.289 (*) ( 0.%)	-302.5 (*) ( 5.%)	0.0 (*) ( 1.%)	0.0 (*) ( 1.%)	0.00 (*) ( 0.0%)	-4.510 (*) ( 9.%)	0.017 (*) ( 45.%)	-0.071 (*) ( 4.%)	0.0010	0.135
			4.4 (*) ( 0.5%)	0.0 (*) ( 0.5%)	0.0 (*) ( 0.5%)	0.0 (*) ( 0.5%)	0.0 (*) ( 0.5%)	0.0 (*) ( 0.5%)	0.0 (*) ( 0.5%)	0.00 (*) ( 0.0%)	-0.025 (*) ( 6.%)	-0.001 (*) ( 8.%)	-0.040 (*) ( 8.%)	0.0011	7.613

Table 10. Six-degree-of-freedom aerodynamic coefficients – Single fits (continued)

Shot Number	Mach Number	DBSQ ABARM	CX CX2	CNa CNa3	CYpa Cnpa	Cma Cma3	Cmq Cmq2	CZga3 Cmga3	CYga3 Cnga3	Clga2 Cnsm	Clp Cld	CNda CndB	Cmda CmDB	Standard Error	
														X(m) Y-Z(m)	Angle(deg) Roll(deg)
K030508	2.642	2.0	1.010 ( 0.%) ( 3.%)	5.53 (*) ( 0.%) ( 3.%)	0.00 (*) ( 0.%) ( 3.%)	-7.296 (*) ( 0.%) ( 3.%)	-262.7 (*) ( 5.%) ( 3.%)	0.0 (*) ( 0.%) ( 3.%)	0.0 (*) ( 0.%) ( 3.%)	0.00 (*) ( 3.%) ( 11.%)	-5.455 (*) ( 4.%) ( 37.%)	0.017 (*) ( 6.%) ( 6.%)	-0.045 (*) ( 2.%) ( 2.%)	0.0009	0.084
	3.0	0.5	0.0 (*) ( 0.%) ( 3.%)	0.0 (*) ( 0.%) ( 3.%)	0.0 (*) ( 0.%) ( 3.%)	0.0 (*) ( 0.%) ( 3.%)	0.0 (*) ( 0.%) ( 3.%)	0.0 (*) ( 0.%) ( 3.%)	0.0 (*) ( 0.%) ( 3.%)	0.00 (*) ( 3.%) ( 11.%)	-0.034 (*) ( 4.%) ( 37.%)	-0.003 (*) ( 6.%) ( 6.%)	0.024 (*) ( 2.%) ( 2.%)	0.0009	5.788
K030509	2.710	2.8	1.012 ( 0.%) ( 2.%)	5.47 (*) ( 0.%) ( 3.%)	0.00 (*) ( 0.%) ( 3.%)	-6.040 (*) ( 0.%) ( 3.%)	-251.3 (*) ( 4.%) ( 3.%)	0.0 (*) ( 0.%) ( 3.%)	0.0 (*) ( 0.%) ( 3.%)	0.00 (*) ( 3.%) ( 11.%)	-5.225 (*) ( 4.%) ( 37.%)	0.014 (*) ( 6.%) ( 6.%)	-0.084 (*) ( 2.%) ( 2.%)	0.0008	0.074
	3.2	0.5	0.0 (*) ( 0.%) ( 2.%)	0.0 (*) ( 0.%) ( 2.%)	0.0 (*) ( 0.%) ( 2.%)	0.0 (*) ( 0.%) ( 2.%)	0.0 (*) ( 0.%) ( 2.%)	0.0 (*) ( 0.%) ( 2.%)	0.0 (*) ( 0.%) ( 2.%)	0.00 (*) ( 3.%) ( 11.%)	-0.027 (*) ( 4.%) ( 37.%)	0.021 (*) ( 6.%) ( 6.%)	-0.006 (*) ( 2.%) ( 2.%)	0.0011	6.697
K030510	3.124	15.3	0.955 ( 0.%) ( 1.%)	6.34 (*) ( 0.%) ( 1.%)	0.00 (*) ( 0.%) ( 1.%)	-7.628 (*) ( 0.%) ( 1.%)	-368.1 (*) ( 2.%) ( 2.%)	0.0 (*) ( 0.%) ( 1.%)	0.0 (*) ( 0.%) ( 1.%)	0.00 (*) ( 3.%) ( 11.%)	-4.458 (*) ( 4.%) ( 37.%)	-0.022 (*) ( 6.%) ( 6.%)	0.004 (*) ( 2.%) ( 2.%)	0.0008	0.110
	8.1	0.5	0.0 (*) ( 0.%) ( 1.%)	0.0 (*) ( 0.%) ( 1.%)	0.0 (*) ( 0.%) ( 1.%)	-128.0 (*) ( 0.%) ( 1.%)	0.0 (*) ( 0.%) ( 1.%)	0.0 (*) ( 0.%) ( 1.%)	130.0 (*) ( 0.%) ( 1.%)	0.00 (*) ( 3.%) ( 11.%)	-0.025 (*) ( 4.%) ( 37.%)	0.009 (*) ( 6.%) ( 6.%)	-0.070 (*) ( 2.%) ( 2.%)	0.0014	6.559
K030511	3.197	17.3	0.941 ( 0.%) ( 1.%)	6.52 (*) ( 0.%) ( 1.%)	0.00 (*) ( 0.%) ( 1.%)	-7.381 (*) ( 0.%) ( 1.%)	-338.3 (*) ( 2.%) ( 2.%)	0.0 (*) ( 0.%) ( 1.%)	0.0 (*) ( 0.%) ( 1.%)	0.00 (*) ( 3.%) ( 11.%)	-4.474 (*) ( 4.%) ( 37.%)	0.005 (*) ( 6.%) ( 6.%)	-0.023 (*) ( 2.%) ( 2.%)	0.0009	0.087
	8.8	0.5	0.0 (*) ( 0.%) ( 1.%)	0.0 (*) ( 0.%) ( 1.%)	0.0 (*) ( 0.%) ( 1.%)	-145.8 (*) ( 0.%) ( 1.%)	0.0 (*) ( 0.%) ( 1.%)	0.0 (*) ( 0.%) ( 1.%)	141.4 (*) ( 0.%) ( 1.%)	0.00 (*) ( 3.%) ( 11.%)	-0.025 (*) ( 4.%) ( 37.%)	0.015 (*) ( 6.%) ( 6.%)	0.045 (*) ( 2.%) ( 2.%)	0.0012	8.571
K030512	3.344	5.4	0.963 ( 0.%) ( 2.%)	5.90 (*) ( 0.%) ( 2.%)	0.00 (*) ( 0.%) ( 2.%)	-6.618 (*) ( 0.%) ( 2.%)	-283.9 (*) ( 3.%) ( 3.%)	0.0 (*) ( 0.%) ( 2.%)	0.0 (*) ( 0.%) ( 2.%)	0.00 (*) ( 3.%) ( 11.%)	-5.024 (*) ( 4.%) ( 37.%)	-0.008 (*) ( 6.%) ( 6.%)	-0.018 (*) ( 2.%) ( 2.%)	0.0011	0.095
	4.3	0.5	0.0 (*) ( 0.%) ( 2.%)	0.0 (*) ( 0.%) ( 2.%)	0.0 (*) ( 0.%) ( 2.%)	-100.0 (*) ( 0.%) ( 2.%)	0.0 (*) ( 0.%) ( 2.%)	0.0 (*) ( 0.%) ( 2.%)	0.0 (*) ( 0.%) ( 2.%)	0.00 (*) ( 3.%) ( 11.%)	-0.028 (*) ( 4.%) ( 37.%)	0.018 (*) ( 6.%) ( 6.%)	0.038 (*) ( 2.%) ( 2.%)	0.0012	6.676

Table 11. Six-degree-of-freedom aerodynamic coefficients – Multiple fits

Shot Numbers	Mach Number	DBSQ ABARM	CX CX2 CX4	CNa CNa3 CNa5	CYpa Cnpa Cnpa3	Cma Cma3 Cma5	Cmq Cmq2 Cmq4	CZga3 Cnga3 Cnga	CYga3 Cnga3 Cnga5	CLga2 CXga2 CLp	CXM CmaM CnsM	Standard Error	
												X(m) Y-Z(m)	Angle(deg) Roll(deg)
K030501	K030502	1.472	23.0 ( 0.%) ( 3.%) 10.5	1.230 ( 0.%) ( 3.%) 0.5	4.65 ( 0.%) ( 3.%) 24.0	0.00 (*) ( 1.%) ( 5.%) 0.0	-3.893 (*) ( 1.%) ( 5.%) -70.9	-285.6 (*) ( 31.%) ( 14.%) 0.0	0.0 (*) ( 1.%) -95.7	0.00 (*) ( 7.%) 0.00	-0.20 (*) ( 7.%) 0.00	0.0013	0.174
K030504	K030505	2.128	5.4 ( 0.%) ( 2.%) 6.3	1.103 ( 0.%) ( 2.%) 0.5	5.11 ( 0.%) ( 2.%) 0.0	0.00 (*) ( 1.%) ( 4.%) 0.0	-3.857 (*) ( 1.%) ( 4.%) -35.0	-265.8 (*) ( 4.%) 0.0	0.0 (*) ( 1.%) 0.0	0.00 (*) ( 1.%) 0.00	-0.21 (*) ( 1.%) -2.34	0.0025	0.230
K030506												0.0017	6.280
K030504													
K030505													
K030506													

Table 11. Six-degree-of-freedom aerodynamic coefficients – Multiple fits (continued)

**Table 12. Roll moment coefficient due to fin cant**

Shot Number	Mach Number	$C_{l\delta}\delta$	$C_{l\delta}$ (/rad)
K01	1.438	-0.0281	-0.805
K02	1.505	-0.0177	-0.507
K04	1.996	-0.0251	-0.719
K05	2.125	-0.0210	-0.602
K06	2.263	-0.0212	-0.607
K07	2.459	-0.0247	-0.708
K08	2.642	-0.0337	-0.965
K09	2.710	-0.0271	-0.776
K10	3.124	-0.0251	-0.719
K11	3.197	-0.0247	-0.708
K12	3.344	-0.0282	-0.808

**Table 13. CFD predictions for wind tunnel model (A3\_1) vs. incidence**  
(Turbulence: SST; Scheme: BF 0.75)

Angle of Attack (deg)	M = 0.6 (Mesh size: 1709K)				M = 1.5 (Mesh size: 1070K)				M = 2.5 (Mesh size: 1070K)				M = 3.0 (Mesh size: 1070K)			
	$C_N$	$C_M^{base}$	$X_{CP}^{base}$ (cal)		$C_N$	$C_M^{base}$	$X_{CP}^{base}$ (cal)		$C_N$	$C_M^{base}$	$X_{CP}^{base}$ (cal)		$C_N$	$C_M^{base}$	$X_{CP}^{base}$ (cal)	
2.5	0.131	0.810	6.18		0.187	0.949	5.07		0.223	1.092	4.90		0.240	0.240	4.72	
5.0	0.284	1.654	5.82		0.387	1.955	5.05		0.465	2.292	4.93		0.511	0.511	4.69	
7.5	0.451	2.359	5.63		0.613	3.080	5.02		0.744	3.724	5.01		0.829	0.829	4.73	
10.0	0.639	3.481	5.45		0.874	4.387	5.02		1.124	5.578	4.96		1.225	1.225	4.73	
15.0	-	-	-		1.473	7.810	5.30		2.135	10.343	4.84		2.165	10.116	4.67	

**Table 14.  $C_{X0}$  CFD predictions for wind tunnel model (A3\_1) vs. Mach number**  
(Mess size: 1070K; Turbulence: SST; Scheme: BF 0.75)

Mach	$C_{X0}$
0.6	0.940
1.5	1.214
2.5	0.951
3.0	0.892

**Table 15. CFD predicted slopes for wind tunnel model (A3\_1) vs. Mach number**

Mach	$C_{X0}$	$C_{N\alpha}$	$C_{M\alpha}^b$	$C_{M\alpha}^{cg}$	$X_{CP0}$
0.6	0.940	3.00	18.56	0.710	6.19
1.5	1.214	4.29	21.75	-3.775	5.07
2.5	0.951	5.11	25.03	-5.375	4.90
3.0	0.892	5.50	25.97	-6.755	4.72

**Table 16. CFD predictions for aeroballistic range model at  $\alpha = 2.5^\circ$**   
(Turbulence: SST; Mesh size: 1070 K)

Scheme	Mach	$C_N$	$C_M^{base}$	$X_{CP}^{base}$ (cal)
HR	1.5	0.182	0.963	5.29
BF 0.75	2.5	0.210	1.115	5.31
HR	3.5	0.233	1.150	4.94

**Table 17.  $C_{X0}$  CFD predictions for aeroballistic range model vs. Mach number**

(Mess size: 1709K; Turbulence:  $\kappa$ - $\epsilon$ ; Scheme: LR)

Mach	$C_{X0}$
1.5	1.196
2.5	0.999
3.0	0.893



**Table 18.  $C_{lp}$  CFD predictions for aeroballistic range model vs. Mach number**

(Turbulence:  $\kappa$ - $\epsilon$ ; Mesh size: 873 K,  $\alpha = 0.0^\circ$ )

Scheme	Mach	Spin rate (rad/s)	$C_{lp}$
BF 0.75	1.5	257.3	-4.133
BF 0.75	2.5	428.9	-4.336
BF 0.50	3.5	600.5	-3.608

**Table 19. CFD predicted slopes for aeroballistic range model vs. Mach number**

Mach	$C_{N\alpha}$	$C_{M\alpha}^b$	$C_{M\alpha}^{cg}$	$X_{CP0}$ (cal)
1.5	4.17	22.07	-2.74	5.29
2.5	4.81	25.55	-3.07	5.31
3.5	5.34	26.36	-5.41	4.94

**Table 20. Wind tunnel aerodynamic data used for Mach number comparison**

Mach	$C_{X0}$	$C_{N\alpha}$	$C_{M\alpha}^b$	$C_{M\alpha}^{cg}$	$X_{CP0}$	Run Number
1.487	1.251	4.08	19.25	-5.00	4.72	R7064
1.987	1.018	5.18	25.23	-5.57	4.87	R7025
2.487	0.873	6.27	27.01	-10.28	4.31	R7002
2.491	0.876	6.23	27.09	-10.00	4.35	R7003
2.981	0.799	7.09	26.07	-16.12	3.68	R7018
2.983	0.805	7.06	25.84	-16.16	3.66	R7019
3.000	0.944	6.76	28.81	-11.42	4.26	ISL

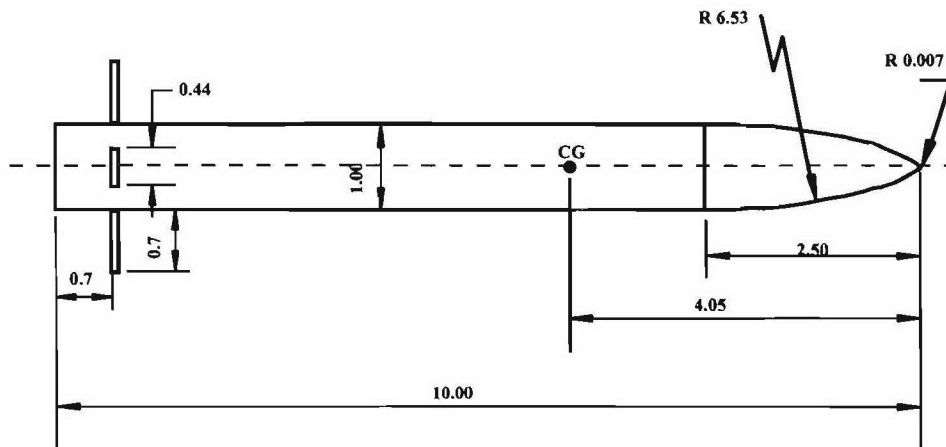


Figure 1a. Projectile body

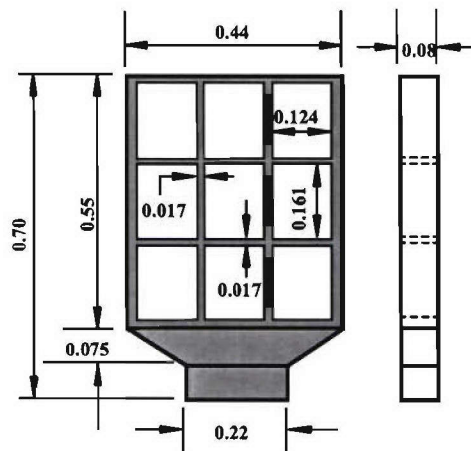


Figure 1b. Thick walled reference fin (A3\_1)

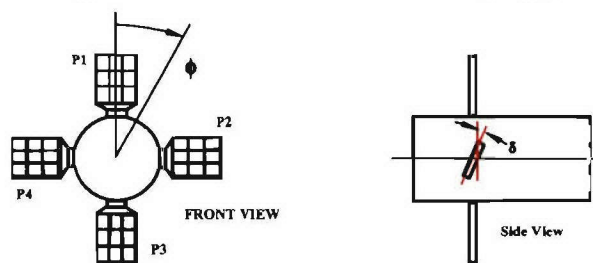


Figure 1c. Sign conventions for fin deflections.

**Figure 1. Wind tunnel configuration A3\_1– Projectile Geometry (all dimensions in caliber, 1 cal = 20.0 mm)**

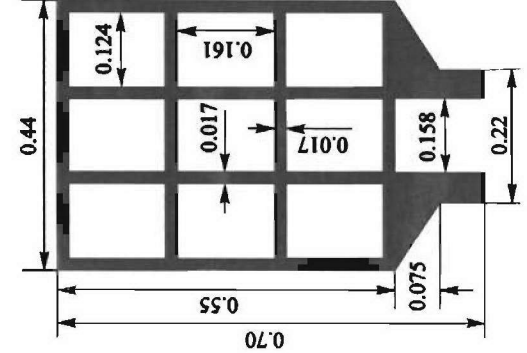


Figure 2a. Open base type

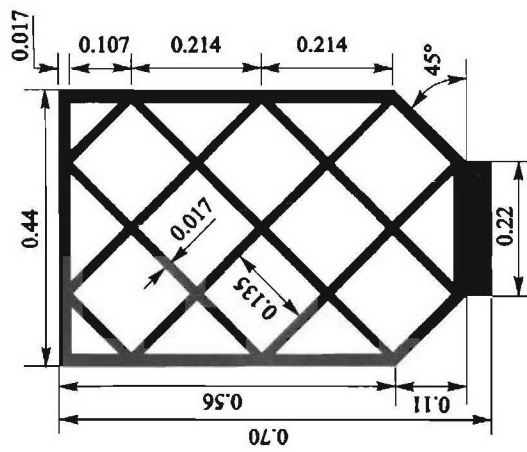


Figure 2b. Hexagonal shape type

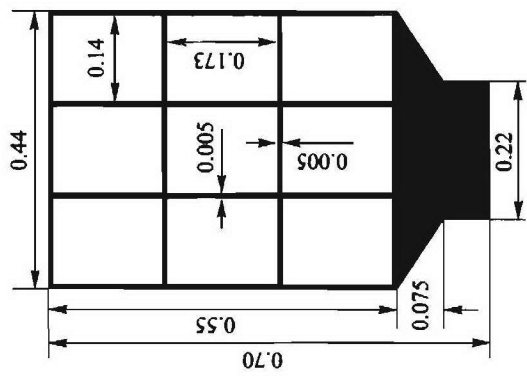


Figure 2c. Thin fin type

Figure 2 - Wind tunnel configurations – various lattice fin types (all dimensions in calibers, 1 cal = 20.0 mm)



Figure 3a. Wind tunnel model



Figure 3b. Thick fin model (A3\_1)

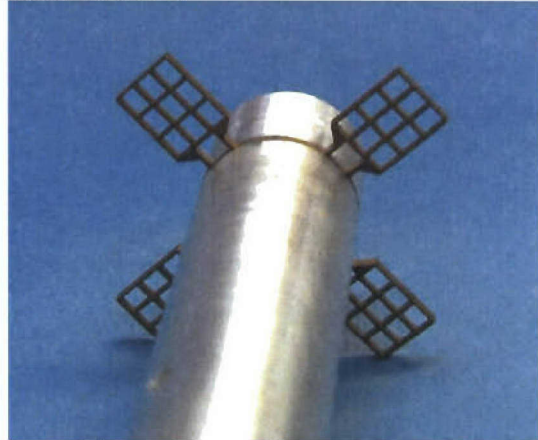


Figure 3c. Open base type

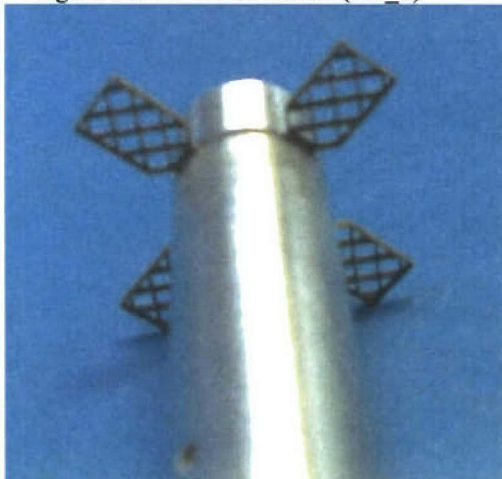


Figure 3d. Hexagonal shape type

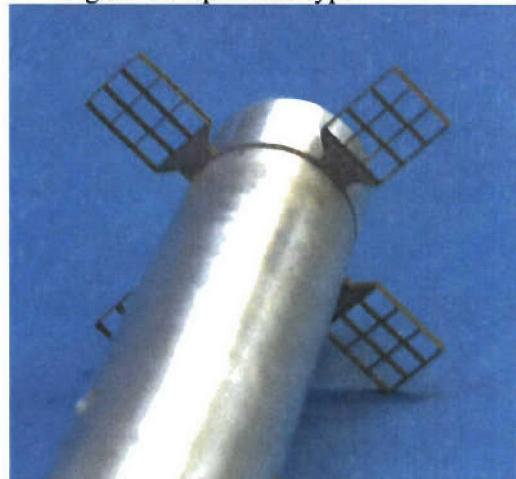


Figure 3e. Thin fin type

**Figure 3. Photographs of wind tunnel model**

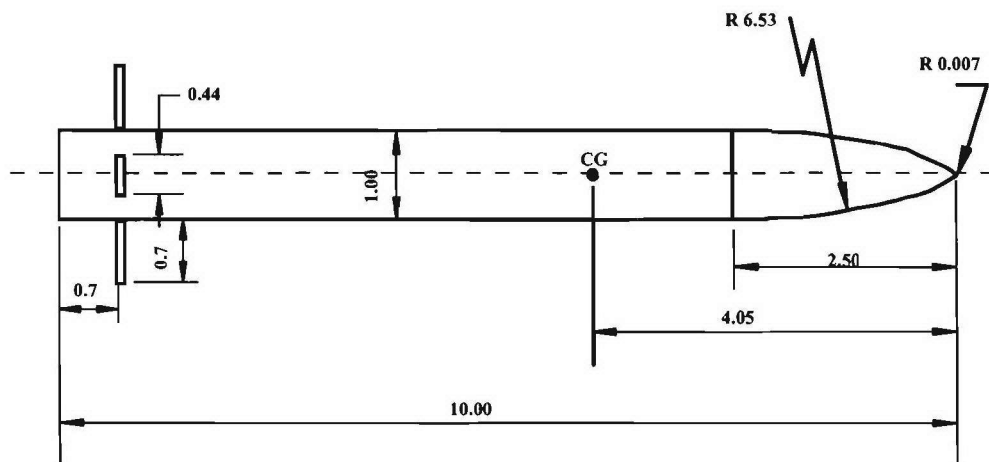


Figure 4a. Projectile body

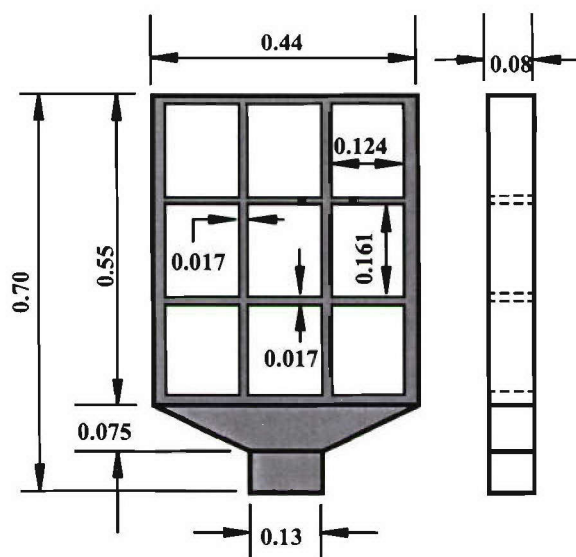
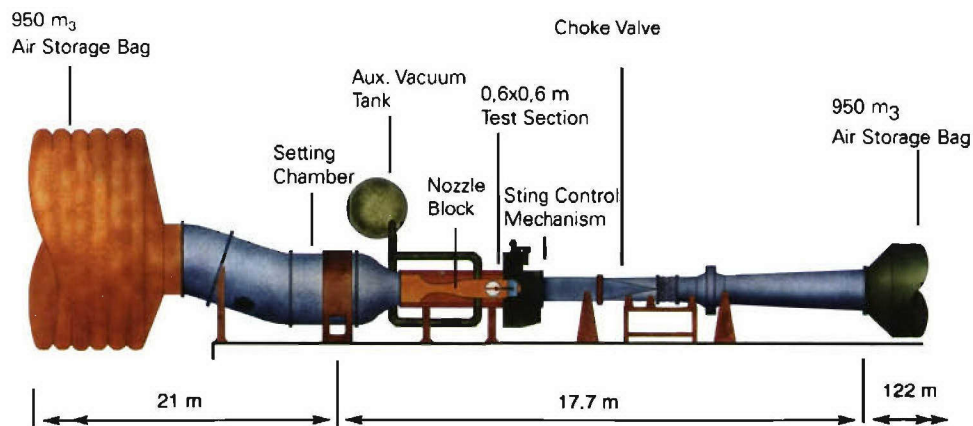


Figure 4b. Fin dimensions

**Figure 4. Aeroballistic range configuration - Projectile Geometry (all dimensions in caliber, 1 cal = 30.0 mm)**



**Figure 5. Photograph of aeroballistic range model**



**Figure 6a. DRDC's 0.6 m x 0.6 m trisonic indraft wind tunnel**

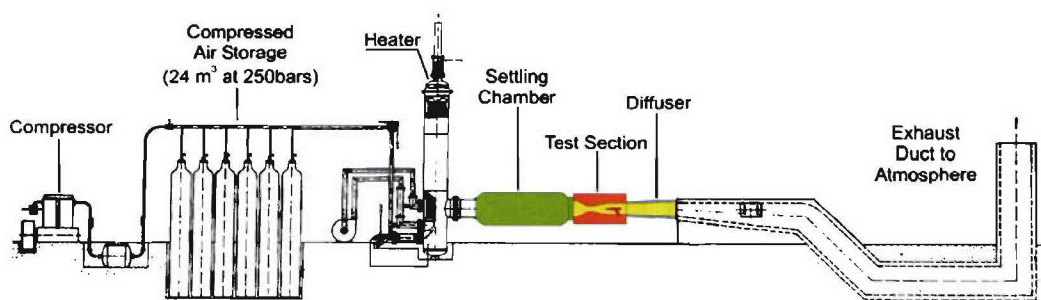
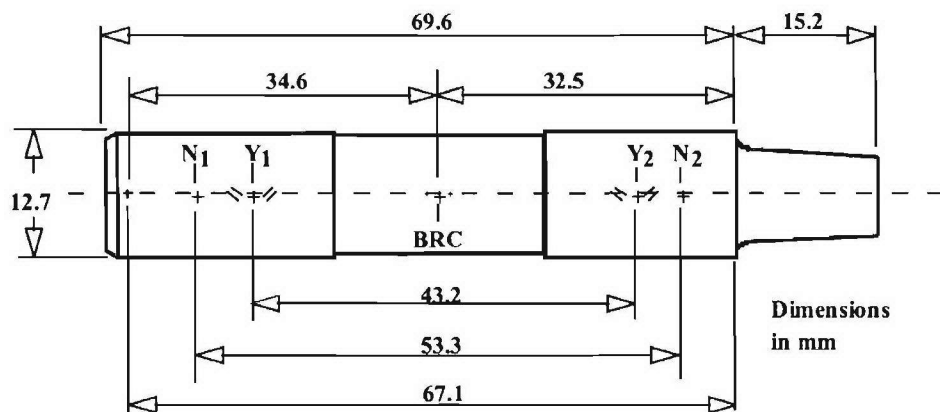


**Figure 6b – ISL's 0.2 m x 0.2 m blow down wind tunnel**

**Figure 6 - Wind tunnel facilities**



	DRDC	ISL
Rated loads: Total Normal Force (Pitching Moment = 0)	445 N	1000 N
Total Side Force (Yawing Moment = 0)	445 N	935 N
Total Axial Force	220 N	225 N
Rolling Moment	1.69 Nm	5.08 Nm
Pitching Moment (Normal Force = 0)	11.86 Nm	26.69 Nm
Yawing Moment (Side Force = 0)	9.60 Nm	20.80 Nm

**Figure 7. Dimensions and characteristics of the 12.70 mm MK-LX-B balance**



**Figure 8. Model shown in DRDC wind tunnel facility**



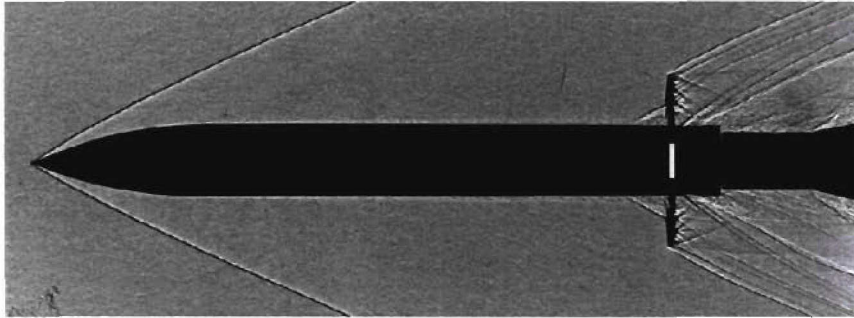


Figure 9a. A3\_1 ( $\delta = 0^\circ$ )

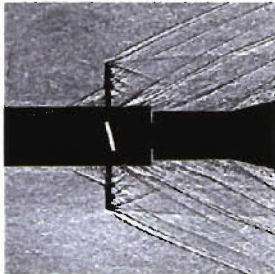


Figure 9b. A3\_7 (2 fins at  $\delta = 15^\circ$ )

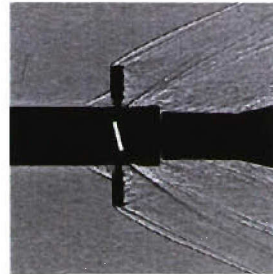


Figure 9c. A3\_4 (4 fins at  $\delta = 15^\circ$ )

**Figure 9. Wind tunnel shadowgraph for  $\alpha = 0^\circ$  at Mach = 3.0**

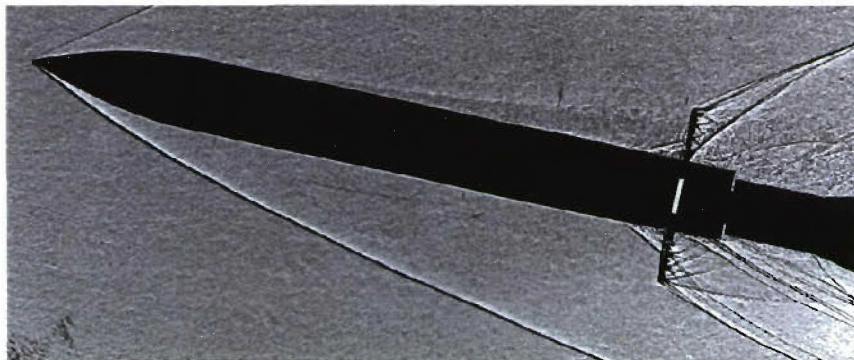


Figure 10a. A3\_1 ( $\delta = 0^\circ$ )

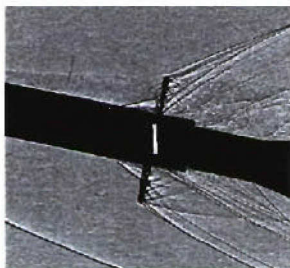


Figure 10b. A3\_7 (2 fins at  $\delta = 15^\circ$ )

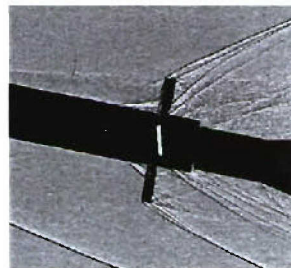
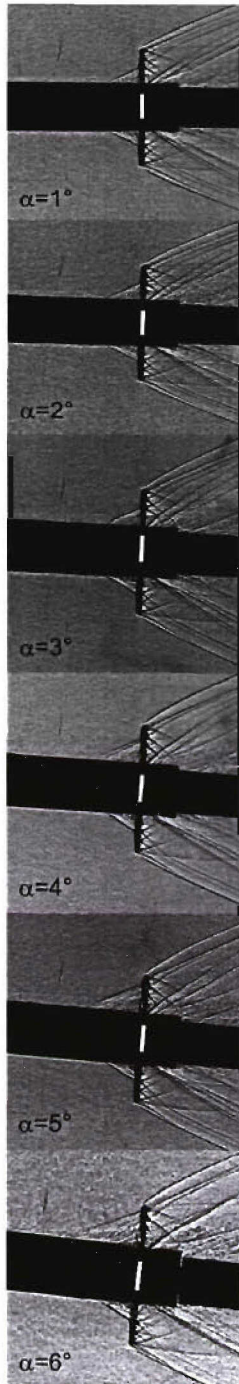
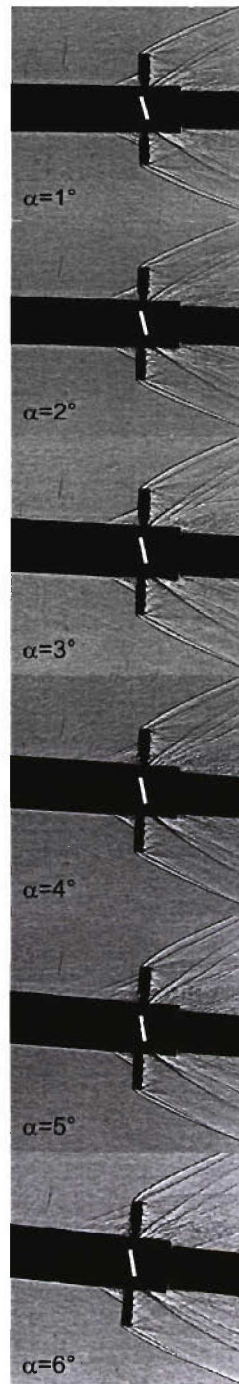


Figure 10c. A3\_4 (4 fins at  $\delta = 15^\circ$ )

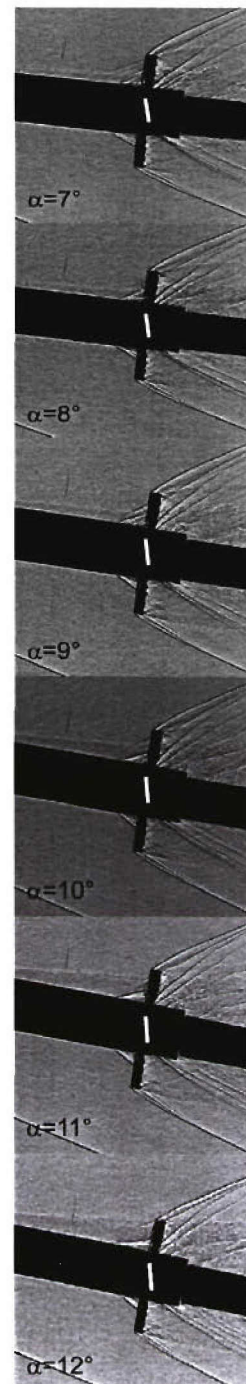
**Figure 10. Wind tunnel shadowgraph for  $\alpha = 12^\circ$  at Mach=3.0**



**Figure 11. Angle of attack effects  
for A3\_1 (4 fins at  $\delta=0^\circ$ ) at Mach =3.0**



**Figure 12. Angle of attack effects  
for A3\_4 (4 fins at  $\delta=15^\circ$ ) at Mach =3.0**



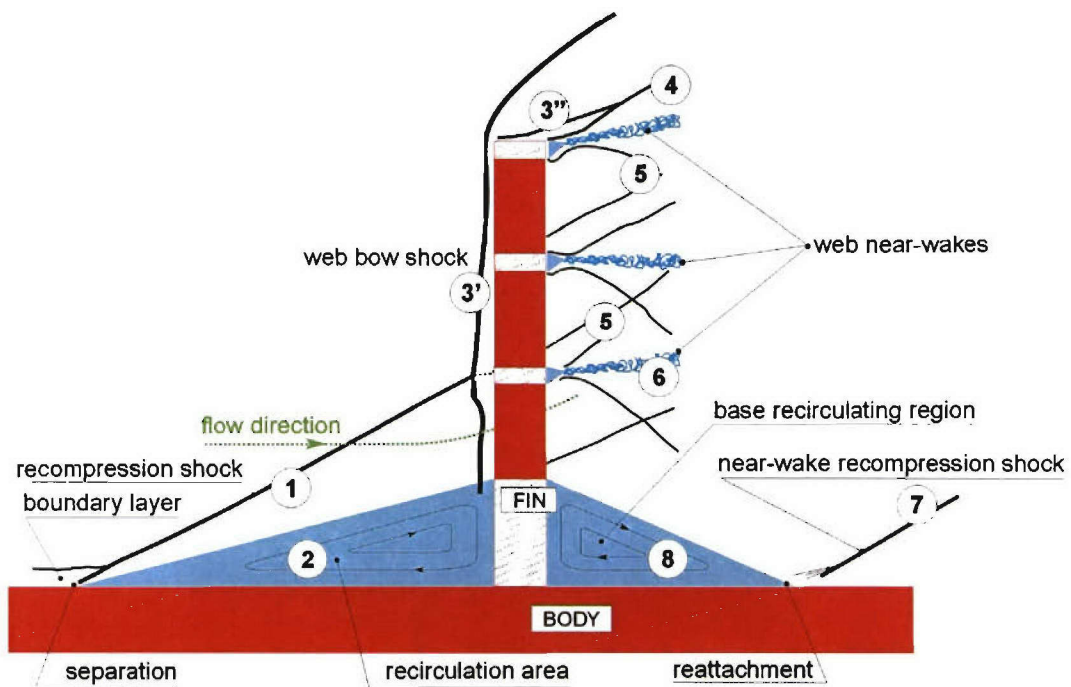


**Figure 13. Schematic of the flow structure**

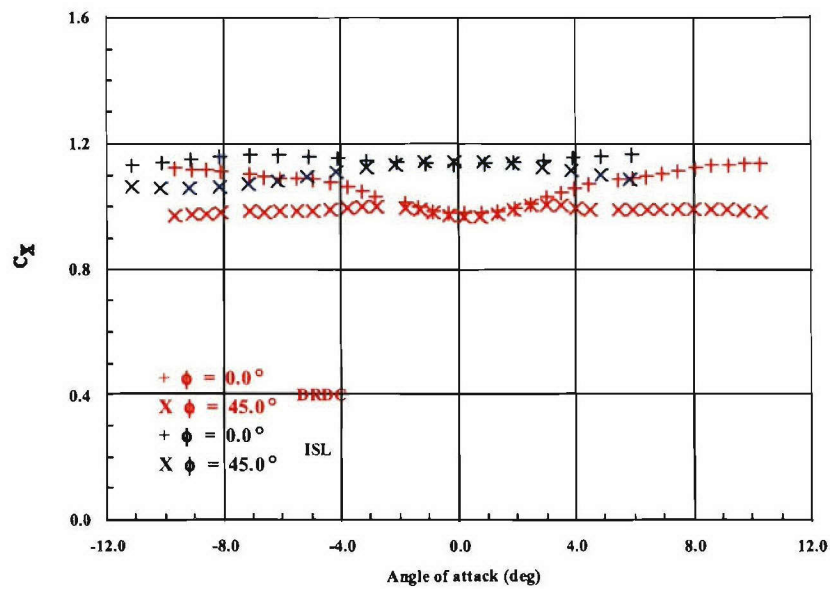


Figure 14a. Axial force coefficient vs. incidence

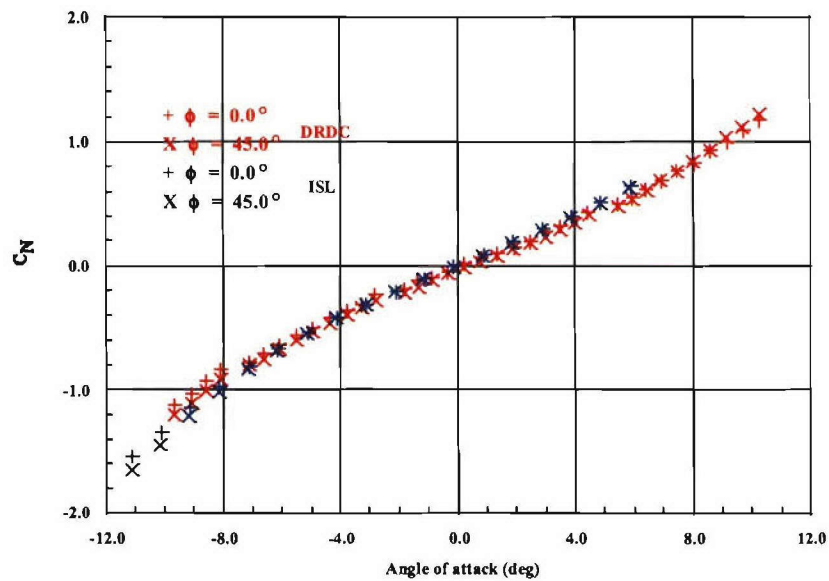


Figure 14b. Normal force coefficient vs. incidence

**Figure 14. Comparison of DRDC and ISL wind tunnel results for A3\_4,  $M = 3.0$**



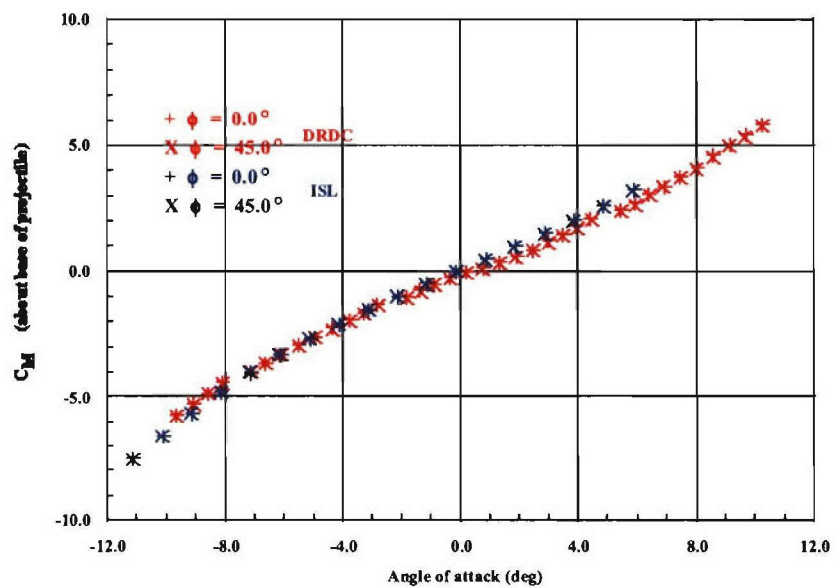


Figure 14c. Pitch moment coefficient about base vs. incidence

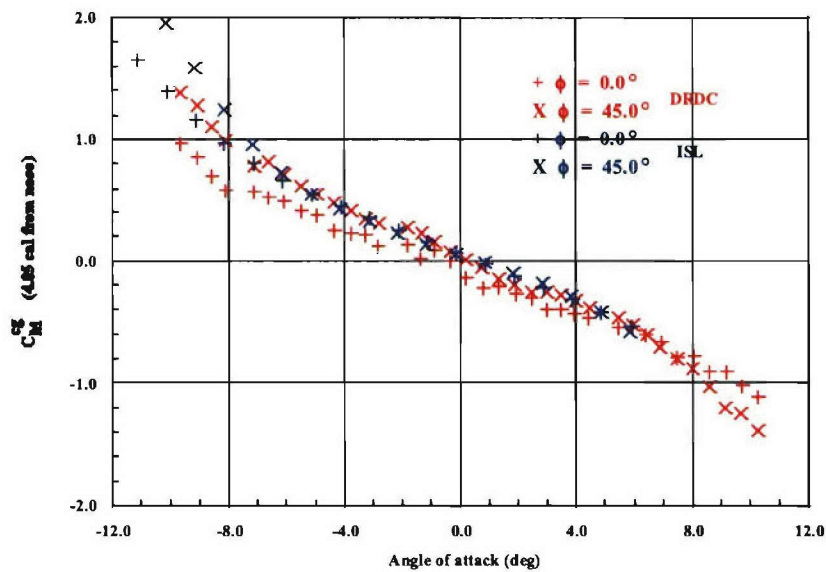


Figure 14d. Pitch moment coefficient about cg vs. incidence

Figure 14. Comparison of DRDC and ISL wind tunnel results for A3\_4,  $M = 3.0$  (cont)

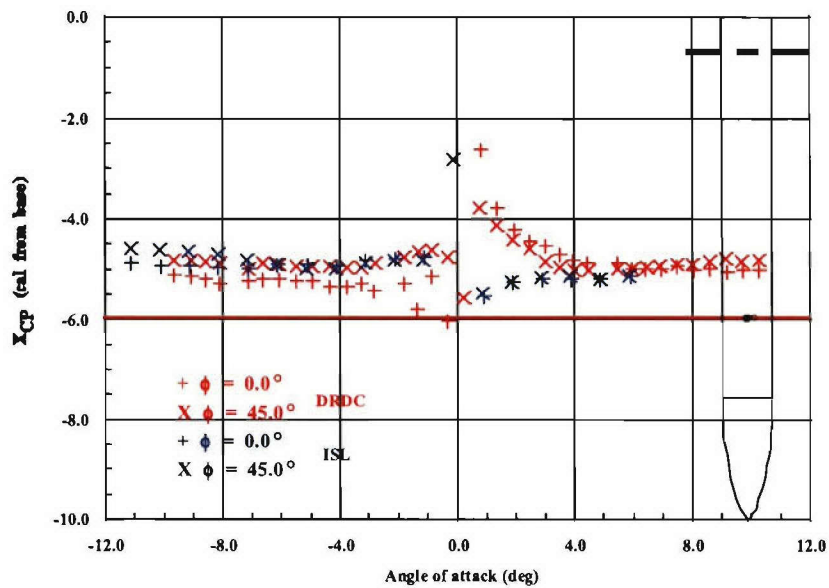


Figure 14e. Center of pressure location vs. incidence

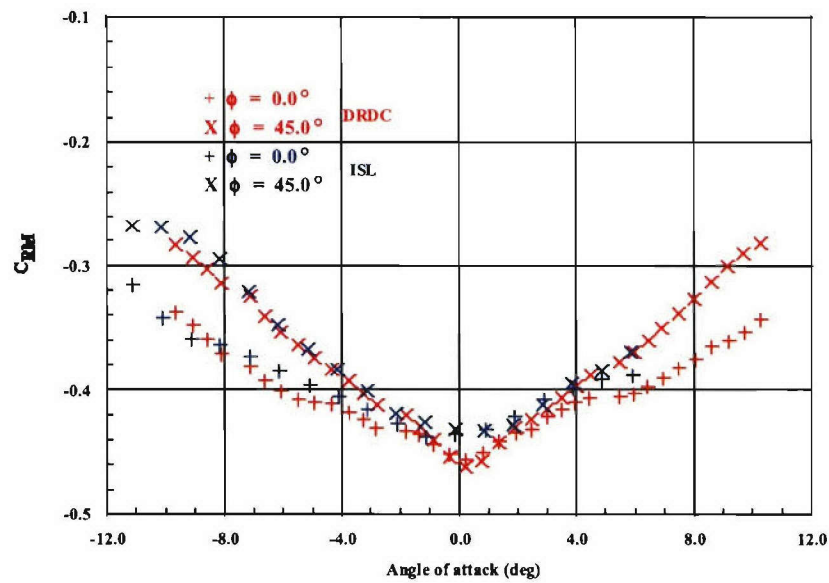


Figure 14f. Roll moment coefficient vs. incidence

Figure 14. Comparison of DRDC and ISL wind tunnel results for A3\_4,  $M = 3.0$  (cont)

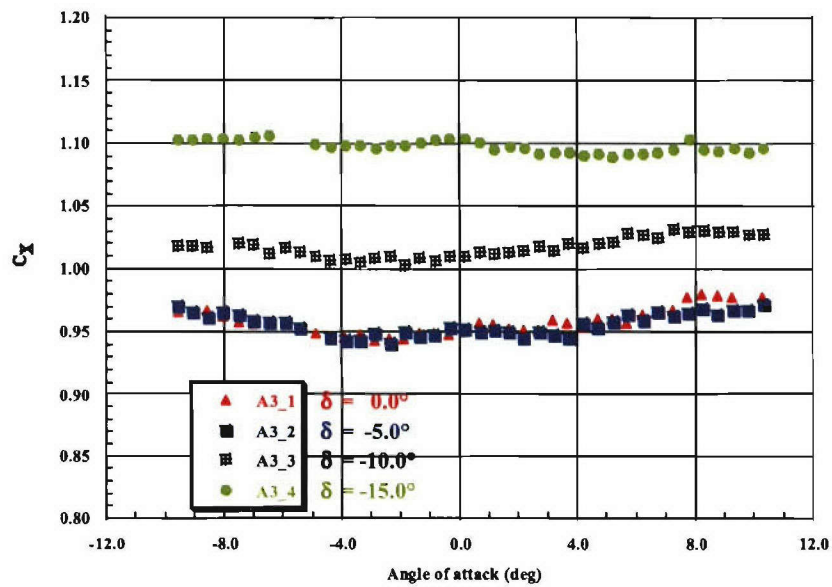


Figure 15a. Axial force coefficient vs. incidence

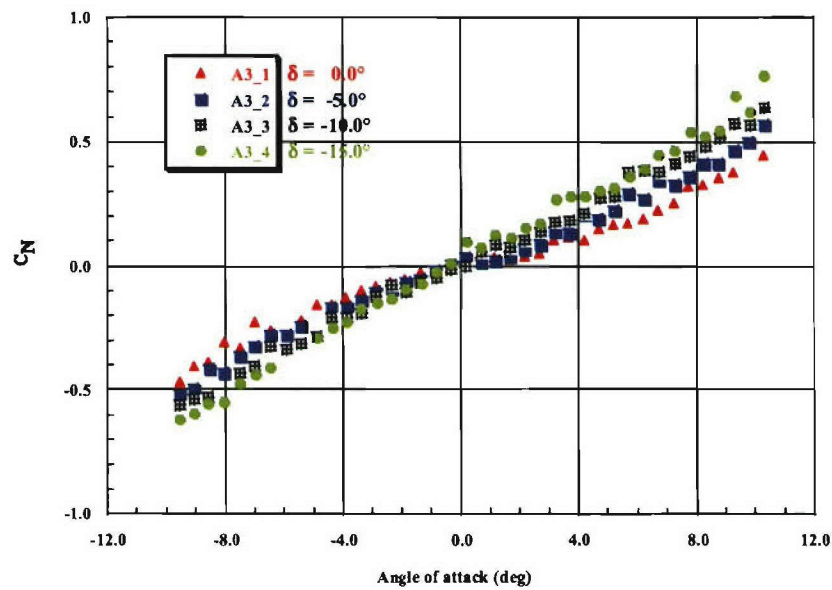


Figure 15b. Normal force coefficient vs. incidence

Figure 15. Comparison of wind tunnel results for Group 1, Mach = 0.6;  $\phi = 0.0^\circ$



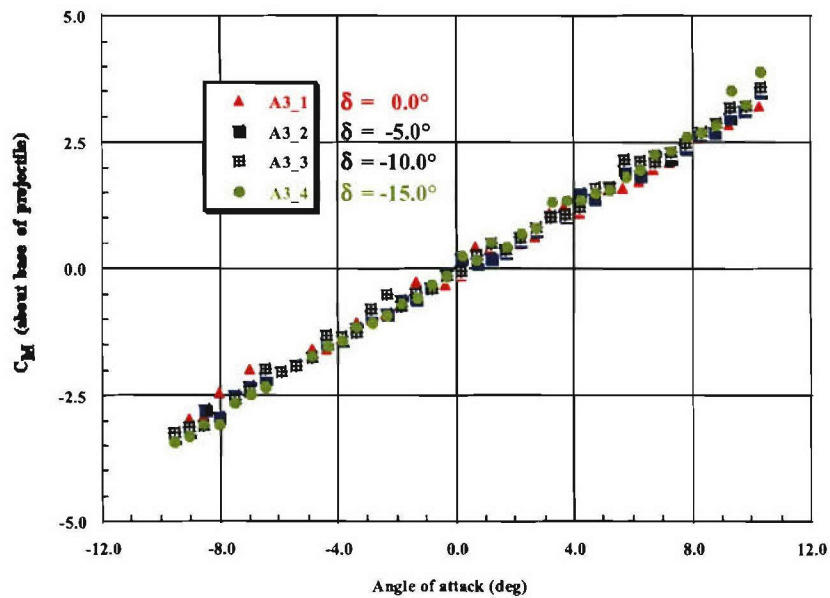


Figure 15c. Pitch moment coefficient about base vs. incidence

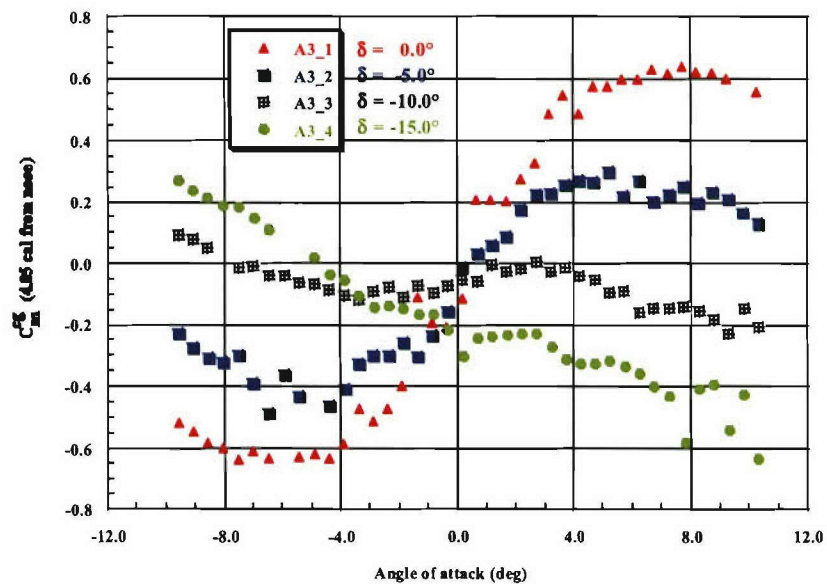


Figure 15d. Pitch moment coefficient about cg vs. incidence

Figure 15. Comparison of wind tunnel results for Group 1, Mach = 0.6;  $\phi = 0.0^\circ$  (cont.)

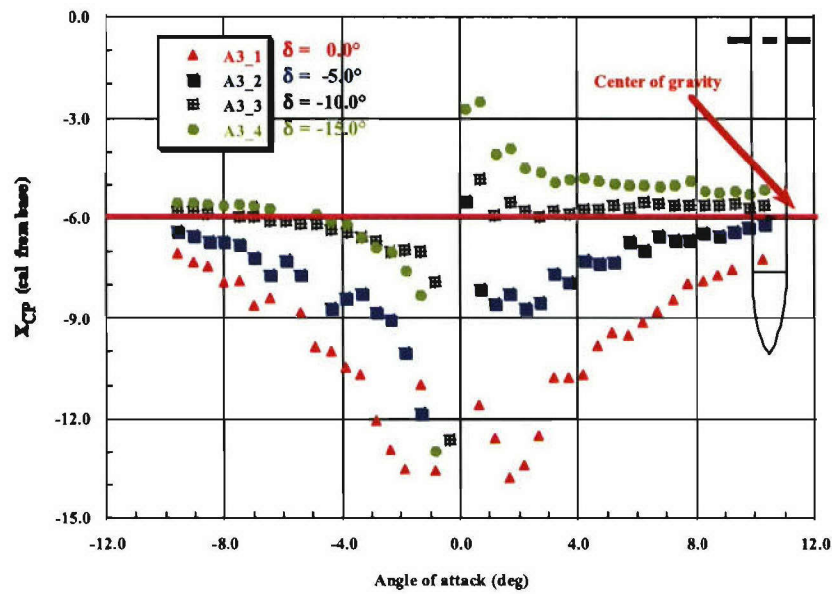


Figure 15e. Center of pressure location vs. incidence

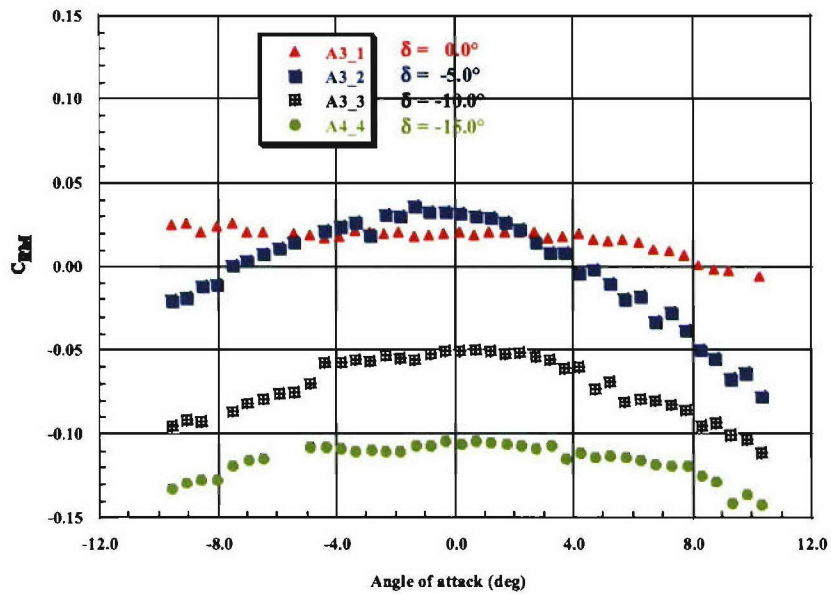


Figure 15f. Roll moment coefficient vs. incidence

Figure 15. Comparison of wind tunnel results for Group 1, Mach = 0.6;  $\phi = 0.0^\circ$  (cont.)

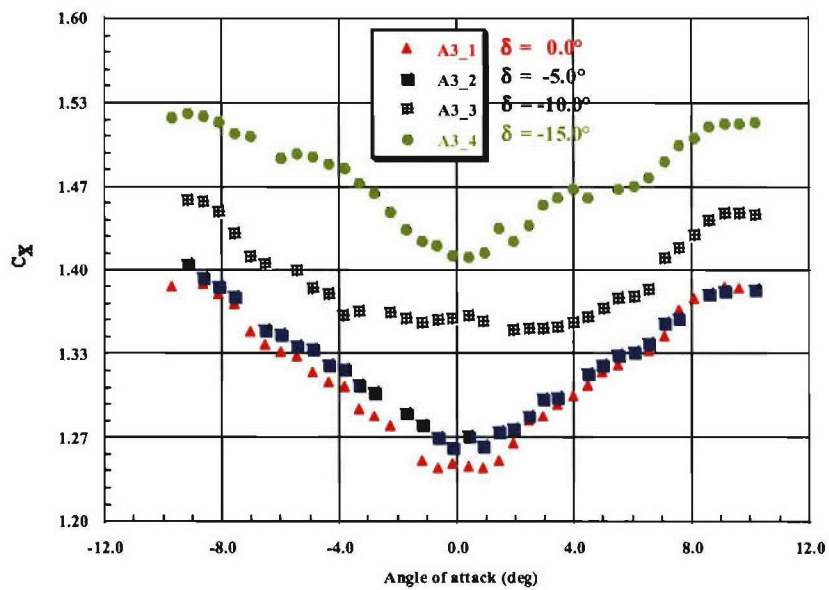


Figure 16a. Axial force coefficient vs. incidence

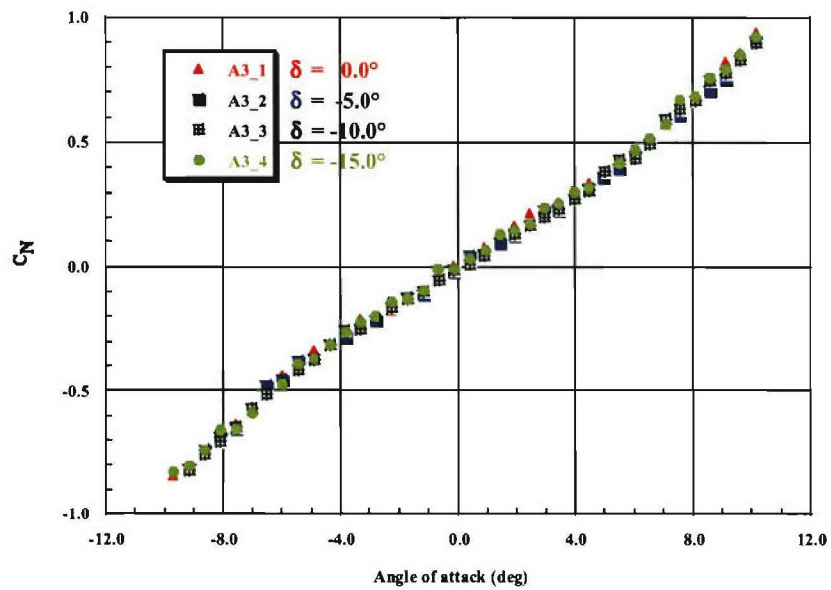


Figure 16b. Normal force coefficient vs. incidence

**Figure 16. Comparison of wind tunnel results for Group 1, Mach = 1.5;  $\phi = 0.0^\circ$**

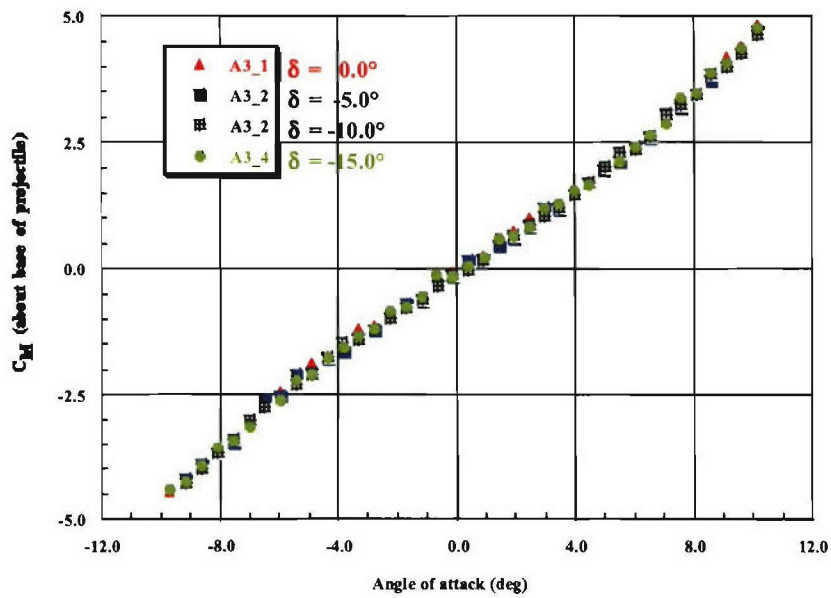


Figure 16c. Pitch moment coefficient about base vs. incidence

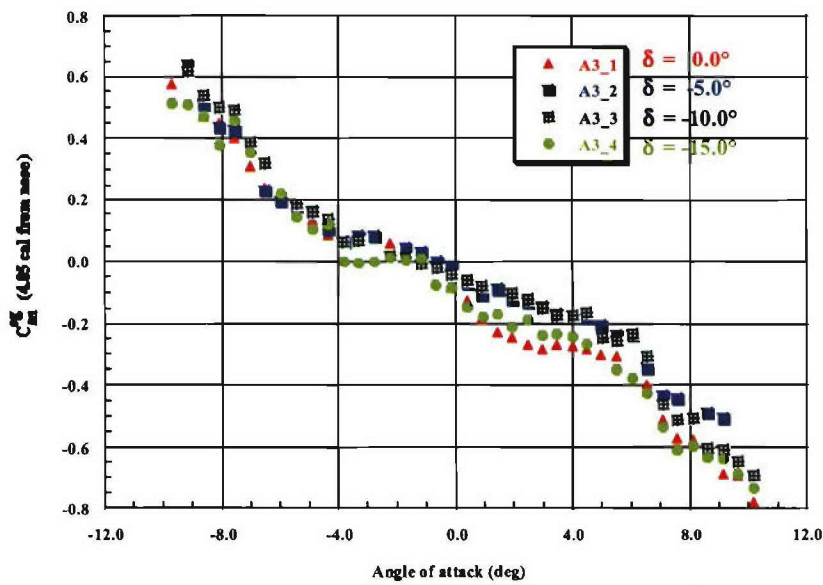


Figure 16d. Pitch moment coefficient about cg vs. incidence

Figure 16. Comparison of wind tunnel results for Group 1, Mach = 1.5;  $\phi = 0.0^\circ$  (cont.)

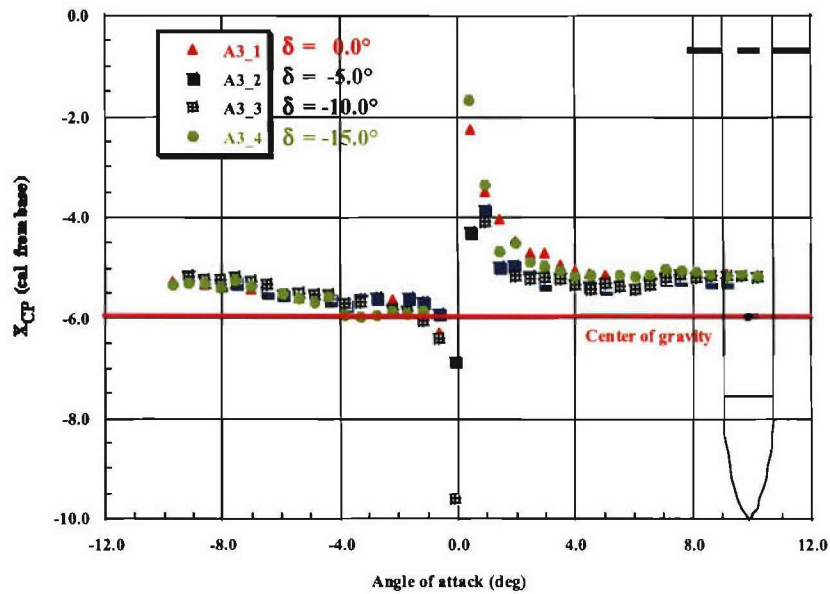


Figure 16e. Center of pressure location vs. incidence

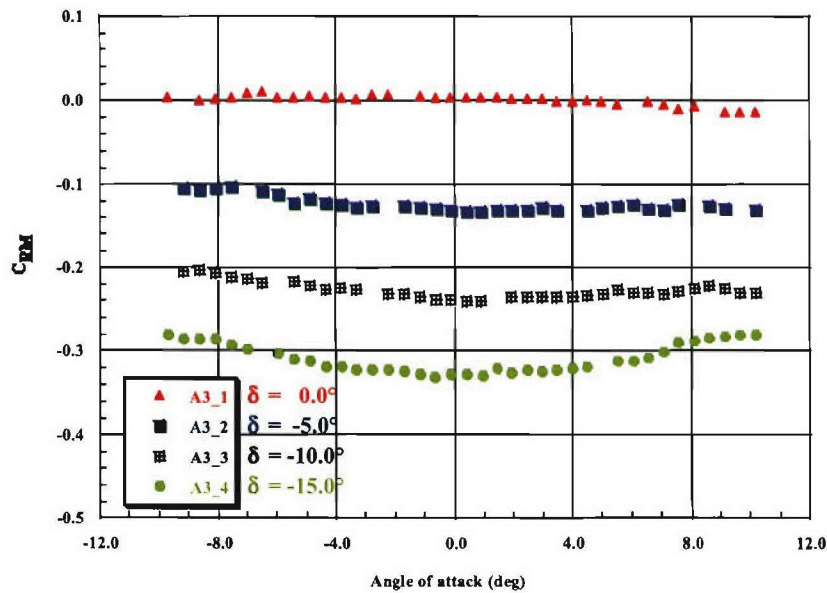


Figure 16f. Roll moment coefficient vs. incidence

Figure 16. Comparison of wind tunnel results for Group 1, Mach = 1.5;  $\phi = 0.0^\circ$  (cont.)

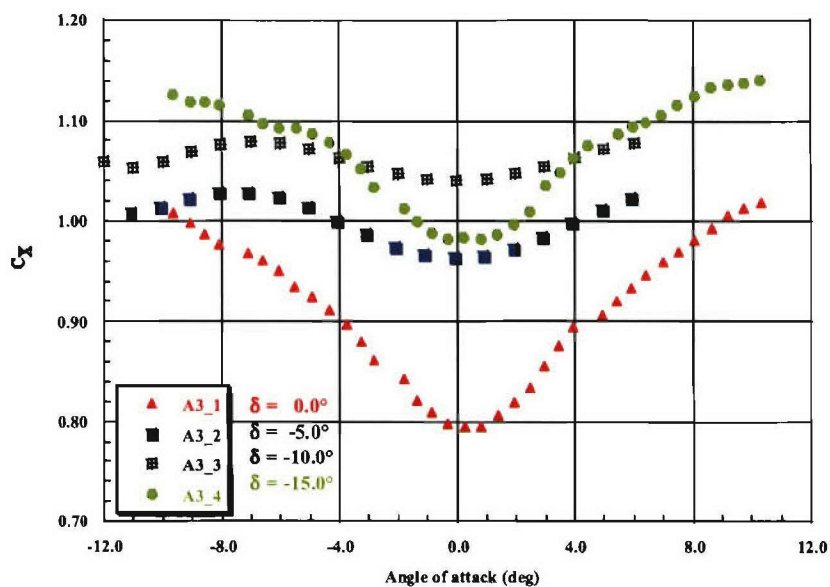


Figure 17a. Axial force coefficient vs. incidence

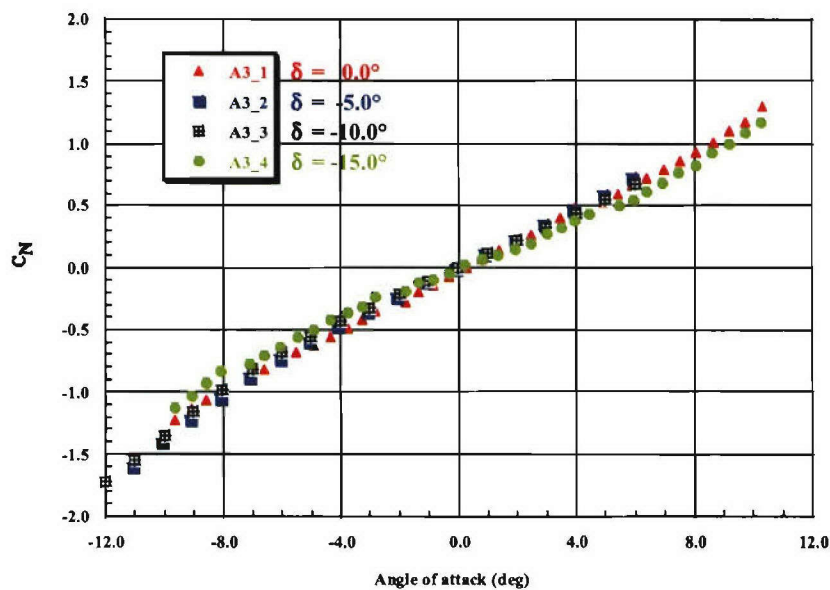


Figure 17b. Normal force coefficient vs. incidence

**Figure 17. Comparison of wind tunnel results for Group 1, Mach = 3.0;  $\phi = 0.0^\circ$**

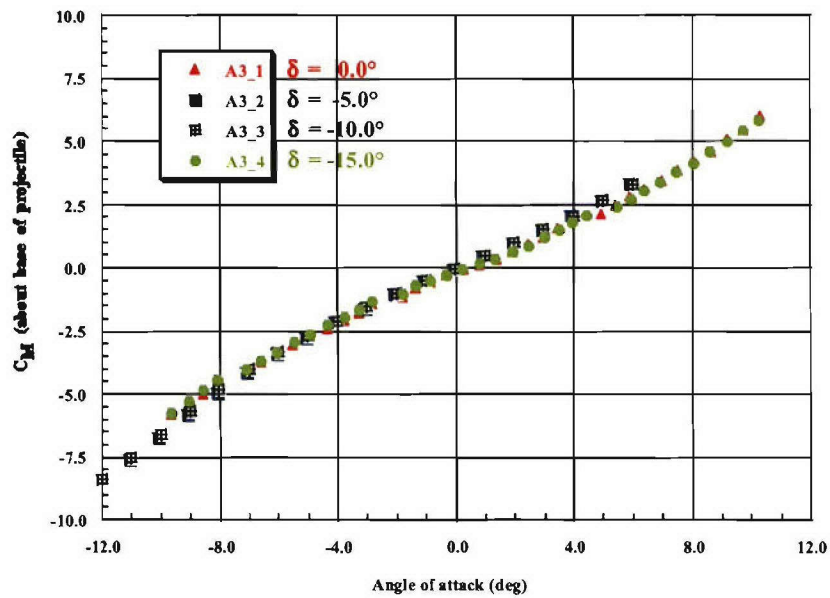


Figure 17c. Pitch moment coefficient about base vs. incidence

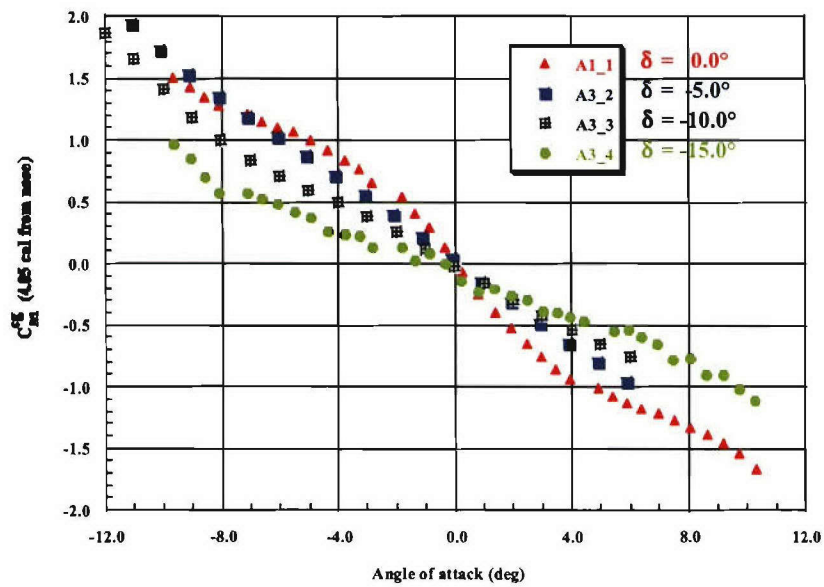


Figure 17d. Pitch moment coefficient about cg vs. incidence

Figure 17. Comparison of wind tunnel results for Group 1, Mach = 3.0;  $\phi = 0.0^\circ$  (cont)



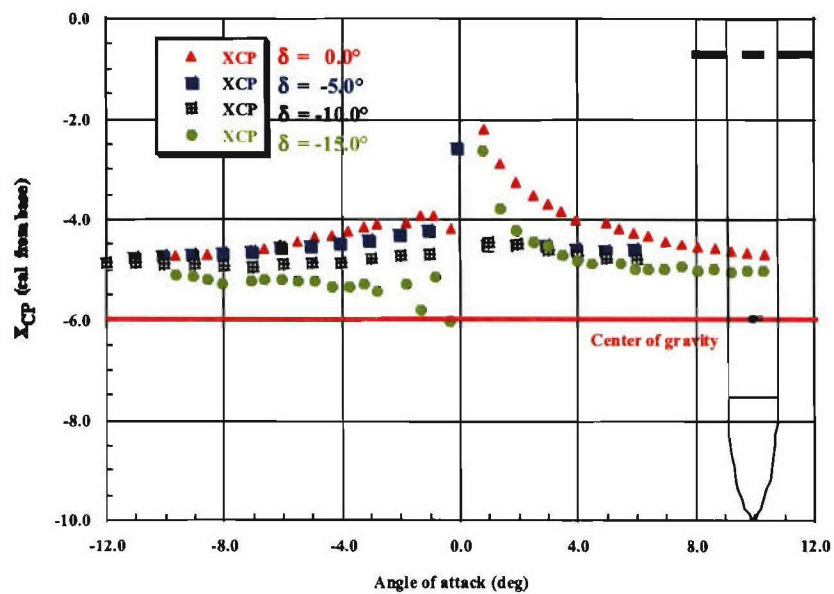


Figure 17e. Center of pressure location vs. incidence

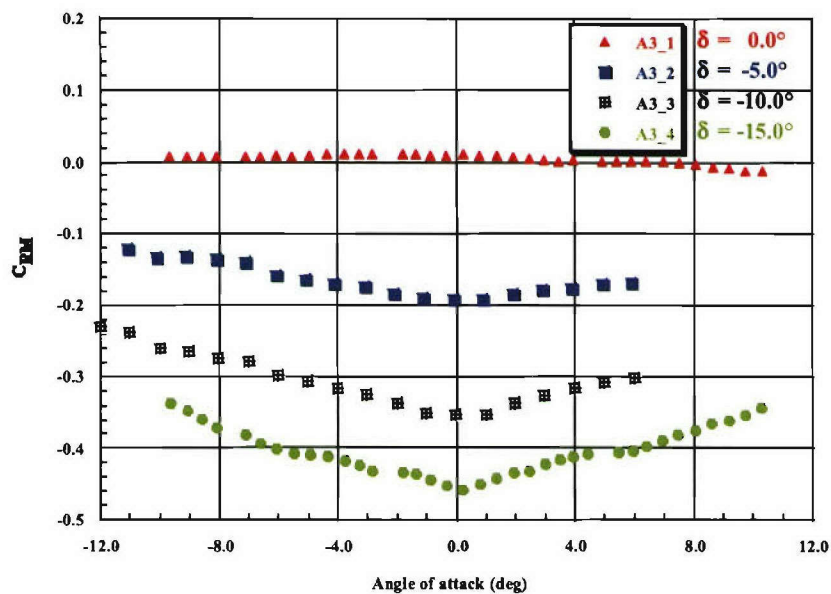


Figure 17f. Roll moment coefficient vs. incidence

Figure 17. Comparison of wind tunnel results for Group 1, Mach = 3.0;  $\phi = 0.0^\circ$  (cont)

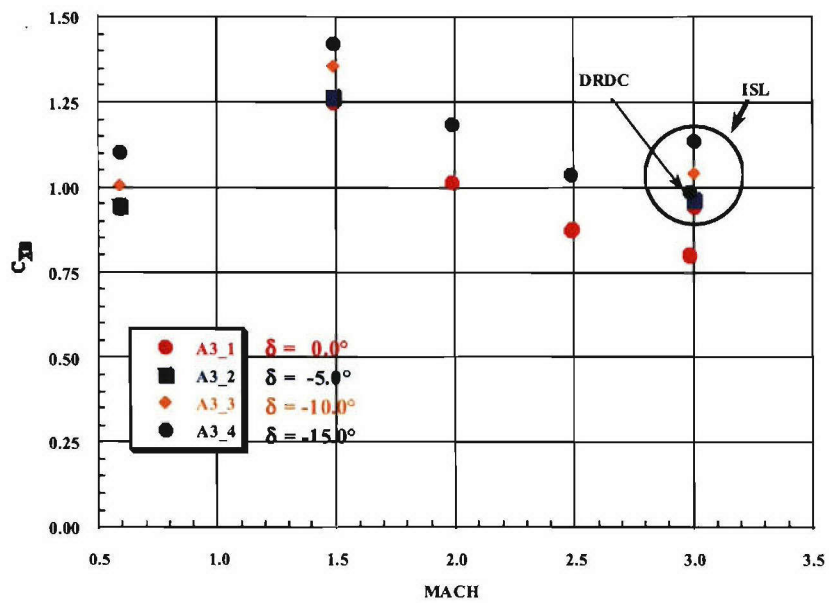


Figure 18a. Axial force coefficient at  $\alpha = 0.0^\circ$

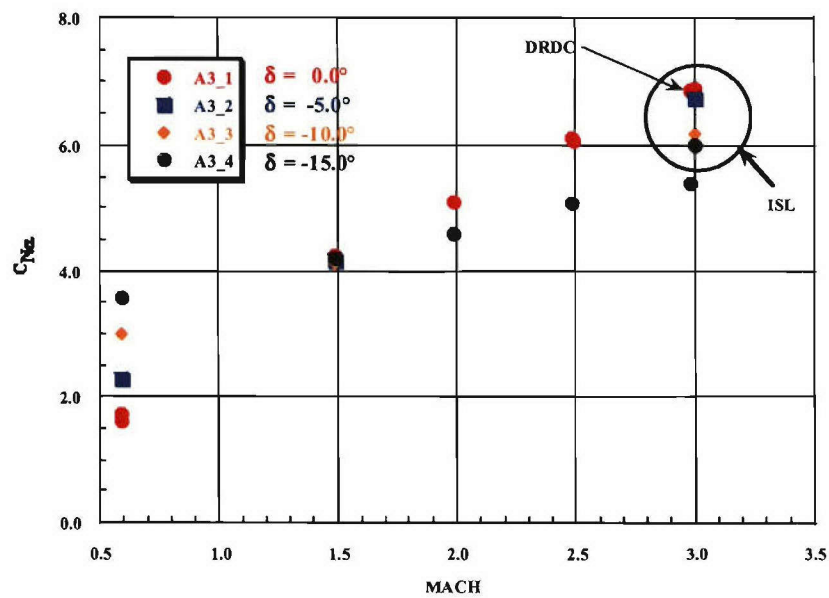


Figure 18b. Normal force coefficient slope

Figure 18. Comparison of wind tunnel results for Group 1 vs. Mach number;  $\phi = 0.0^\circ$

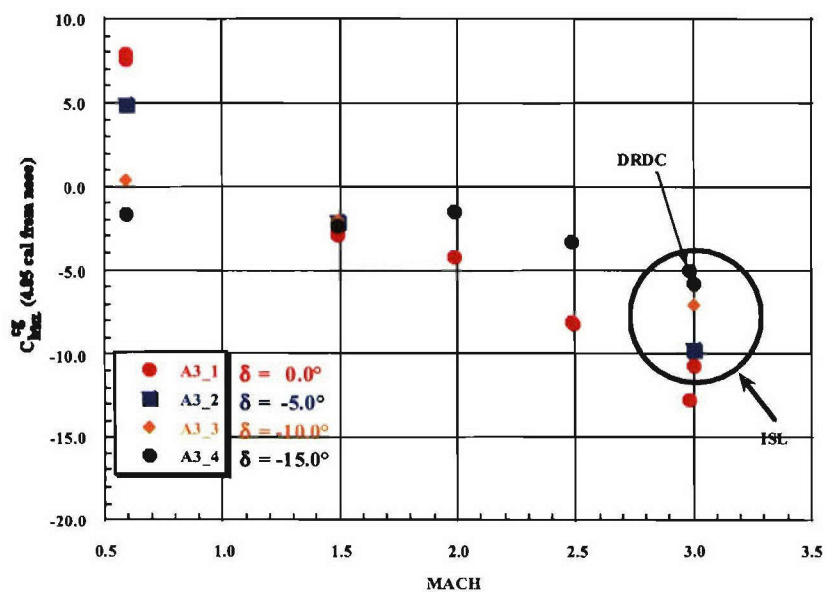


Figure 18c. Pitch moment coefficient slope about cg

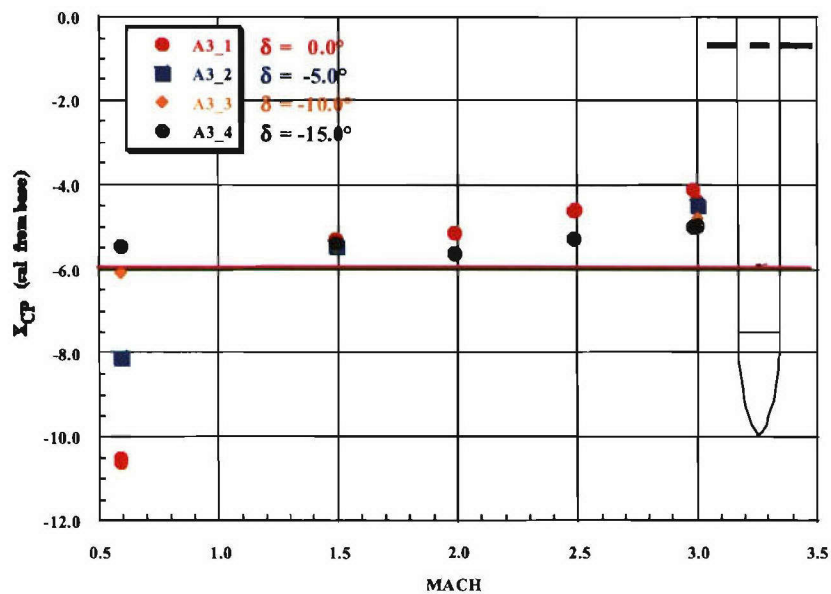


Figure 18d. Center of pressure location

Figure 18. Comparison of wind tunnel results for Group 1 vs. Mach number;  $\phi = 0.0^\circ$  (cont)

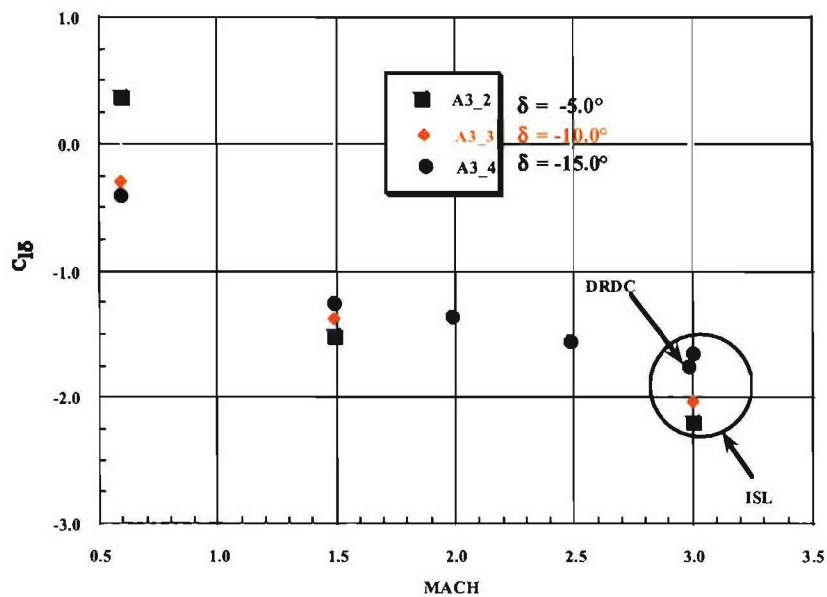


Figure 18e. Roll moment coefficient

Figure 18. Comparison of wind tunnel results for Group 1 vs. Mach number;  $\phi = 0.0^\circ$  (cont)

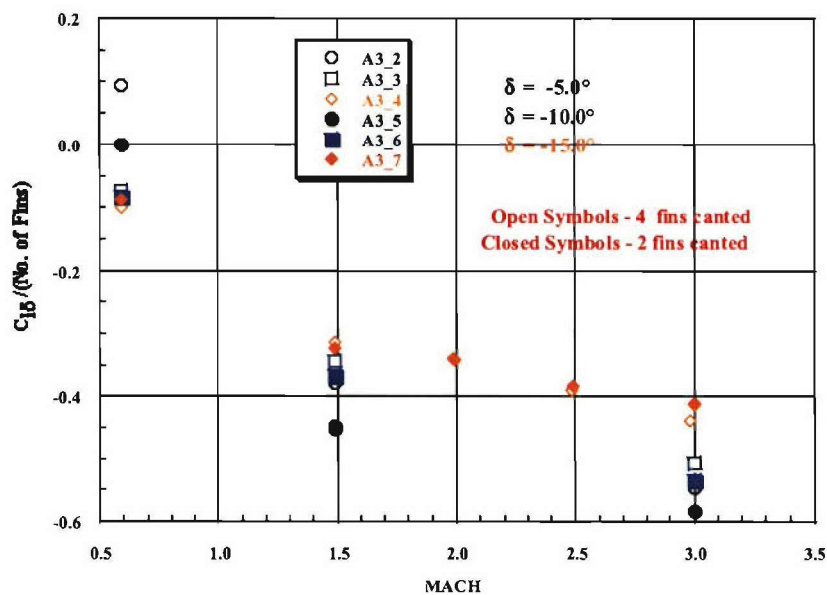


Figure 19. Comparison of wind tunnel  $C_{l\delta}$  results for Group 2 vs. Mach number;  $\phi = 0.0^\circ$

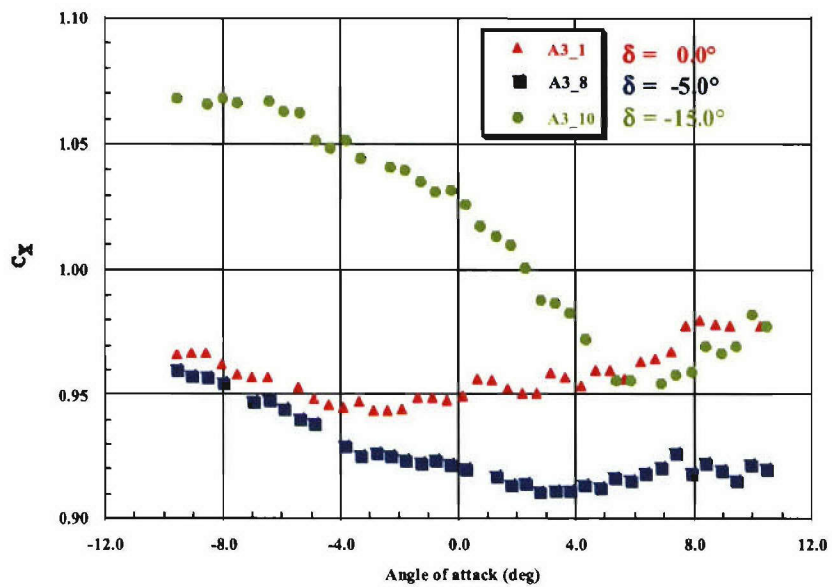


Figure 20a. Axial force coefficient vs. incidence

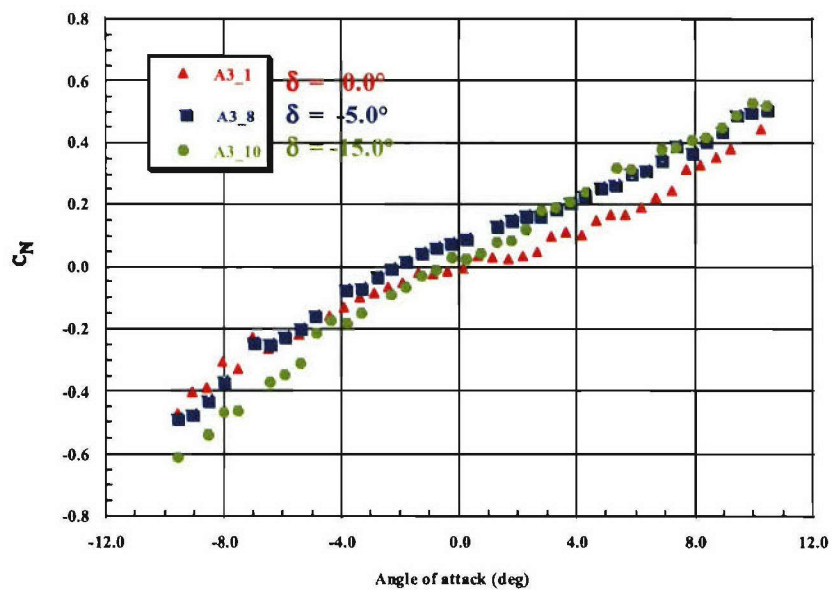


Figure 20b. Normal force coefficient vs. incidence

**Figure 20. Comparison of wind tunnel results for Group 3, Mach = 0.6;  $\phi = 0.0^\circ$**

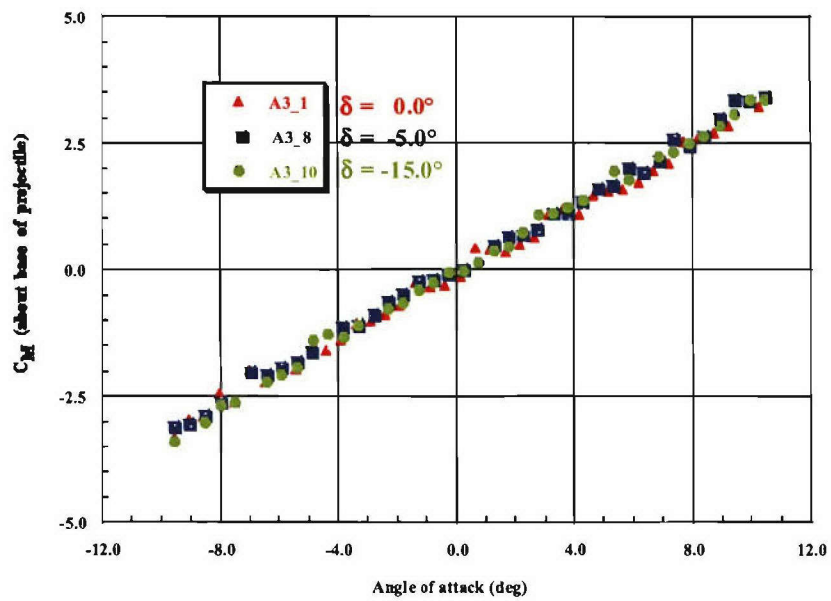


Figure 20c. Pitch moment coefficient about base vs. incidence

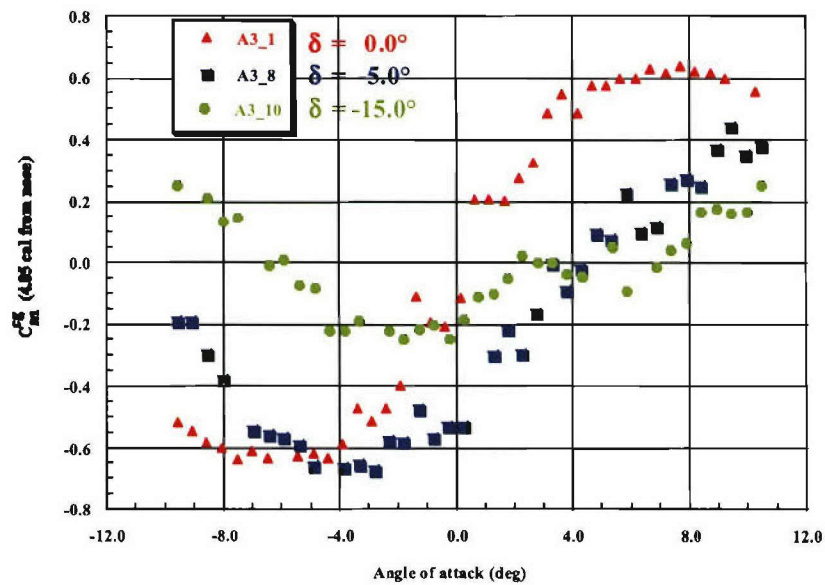


Figure 20d. Pitch moment coefficient about cg vs. incidence

Figure 20. Comparison of wind tunnel results for Group 3, Mach = 0.6;  $\phi = 0.0^\circ$  (cont)

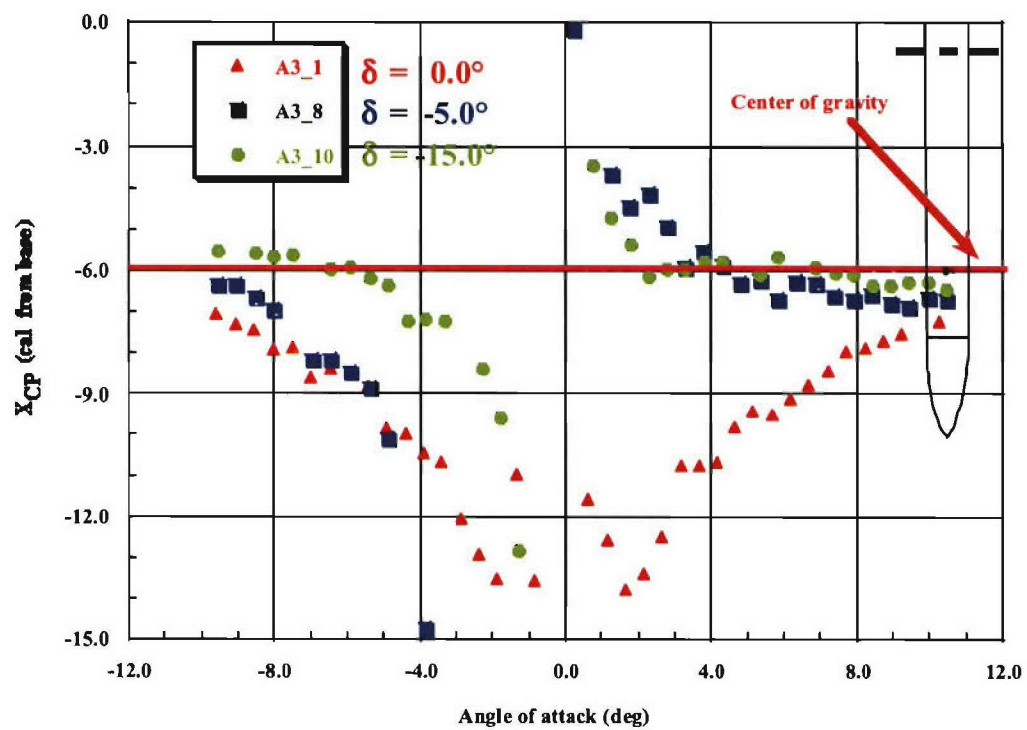


Figure 20e. Center of pressure location vs. incidence

Figure 20. Comparison of wind tunnel results for Group 3, Mach = 0.6;  $\phi = 0.0^\circ$  (cont)



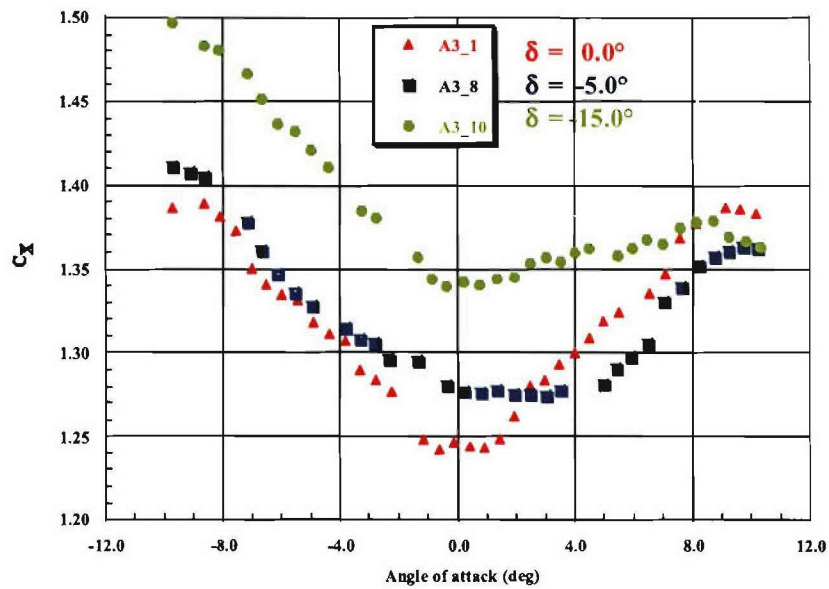


Figure 21a. Axial force coefficient vs. incidence

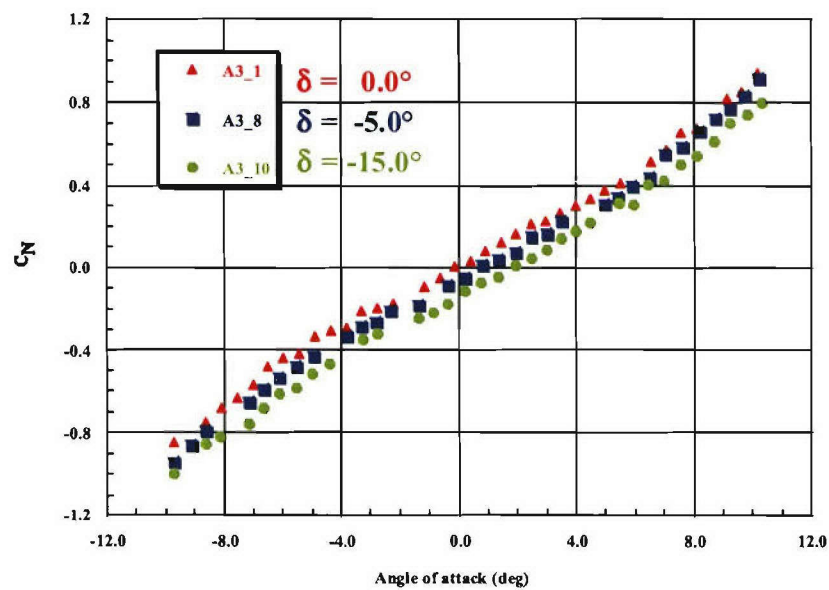


Figure 21b. Normal force coefficient vs. incidence

Figure 21. Comparison of wind tunnel results for Group 3, Mach = 1.5;  $\phi = 0.0^\circ$

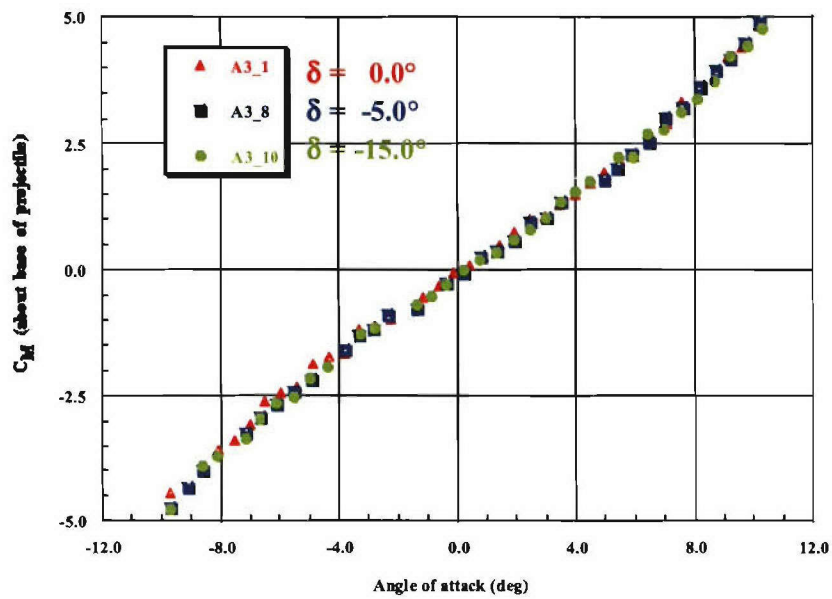


Figure 21c. Pitch moment coefficient about base vs. incidence

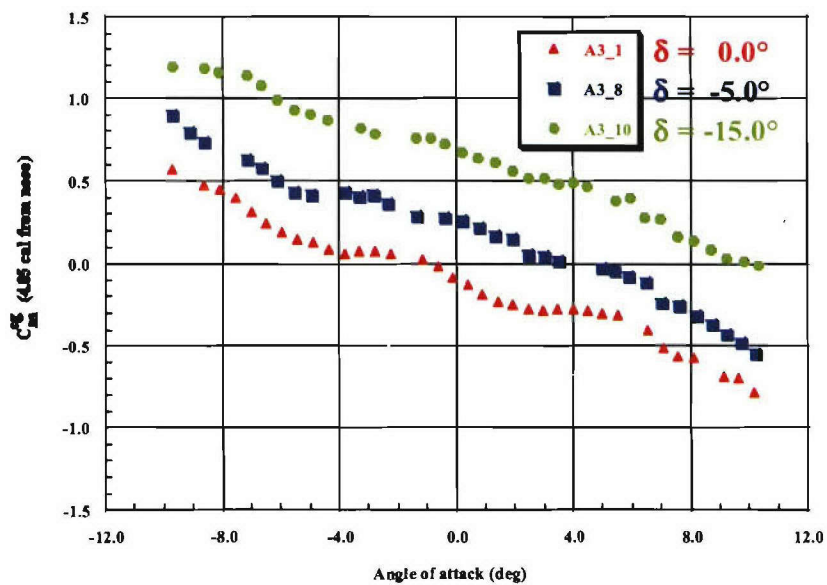


Figure 21d. Pitch moment coefficient about cg vs. incidence

Figure 21. Comparison of wind tunnel results for Group 3, Mach = 1.5;  $\phi = 0.0^\circ$  (cont)

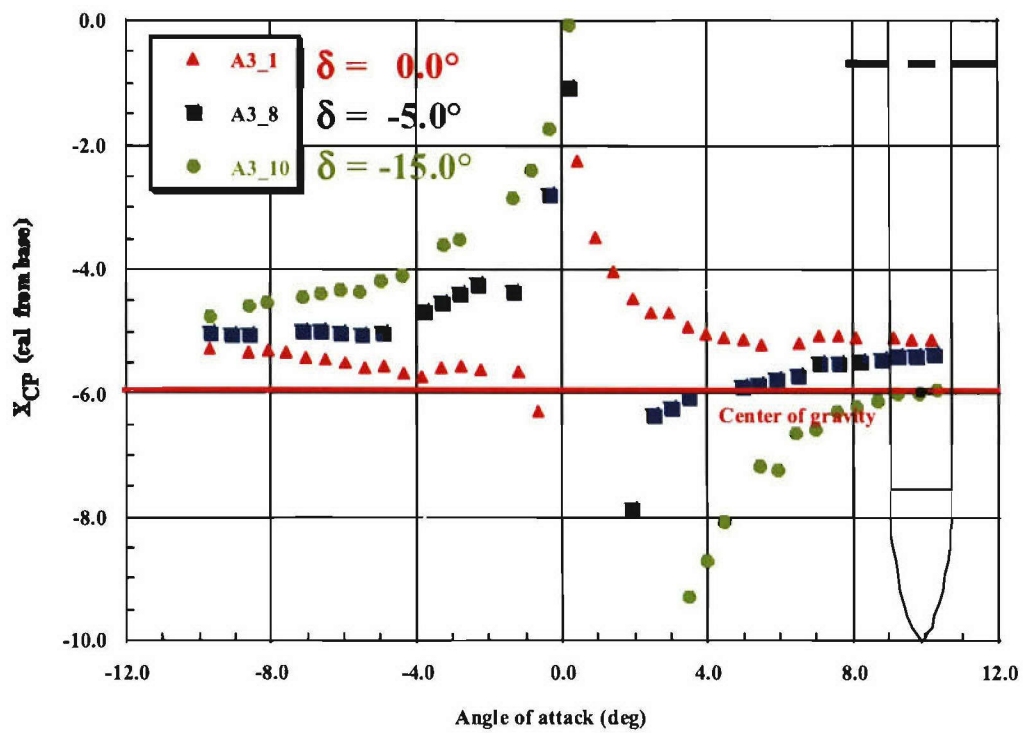


Figure 21e. Center of pressure location vs. incidence

Figure 21. Comparison of wind tunnel results for Group 3, Mach = 1.5;  $\phi = 0.0^\circ$  (cont)

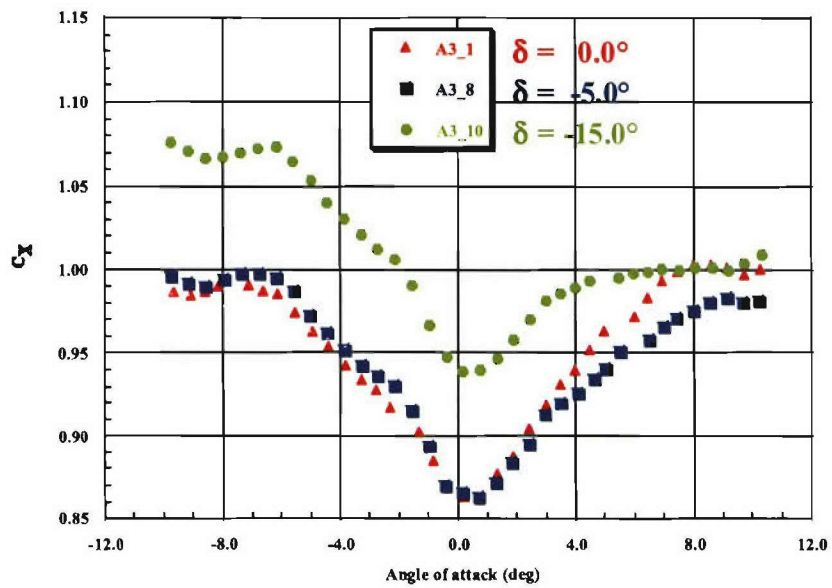


Figure 22a. Axial force coefficient vs. incidence

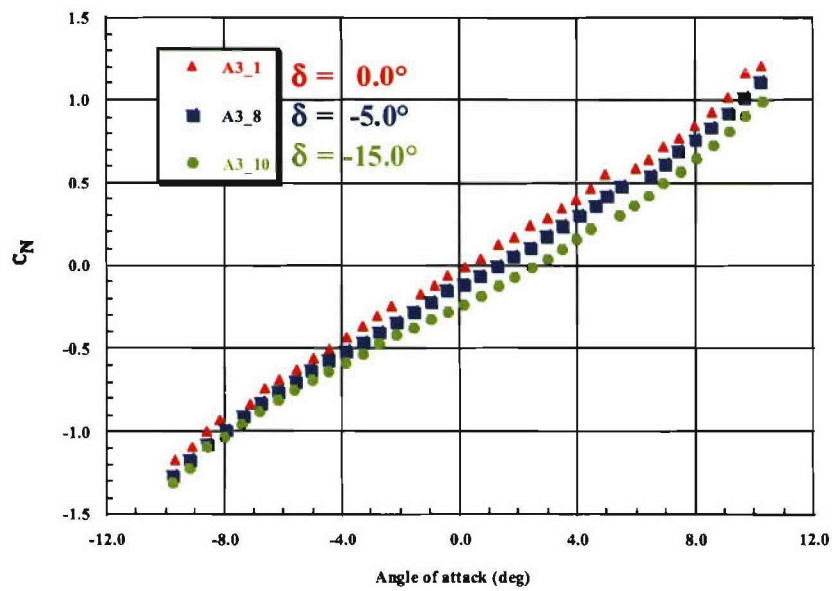


Figure 22b. Normal force coefficient vs. incidence

**Figure 22. Comparison of wind tunnel results for Group 3, Mach = 2.5;  $\phi = 0.0^\circ$**

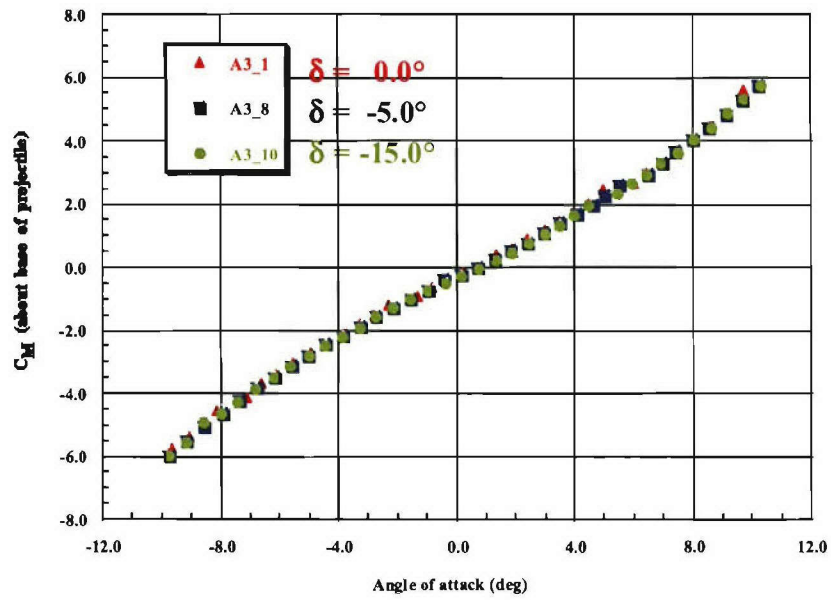


Figure 22c. Pitch moment coefficient about base vs. incidence

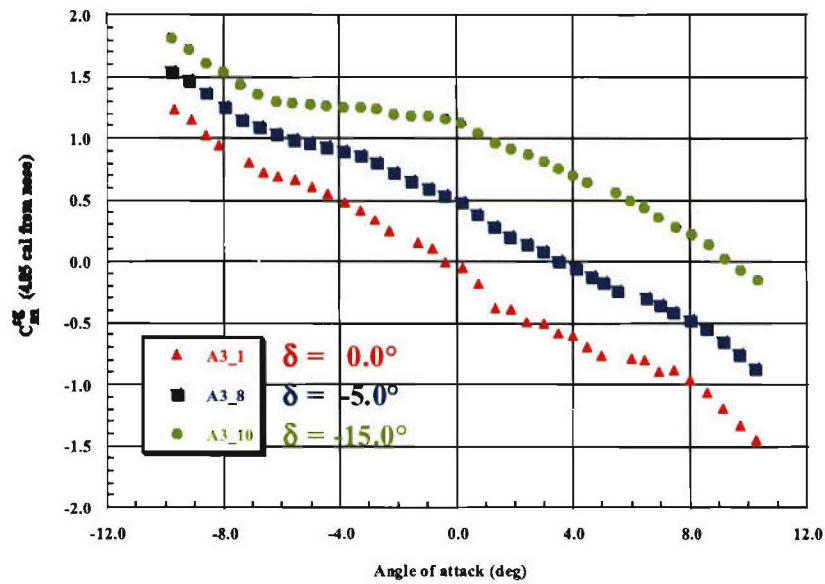


Figure 22d. Pitch moment coefficient about cg vs. incidence

Figure 22. Comparison of wind tunnel results for Group 3, Mach = 2.5;  $\phi = 0.0^\circ$  (cont)

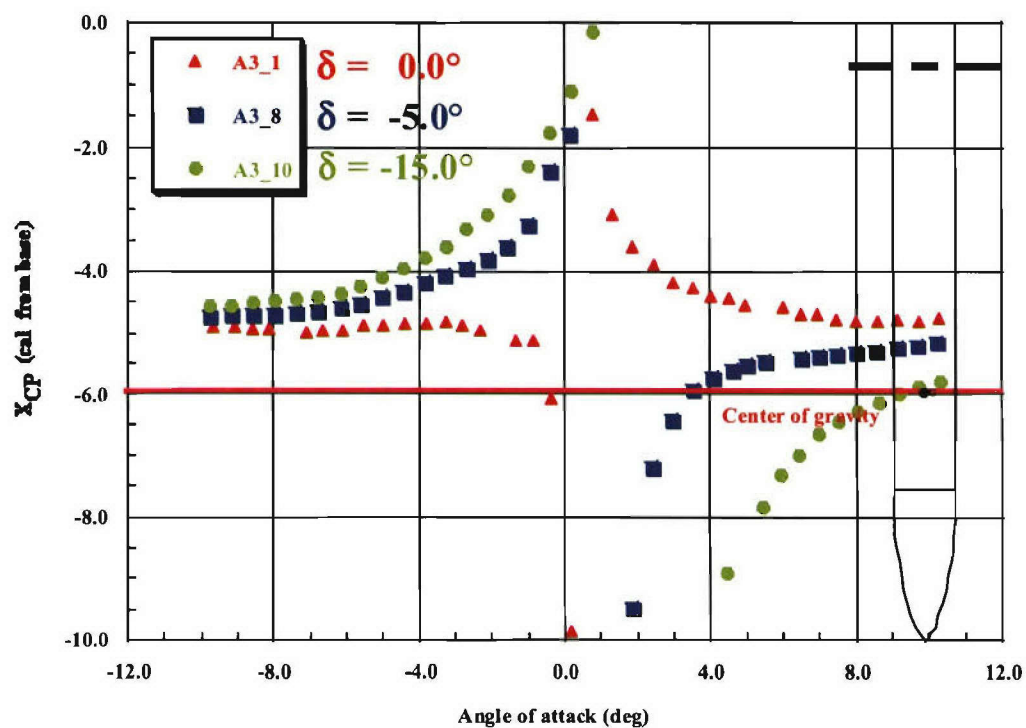


Figure 22e. Center of pressure location vs. incidence

Figure 22. Comparison of wind tunnel results for Group 3, Mach = 2.5;  $\phi = 0.0^\circ$  (cont)

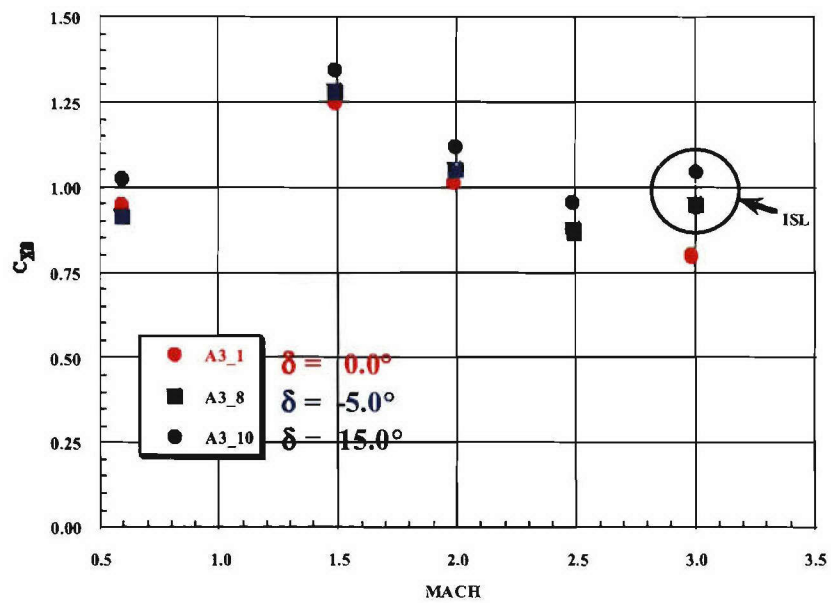


Figure 23a. Axial force coefficient at  $\alpha = 0.0^\circ$

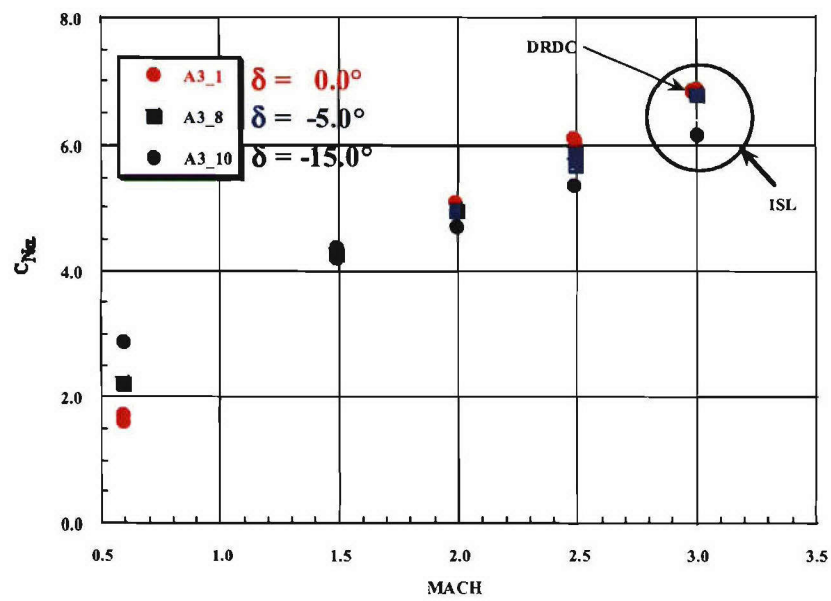


Figure 23b. Normal force coefficient slope

Figure 23. Comparison of wind tunnel results for Group 3 vs. Mach number;  $\phi = 0.0^\circ$



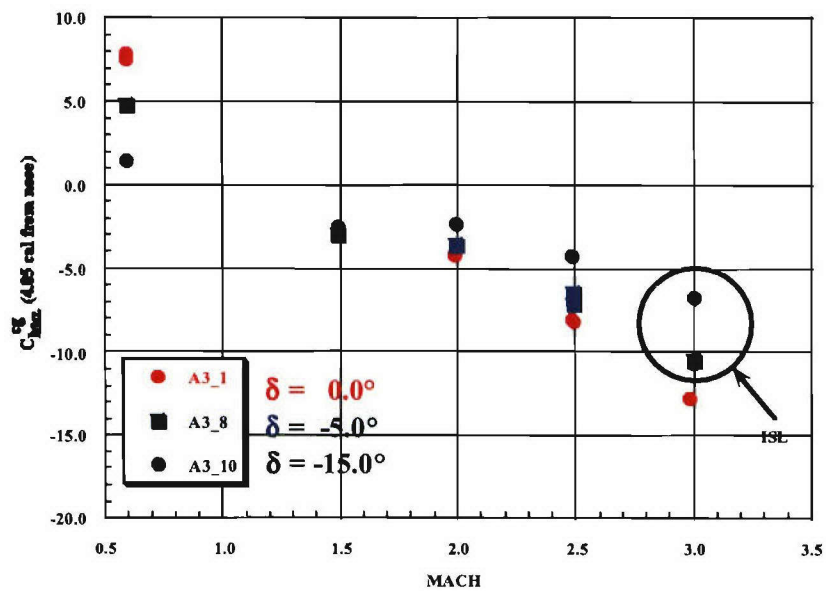


Figure 23c. Pitch moment coefficient slope about cg

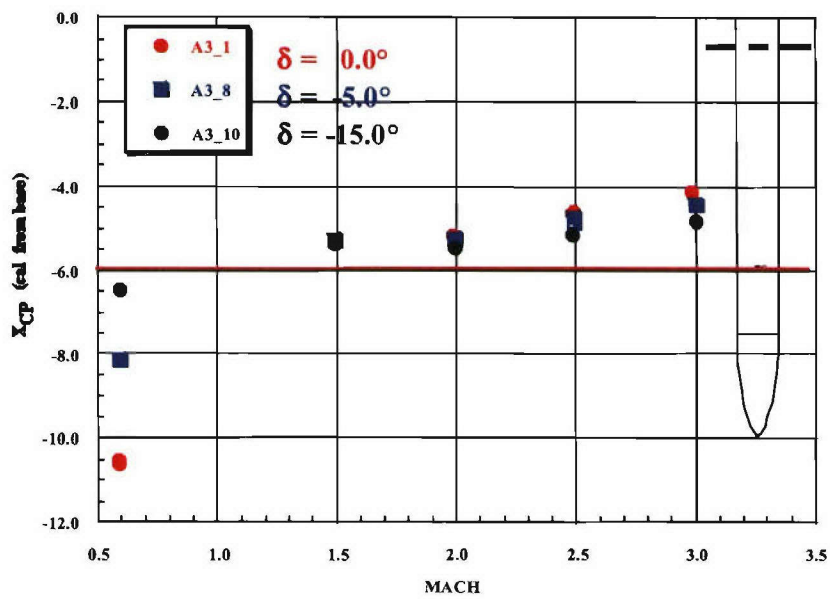


Figure 23d. Center of pressure location

Figure 23. Comparison of wind tunnel results for Group 3 vs. Mach number;  $\phi = 0.0^\circ$  (cont)

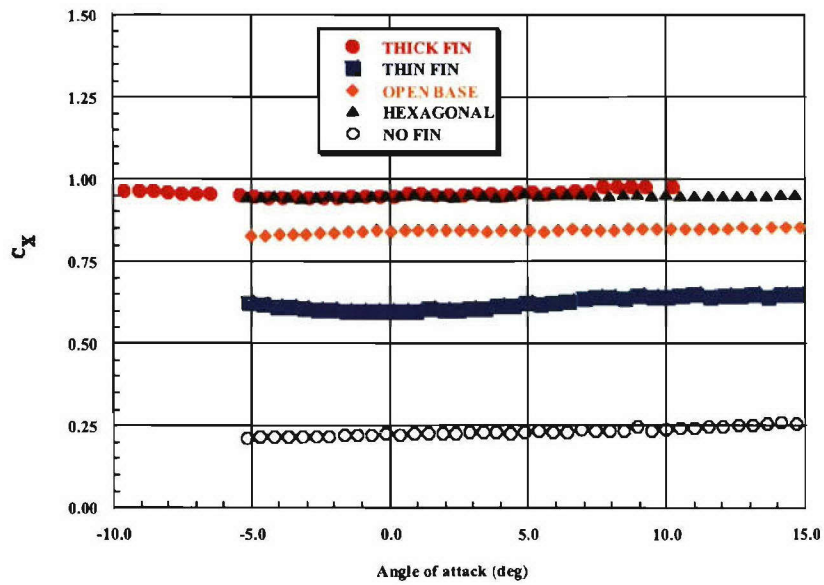


Figure 24a. Axial force coefficient vs. incidence

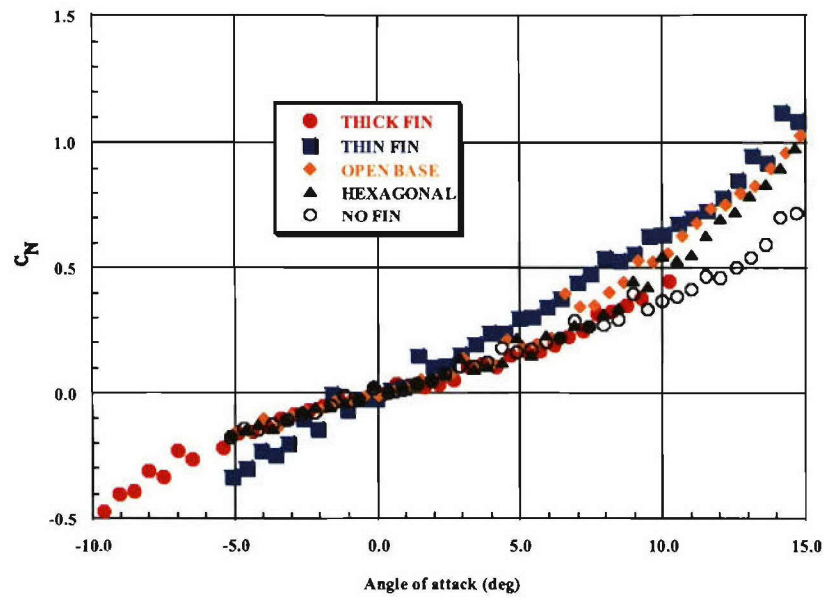


Figure 24b. Normal force coefficient vs. incidence

**Figure 24. Comparison of wind tunnel results for various fin geometries, Mach = 0.6;  $\phi = 0.0^\circ$**

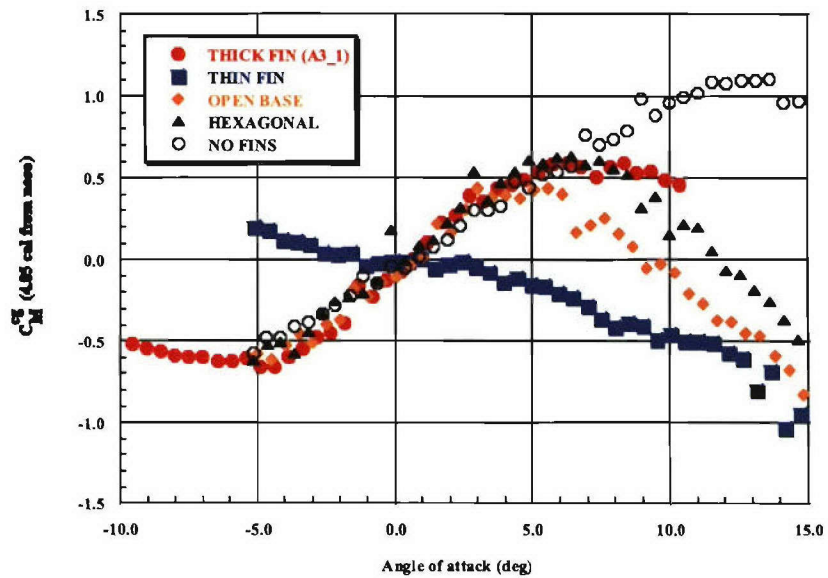


Figure 24c. Pitch moment coefficient about cg vs. incidence

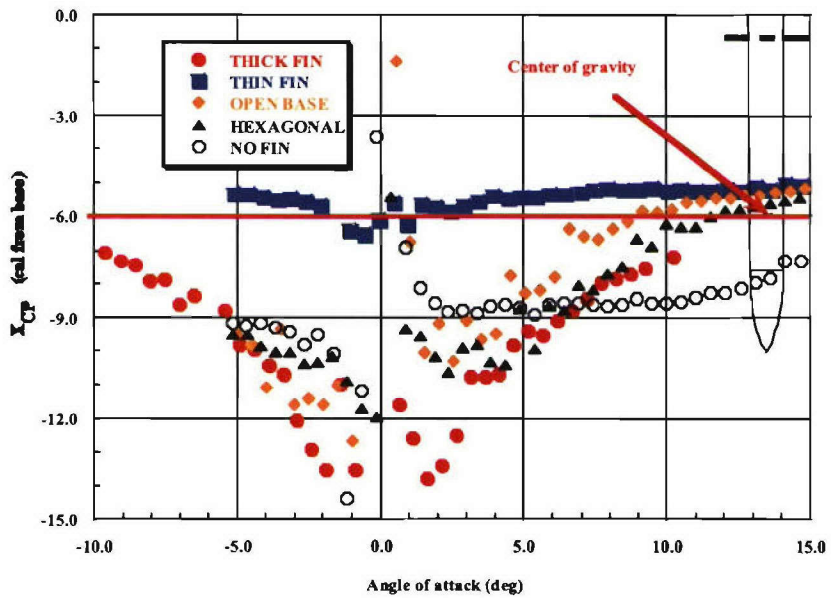


Figure 24d. Center of pressure location vs. incidence

Figure 24. Comparison of wind tunnel results for various fin geometries, Mach = 0.6;  $\phi = 0.0^\circ$   
(cont)

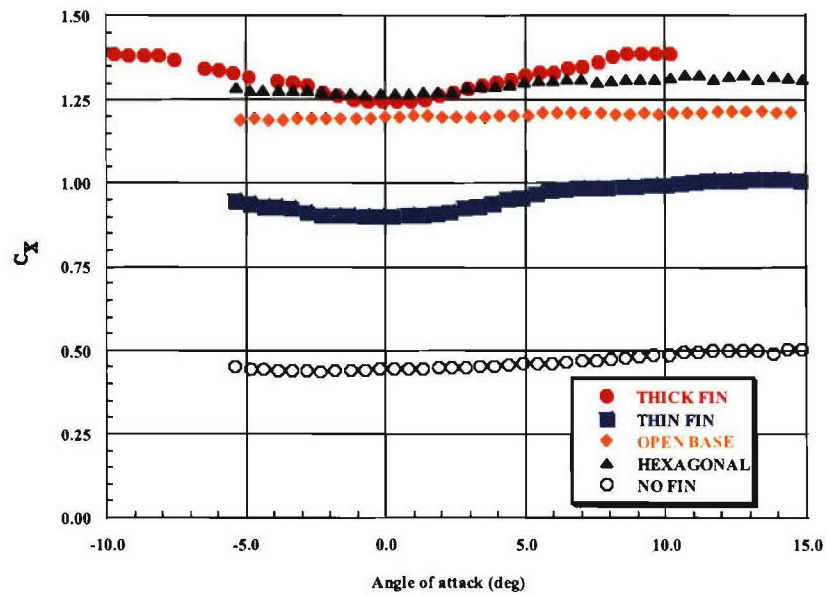


Figure 25a. Axial force coefficient vs. incidence

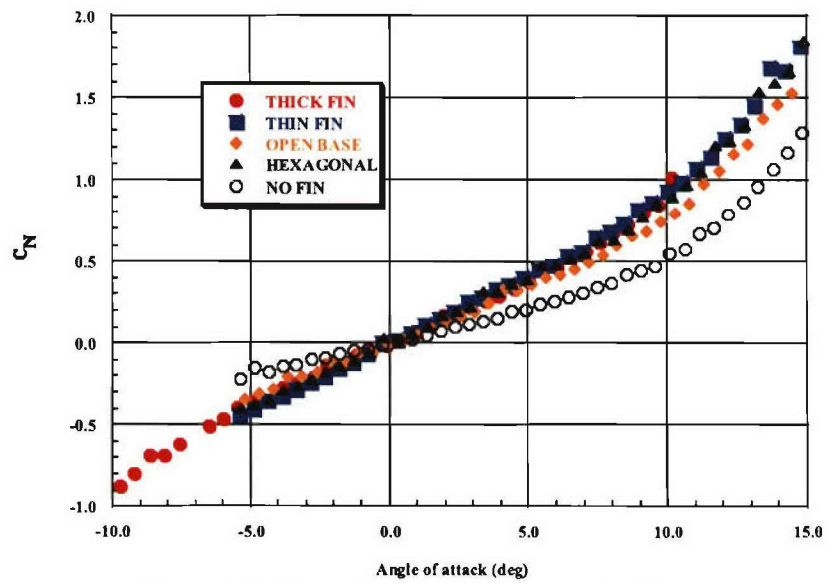


Figure 25b. Normal force coefficient vs. incidence

**Figure 25. Comparison of wind tunnel results for various fin geometries, Mach = 1.5;  $\phi = 0.0^\circ$**

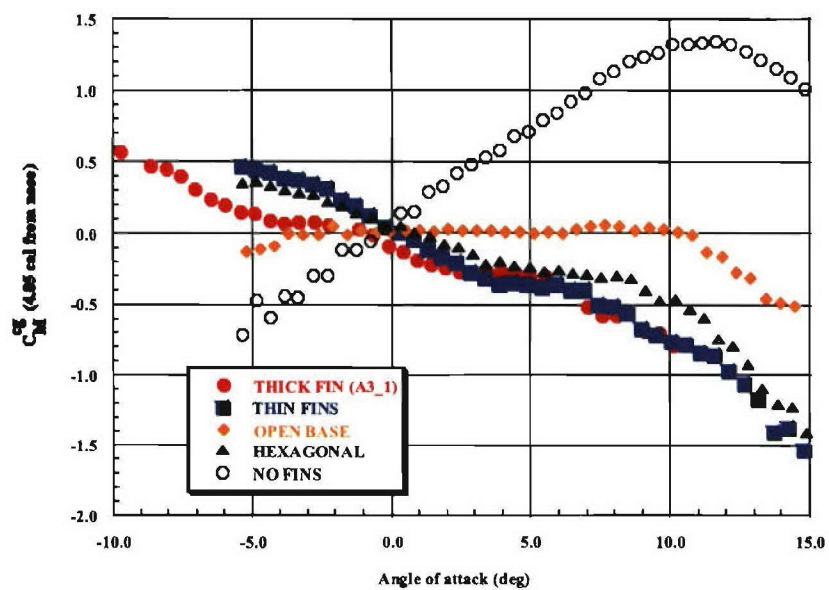


Figure 25c. Pitch moment coefficient about cg vs. incidence

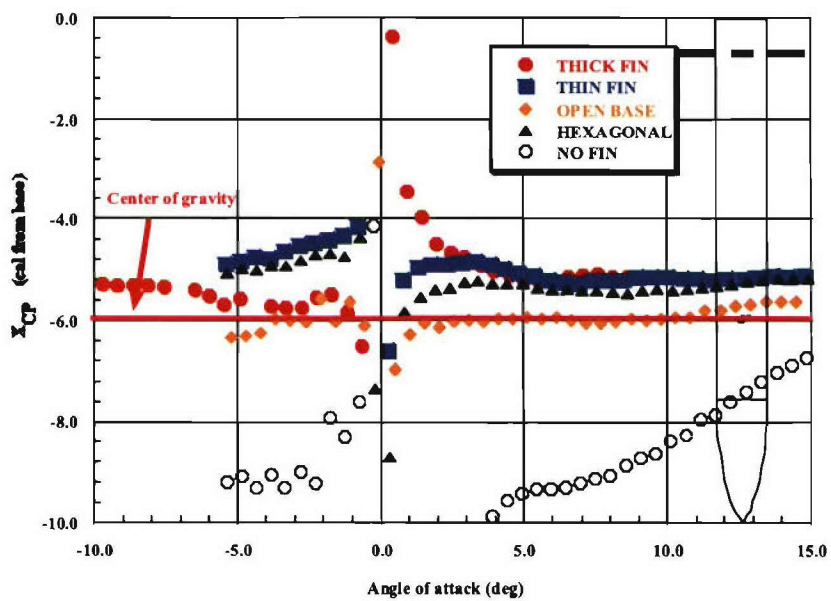


Figure 25d. Center of pressure location vs. incidence

Figure 25. Comparison of wind tunnel results for various fin geometries, Mach = 1.5;  $\phi = 0.0^\circ$   
(cont)

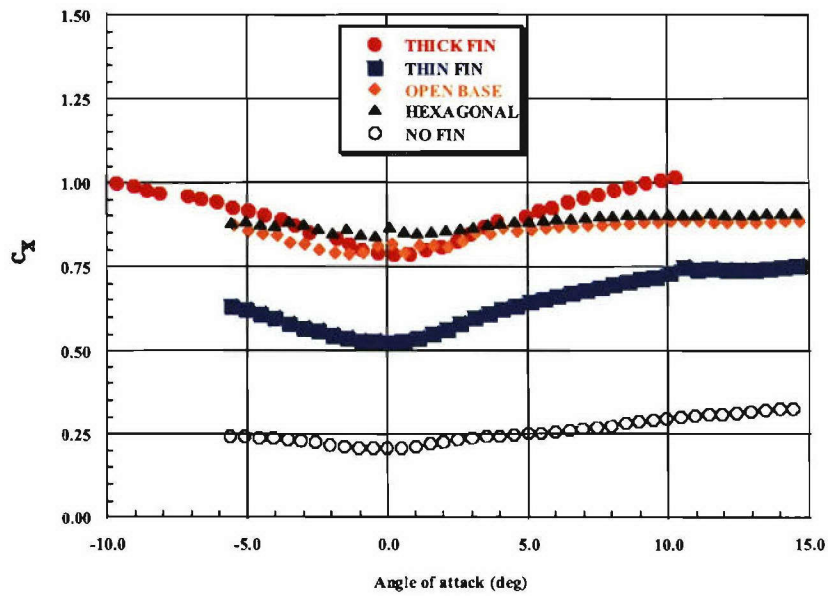


Figure 26a. Axial force coefficient vs. incidence

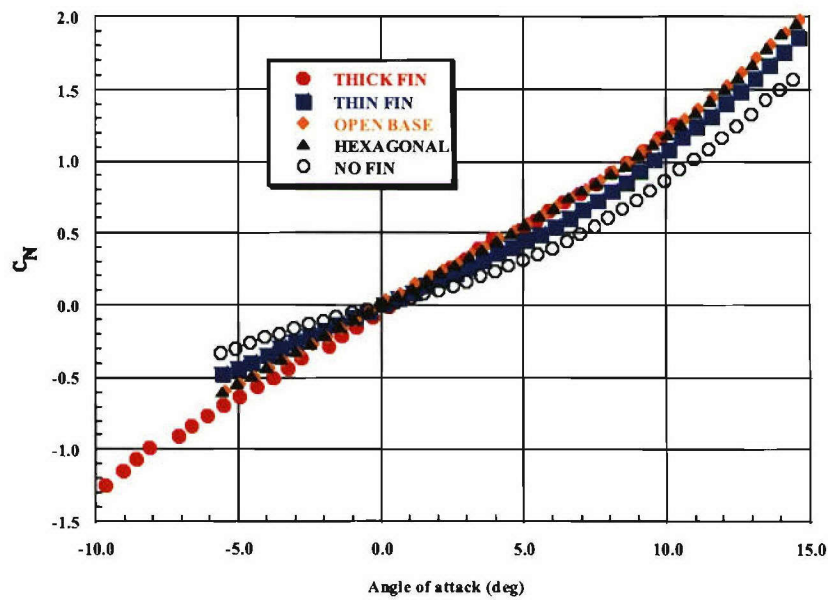


Figure 26b. Normal force coefficient vs. incidence

**Figure 26. Comparison of wind tunnel results for various fin geometries, Mach = 3.0;  $\phi = 0.0^\circ$**

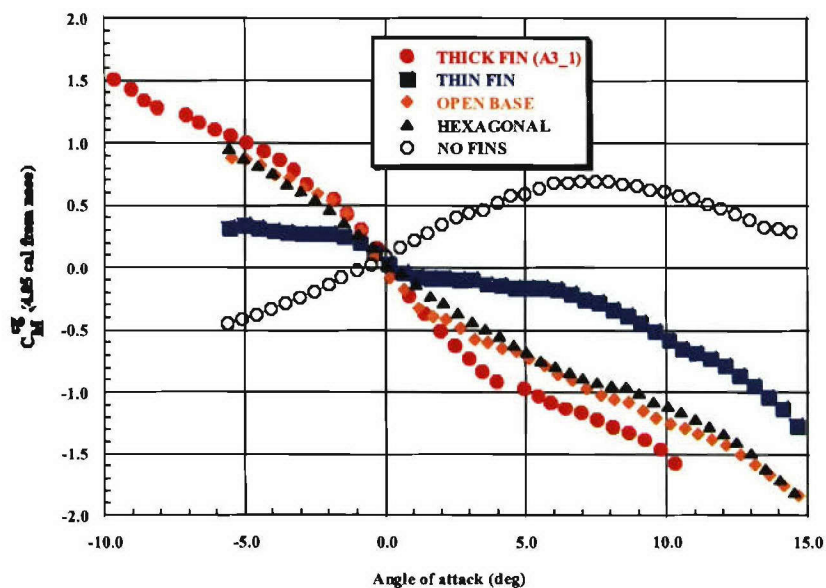


Figure 26c. Pitch moment coefficient about cg vs. incidence

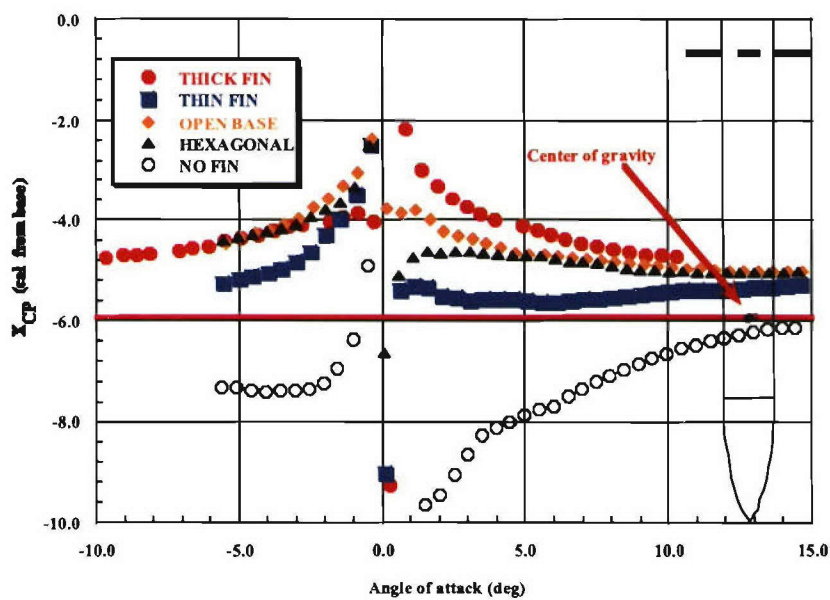


Figure 26d. Center of pressure location vs. incidence

Figure 26. Comparison of wind tunnel results for various fin geometries, Mach = 3.0;  $\phi = 0.0^\circ$   
(cont)



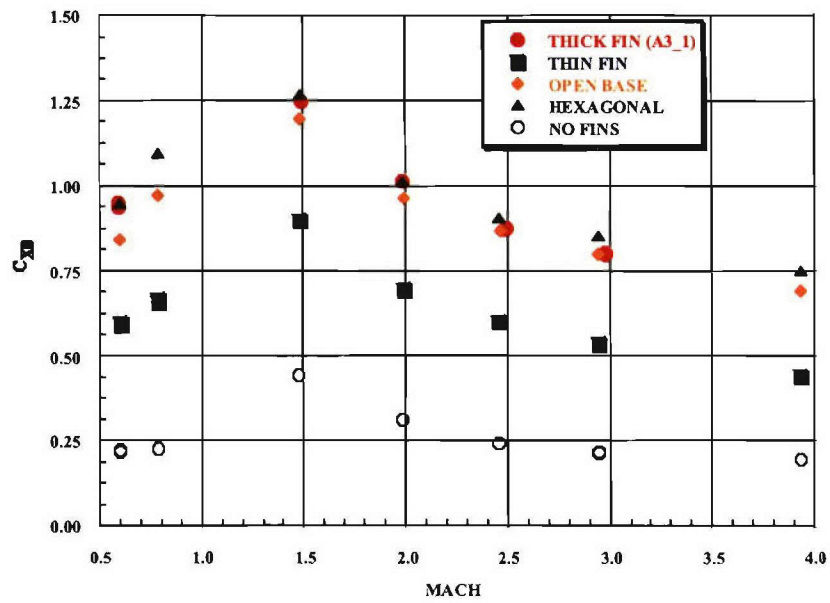


Figure 27a. Axial force coefficient at  $\alpha = 0.0^\circ$

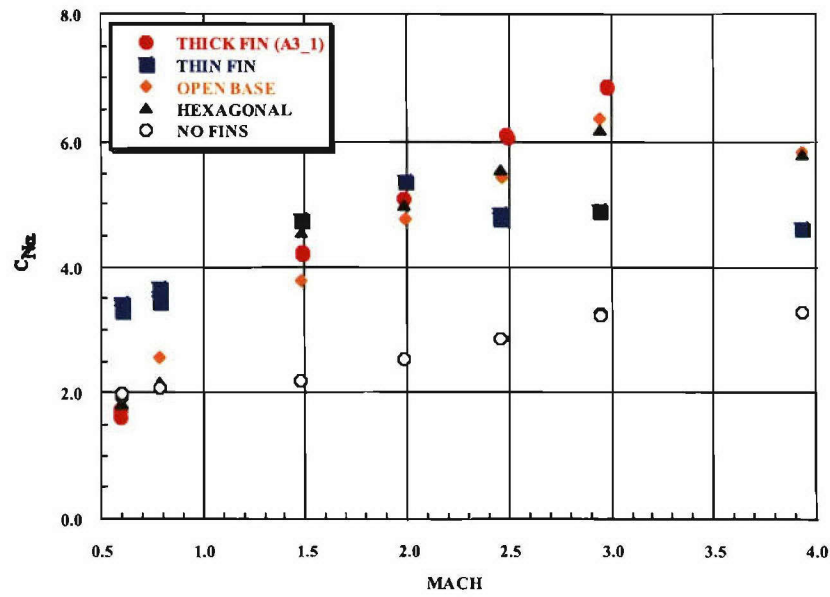


Figure 27b. Normal force coefficient slope

Figure 27. Comparison of wind tunnel results for various fin geometries vs. Mach number;  $\phi = 0.0^\circ$

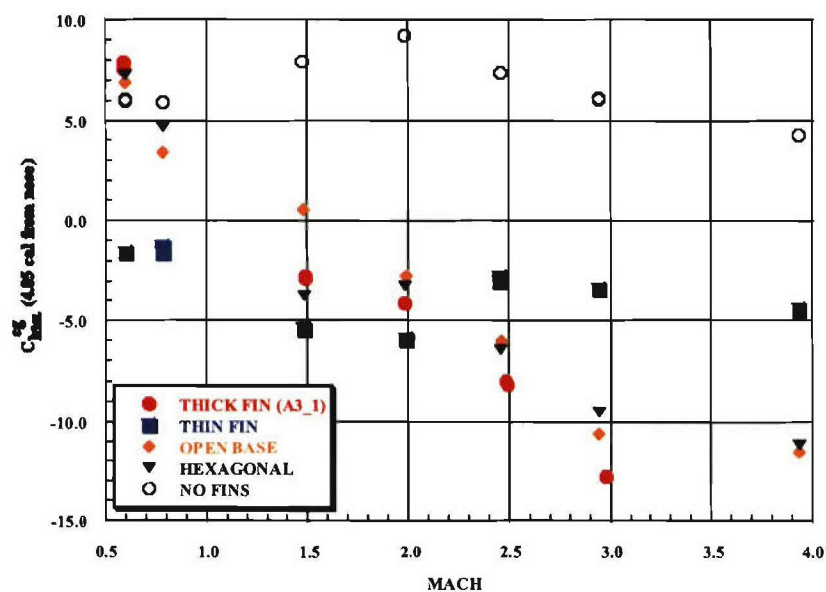


Figure 27c. Pitch moment coefficient slope about cg

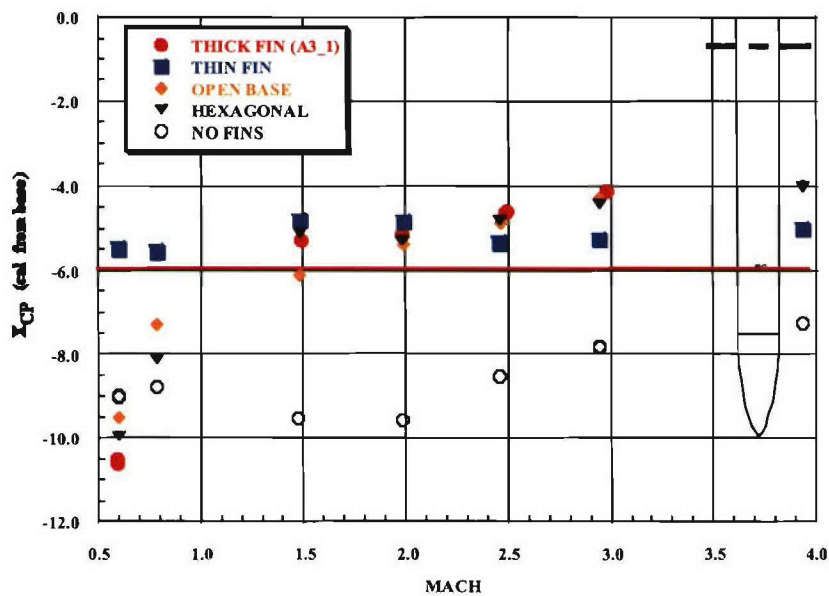


Figure 27d. Center of pressure location

Figure 27. Comparison of wind tunnel results for various fin geometries vs. Mach number;  
 $\phi = 0.0^\circ$  (cont)



Figure 28. Photograph of aeroballistic range complex

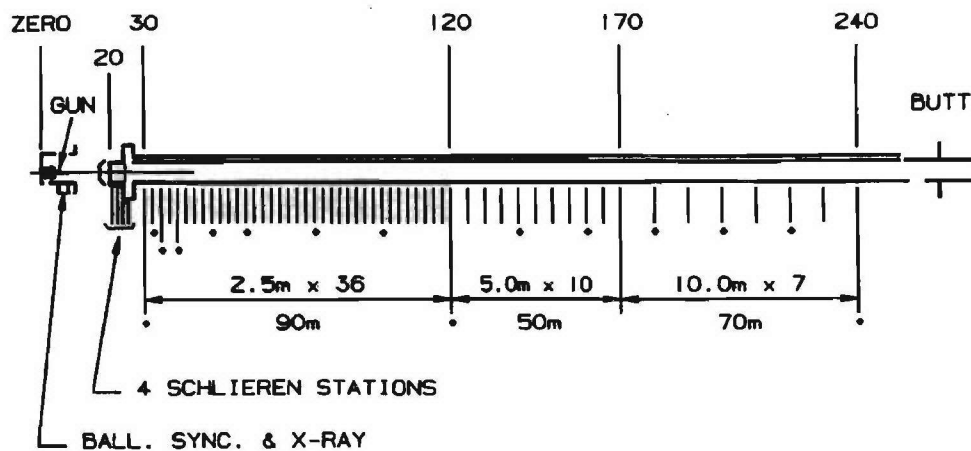
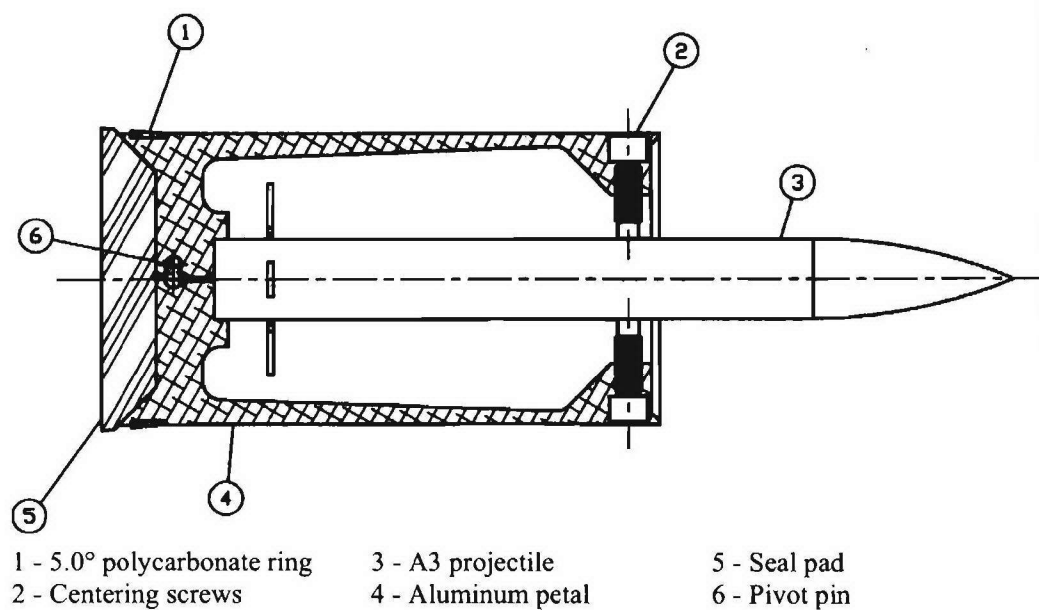


Figure 29. Aeroballistic Range photographic station spacing



**Figure 30. Schematic of sabot design**



**Figure 31. Photograph model-sabot package.**

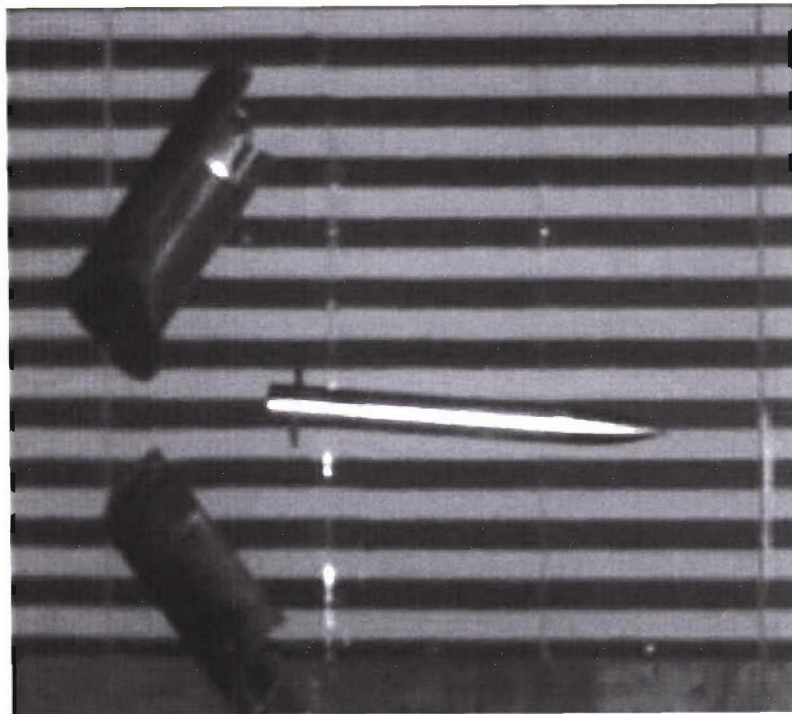


Figure 32a. Shot K02,  $V_{\text{MUZ}} = 541.2 \text{ m/s}$

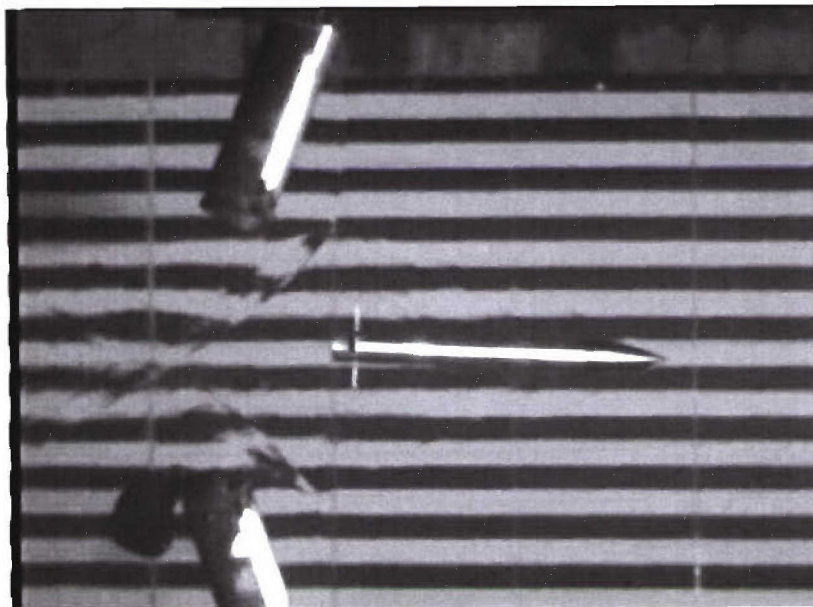


Figure 32b. Shot K10,  $V_{\text{MUZ}} = 1136.9 \text{ m/s}$

**Figure 32. Typical sabot separation**



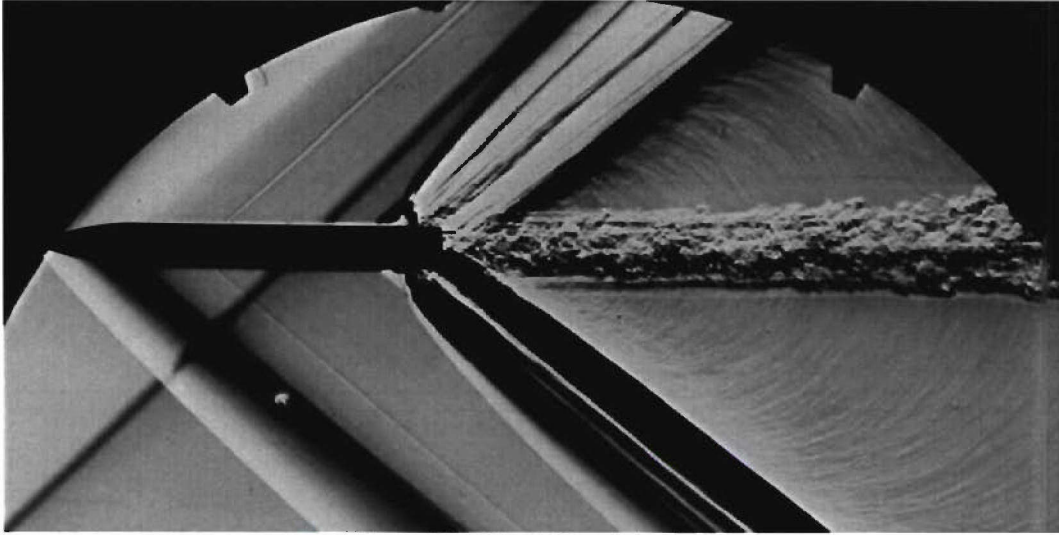


Figure 33a. Shot K01 –  $M = 1.53$

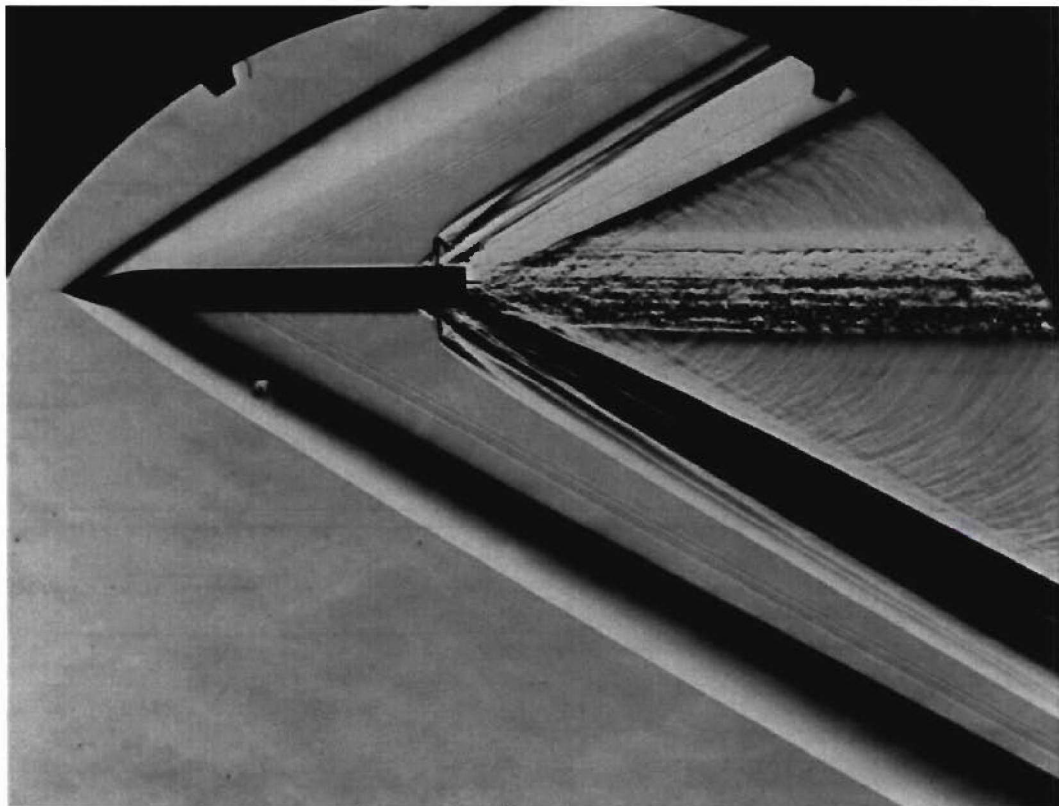


Figure 33b. Shot K04 –  $M = 2.12$

**Figure 33. Free-flight Schlieren photographs**

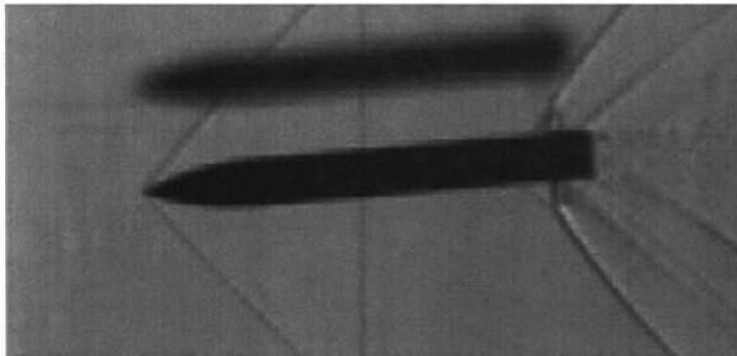


Figure 34a. Station P01 –  $M = 1.53$

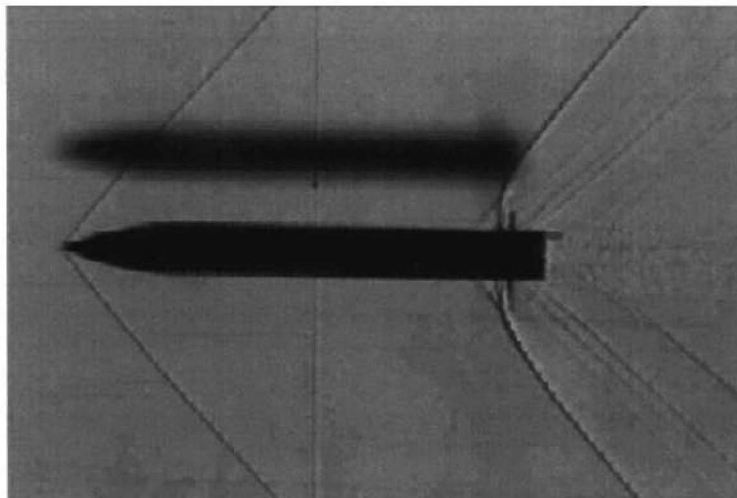


Figure 34b. Station P34 –  $M = 1.46$

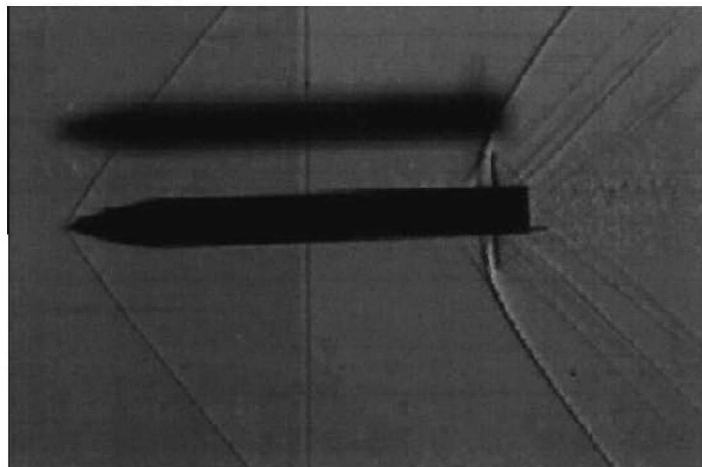
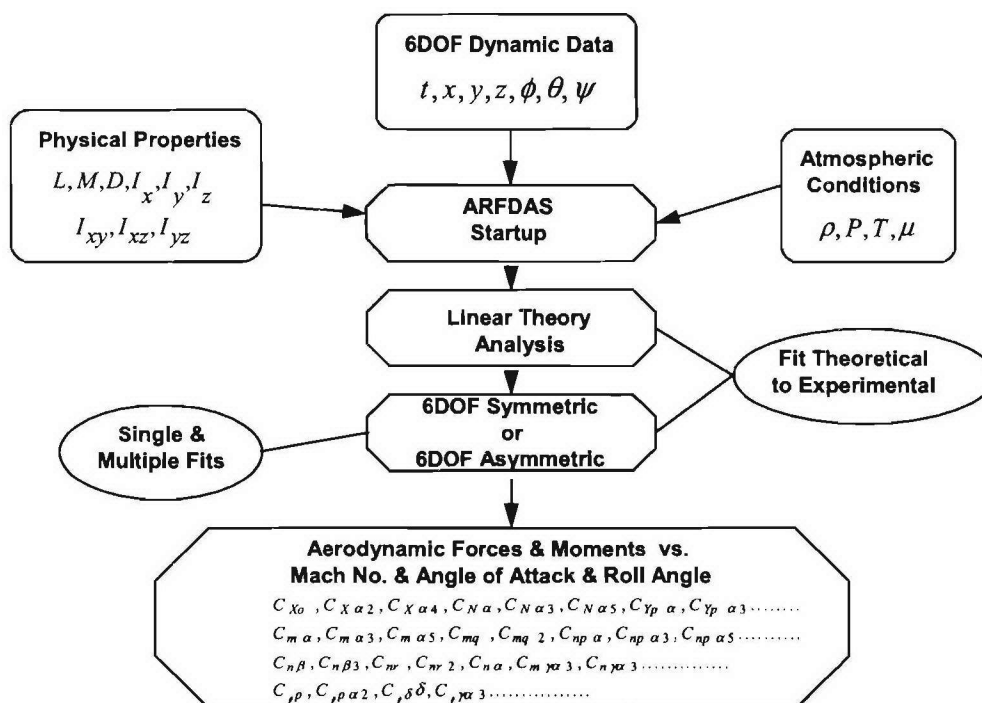


Figure 34c. Station P81 –  $M = 1.36$

**Figure 34. Free-flight shadowgraphs for shot K01**



# **ARFDAS - Aeroballistic Range Facility Data Analysis**



**Figure 35. DRDC Aeroballistic Range Facility Data Analysis System**



Figure 36a. Shadowgraph stations



Figure 36b. Photograph of the test site

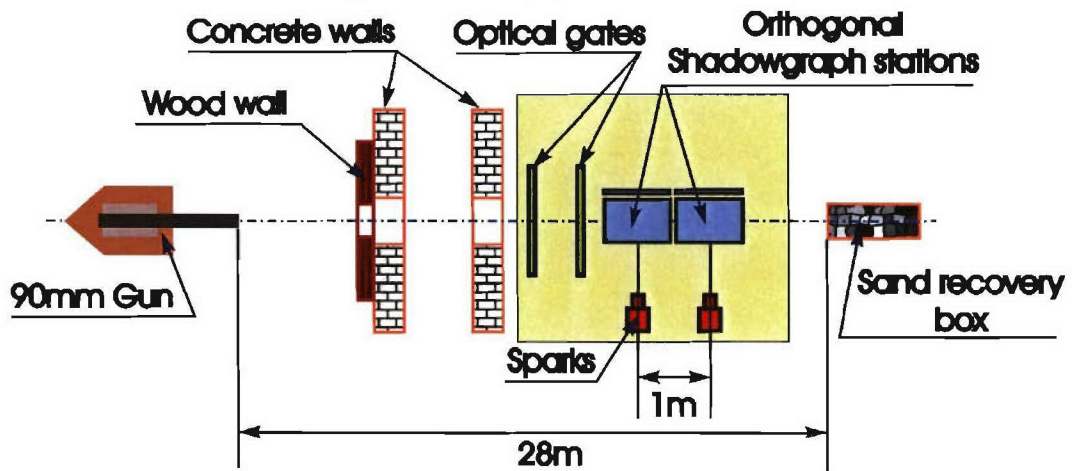
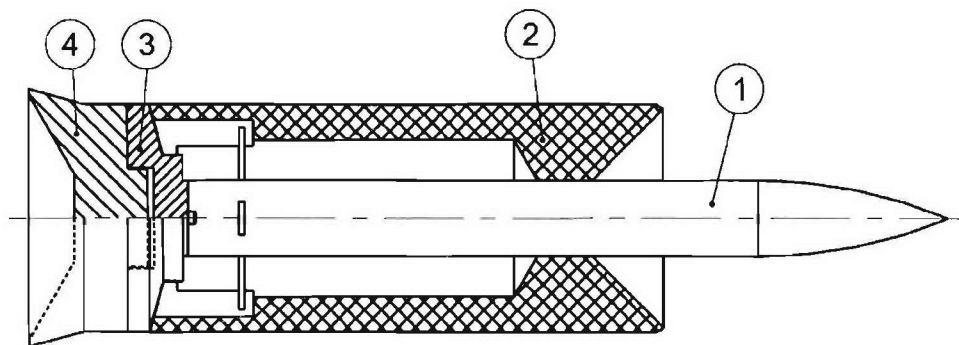


Figure 36c. Schematic of the ISL open range test site

Figure 36. ISL Open Range Test Site Setup



1 - Brass-aluminum model

3 - Aluminum pusher plate

2 - "Polyoxyméthylene" petal

4 - Polyethylene seal pad

Figure 37a. Schematic of ISL sabot design

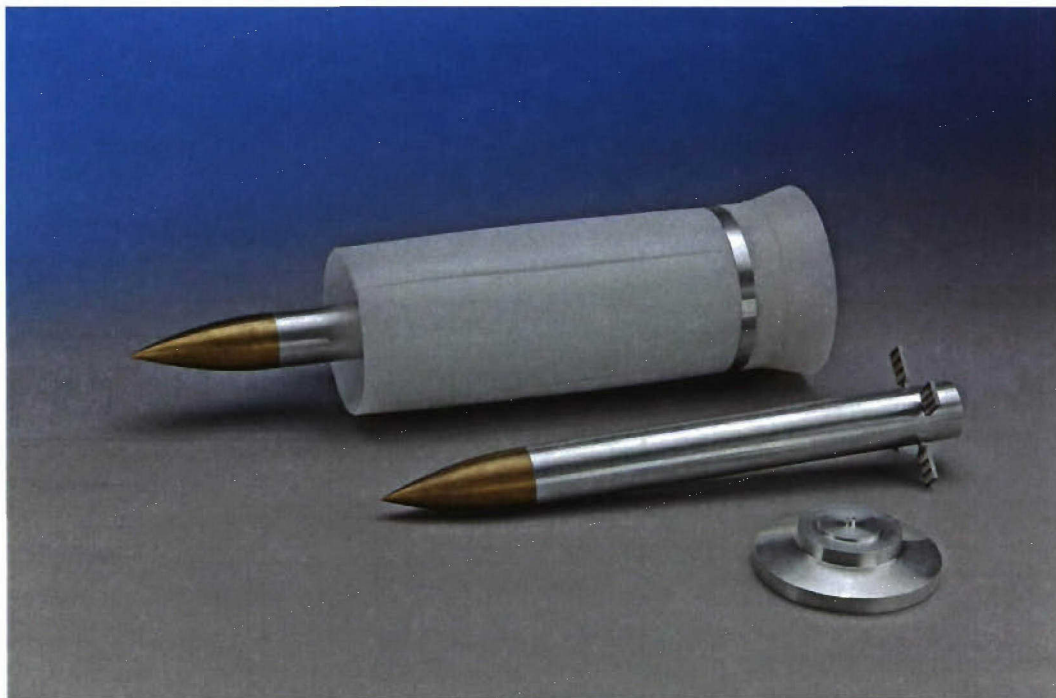


Figure 37b. Photograph of ISL model-sabot package

**Figure 37. ISL Sabot Design**

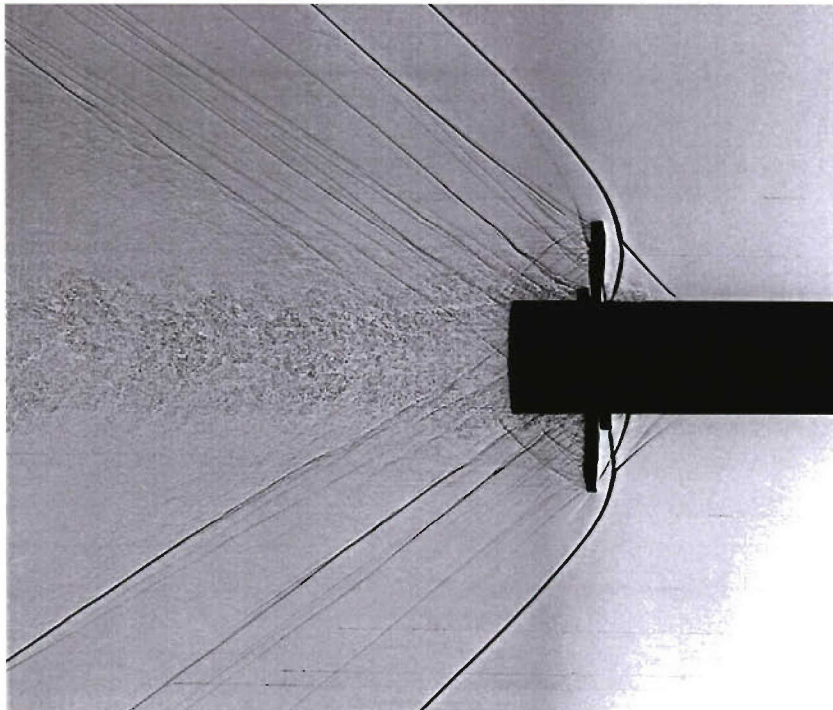


Figure 38a.  $M = 1.6$ ,  $\alpha = 0.2^\circ$

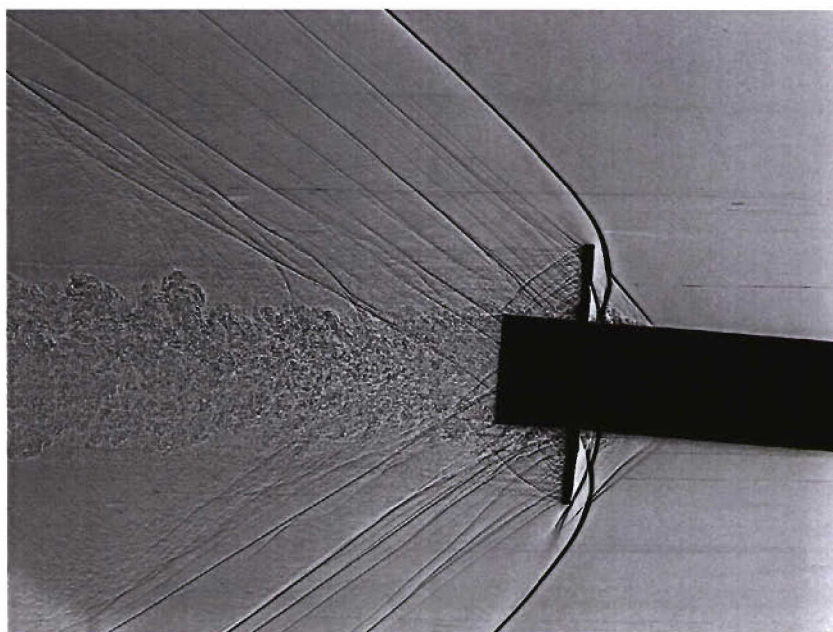


Figure 38b.  $M = 1.6$ ,  $\alpha = 4.8^\circ$

**Figure 38. ISL Free-flight shadowgraphs**

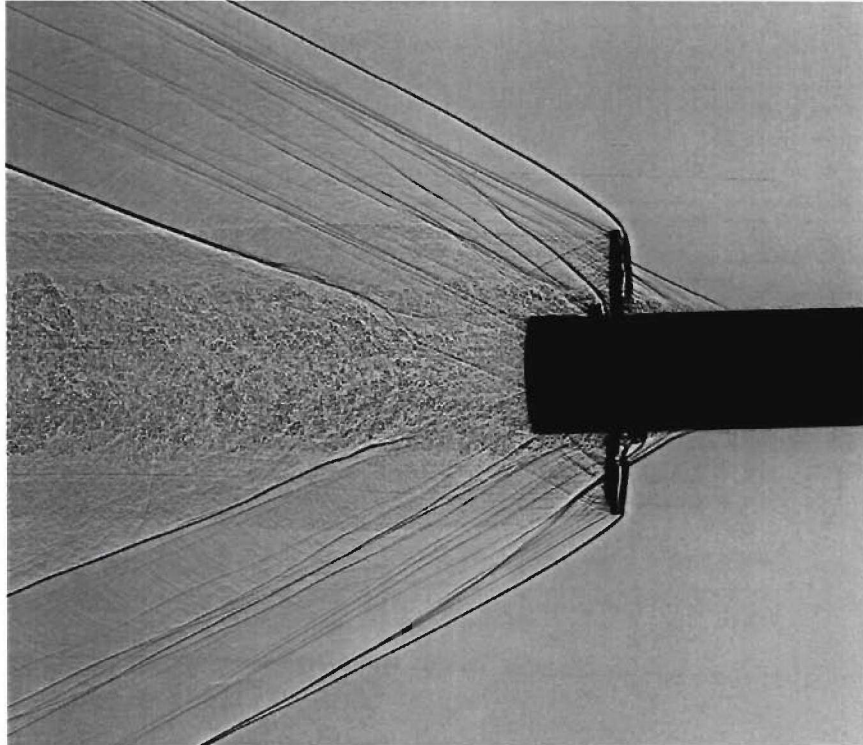


Figure 38c.  $M = 2.4$ ,  $\alpha = 1.7^\circ$

Figure 38. ISL Free-flight shadowgraphs (cont)



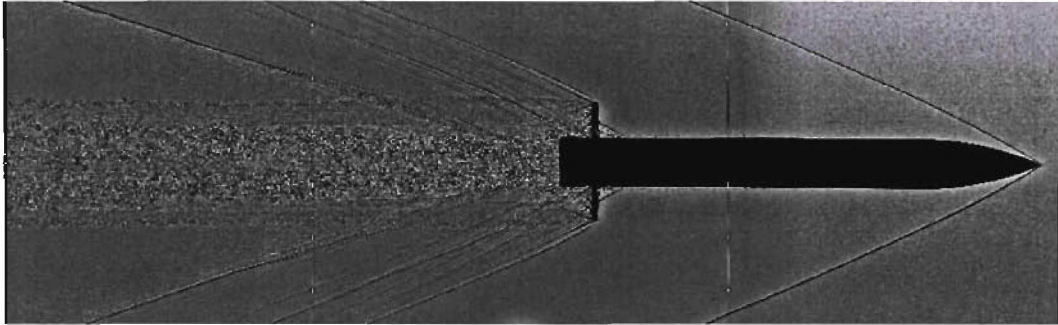


Figure 38d.  $M = 3.0$ ,  $\alpha = 0.7^\circ$

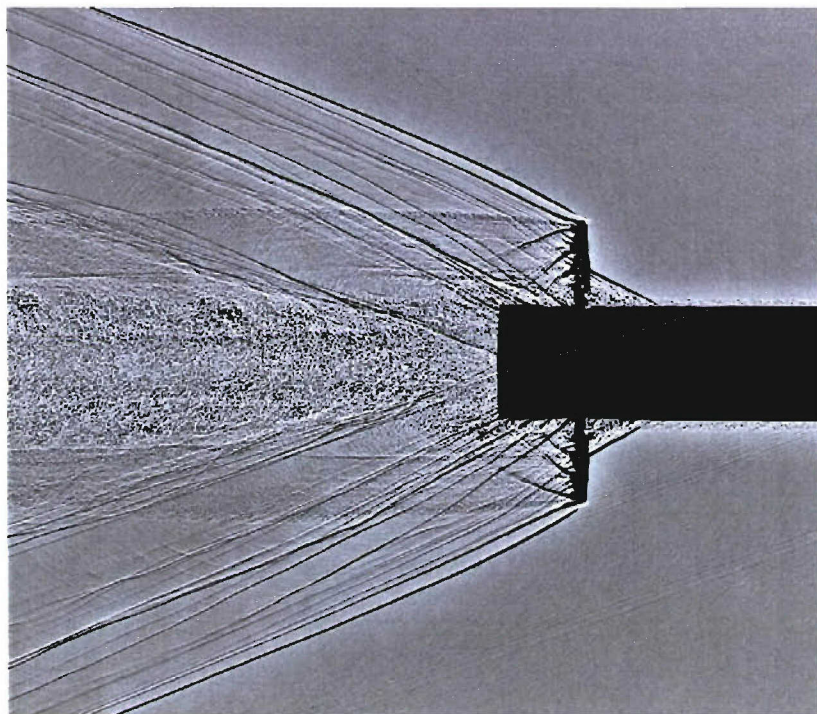


Figure 38e. Base flow details of Fig. 38d

Figure 38. ISL Free-flight shadowgraphs (cont)

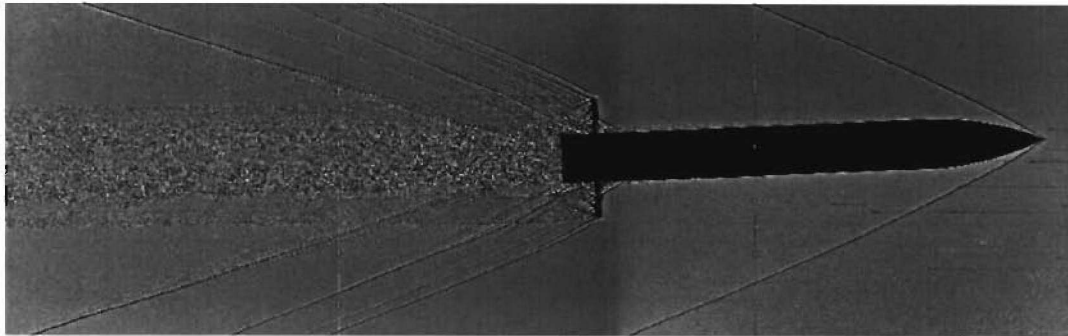


Figure 38f.  $M=3.0$ ,  $\alpha=2.5^\circ$

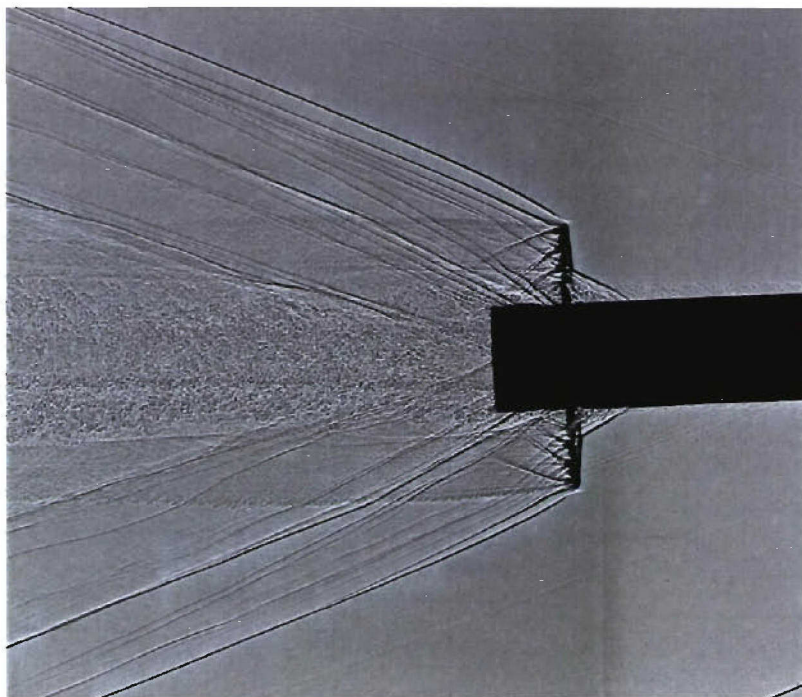


Figure 38g. Base flow details of Fig. 38f

Figure 38. ISL Free-flight shadowgraphs (cont)



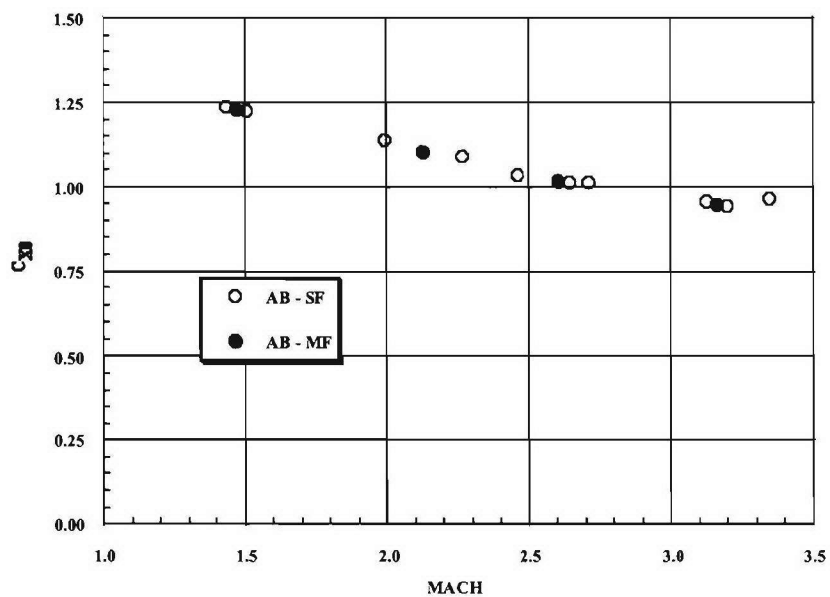


Figure 39a. Axial force coefficient

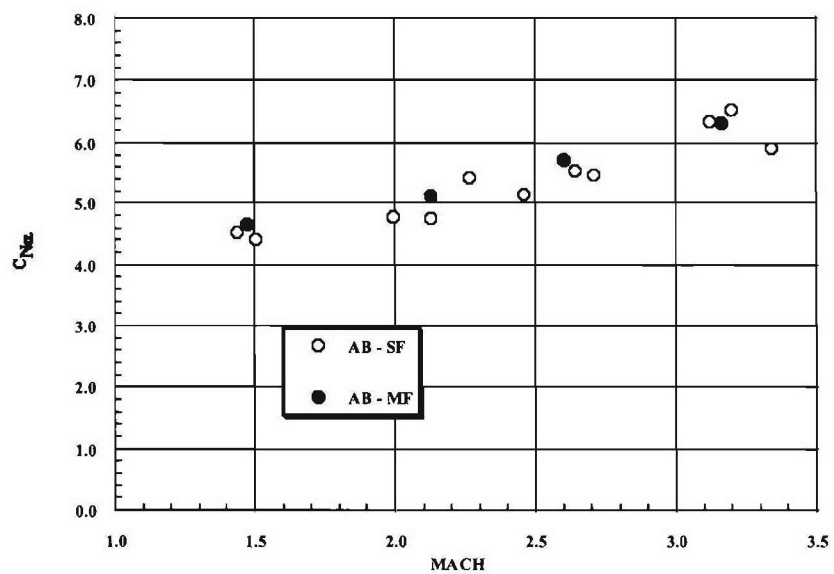


Figure 39b. Normal force coefficient slope

**Figure 39. Comparison of free-flight 6DOF reduced aerodynamic coefficients vs. Mach number**

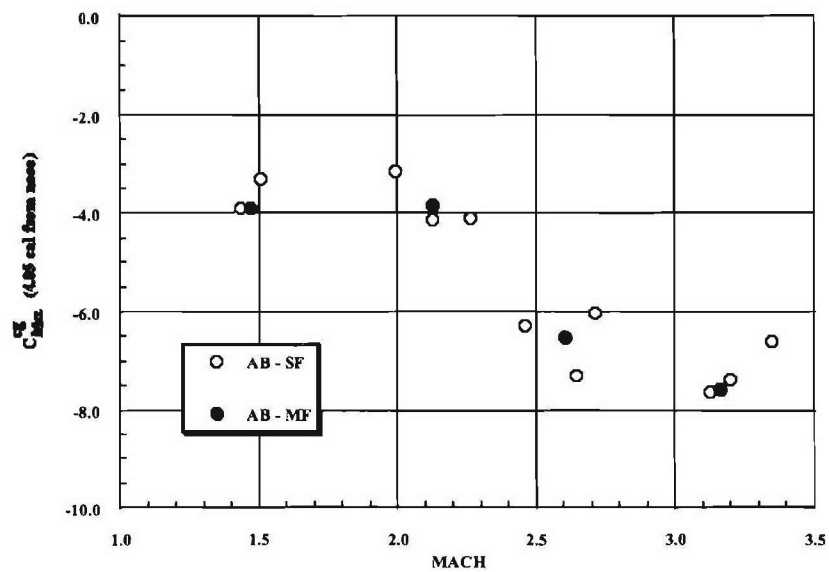


Figure 39c. Pitch moment coefficient slope about cg

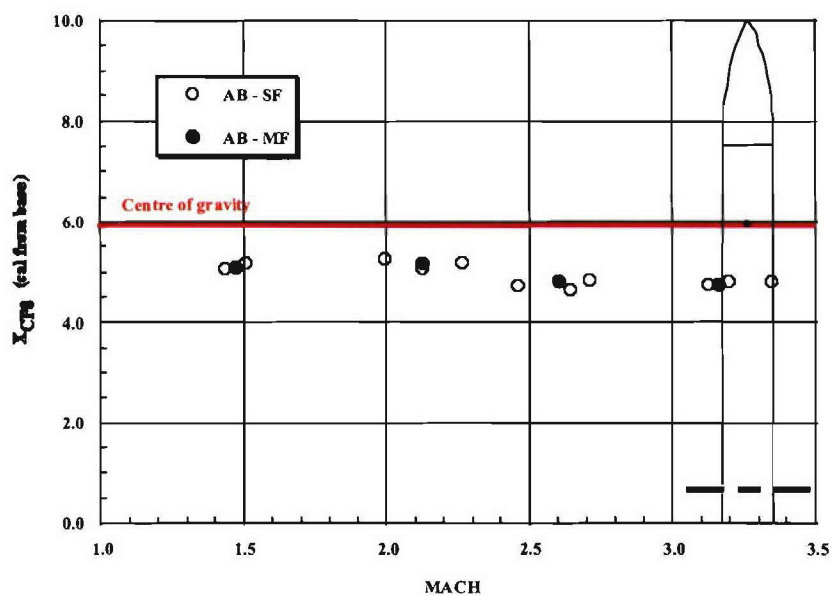


Figure 39d. Center of pressure location

Figure 39. Comparison of free-flight 6DOF reduced aerodynamic coefficients vs. Mach number (cont)

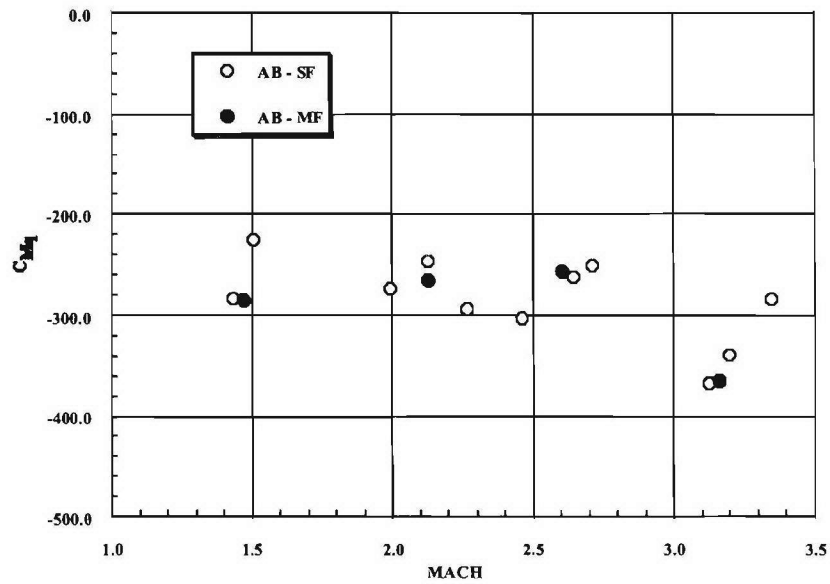


Figure 39e. Pitch damping moment coefficient

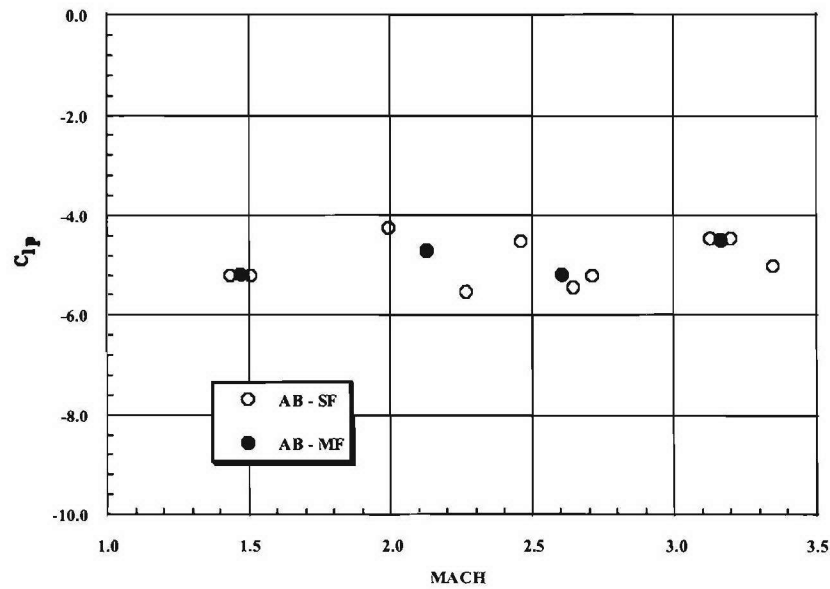


Figure 39f. Roll damping moment coefficient

Figure 39. Comparison of free-flight 6DOF reduced aerodynamic coefficients vs. Mach number (cont)

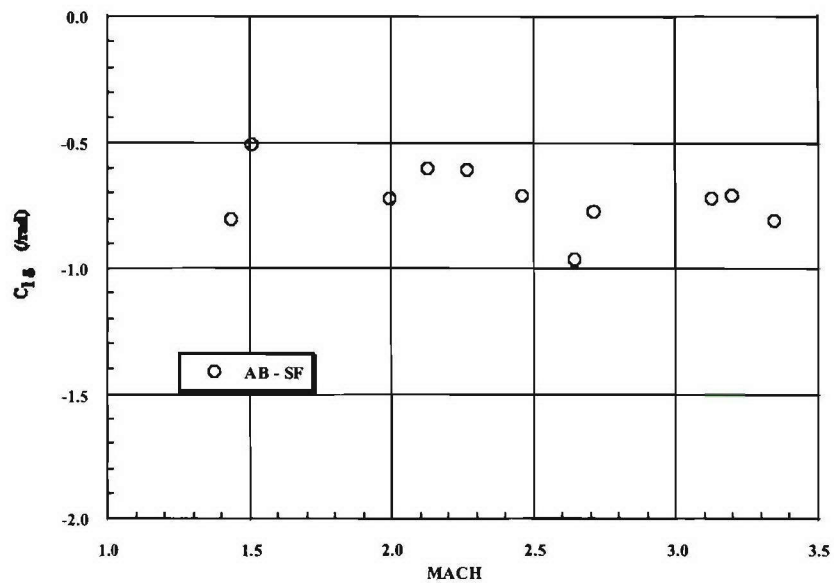


Figure 39g. Roll moment coefficient due to fin cant

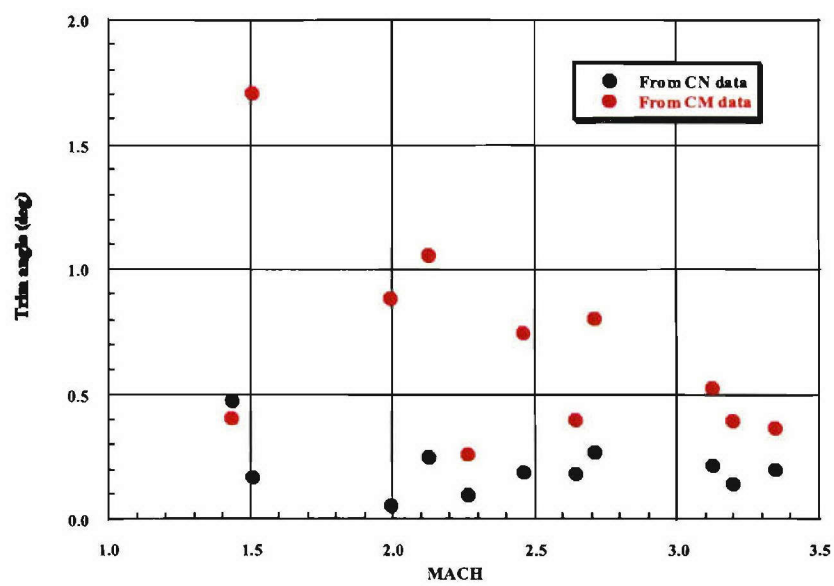


Figure 39h. Trim angle due to deflected fins

Figure 39. Comparison of free-flight 6DOF reduced aerodynamic coefficients vs. Mach number (cont)

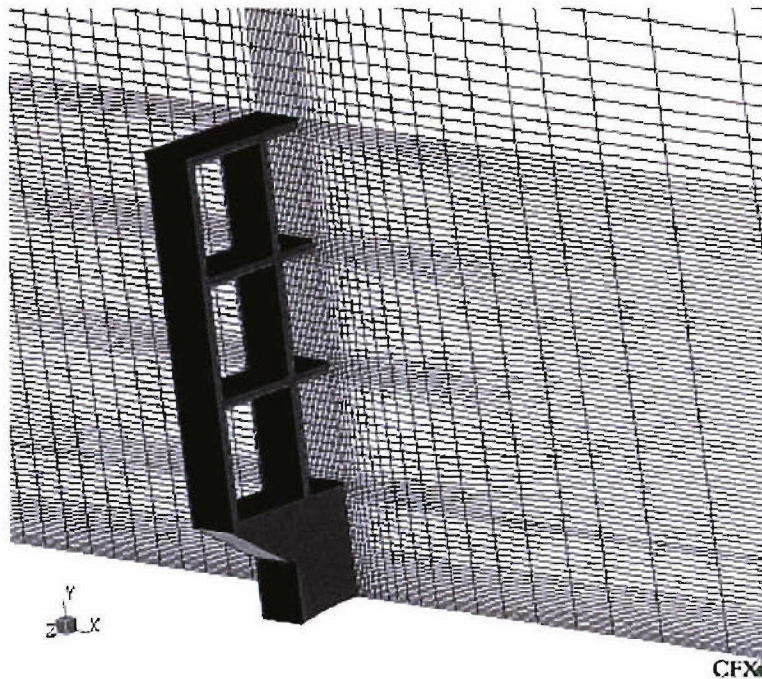


Figure 40a. Mesh details in front of fins

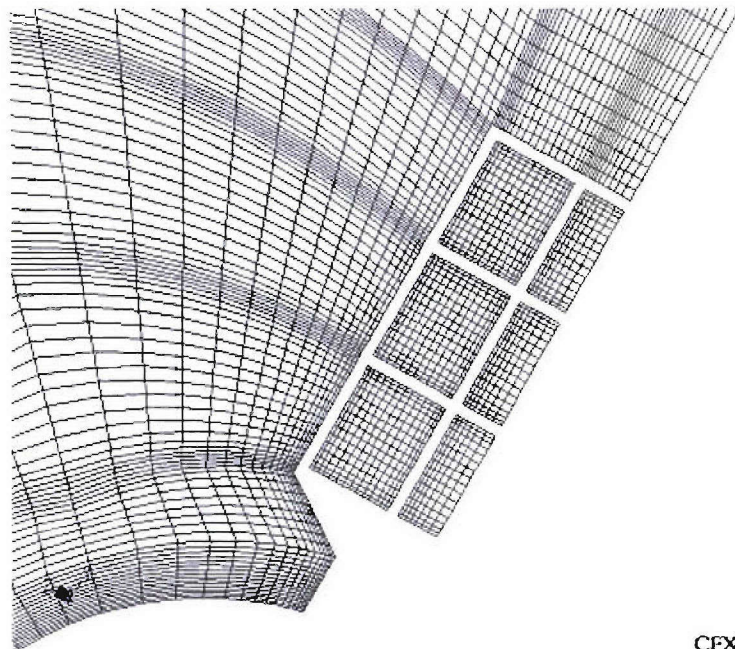


Figure 40b. Mesh in side cell

**Figure 40. Computational mesh for wind tunnel model**

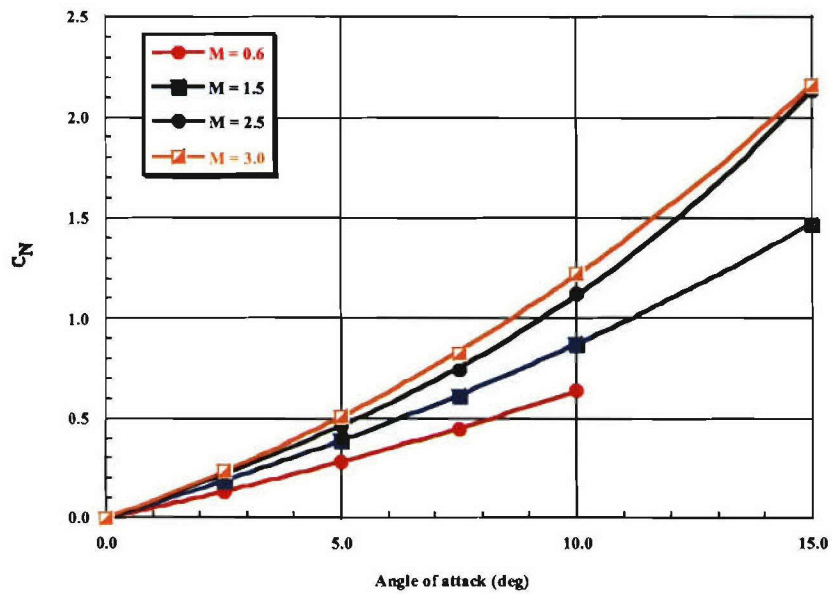


Figure 41a. Normal force coefficient

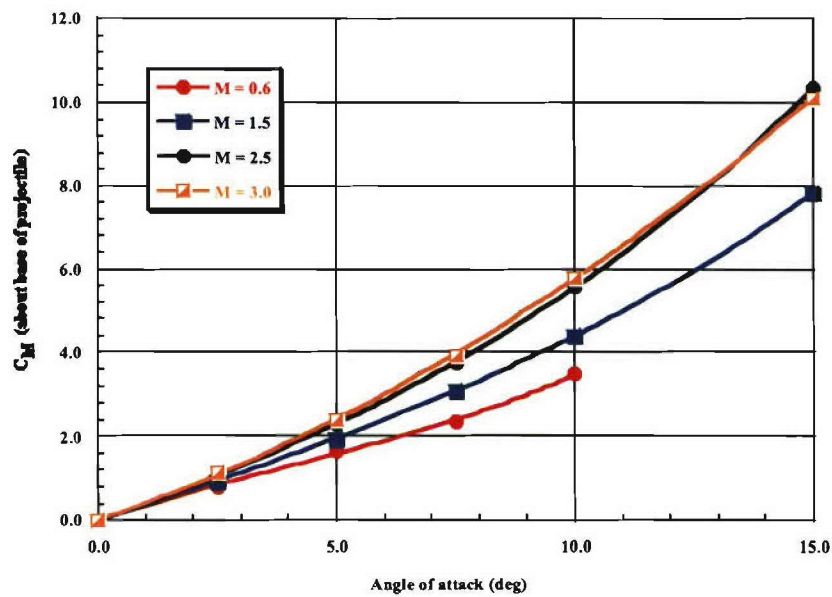


Figure 41b. Pitch moment coefficient about base

Figure 41. CFD predictions (SST, BF0.75) for wind tunnel model vs. angle of attack

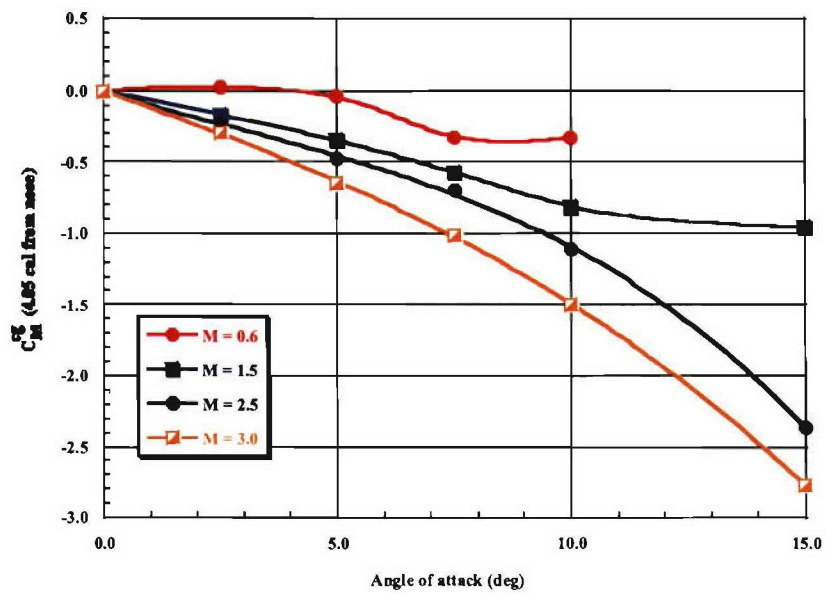


Figure 41c. Pitch moment coefficient about cg

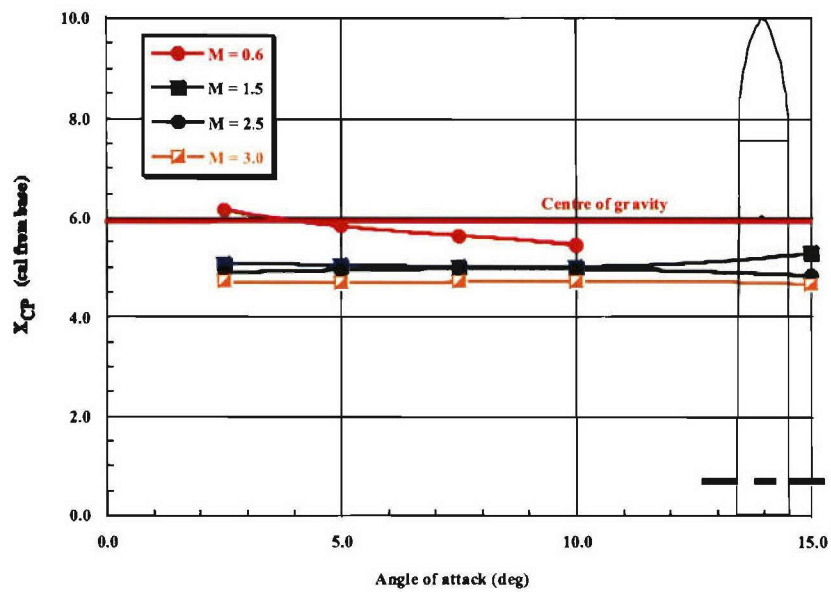


Figure 41d. Center of pressure location

Figure 41. CFD predictions (SST, BF0.75) for wind tunnel model vs. angle of attack (cont)



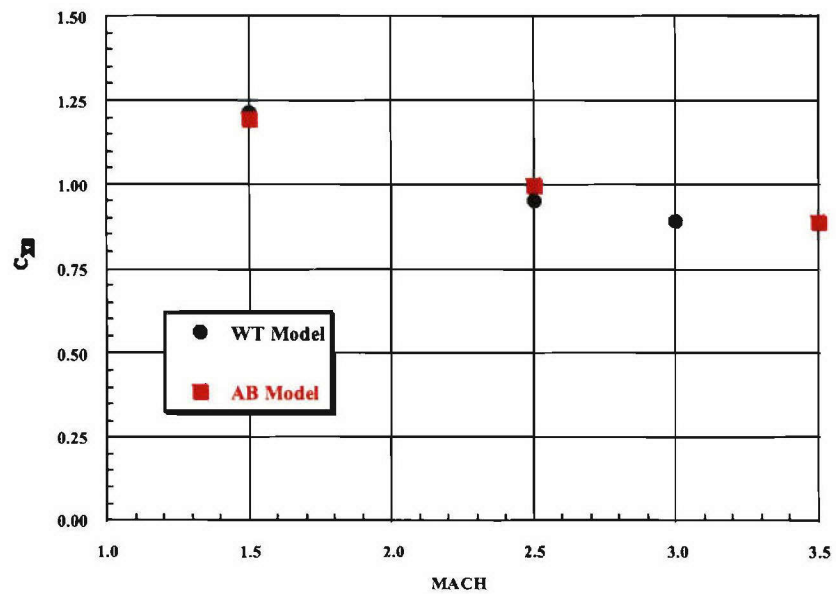


Figure 42a. Axial force coefficient

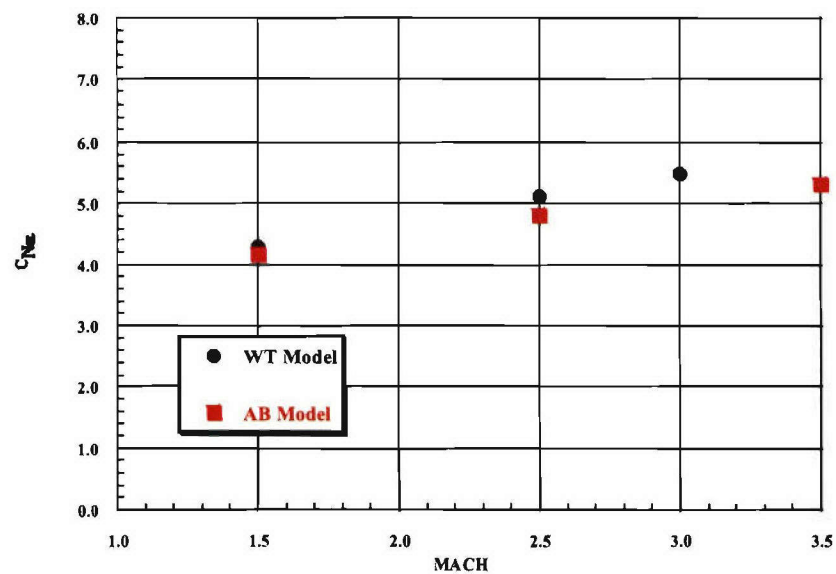


Figure 42b. Normal force coefficient slope

**Figure 42. Comparison of CFD aerodynamic coefficients vs. Mach number for both models**

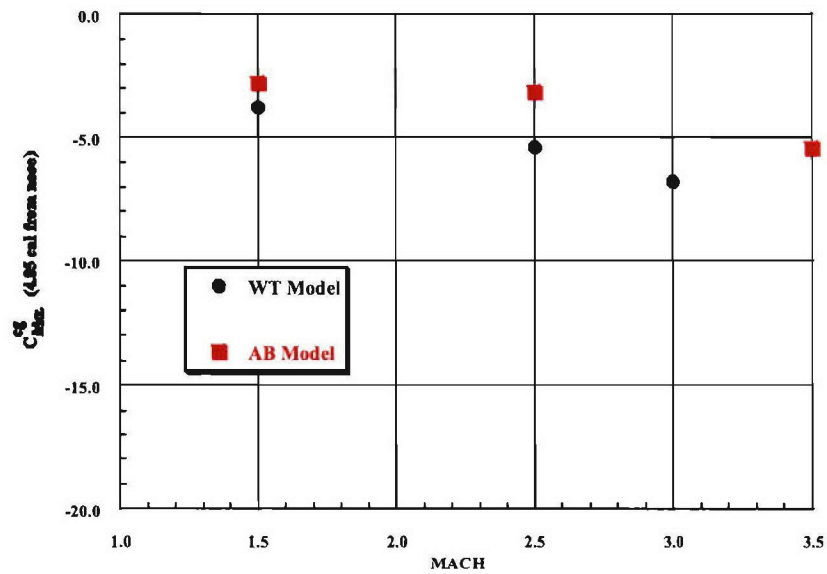


Figure 42c. Pitch moment coefficient slope about cg

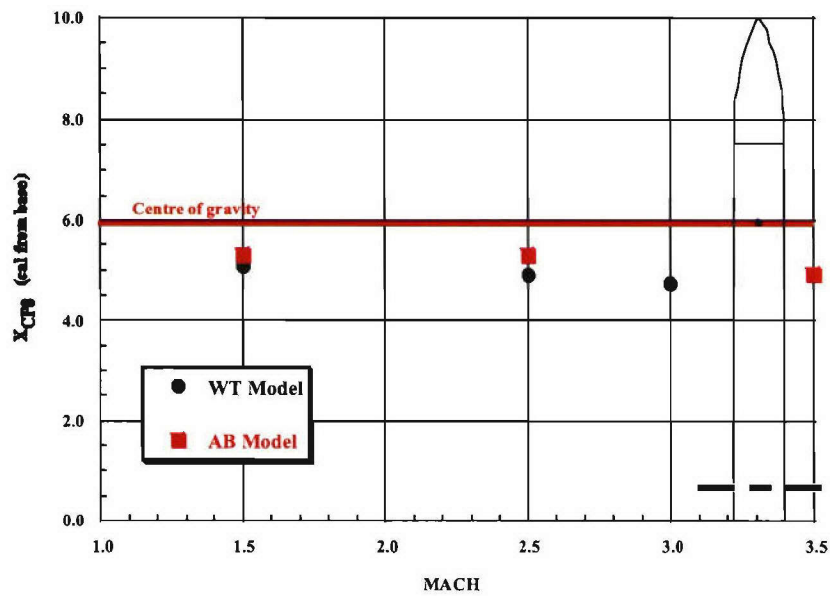
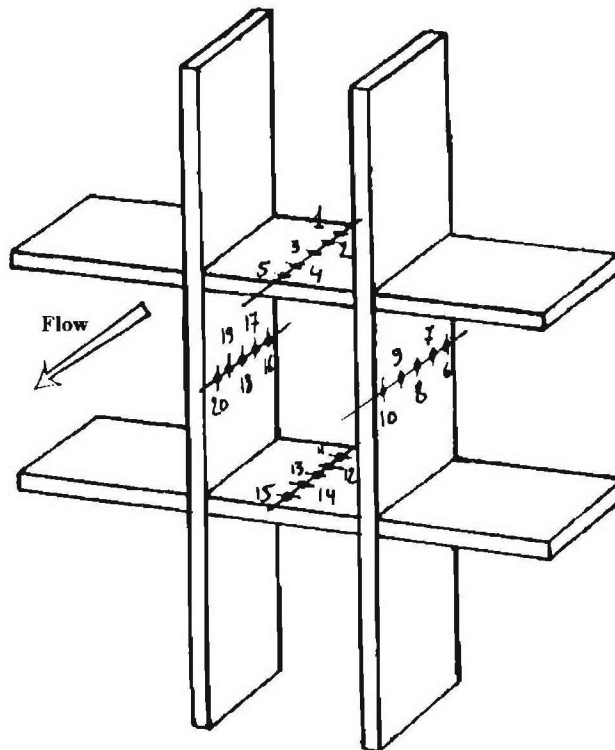


Figure 42d. Center of pressure location

Figure 42. Comparison of CFD aerodynamic coefficients vs. Mach number for both models  
(cont)



**Figure 43. Pressure taps location in central cell.**

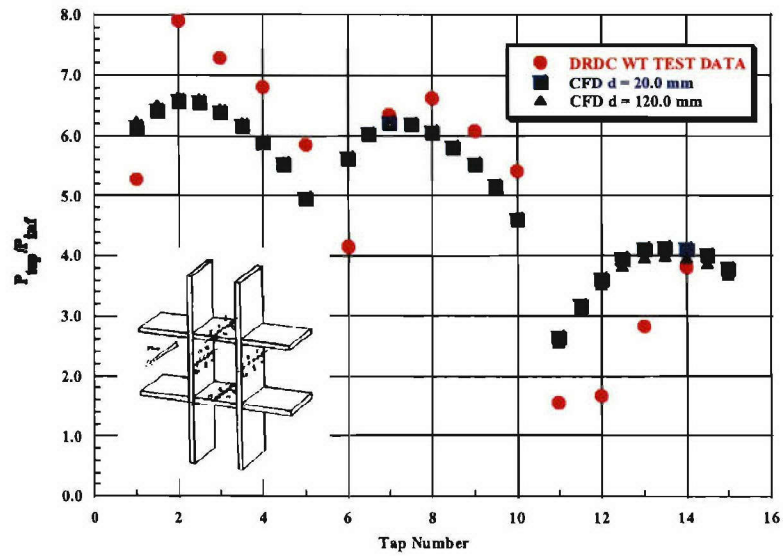


Figure 44a. Mach = 3.0,  $\delta = 0.0^\circ$

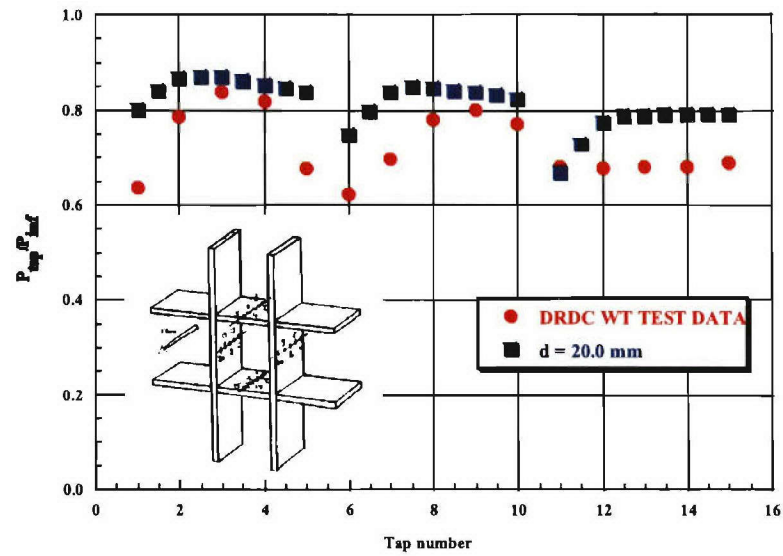


Figure 44b. Mach = 0.6,  $\delta = 0.0^\circ$

Figure 44. Comparison of computed and measured pressures in central cell ( $\kappa$ - $\epsilon$ , BF-0.75)

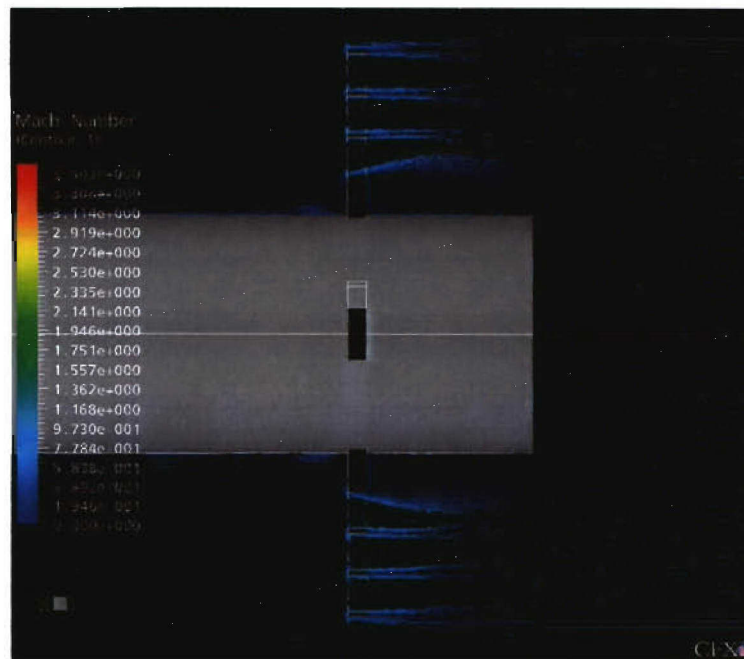


Figure 45a. Mach number contours

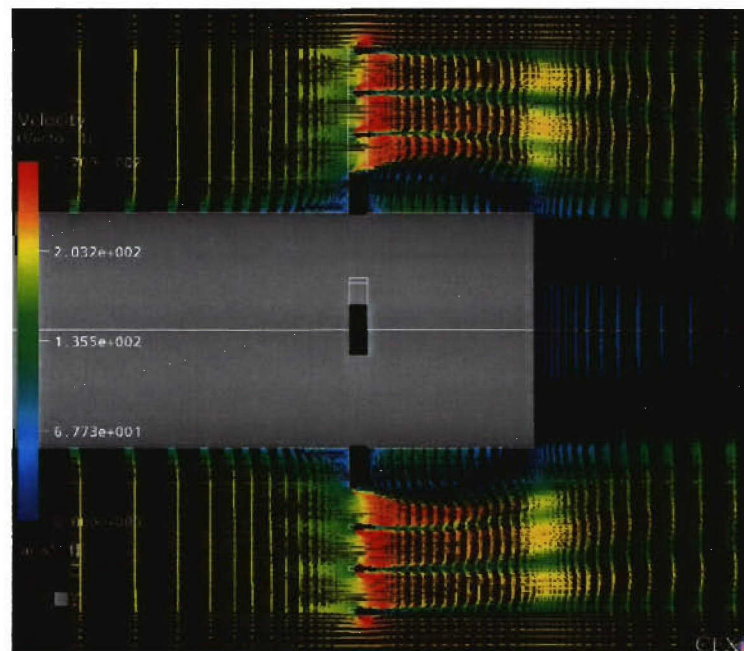


Figure 45b. Velocity vectors

**Figure 45. Flow field for Mach = 0.6,  $\alpha = 0.0^\circ$**

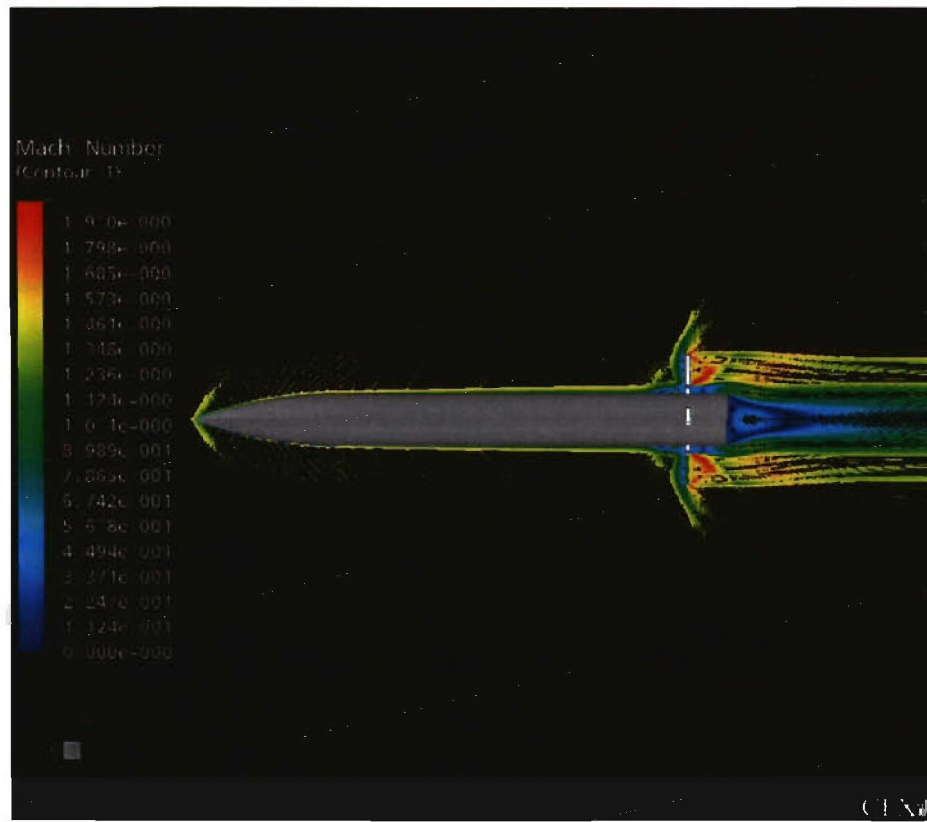


Figure 46a. CFD Mach number contours for whole projectile

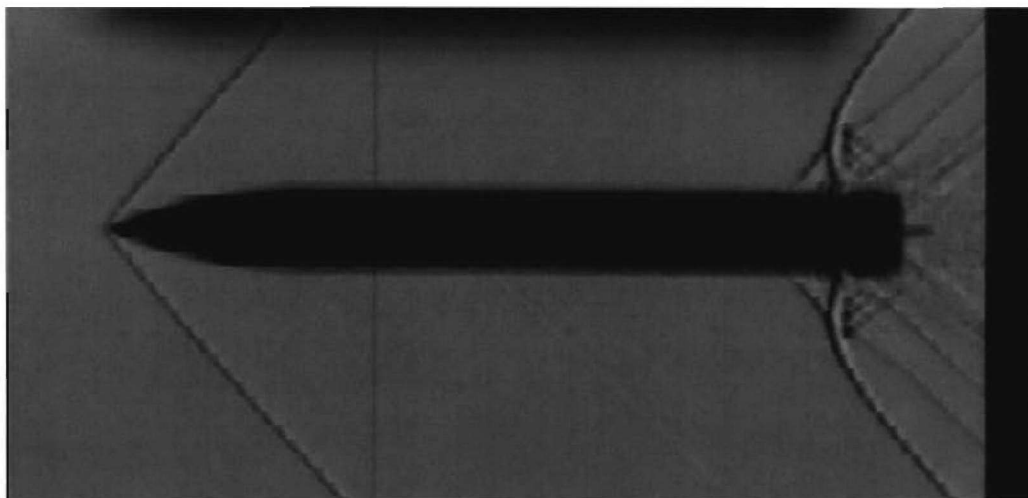


Figure 46b. Free-flight shadowgraph at Mach 1.49 (K02, M31)

**Figure 46. Flow field for Mach = 1.5,  $\alpha = 0.0^\circ$**

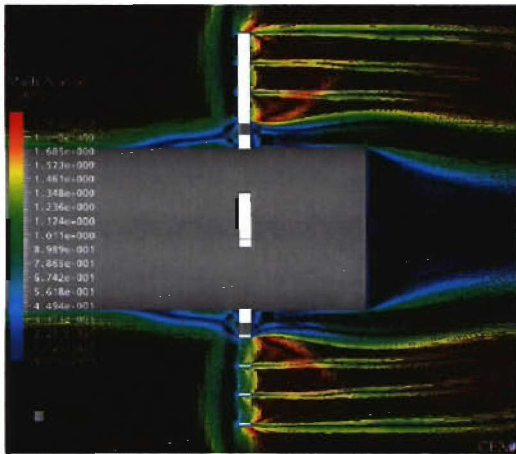


Figure 46c. CFD Mach number contours in fin area

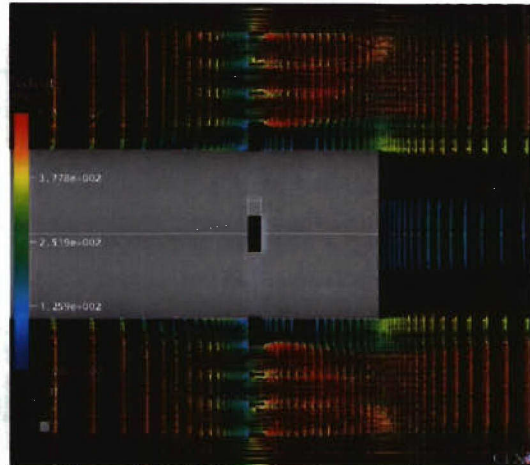


Figure 46d. Velocity vectors in fin area

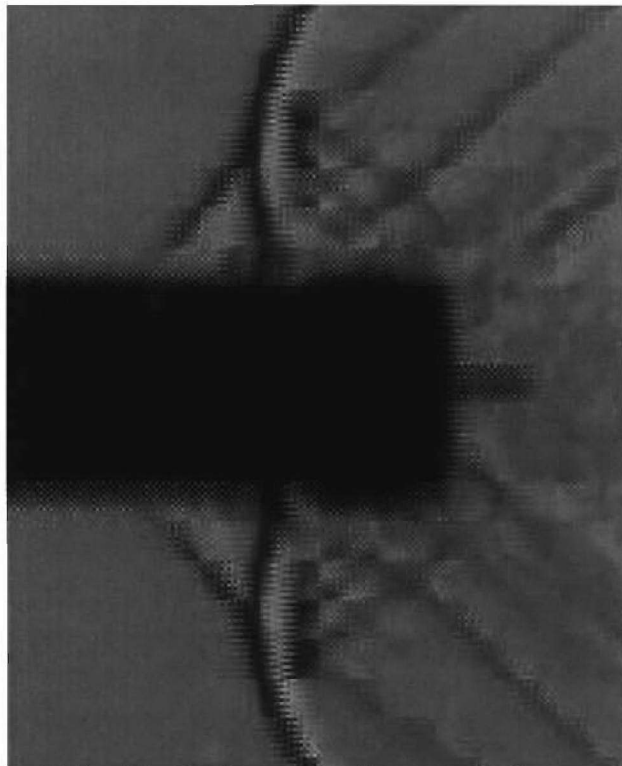


Figure 46e. Shadowgraph enlargement in fin area

Figure 46. Flow field for Mach = 1.5,  $\alpha = 0.0^\circ$  (cont)



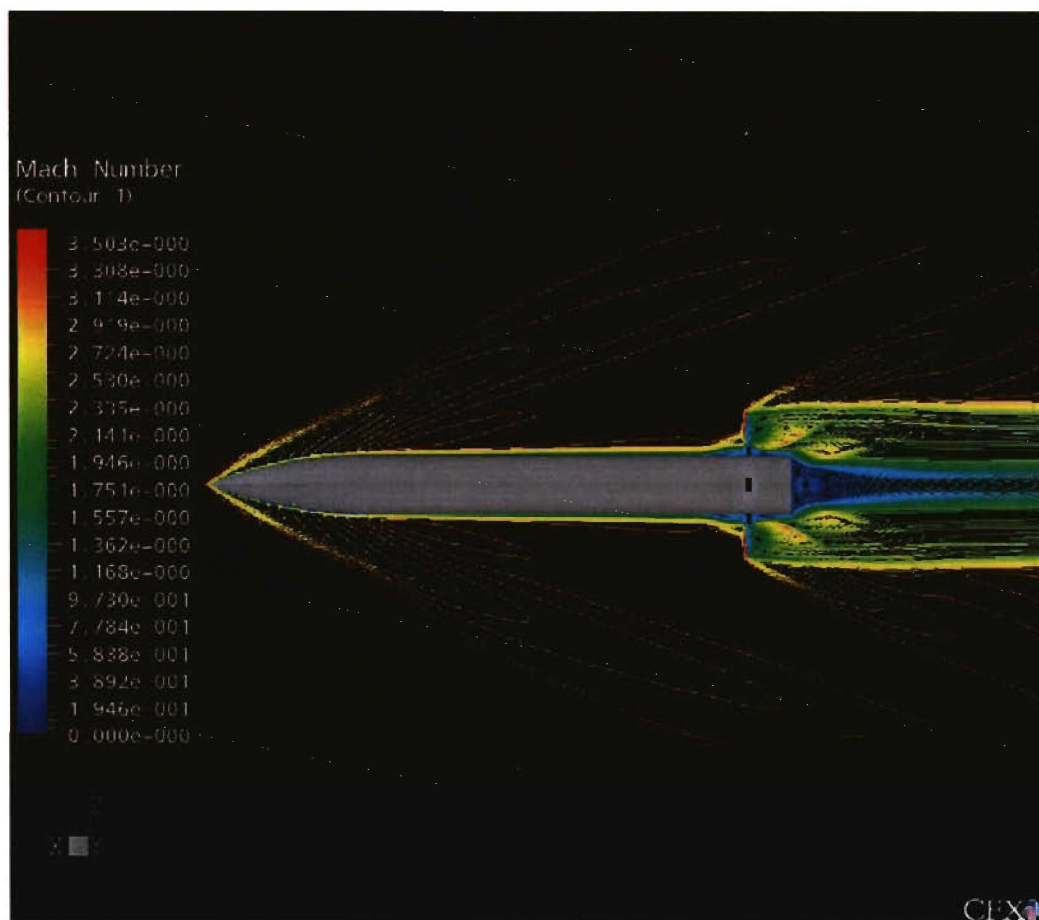


Figure 47a. CFD Mach number contours for whole projectile



Figure 47b. Wind tunnel shadowgraph at Mach 3.0

**Figure 47. Flow field for Mach = 3.0,  $\alpha = 0.0^\circ$**

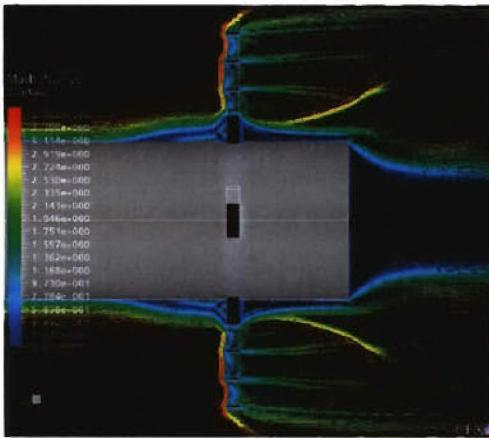


Figure 47c. CFD Mach number contours in fin area

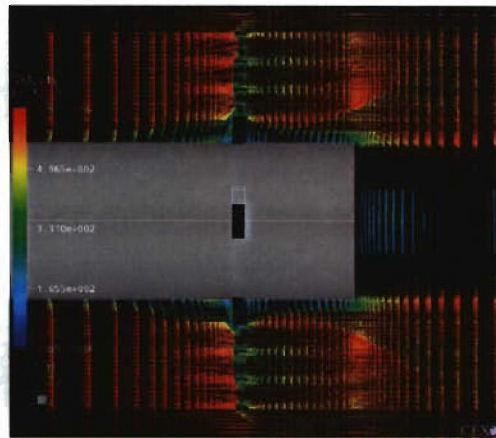


Figure 47d. Velocity vectors in fin area

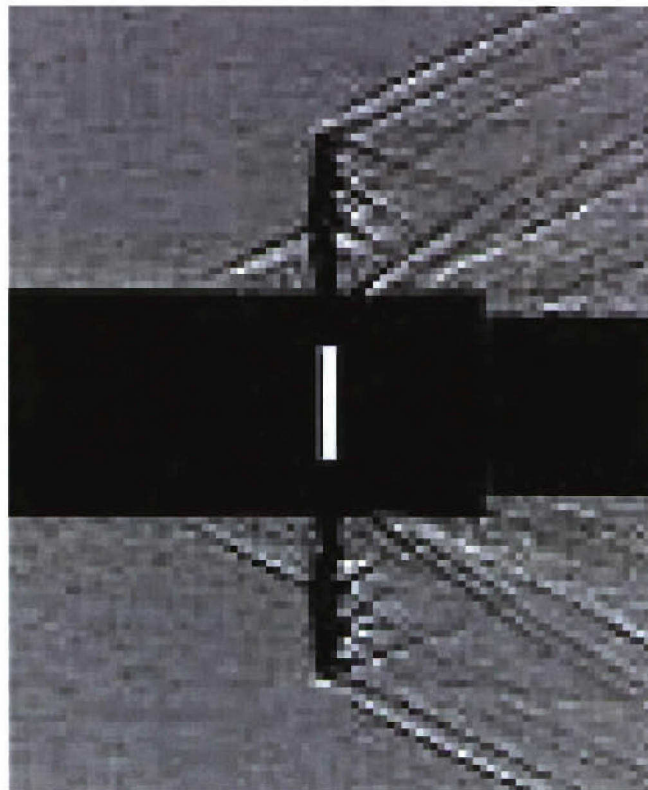


Figure 47e. Shadowgraph enlargement in fin area

Figure 47. Flow field for Mach = 3.0,  $\alpha = 0.0^\circ$  (cont)

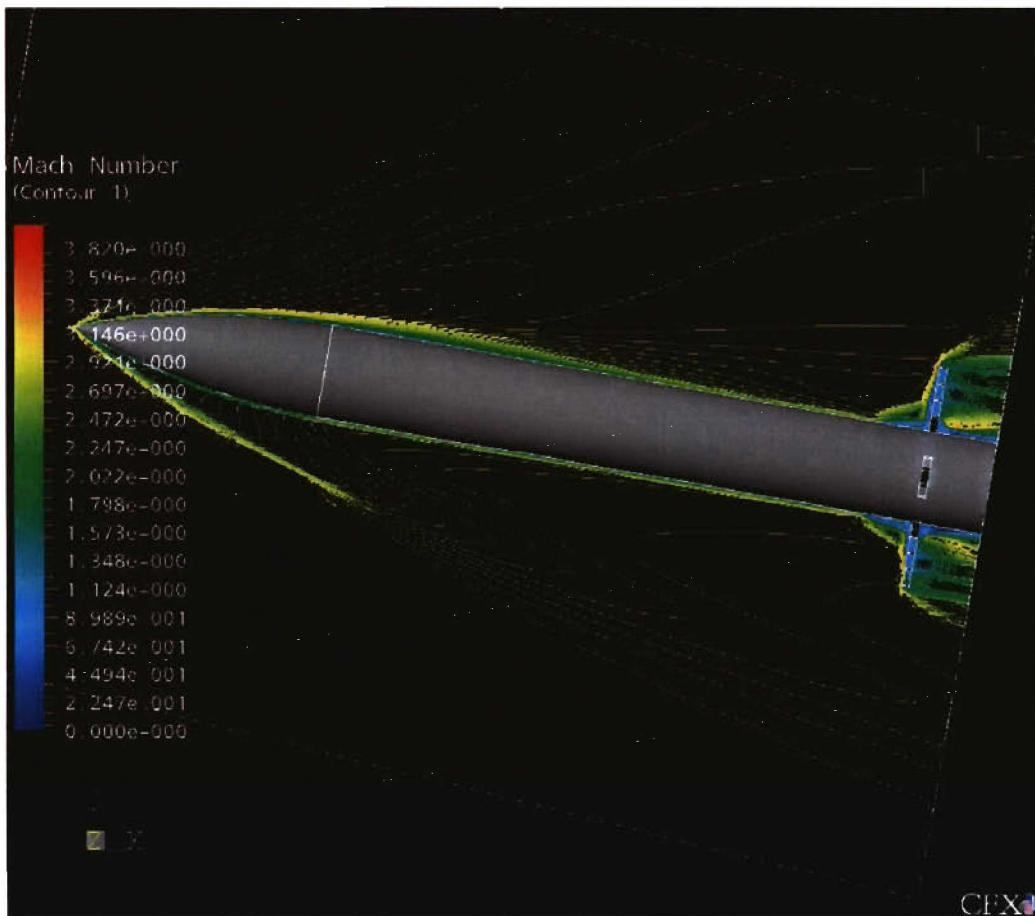


Figure 48a. CFD Mach number contours for whole projectile

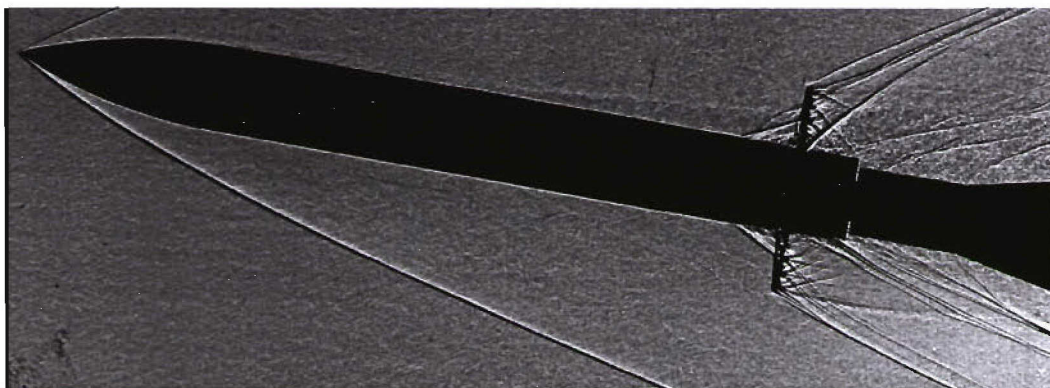


Figure 48b. Wind tunnel shadowgraph at Mach 3.0

**Figure 48. Flow field for Mach = 3.0,  $\alpha = 10.0^\circ$**

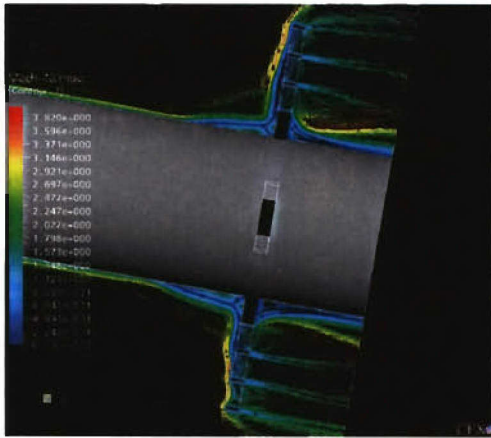


Figure 48c. CFD Mach number contours in fin area

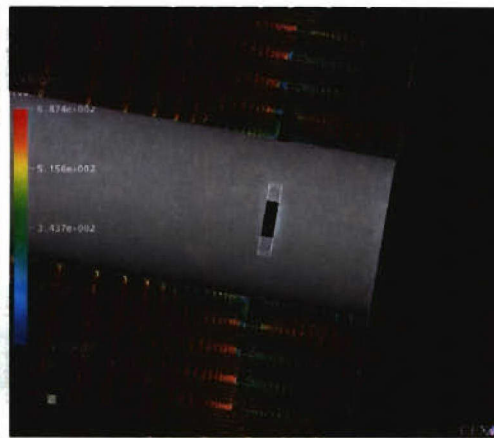


Figure 48d. Velocity vectors in fin area

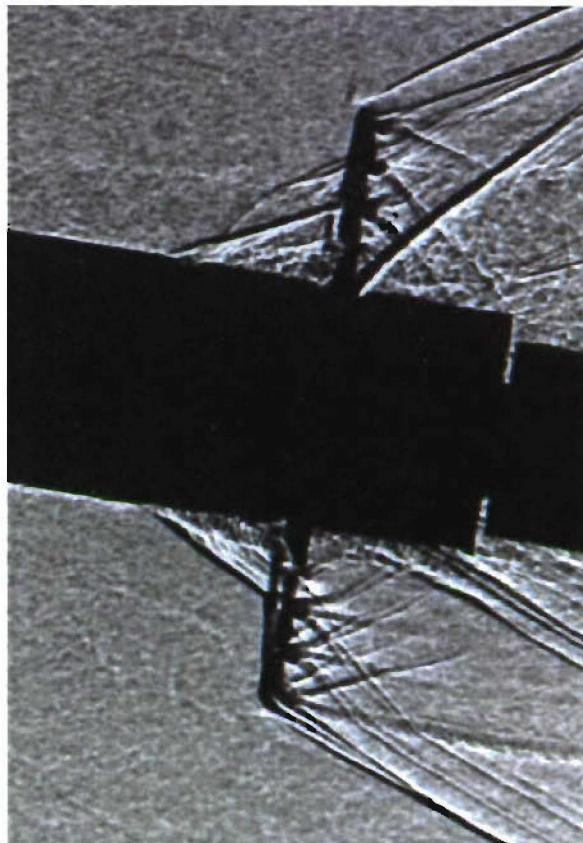


Figure 48e. Shadowgraph enlargement in fin area

Figure 48. Flow field for Mach = 3.0,  $\alpha = 10.0^\circ$  (cont)



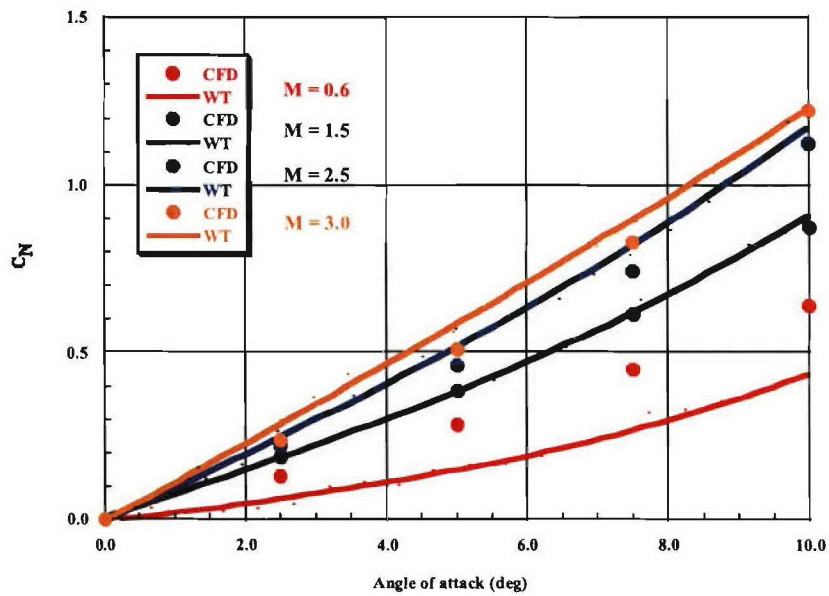


Figure 49a. Normal force coefficient

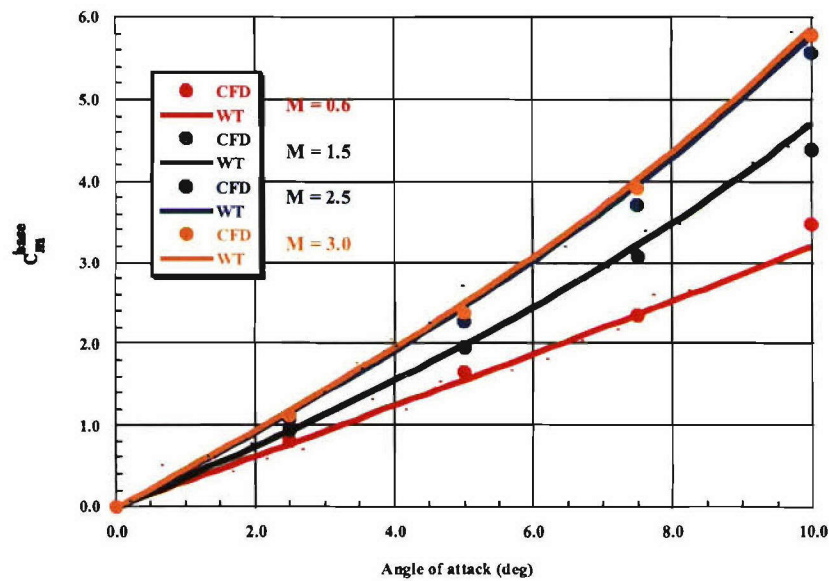


Figure 49b. Pitch moment coefficient about base

Figure 49. Comparison of numerical and wind tunnel experimental results vs. incidence for model A3

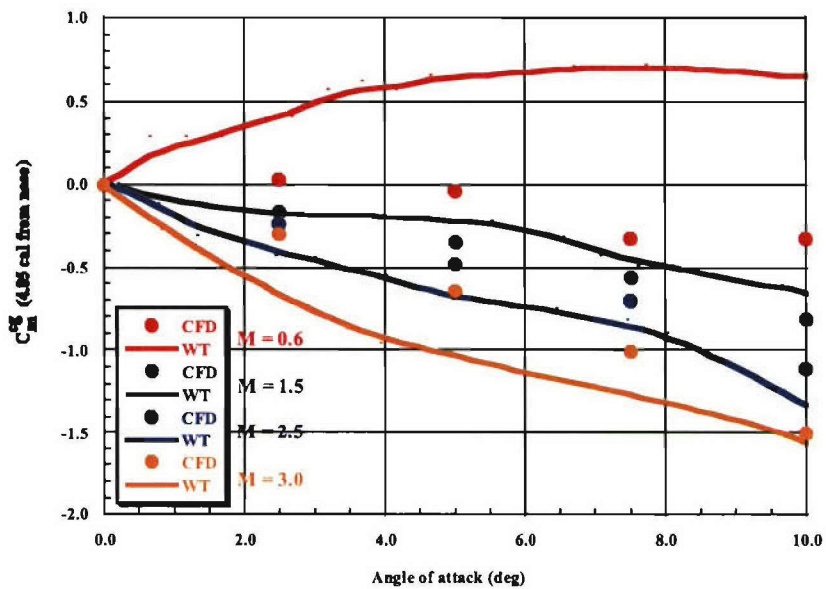


Figure 49c. Pitch moment coefficient about cg

Figure 49. Comparison of numerical and wind tunnel experimental results vs. incidence for model A3 (cont)

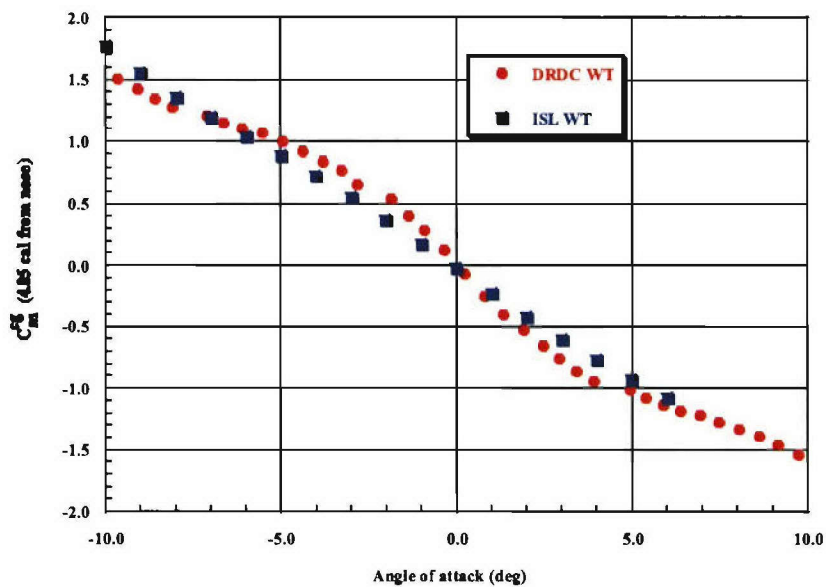


Figure 50. Pitch moment coefficient vs. incidence for model A3\_1 at Mach 3.0

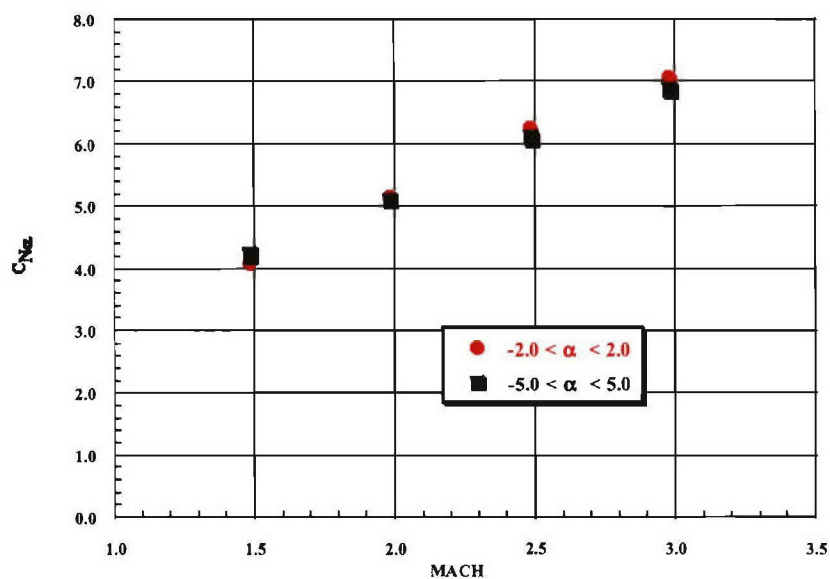


Figure 51a. Normal force coefficient slope

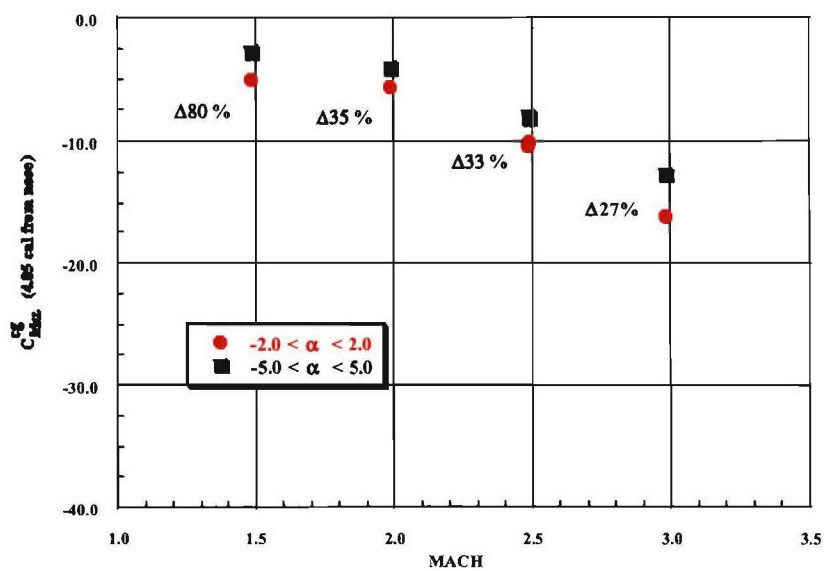


Figure 51b. Pitch moment coefficient slope about cg

**Figure 51. Comparison of wind tunnel aerodynamic coefficient slopes vs. Mach number for model A3\_1**



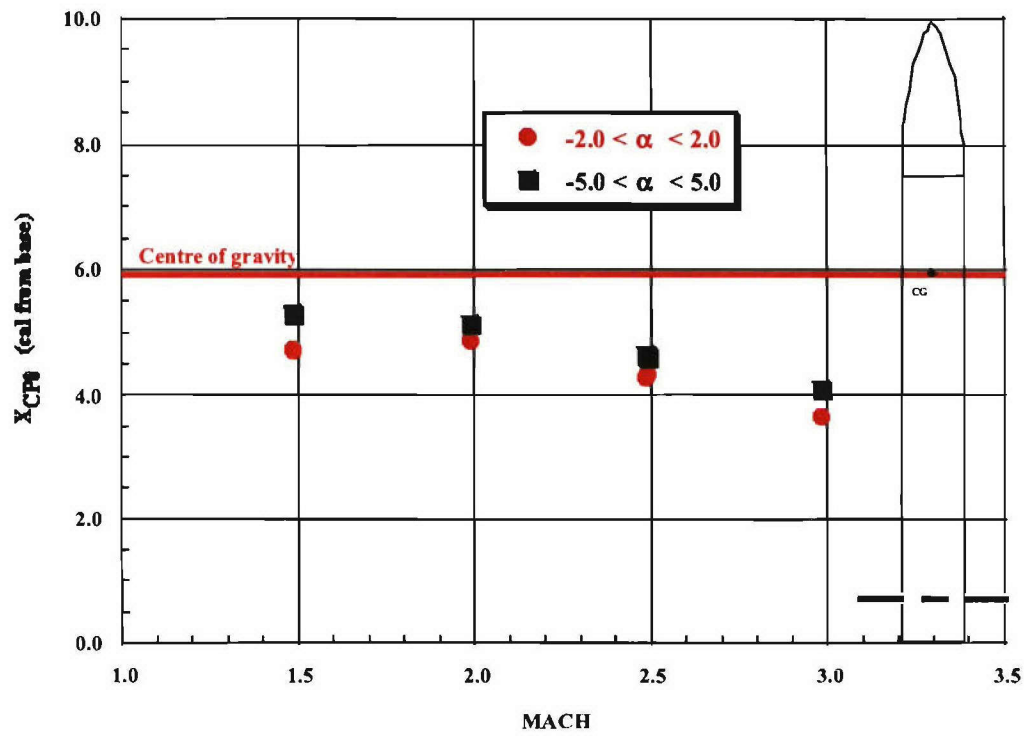


Figure 51c. Center of pressure at zero angle of attack

Figure 51. Comparison of wind tunnel aerodynamic coefficient slopes vs. Mach number for model A3\_1 (cont)

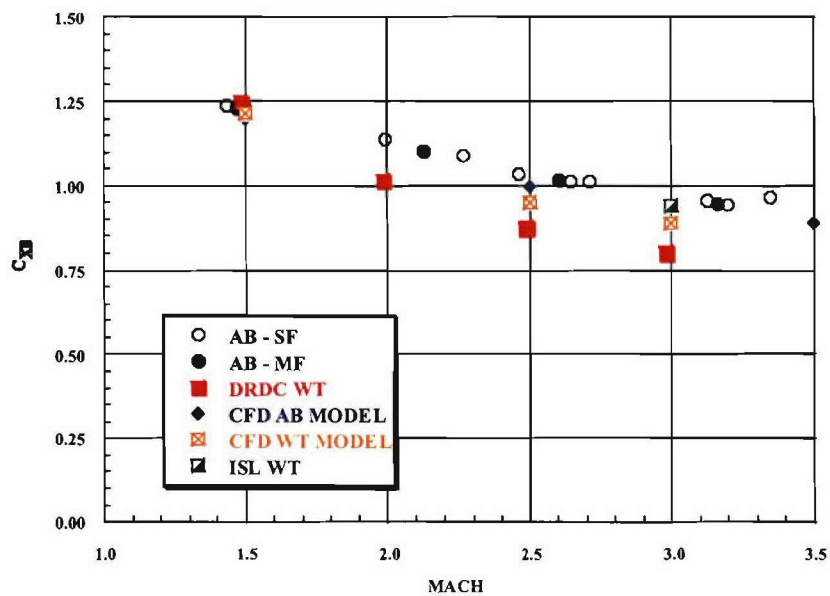


Figure 52a. Axial force coefficient

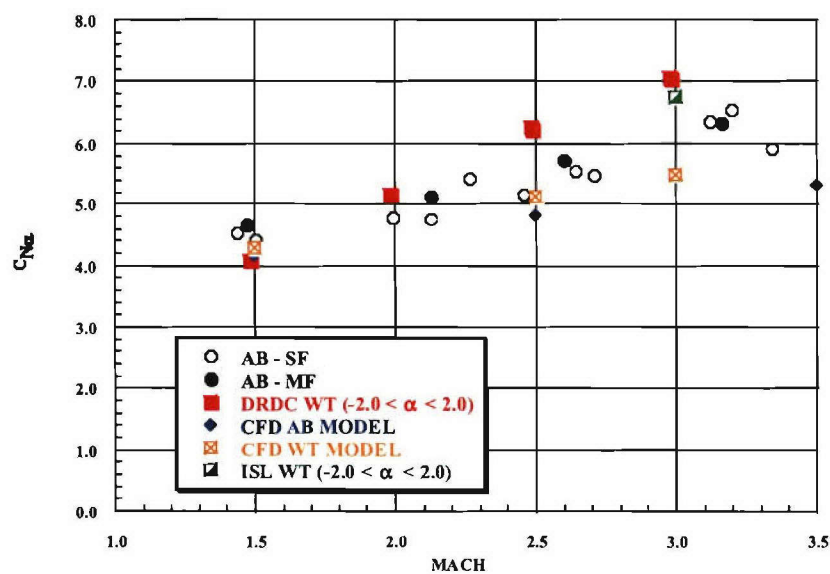


Figure 52b. Normal force coefficient slope

**Figure 52. Comparison of predicted and experimental aerodynamic coefficients vs. Mach number**

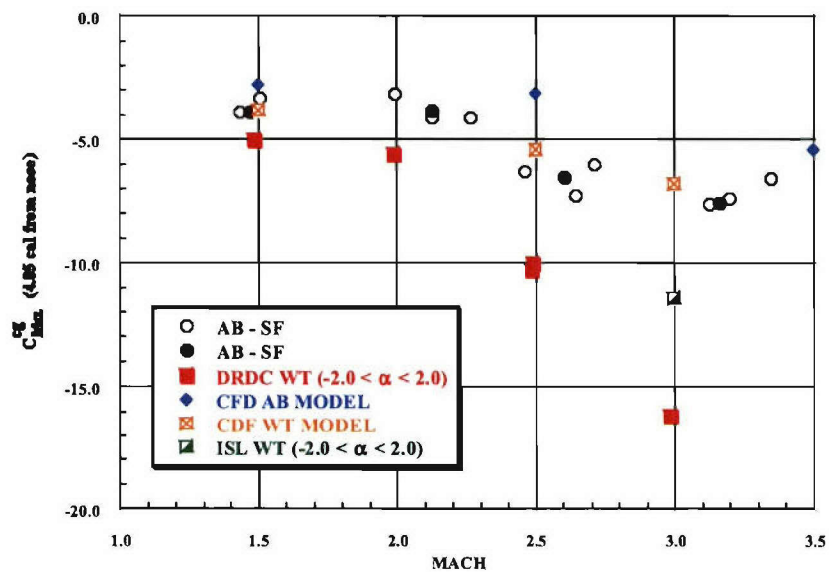


Figure 52c. Pitch moment coefficient slope about cg

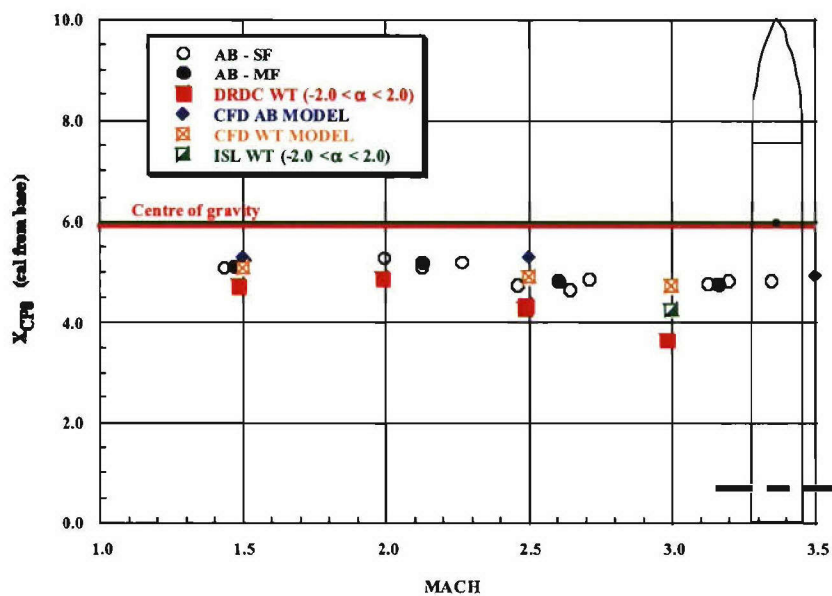


Figure 52d. Center of pressure location

Figure 52. Comparison of predicted and experimental aerodynamic coefficients vs. Mach number (cont)

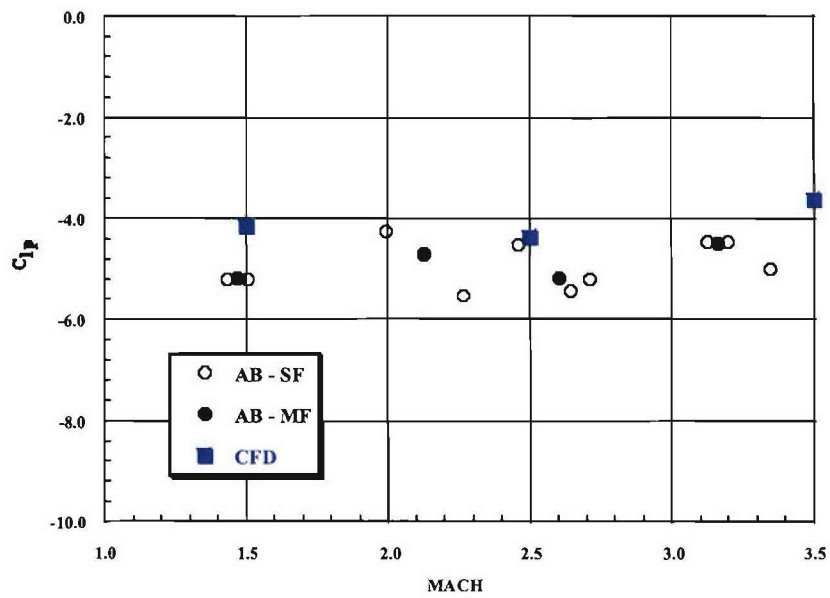


Figure 52e. Roll damping moment

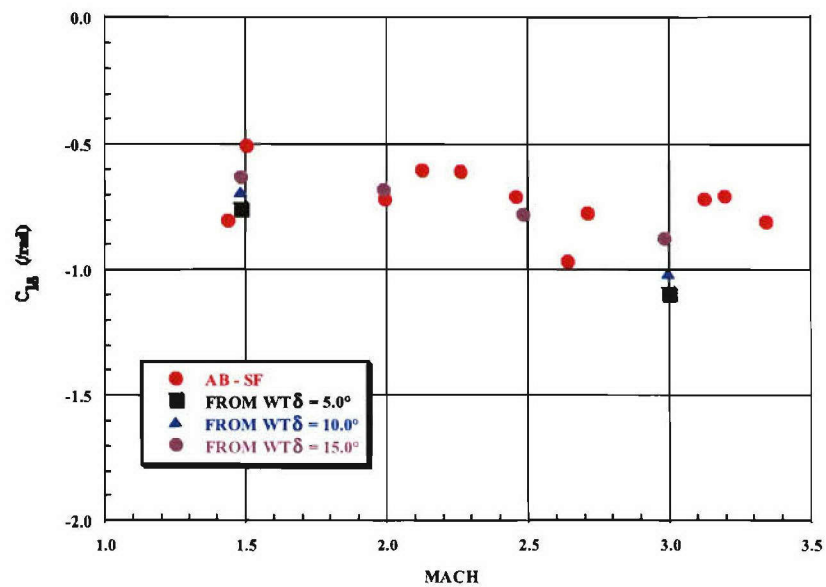


Figure 52f. Roll producing moment for two canted fins at  $2.0^\circ$

Figure 52. Comparison of predicted and experimental aerodynamic coefficients vs. Mach number (cont)

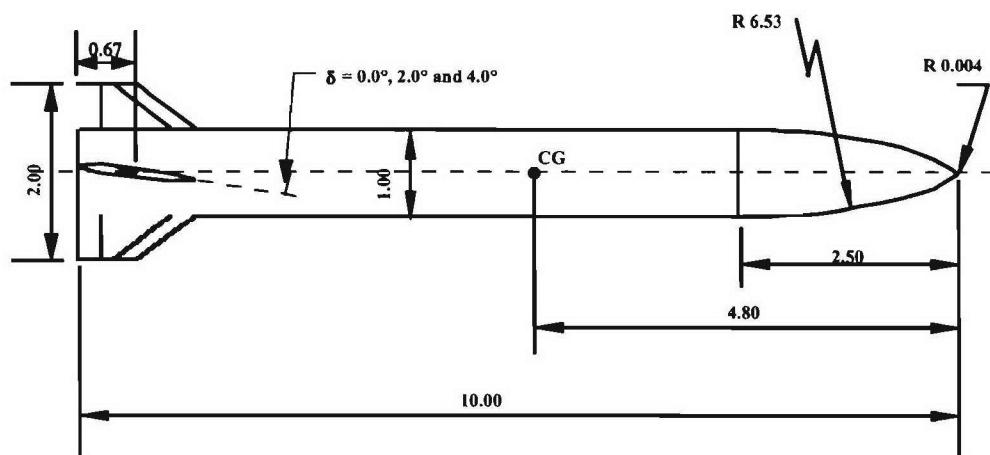


Figure 53a. Air Force Finner geometry

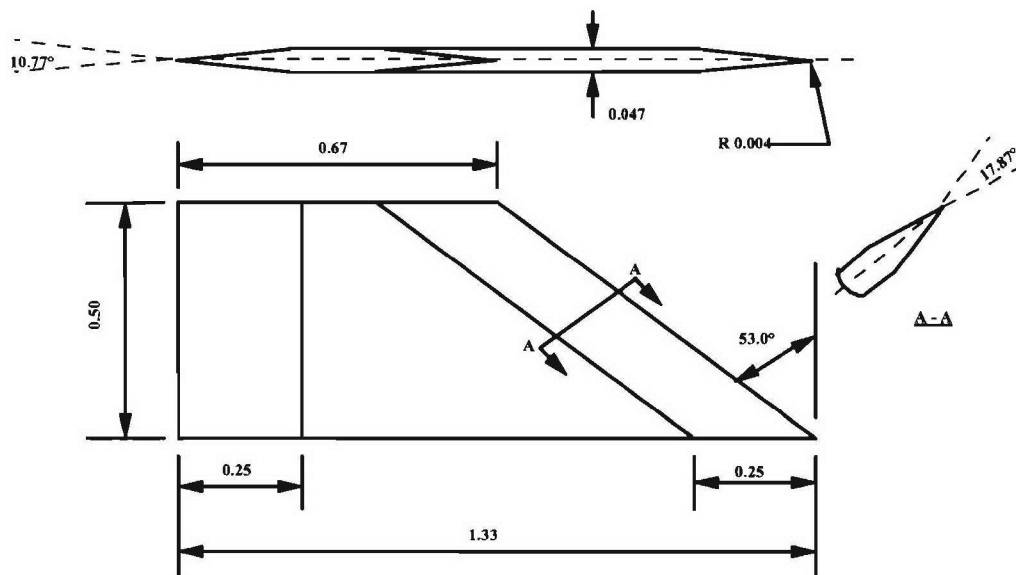


Figure 53b. Fin details

Figure 53. Drawings of Air Force Finner reference projectile (all dimensions in caliber)

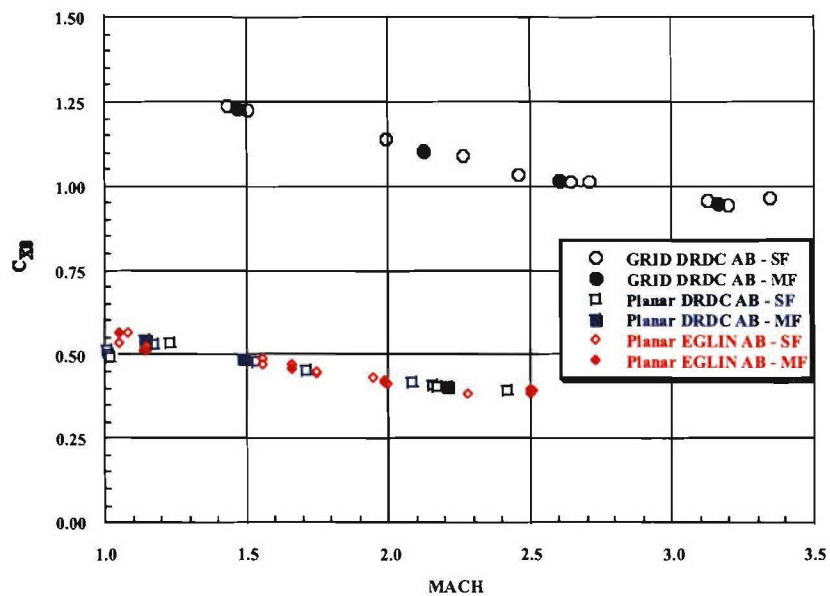


Figure 54a. Axial force coefficient

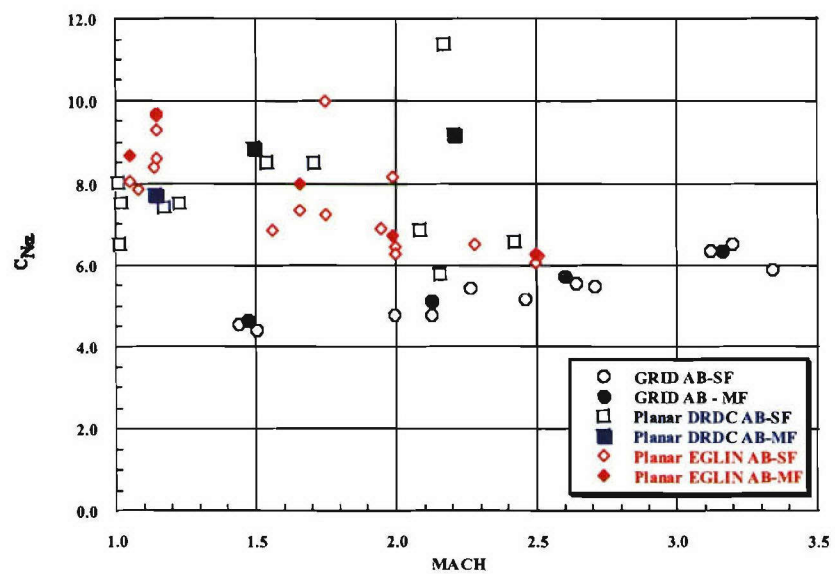


Figure 54b. Normal force coefficient slope

**Figure 54. Comparison of aerodynamic coefficients for grid and classical fins vs. Mach number**

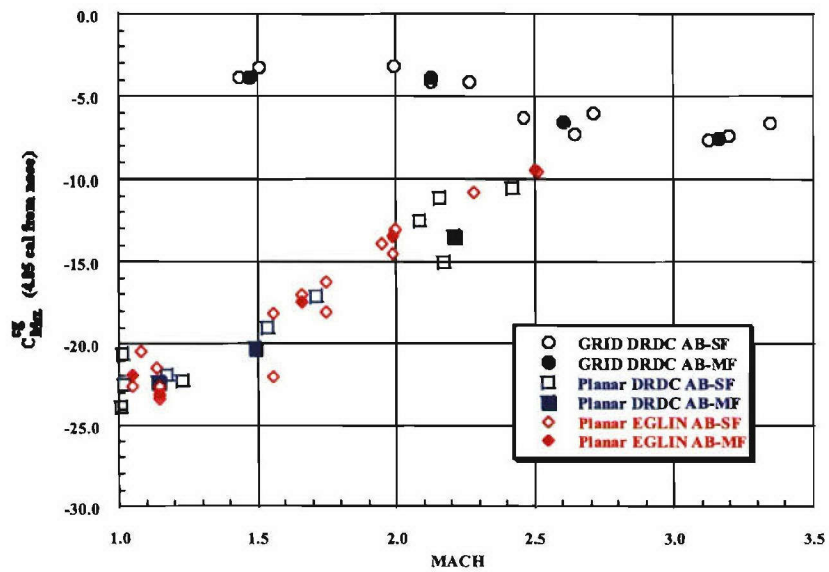


Figure 54c. Pitch moment coefficient slope about cg

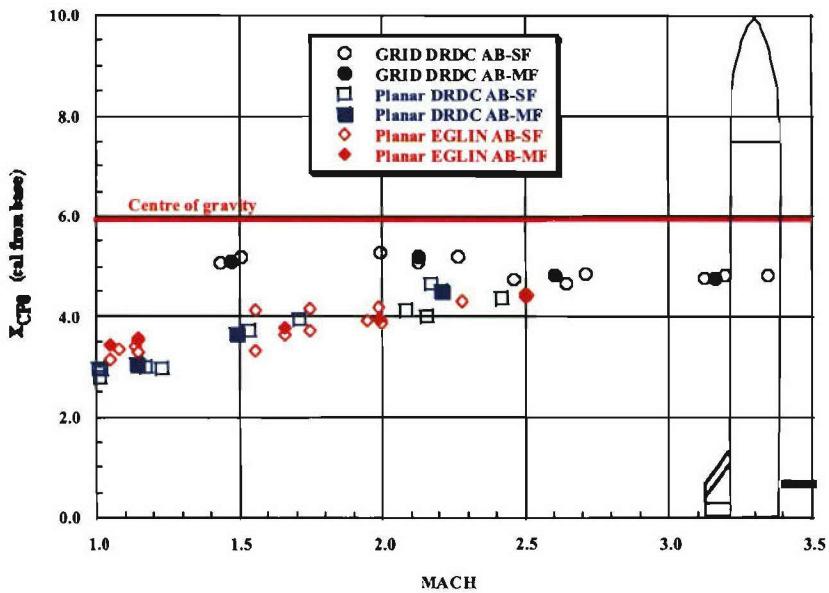


Figure 54d. Center of pressure location

Figure 54. Comparison of aerodynamic coefficients for grid and classical fins vs. Mach number (cont)



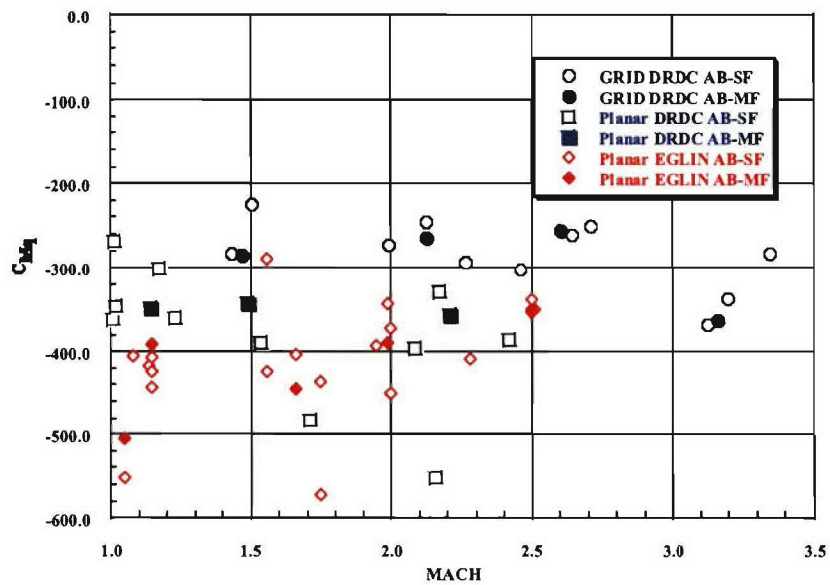


Figure 54e. Pitch damping coefficient about cg

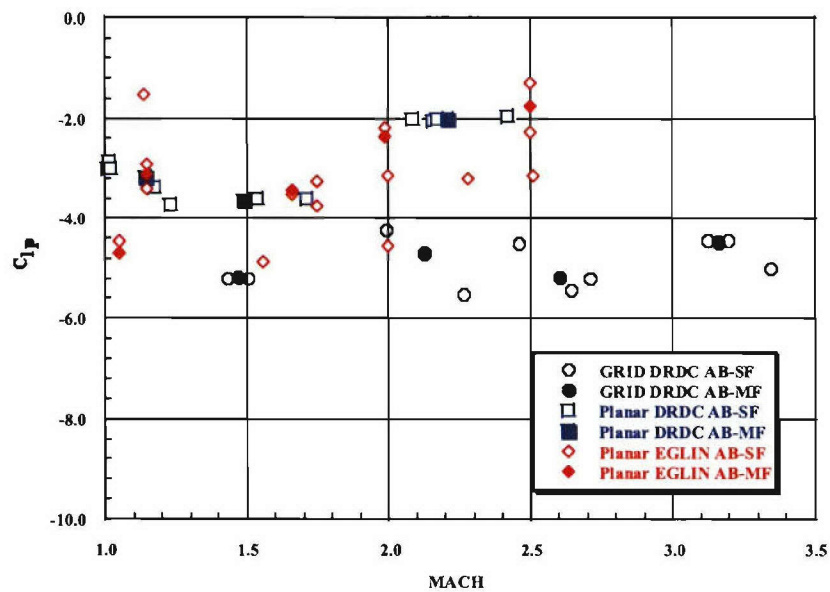


Figure 54f. Roll damping moment

Figure 54. Comparison of aerodynamic coefficients for grid and classical fins  
vs. Mach number (cont)

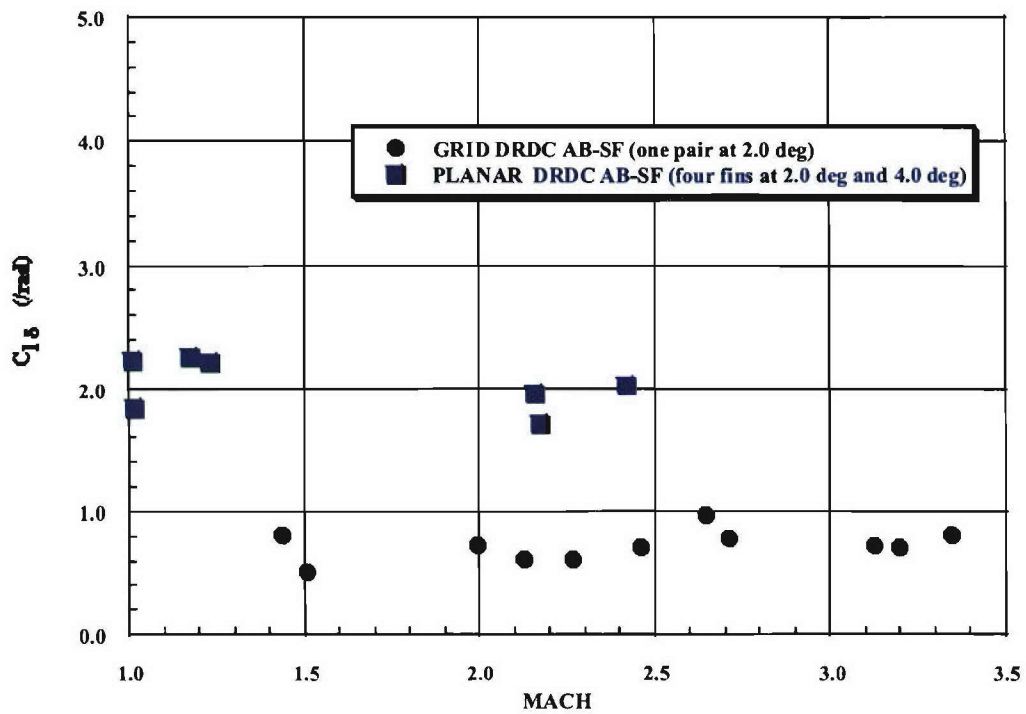
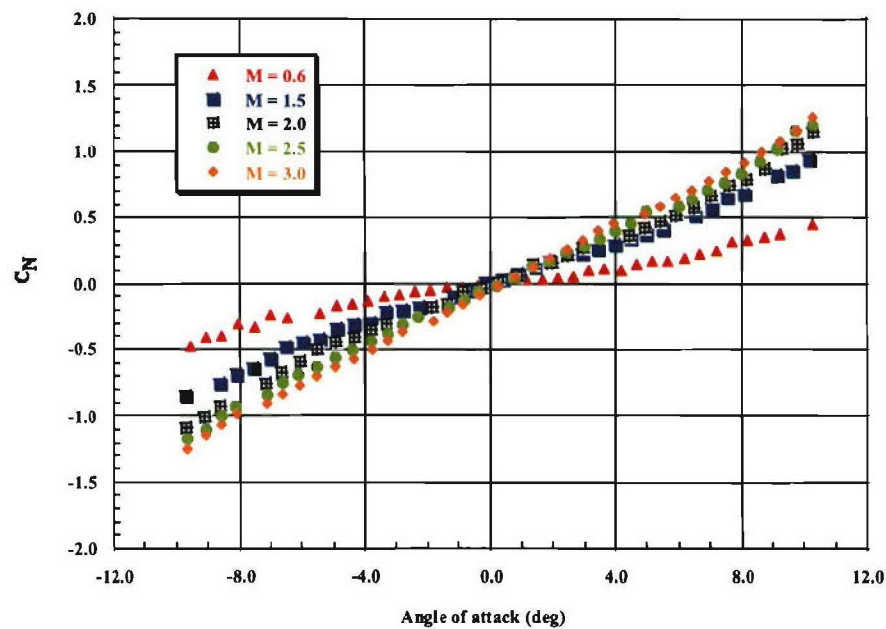
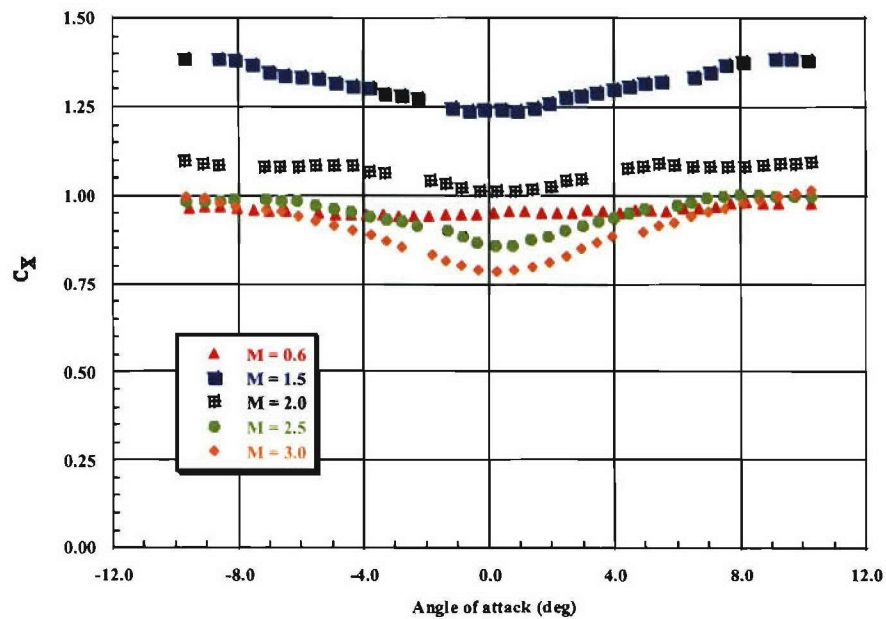


Figure 54g. Roll producing moment for two canted fins at 2.0°

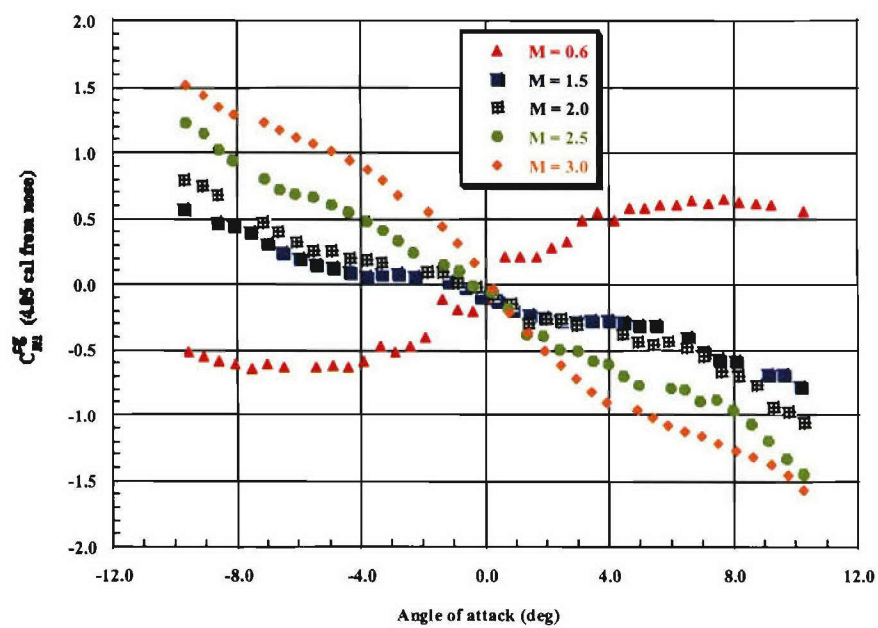
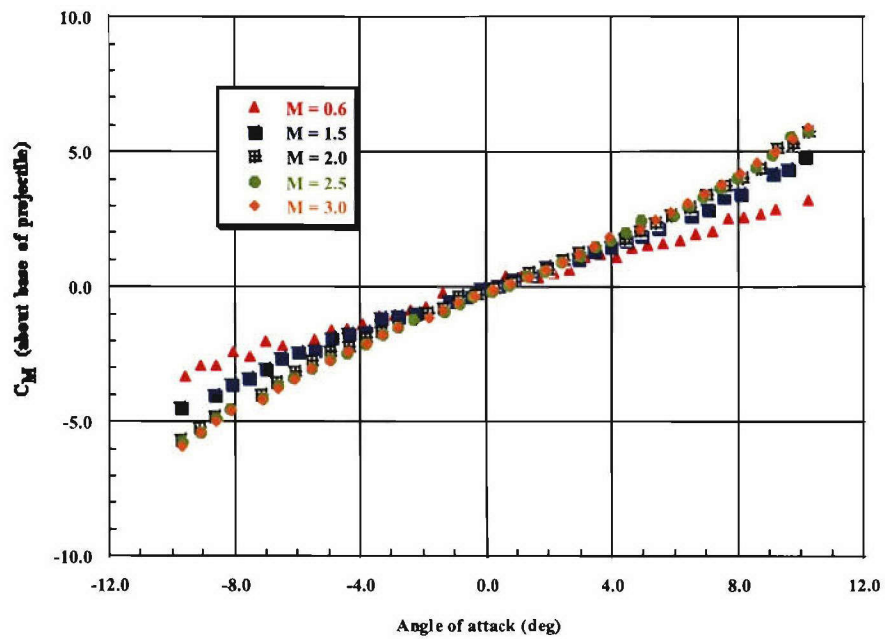
Figure 54. Comparison of aerodynamic coefficients for grid and classical fins  
vs. Mach number (cont)

## Annexe A – Plotted Wind Tunnel Aerodynamic Coefficients for A3 Configurations

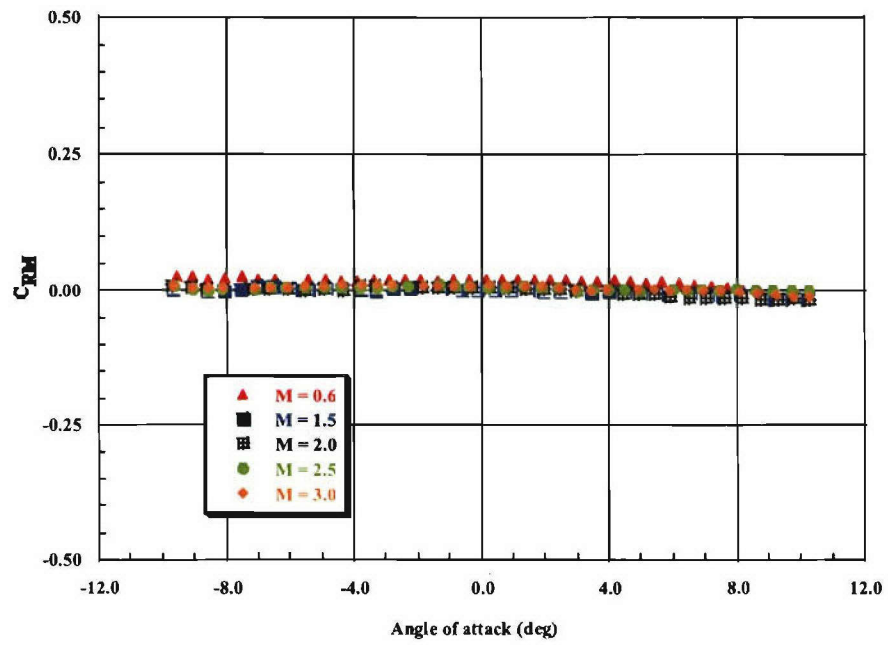
CONFIGURATION: A3\_1 ;  $\phi = 0.0^\circ$



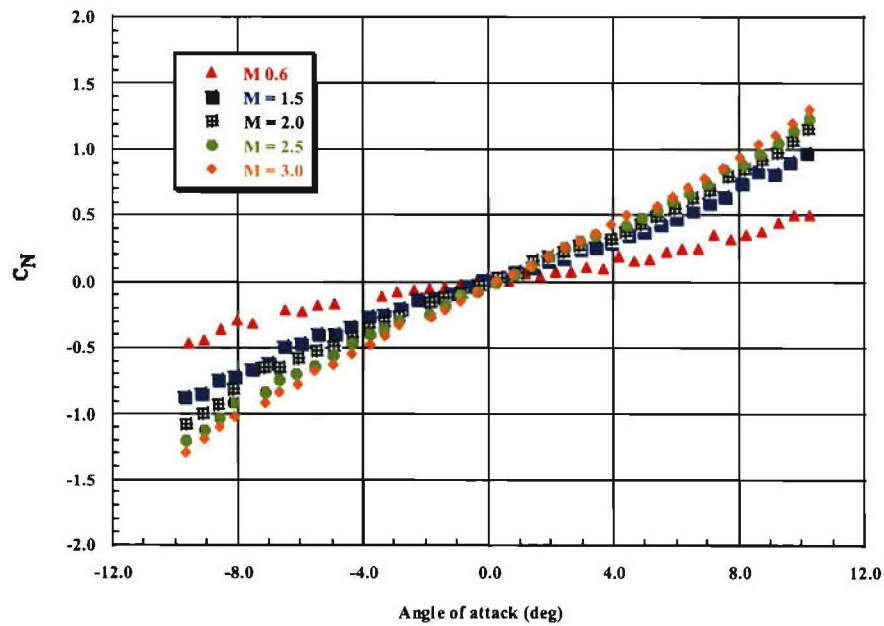
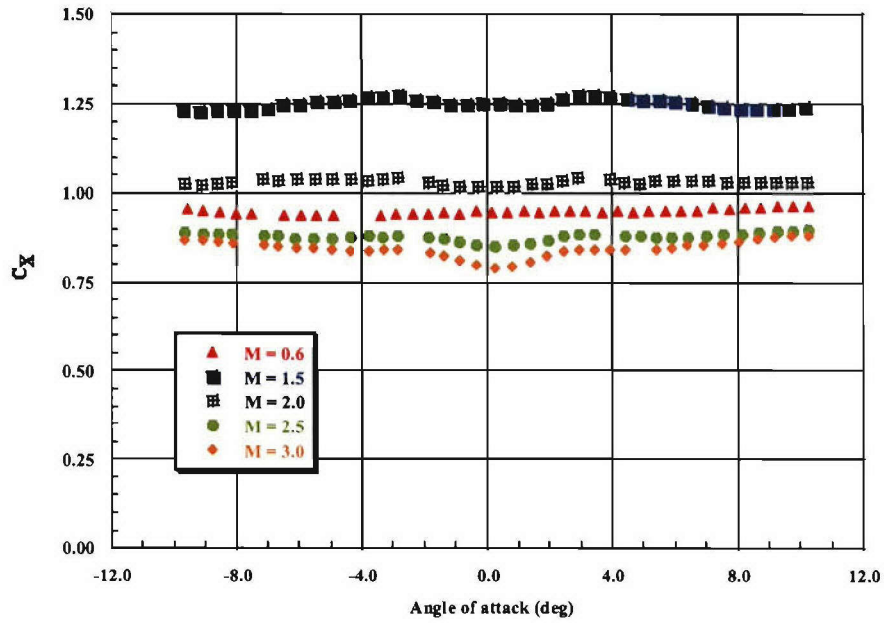
CONFIGURATION: A3\_1 ;  $\phi = 0.0^\circ$



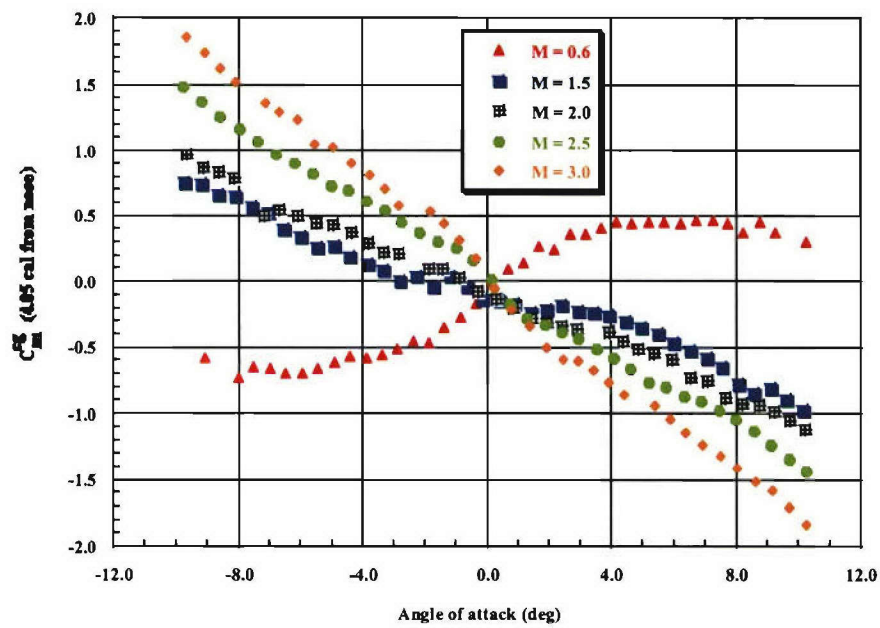
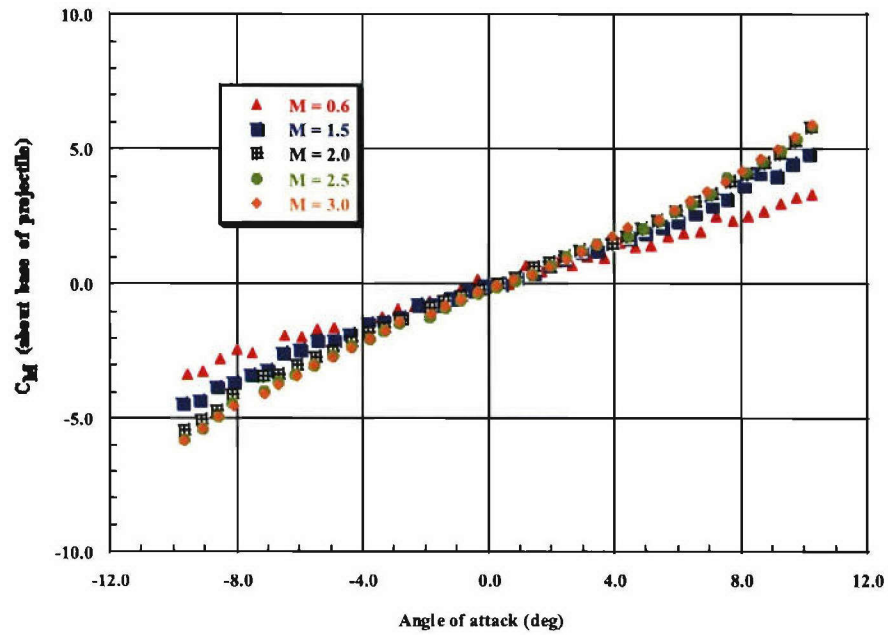
CONFIGURATION: A3\_1 ;  $\phi = 0.0^\circ$



CONFIGURATION: A3\_1 ;  $\phi = 45.0^\circ$

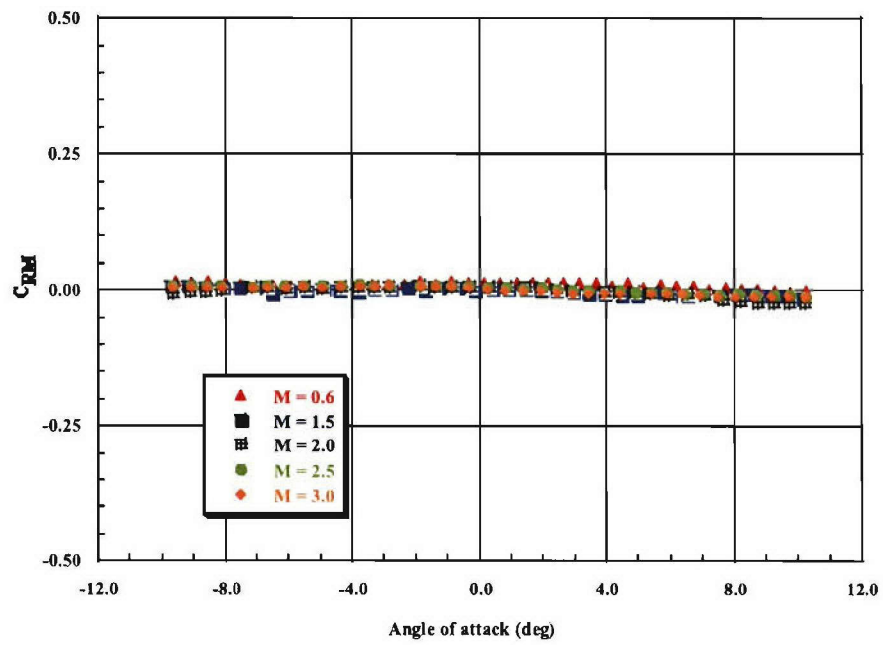


CONFIGURATION: A3\_1 ;  $\phi = 45.0^\circ$

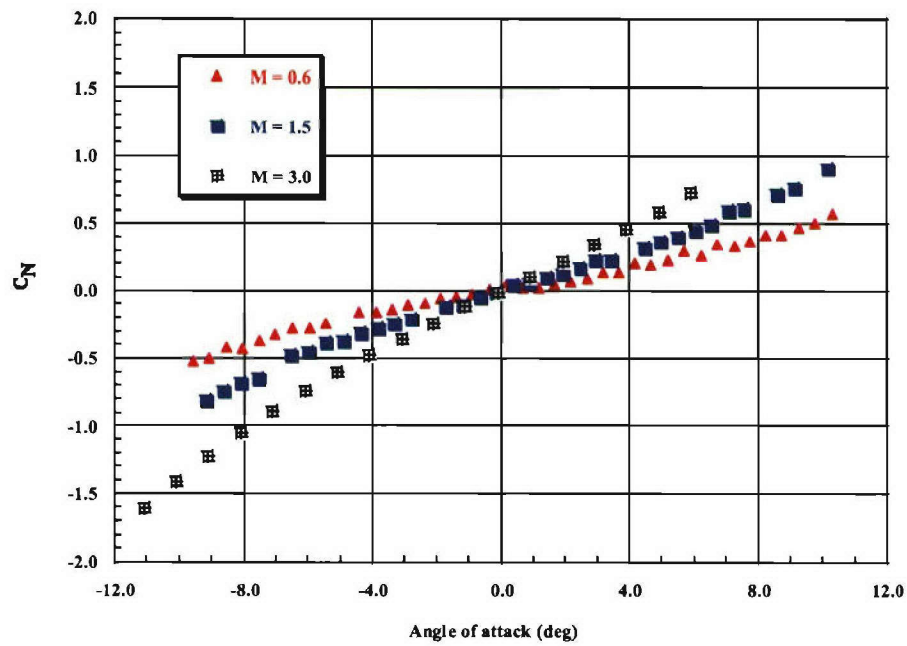
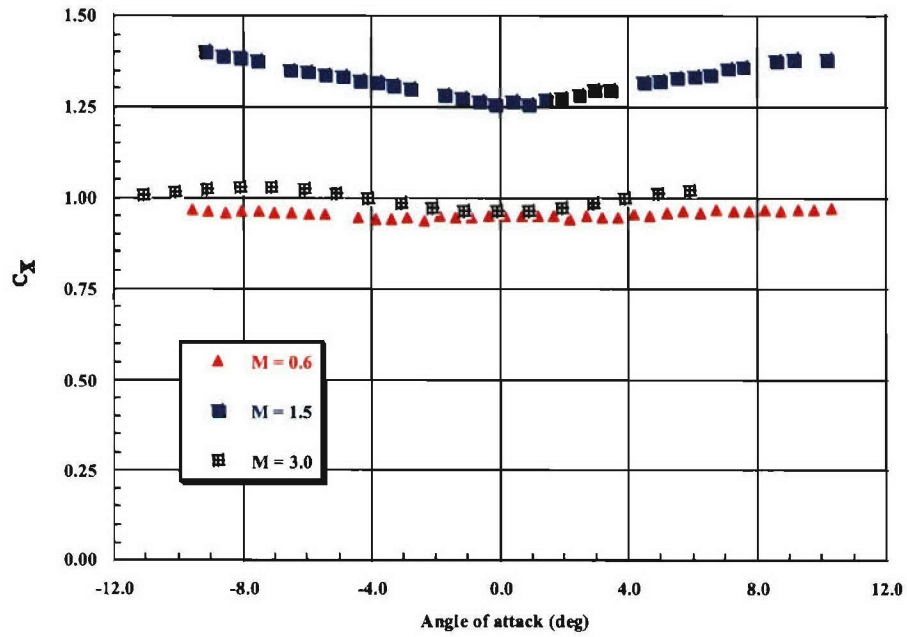




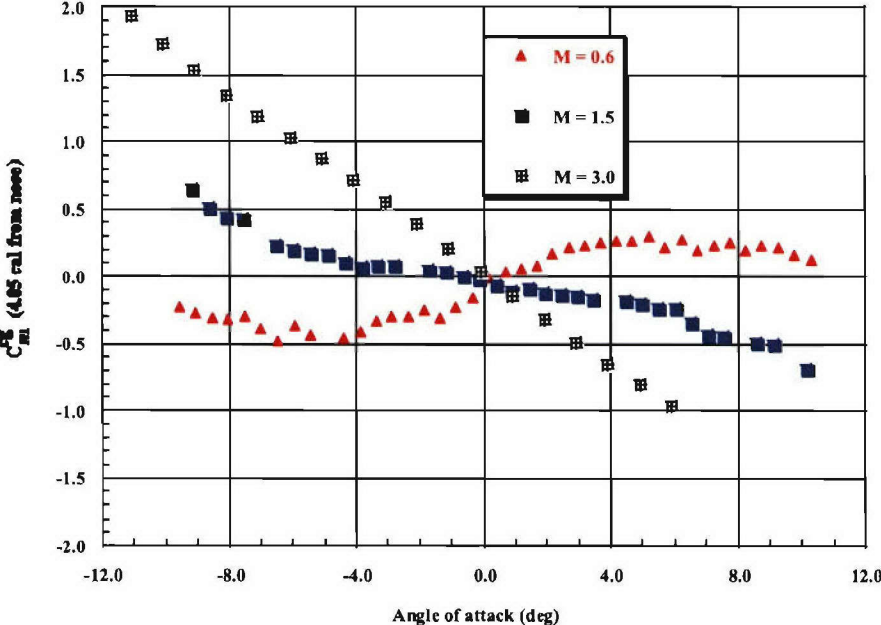
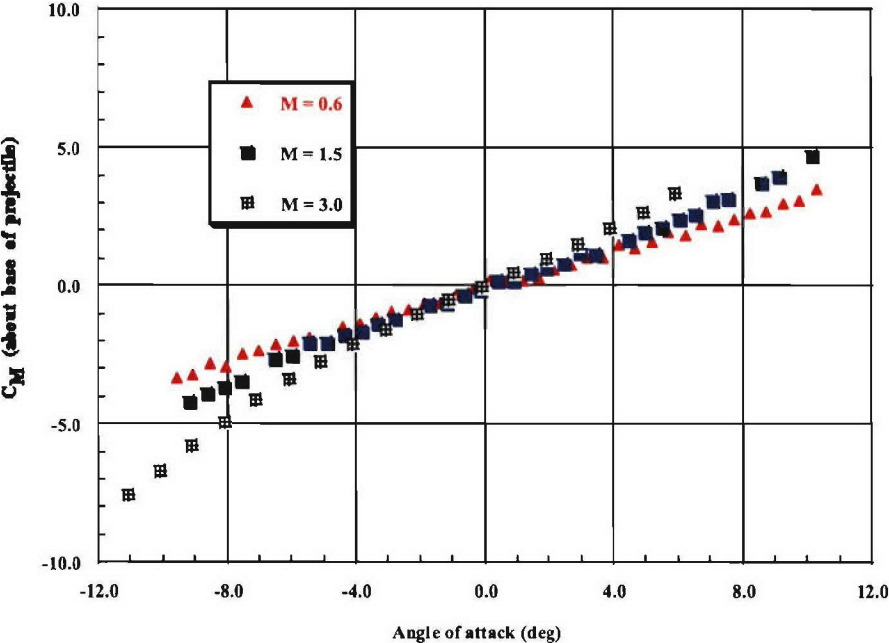
CONFIGURATION: A3\_1 ;  $\phi = 45.0^\circ$



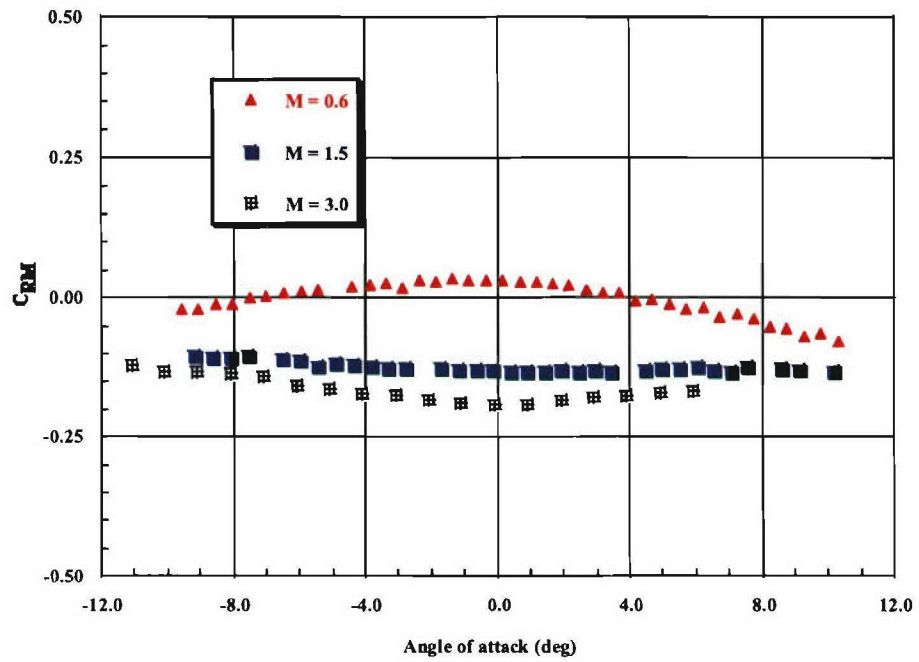
CONFIGURATION: A3\_2 ;  $\phi = 0.0^\circ$



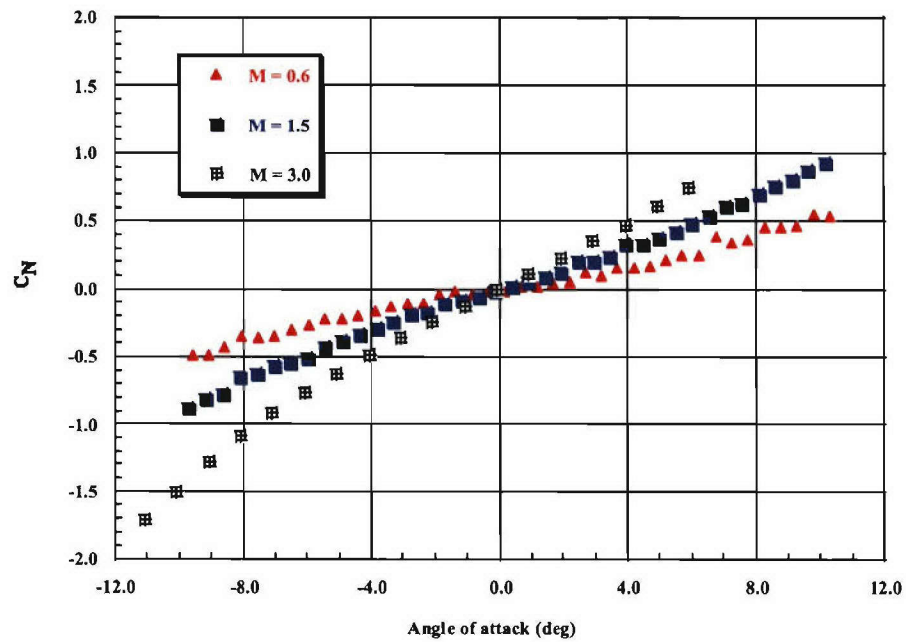
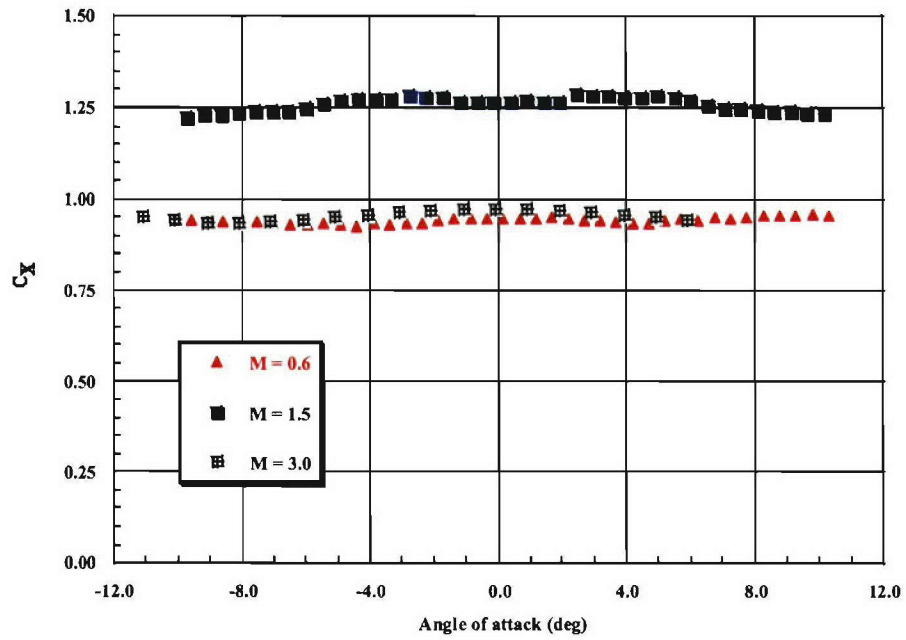
CONFIGURATION: A3\_2 ;  $\phi = 0.0^\circ$



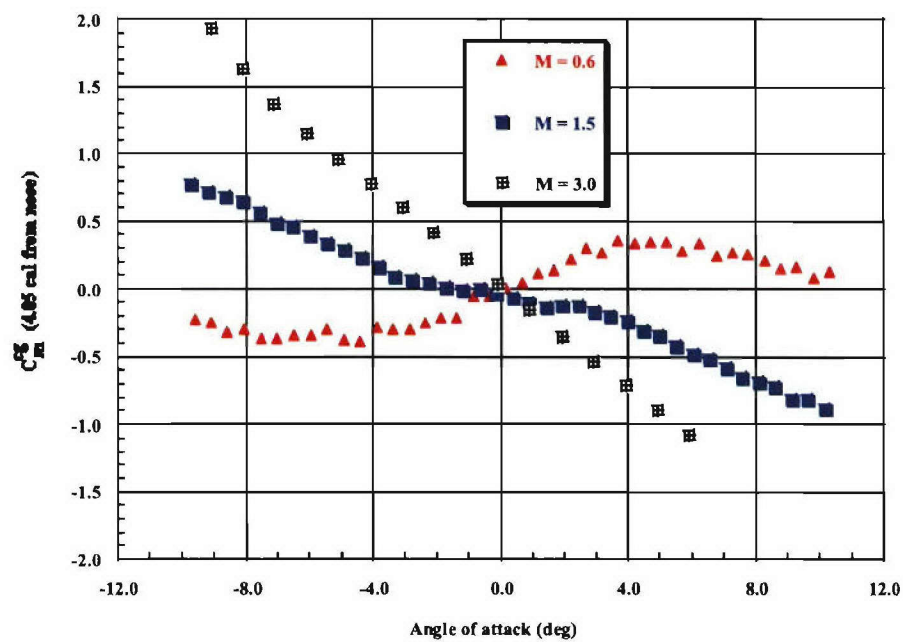
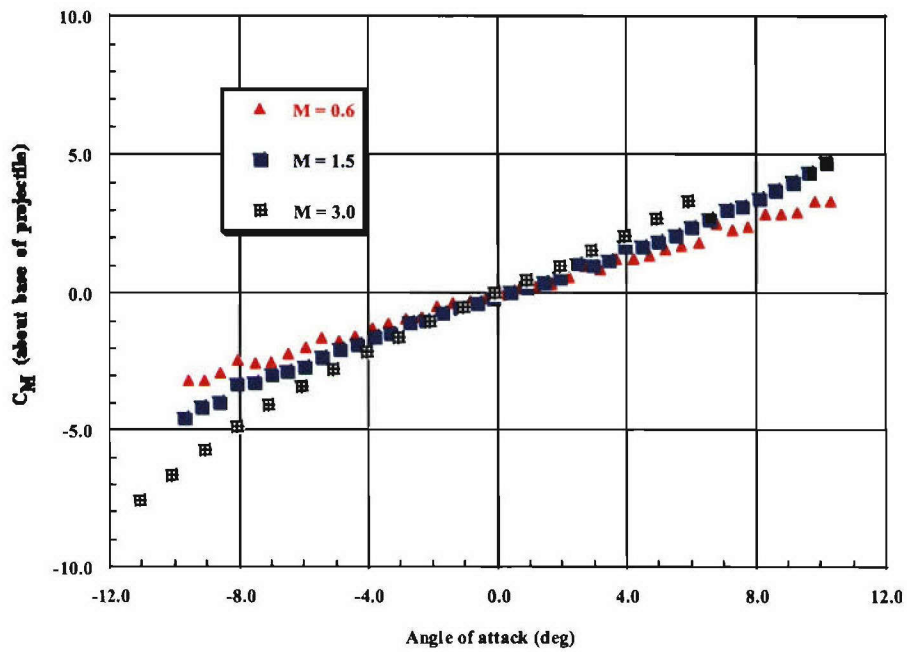
CONFIGURATION: A3\_2 ;  $\phi = 0.0^\circ$



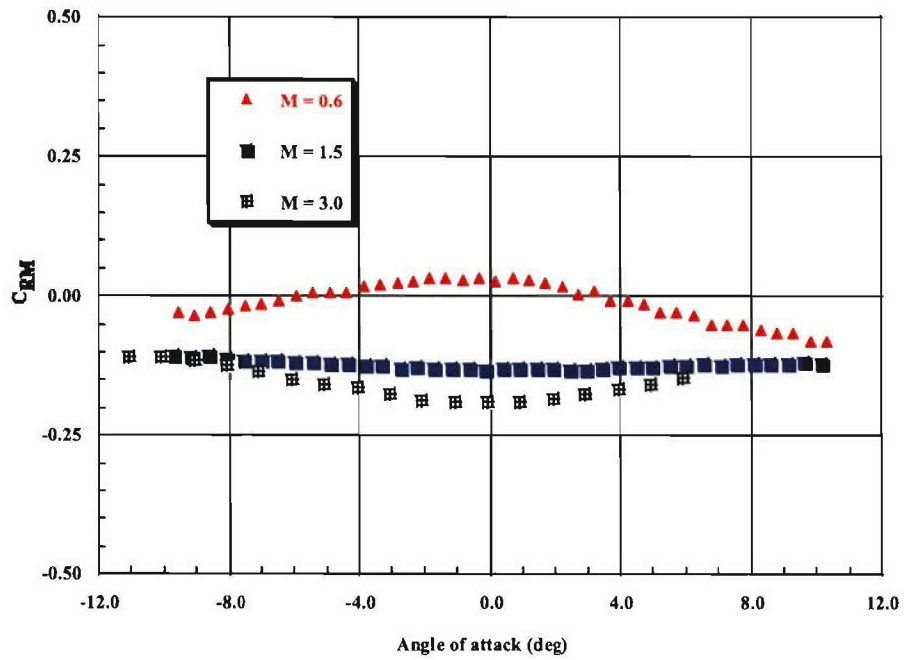
CONFIGURATION: A3\_2 ;  $\phi = 45.0^\circ$



CONFIGURATION: A3\_2 ;  $\phi = 45.0^\circ$

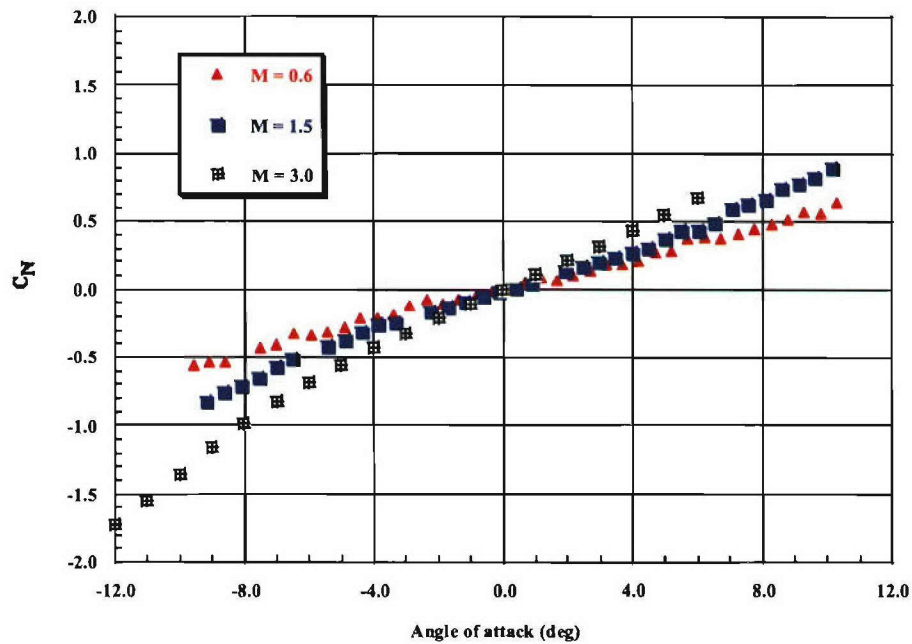
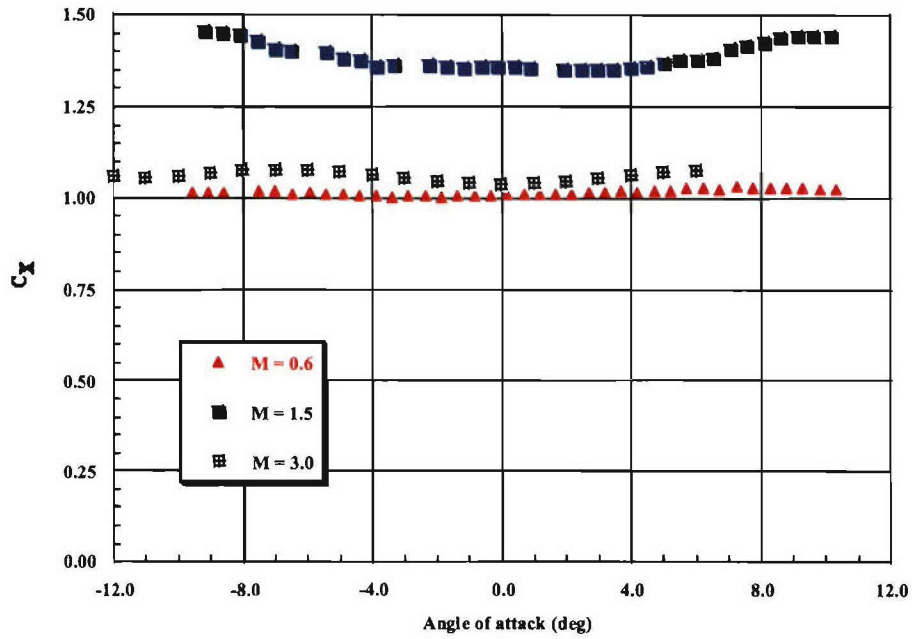


CONFIGURATION: A3\_2 ;  $\phi = 45.0^\circ$

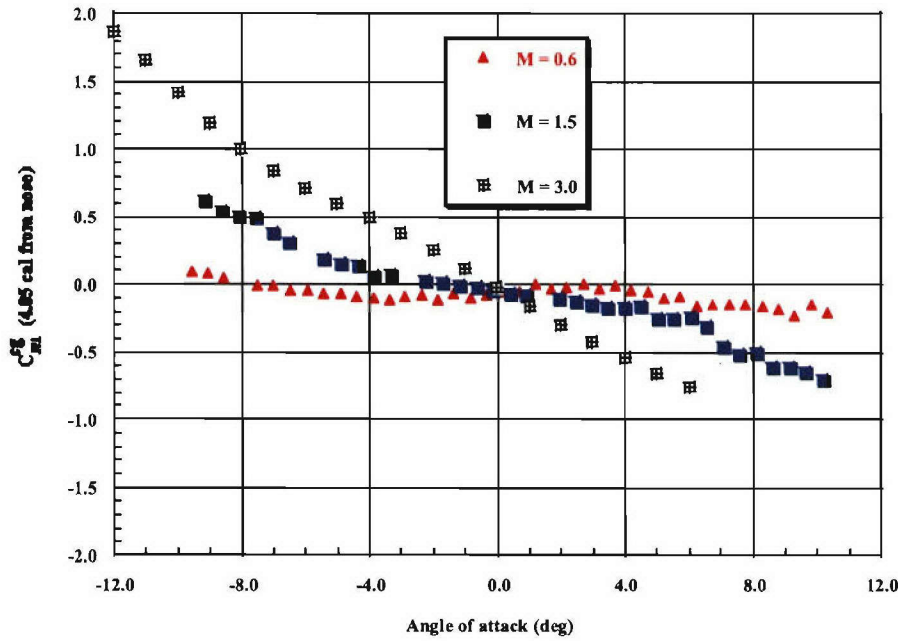
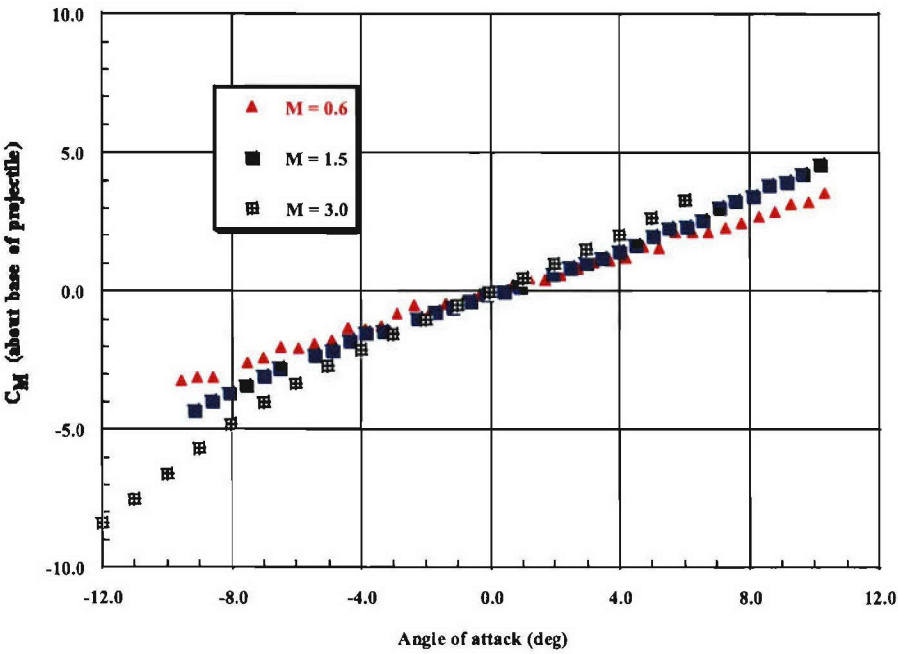




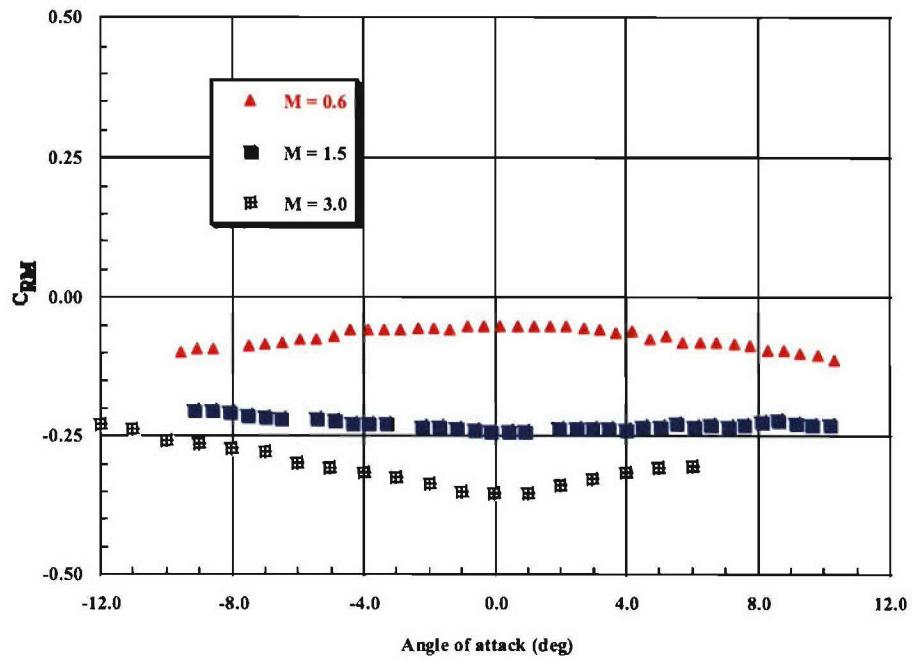
CONFIGURATION: A3\_3 ;  $\phi = 0.0^\circ$



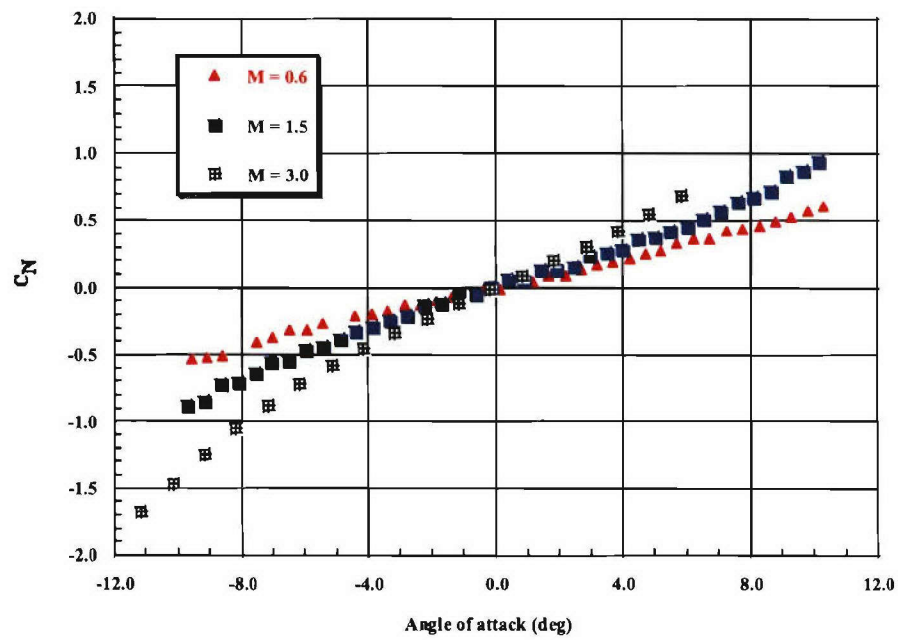
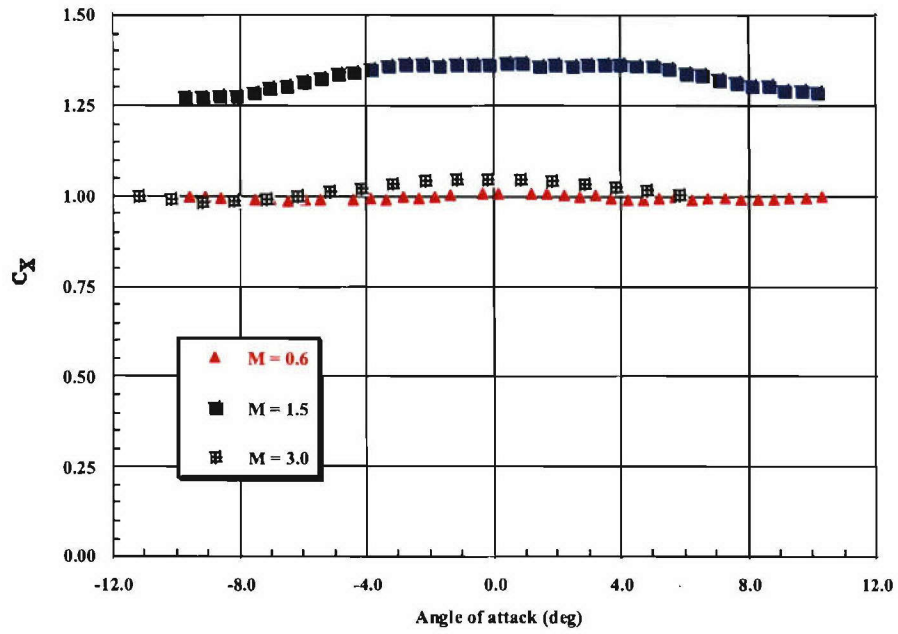
CONFIGURATION: A3\_3 ;  $\phi = 0.0^\circ$



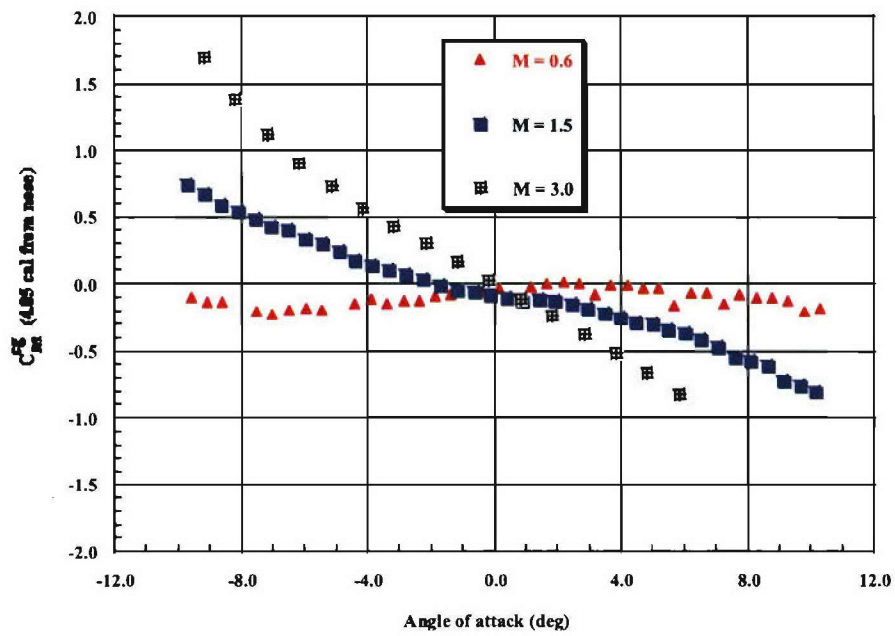
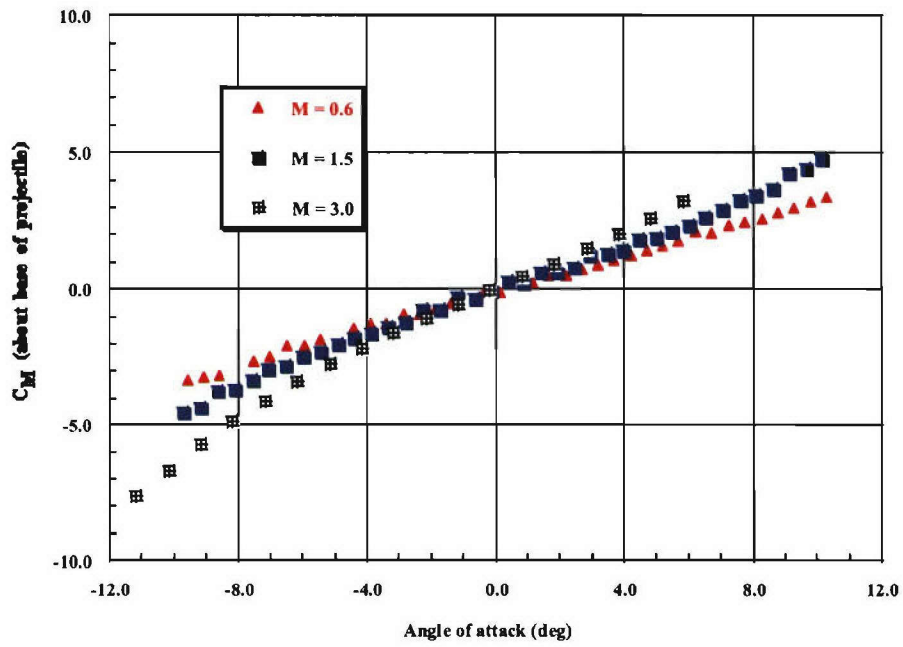
CONFIGURATION: A3\_3 ;  $\phi = 0.0^\circ$



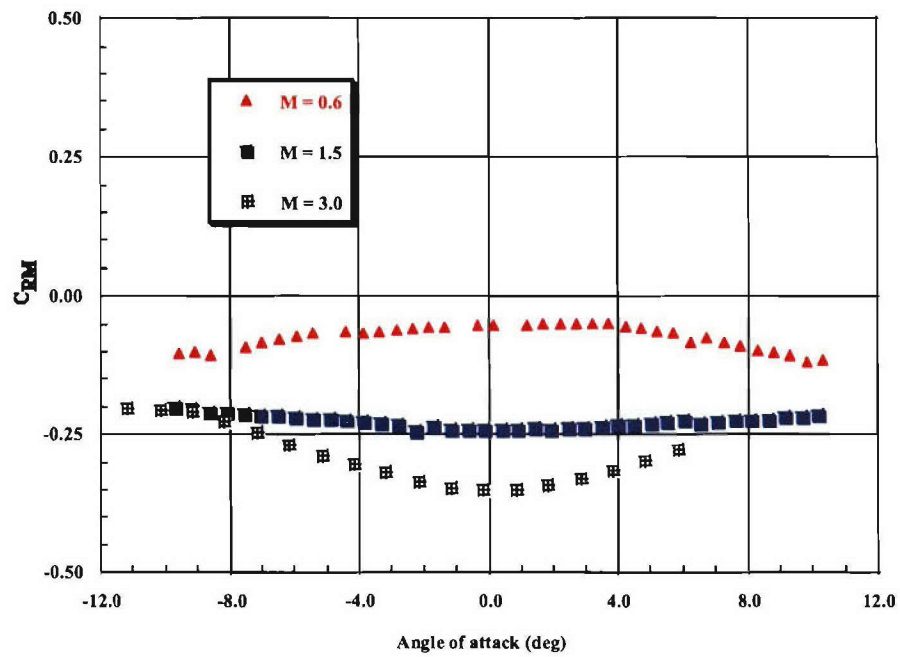
CONFIGURATION: A3\_3 ;  $\phi = 45.0^\circ$



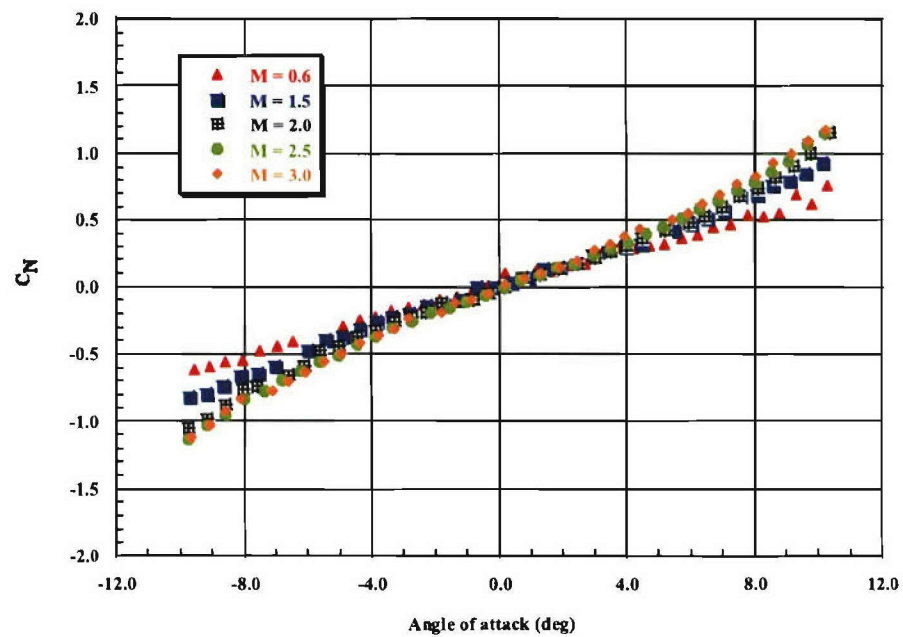
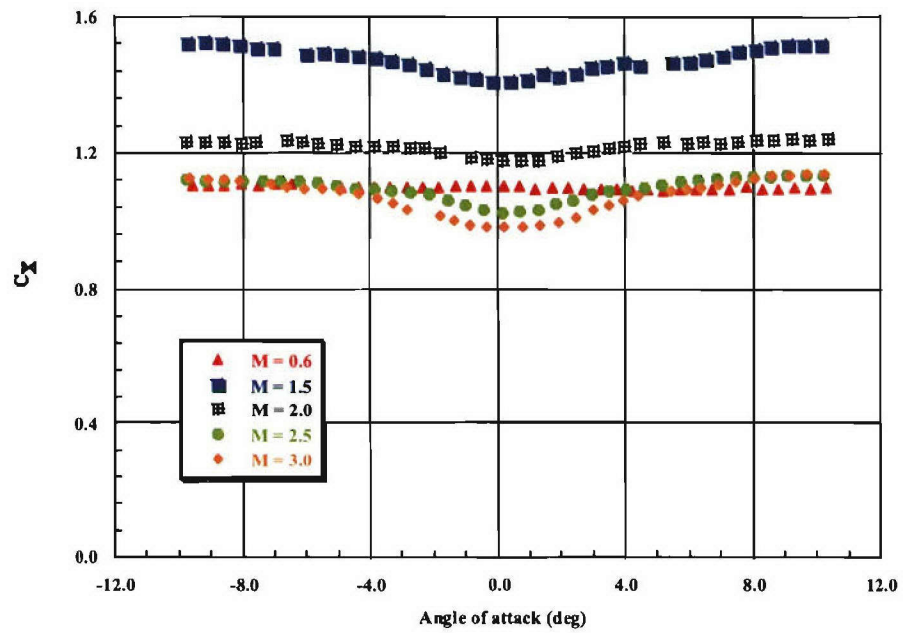
CONFIGURATION: A3\_3 ;  $\phi = 45.0^\circ$



CONFIGURATION: A3\_3 ;  $\phi = 45.0^\circ$

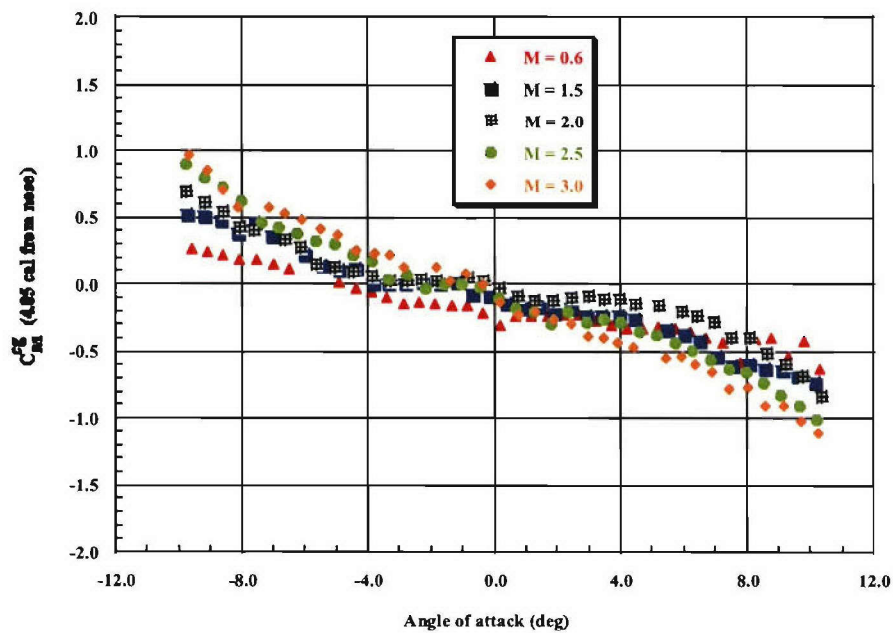
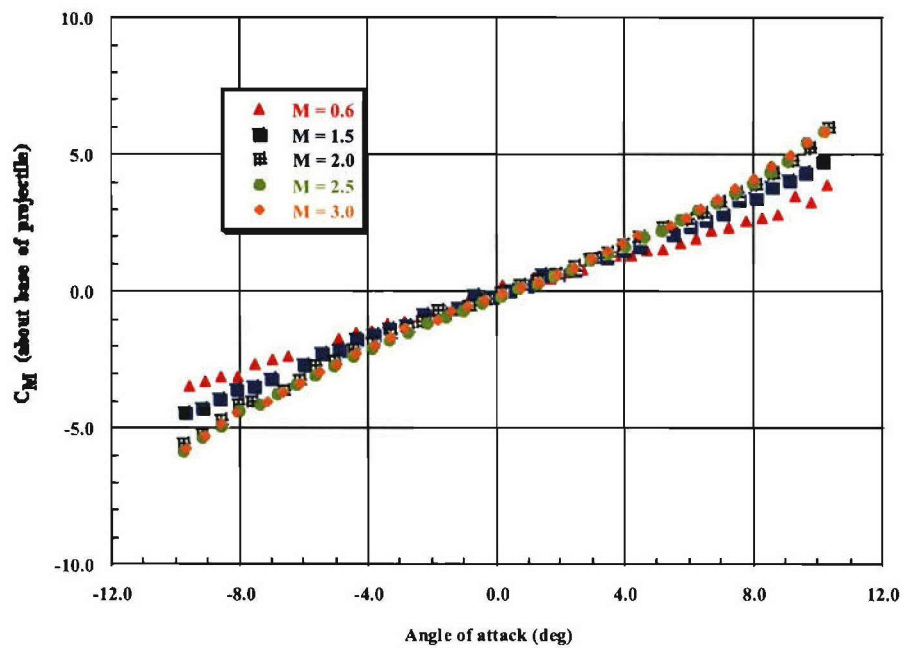


CONFIGURATION: A3\_4 ;  $\phi = 0.0^\circ$

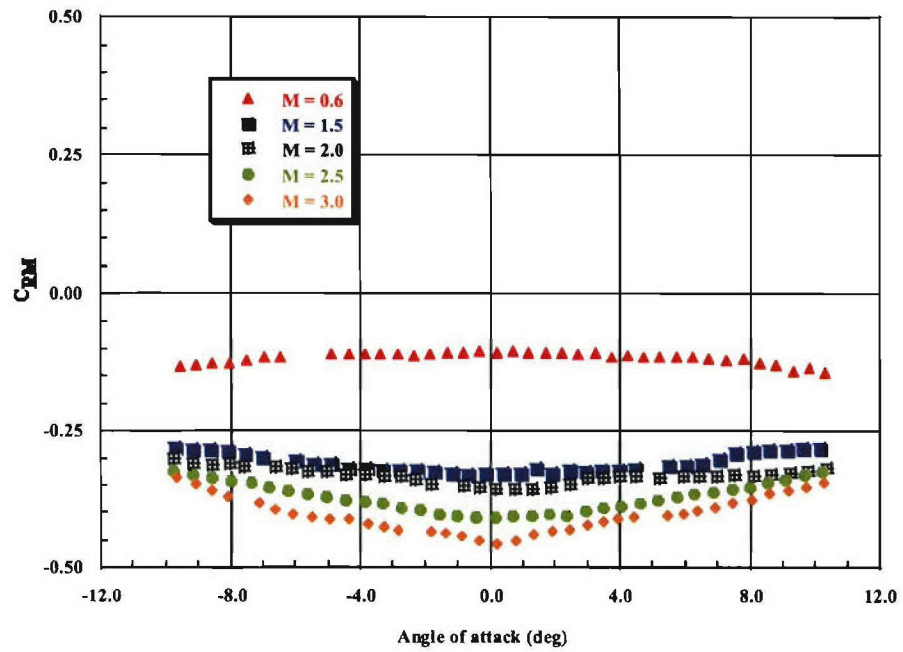




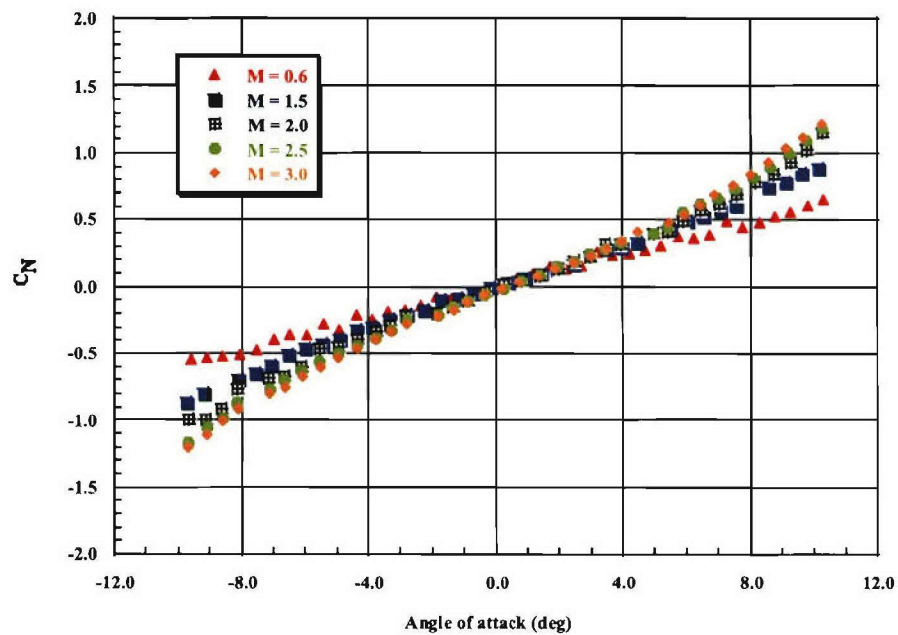
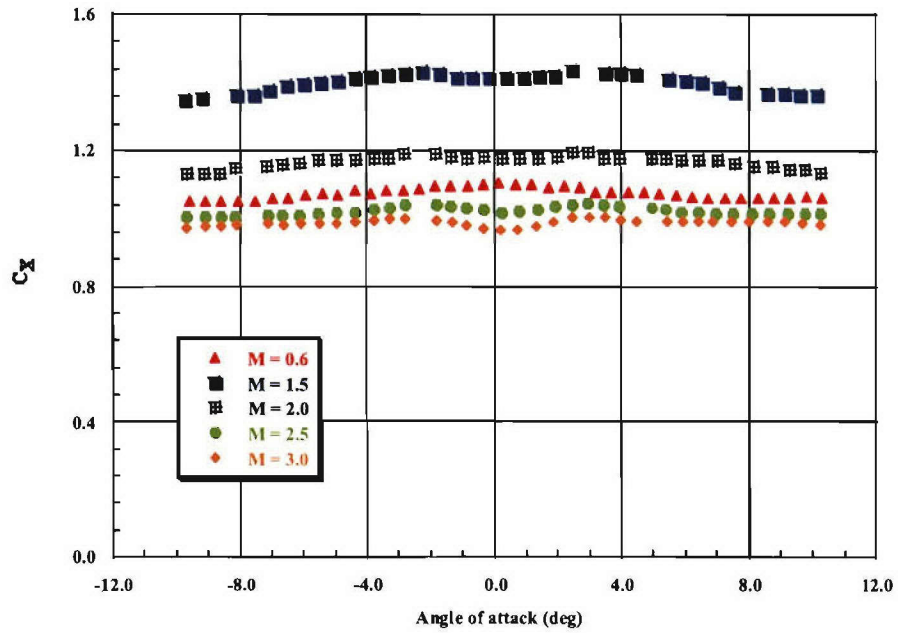
CONFIGURATION: A3\_4 ;  $\phi = 0.0^\circ$



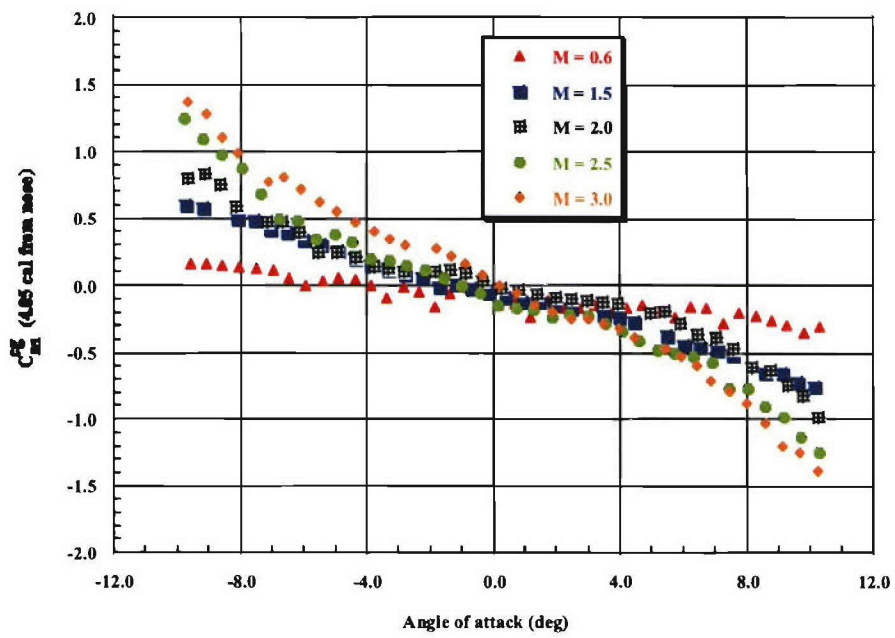
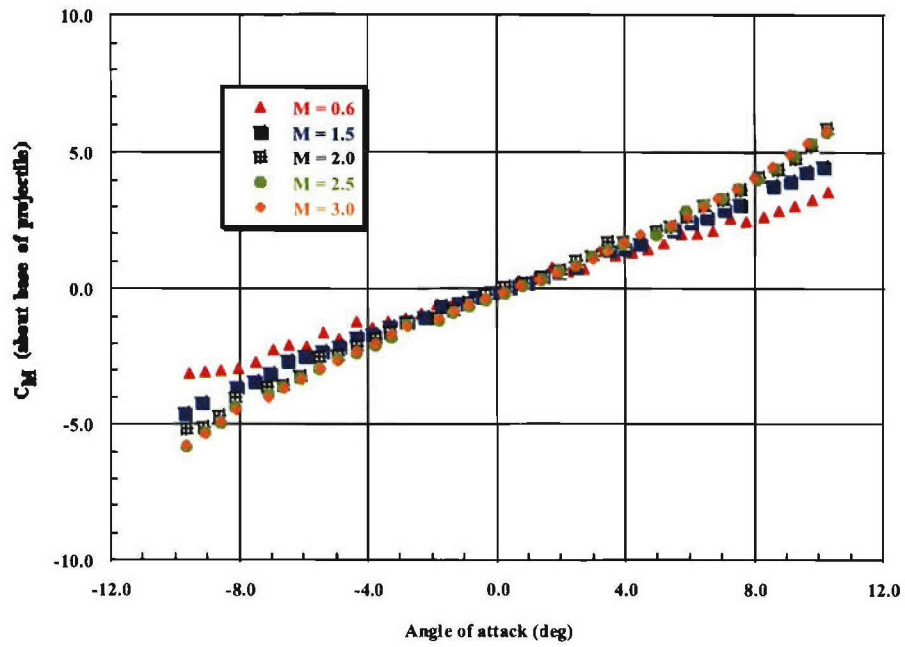
CONFIGURATION: A3\_4 ;  $\phi = 0.0^\circ$



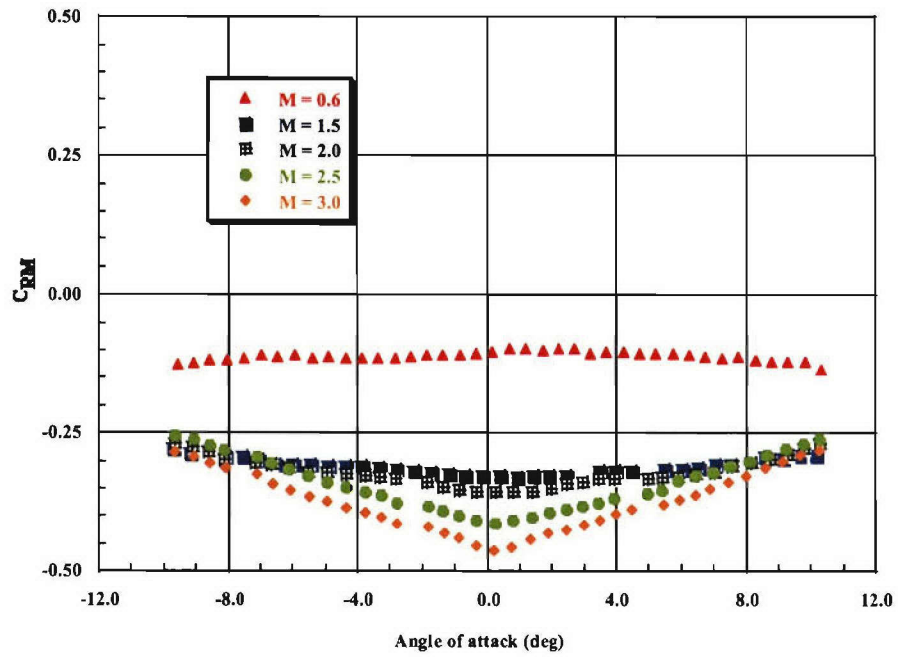
CONFIGURATION: A3\_4 ;  $\phi = 45.0^\circ$



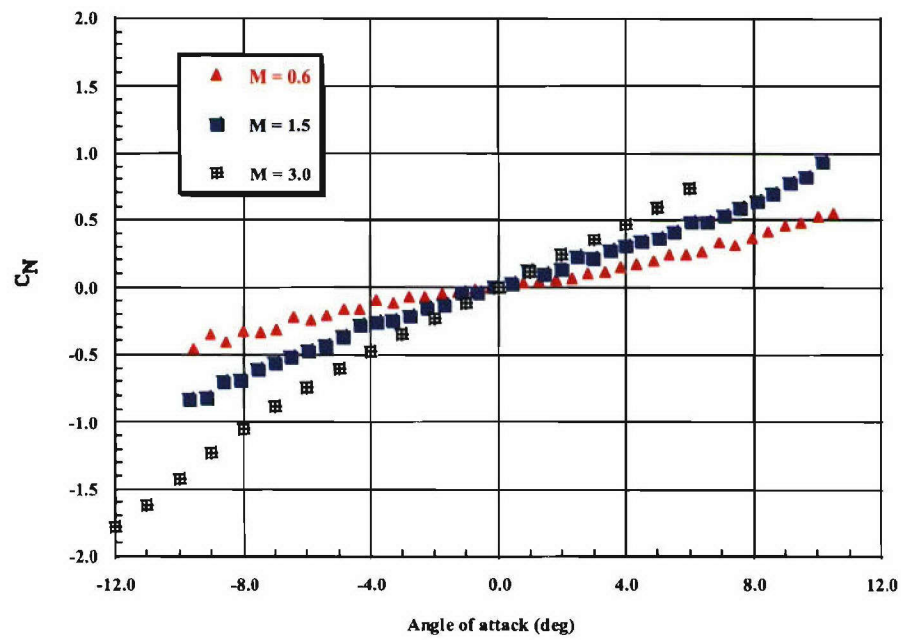
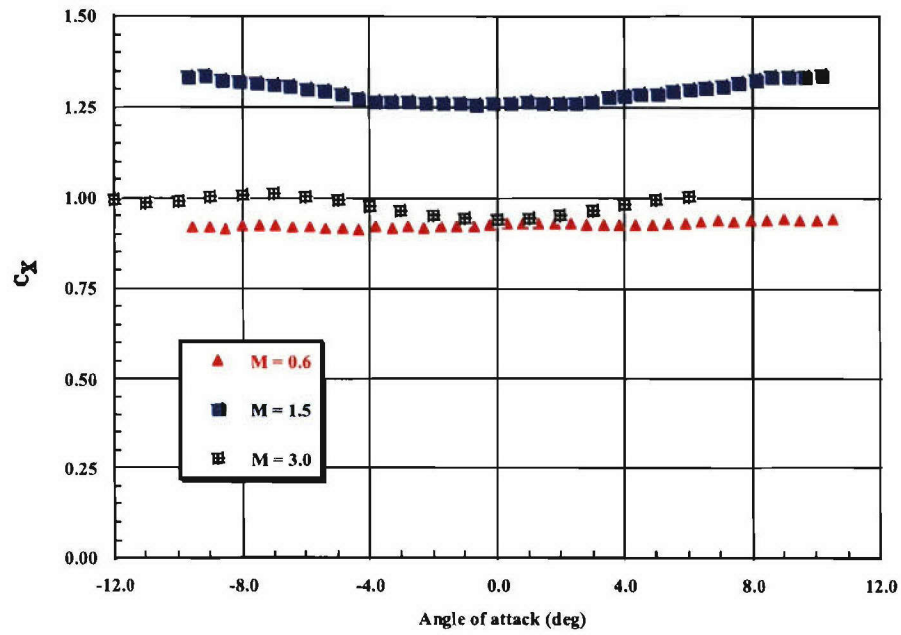
CONFIGURATION: A3\_4 ;  $\phi = 45.0^\circ$



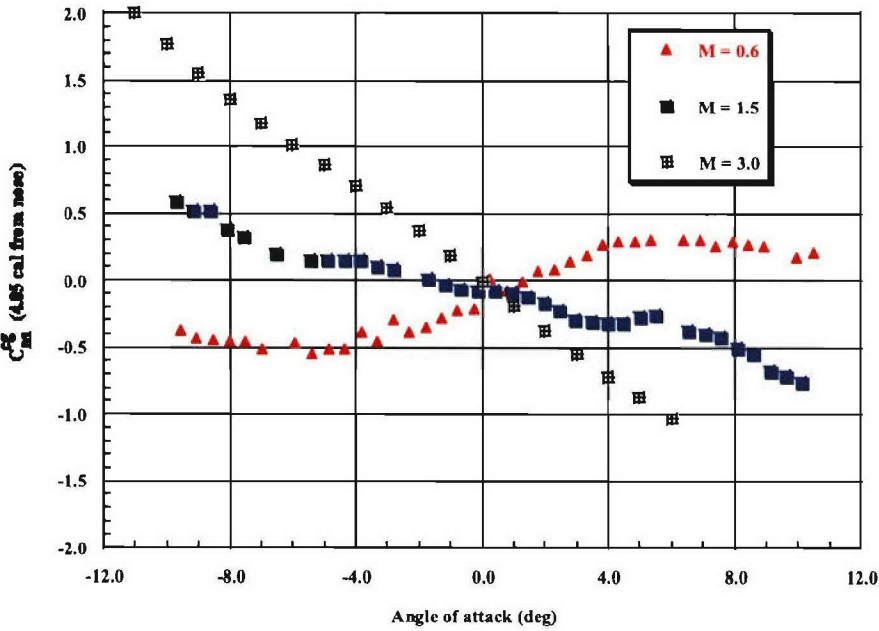
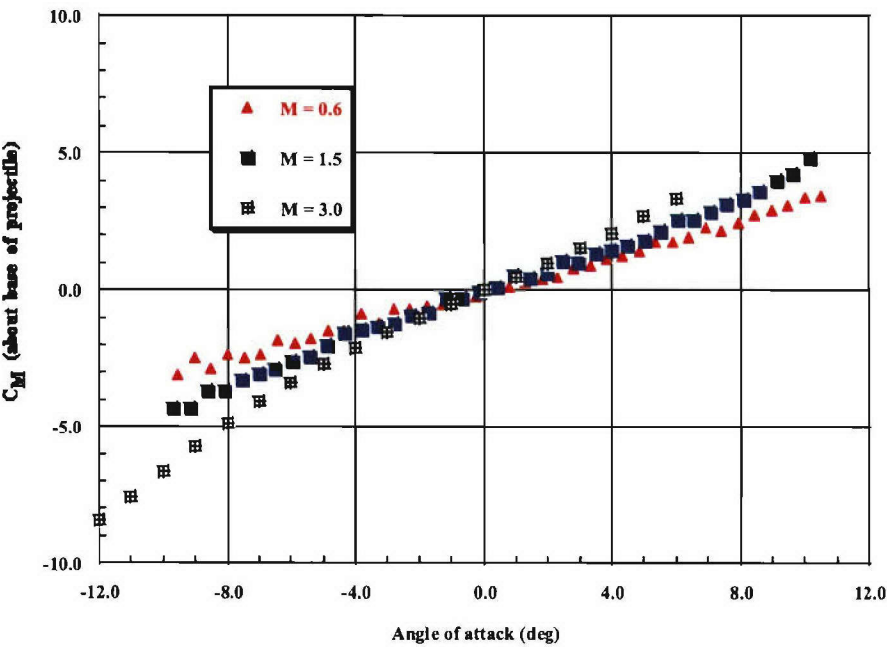
CONFIGURATION: A3\_4 ;  $\phi = 45.0^\circ$



CONFIGURATION: A3\_5 ;  $\phi = 0.0^\circ$

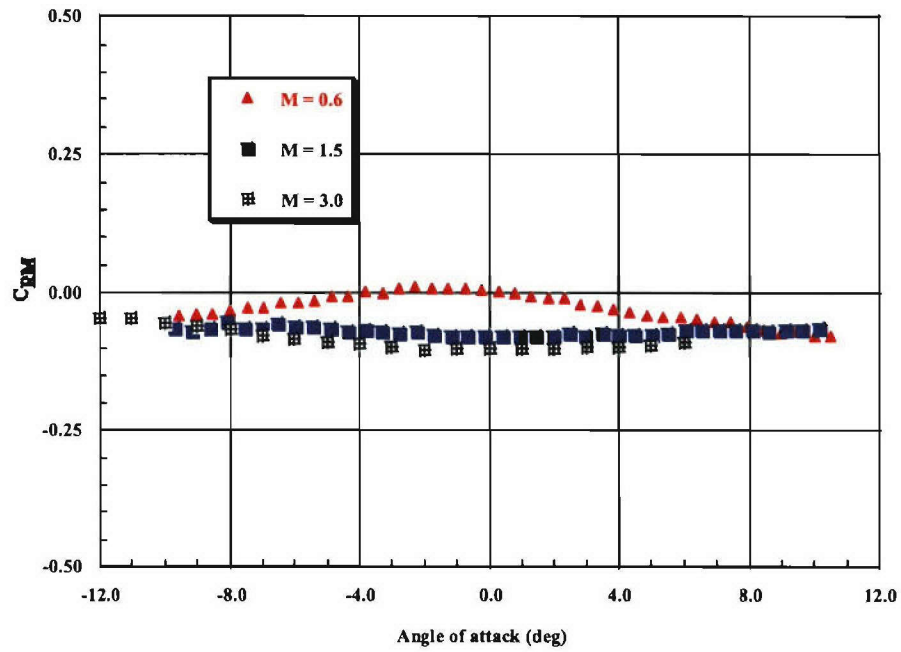


CONFIGURATION: A3\_5 ;  $\phi = 0.0^\circ$

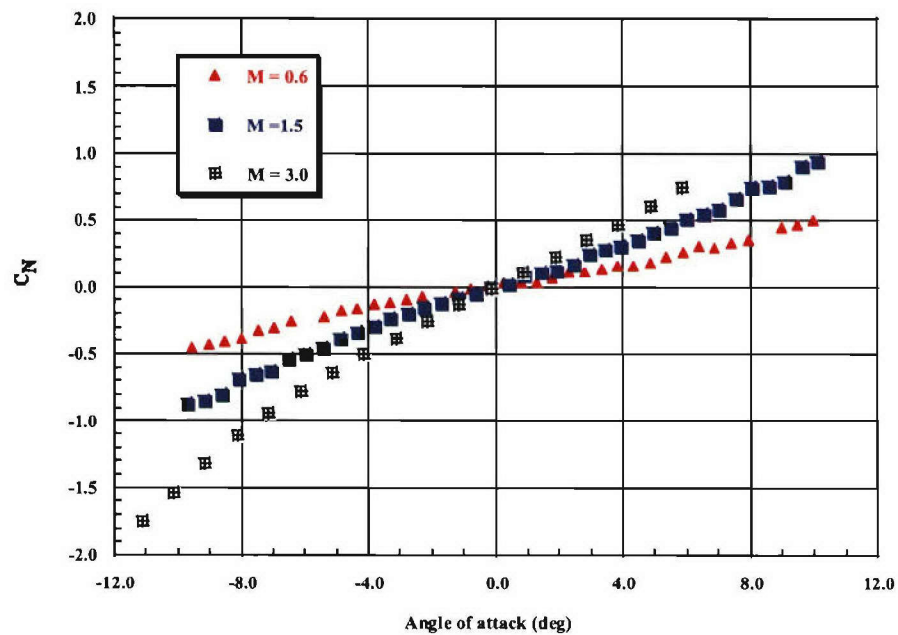
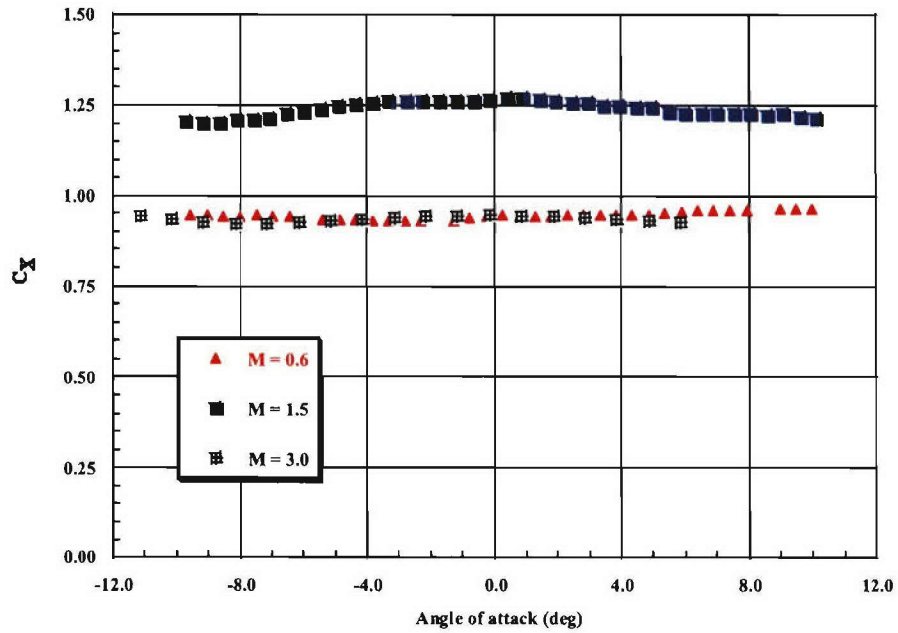




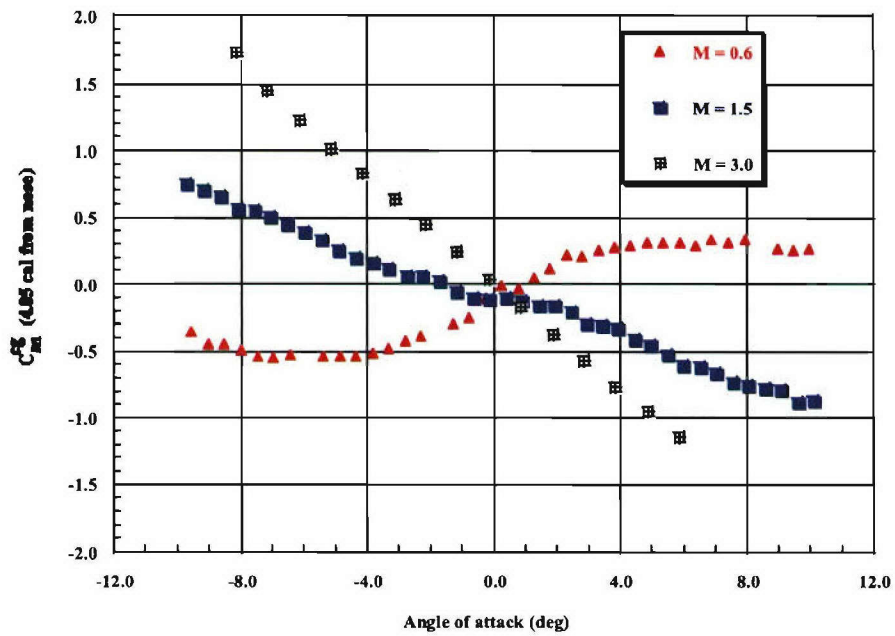
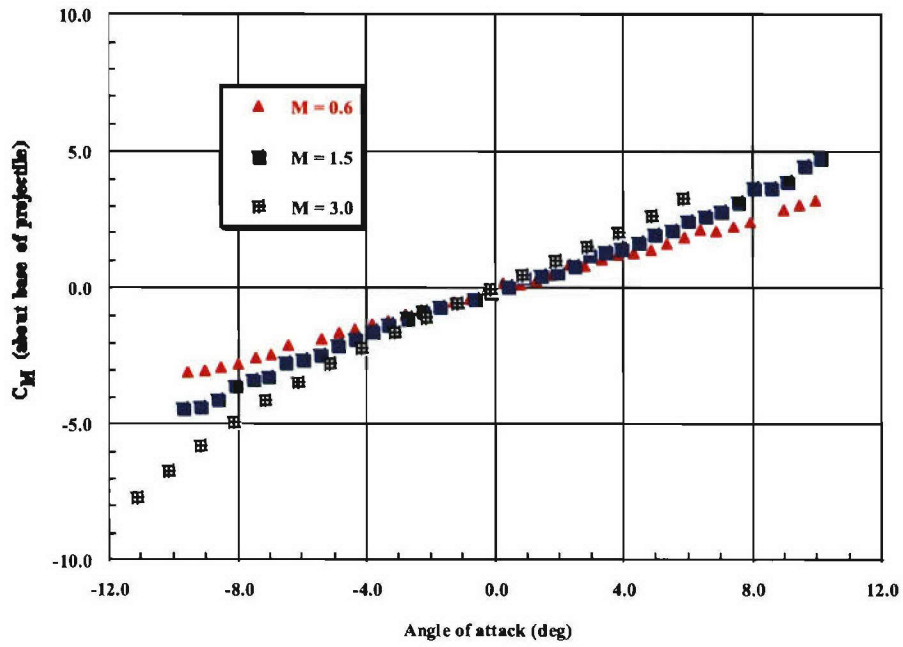
CONFIGURATION: A3\_5 ;  $\phi = 0.0^\circ$



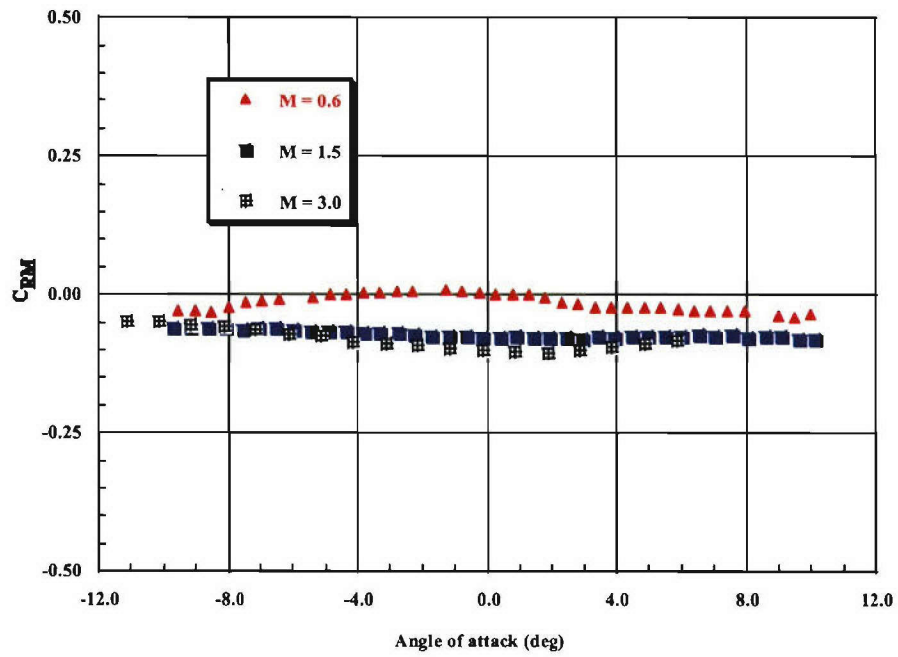
CONFIGURATION: A3\_5 ;  $\phi = 45.0^\circ$



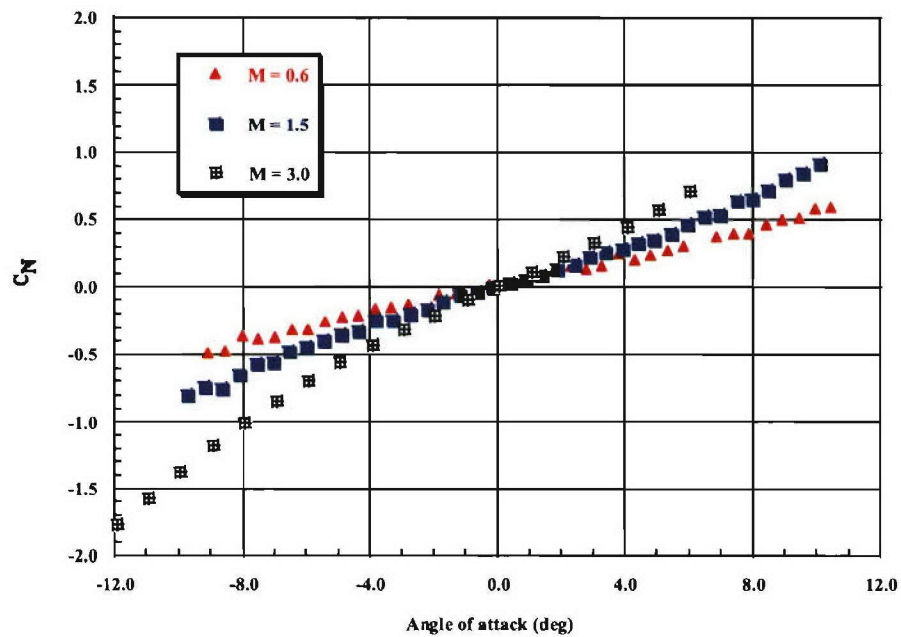
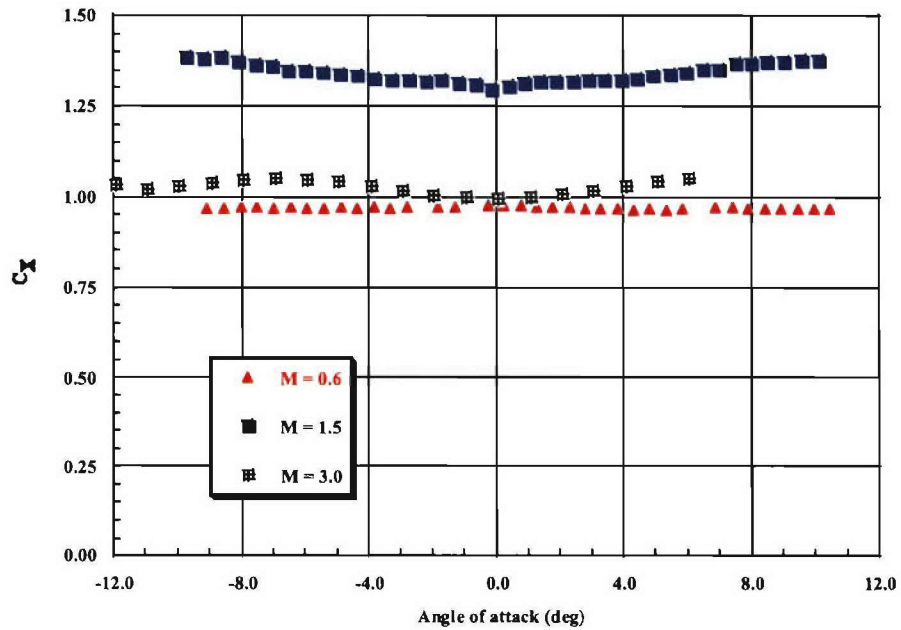
CONFIGURATION: A3\_5 ;  $\phi = 45.0^\circ$



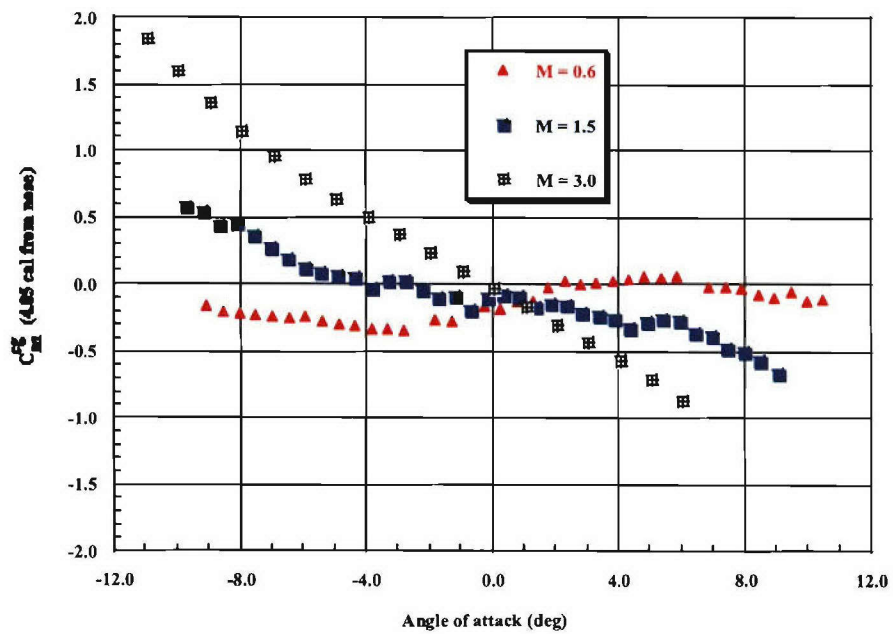
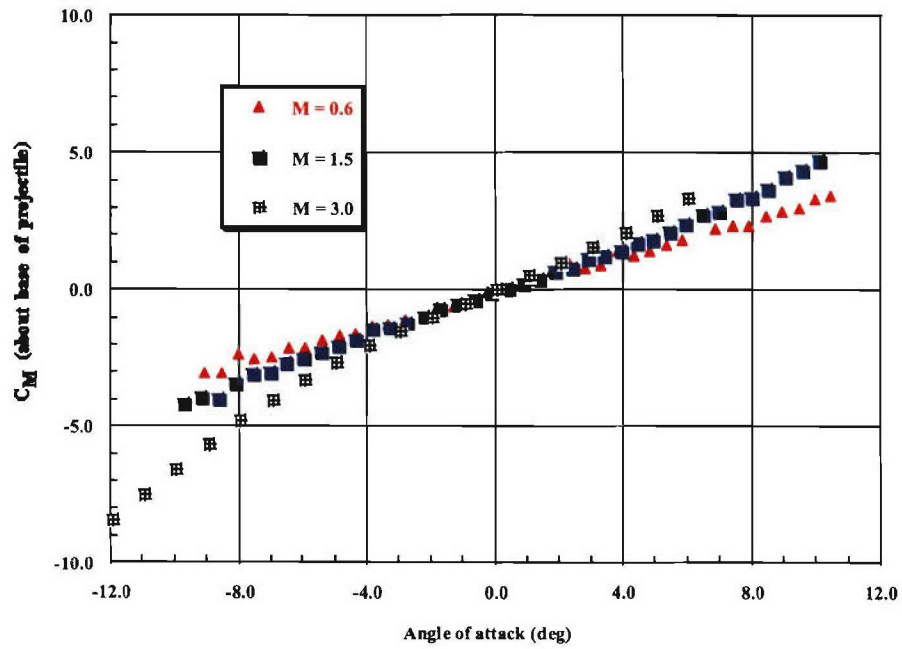
CONFIGURATION: A3\_5 ;  $\phi = 45.0^\circ$



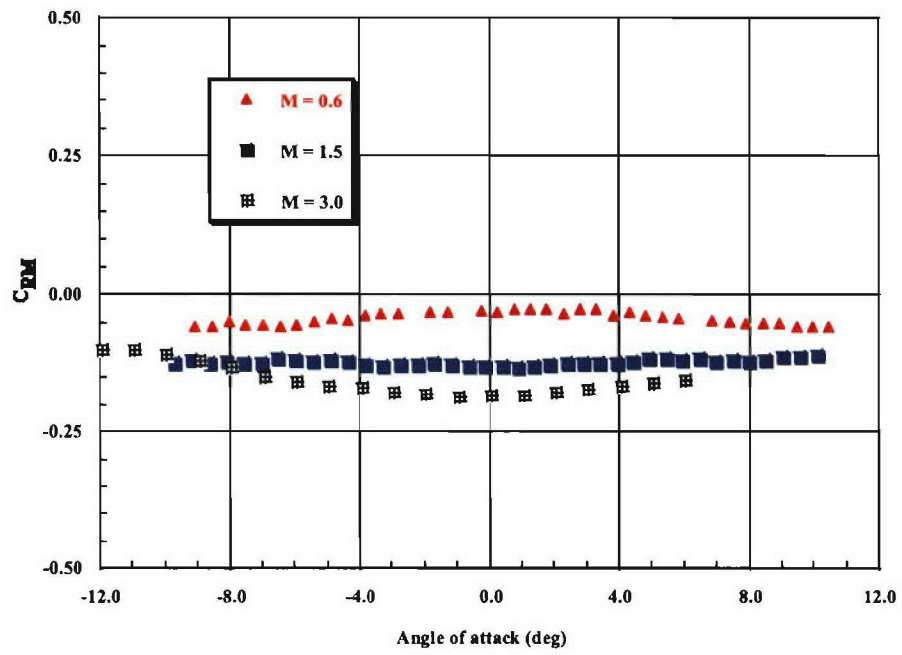
CONFIGURATION: A3\_6 ;  $\phi = 0.0^\circ$



CONFIGURATION: A3\_6 ;  $\phi = 0.0^\circ$

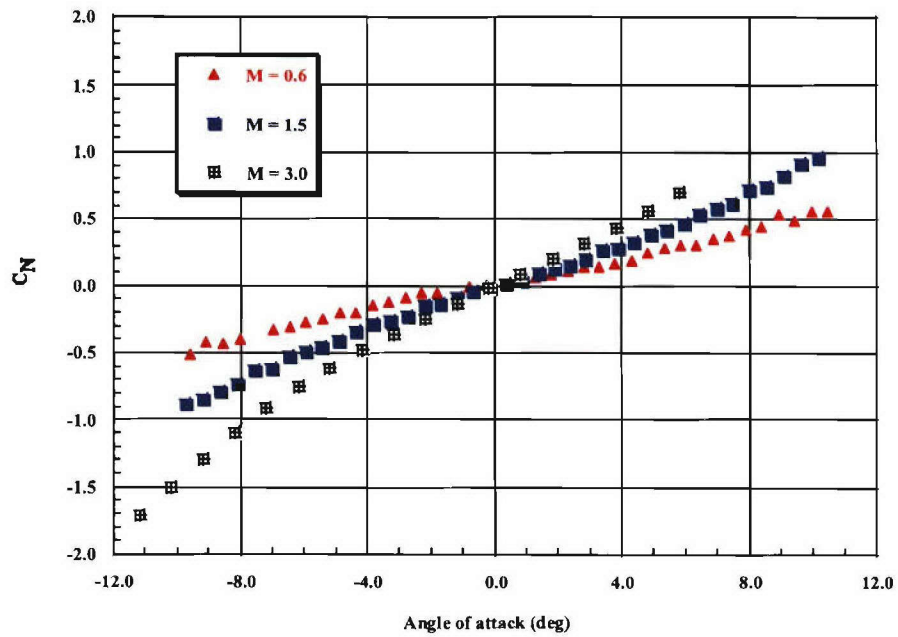
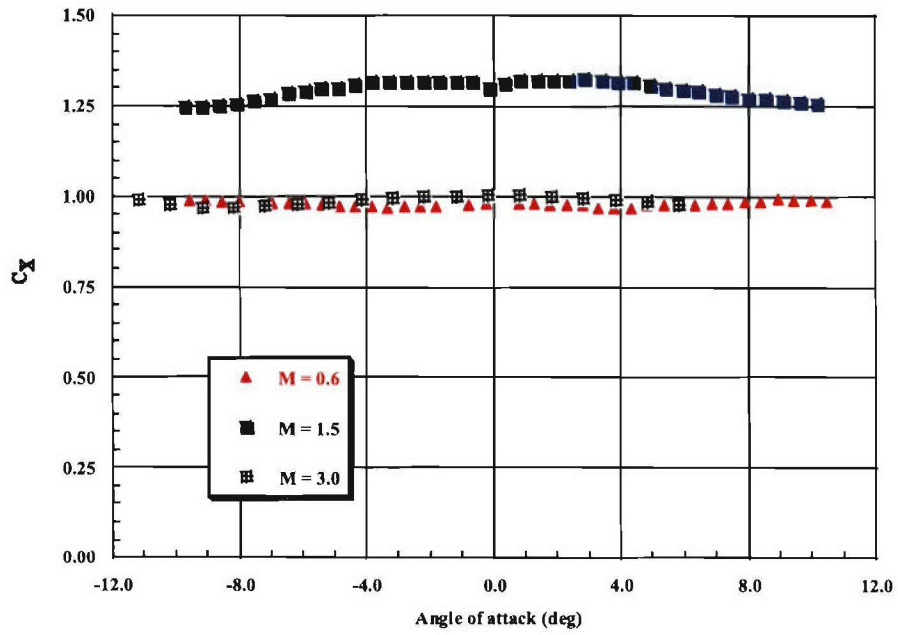


CONFIGURATION: A3\_6 ;  $\phi = 0.0^\circ$

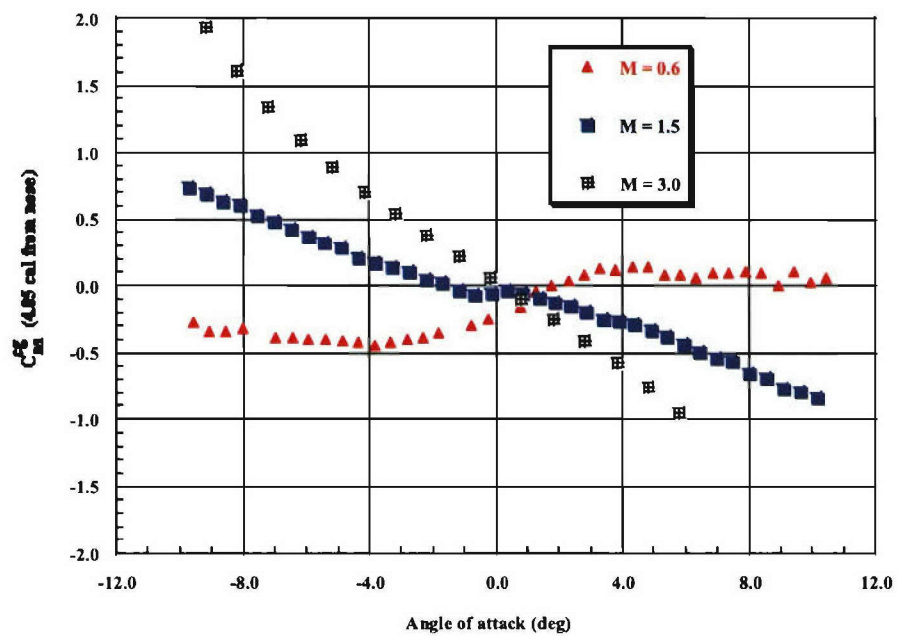
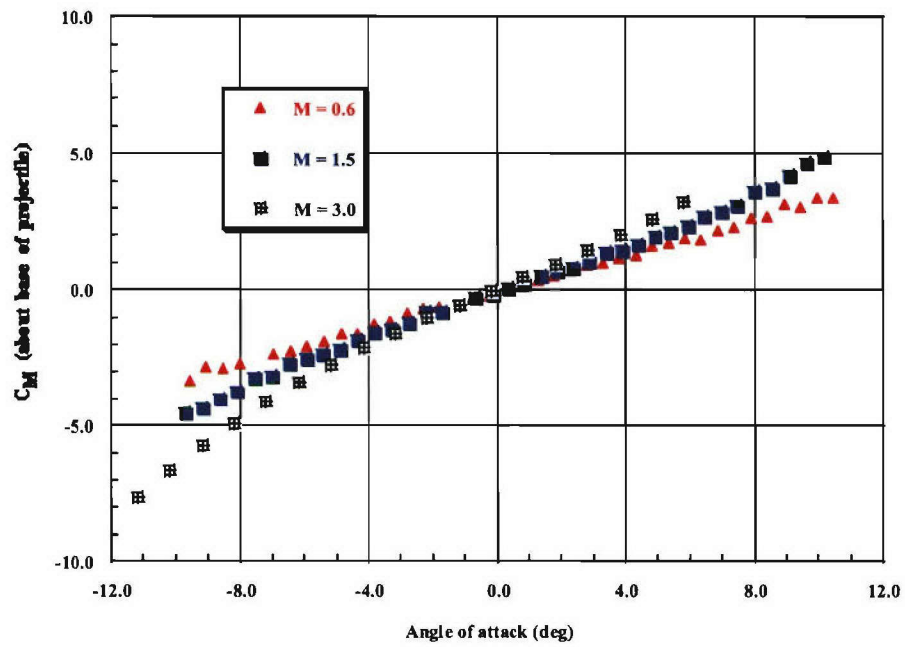




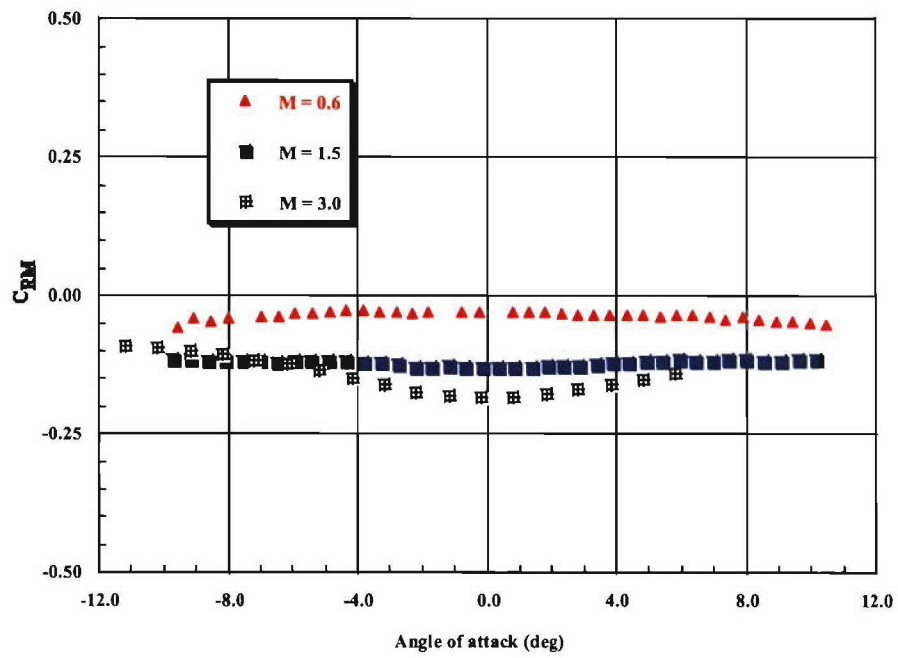
CONFIGURATION: A3\_6 ;  $\phi = 45.0^\circ$



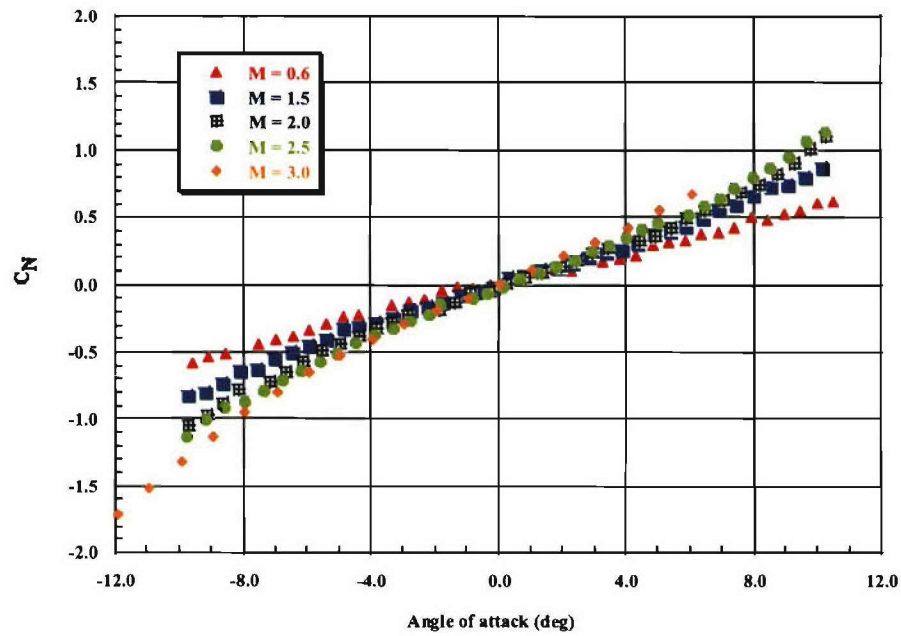
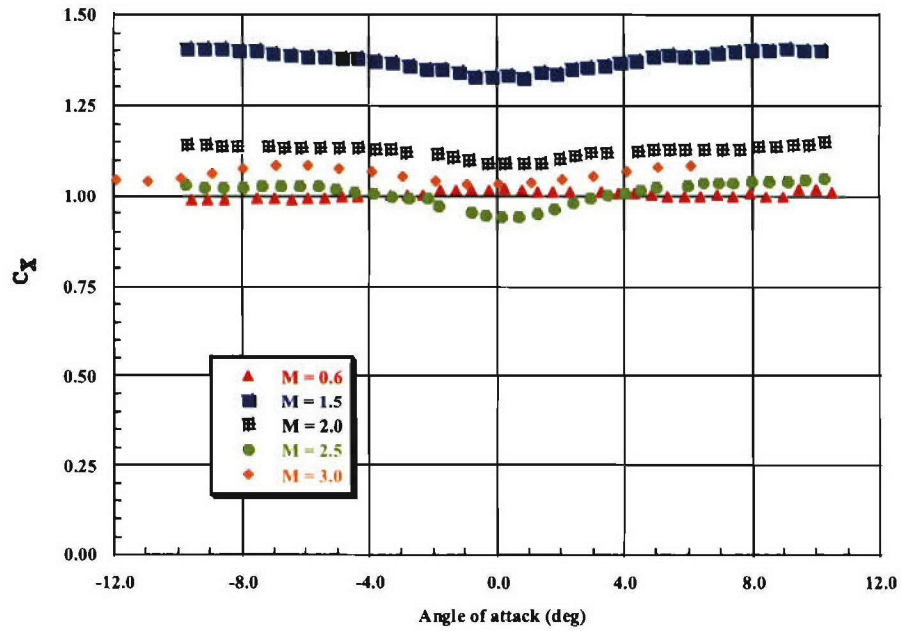
CONFIGURATION: A3\_6 ;  $\phi = 45.0^\circ$



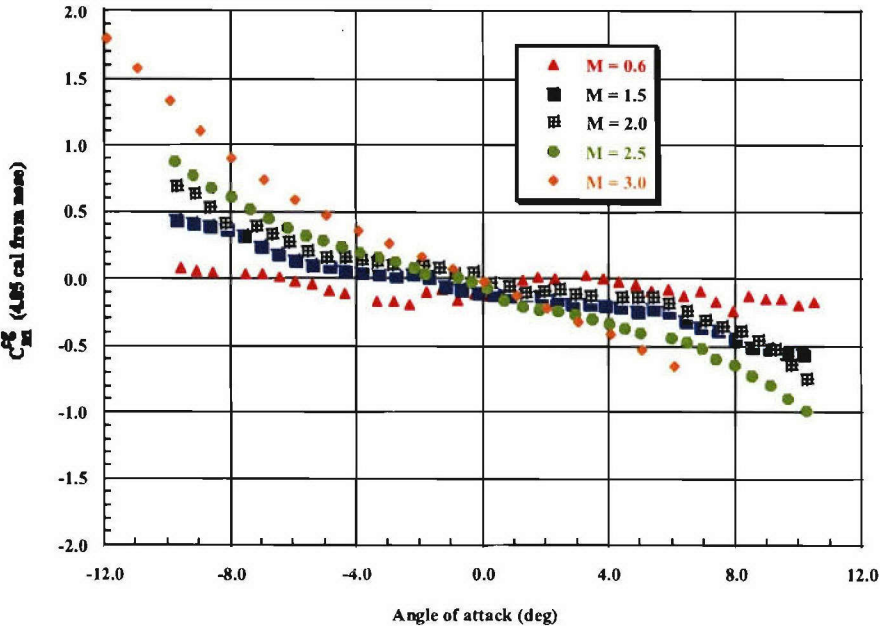
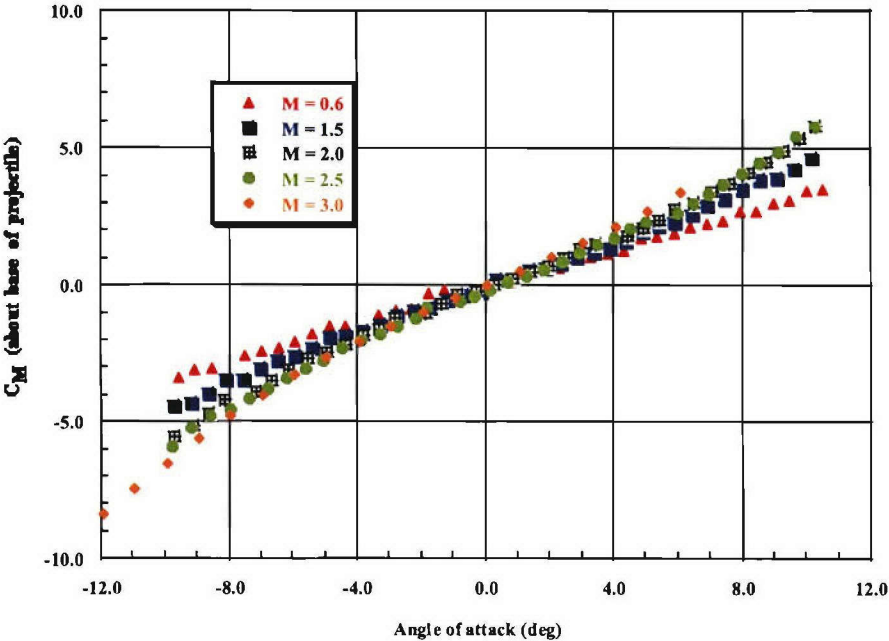
CONFIGURATION: A3\_6 ;  $\phi = 45.0^\circ$



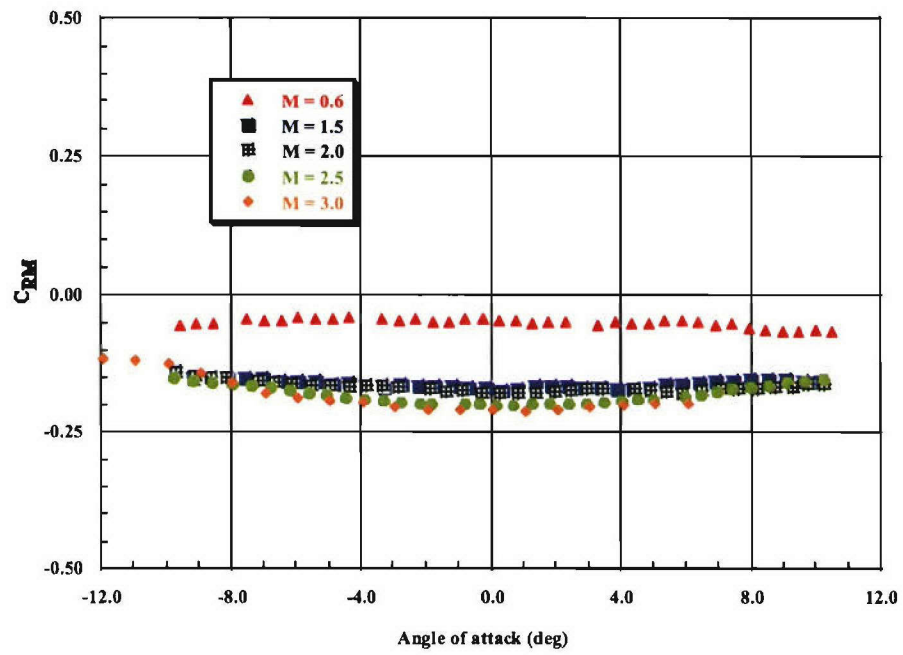
CONFIGURATION: A3\_7 ;  $\phi = 0.0^\circ$



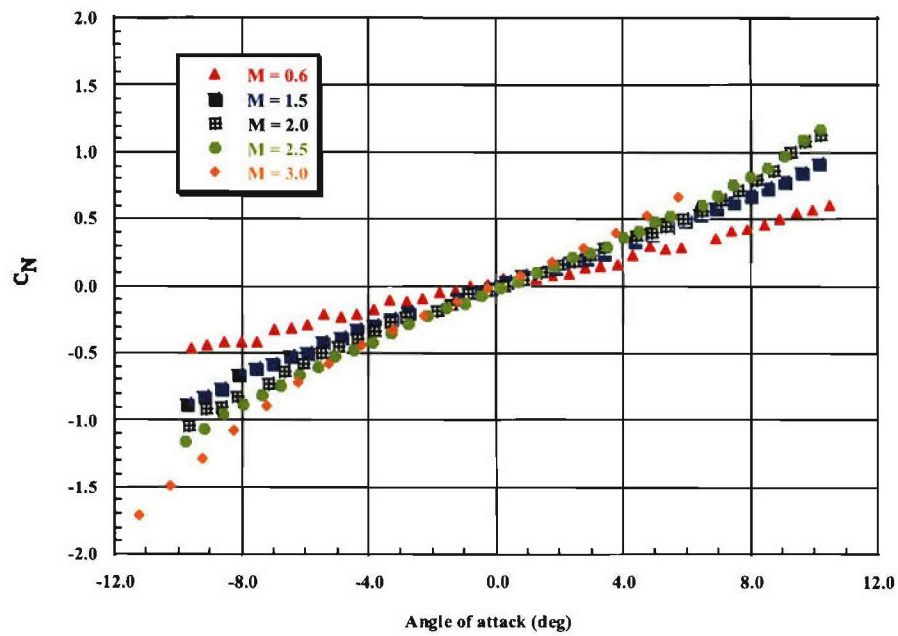
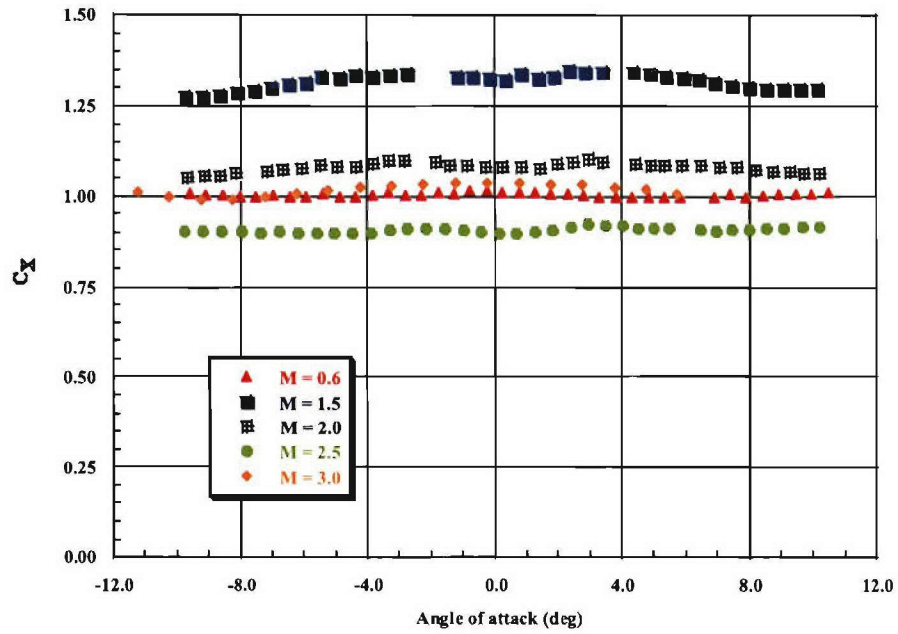
CONFIGURATION: A3\_7 ;  $\phi = 0.0^\circ$



CONFIGURATION: A3\_7 ;  $\phi = 0.0^\circ$

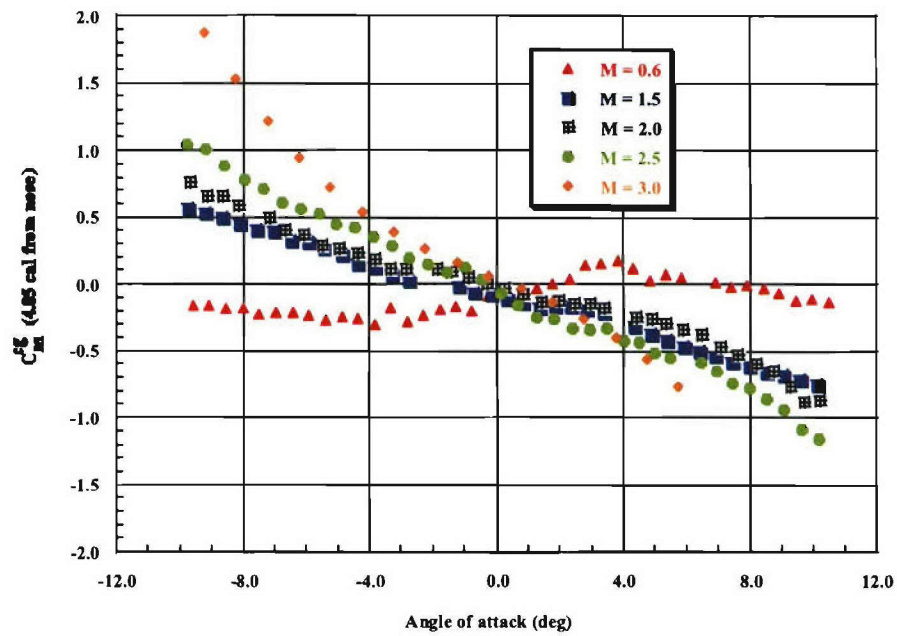
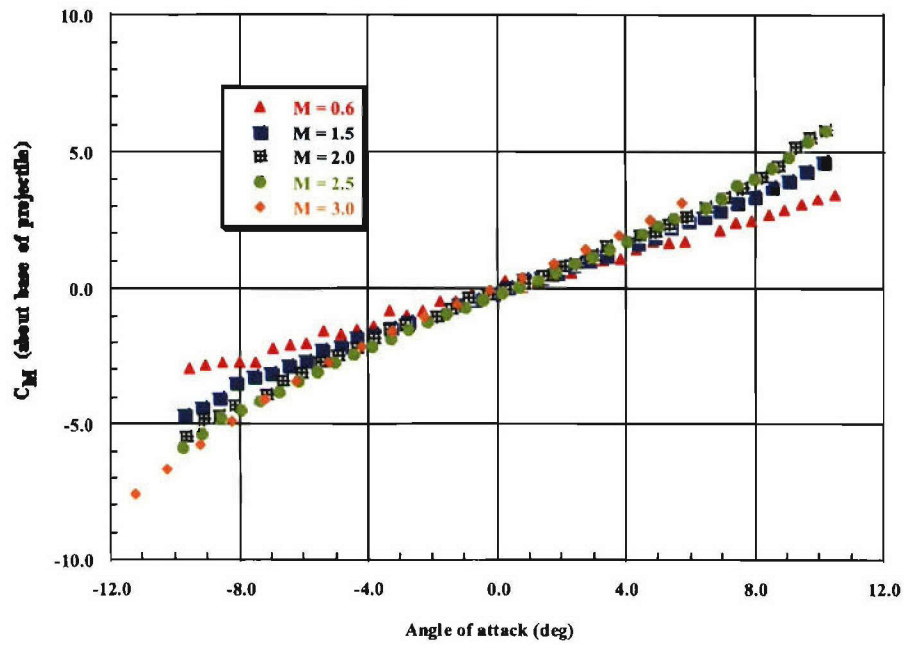


CONFIGURATION: A3\_7 ;  $\phi = 45.0^\circ$

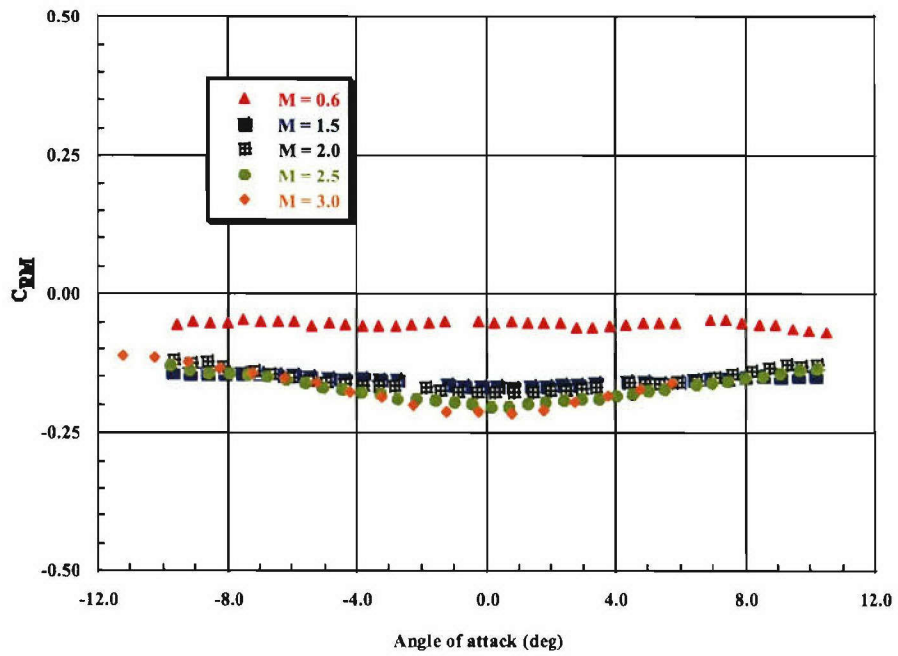




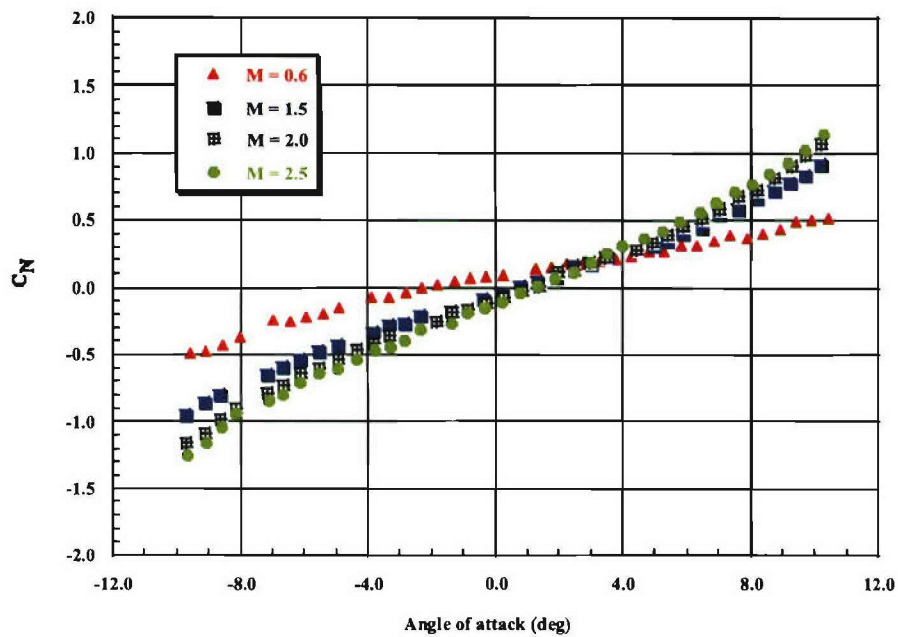
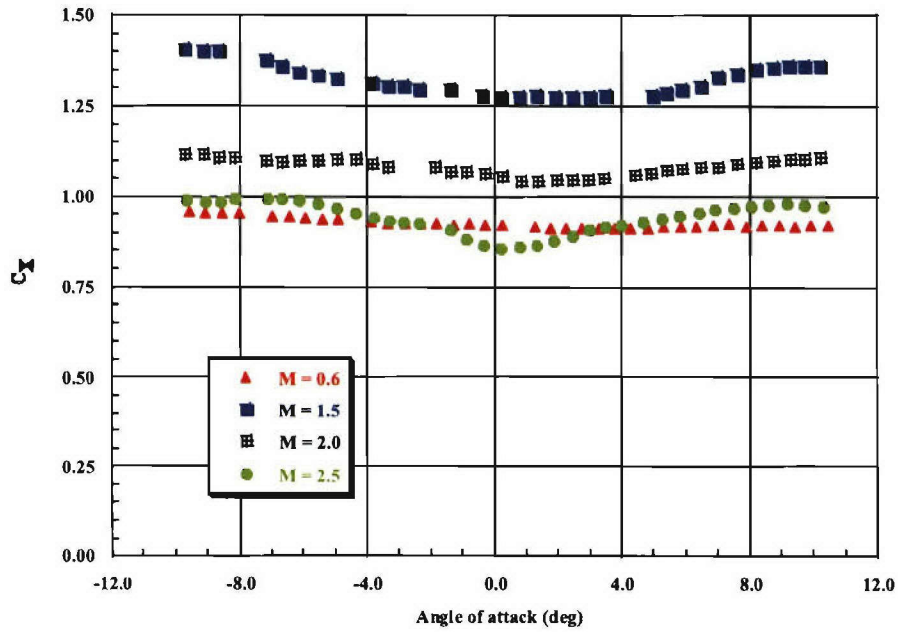
CONFIGURATION: A3\_7 ;  $\phi = 45.0^\circ$



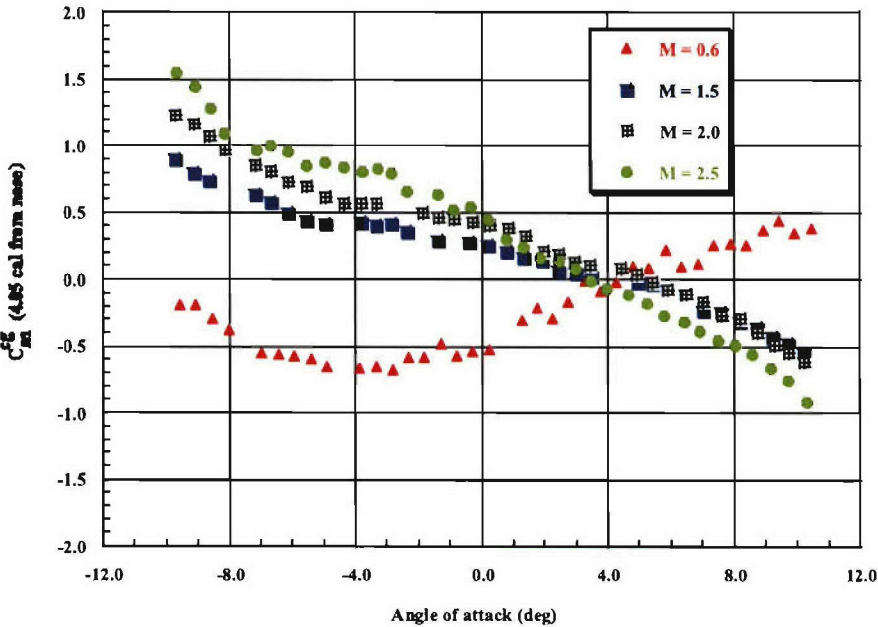
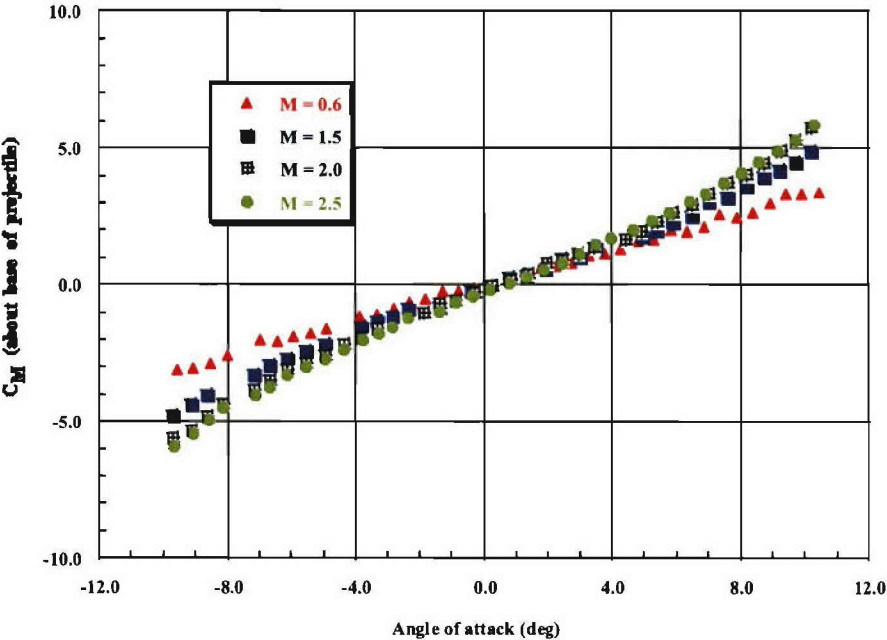
CONFIGURATION: A3\_7 ;  $\phi = 45.0^\circ$



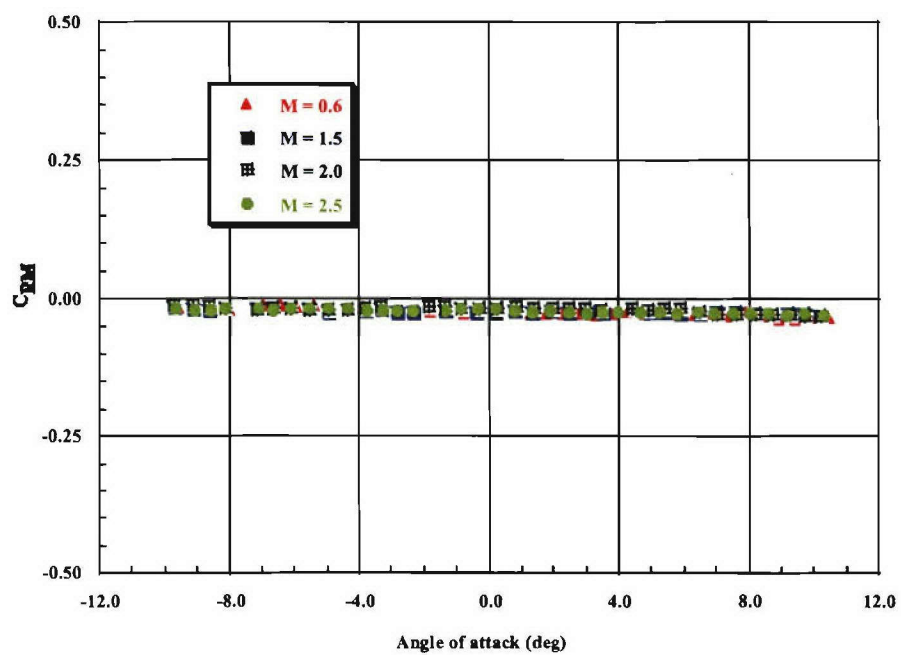
CONFIGURATION: A3\_8 ;  $\phi = 0.0^\circ$



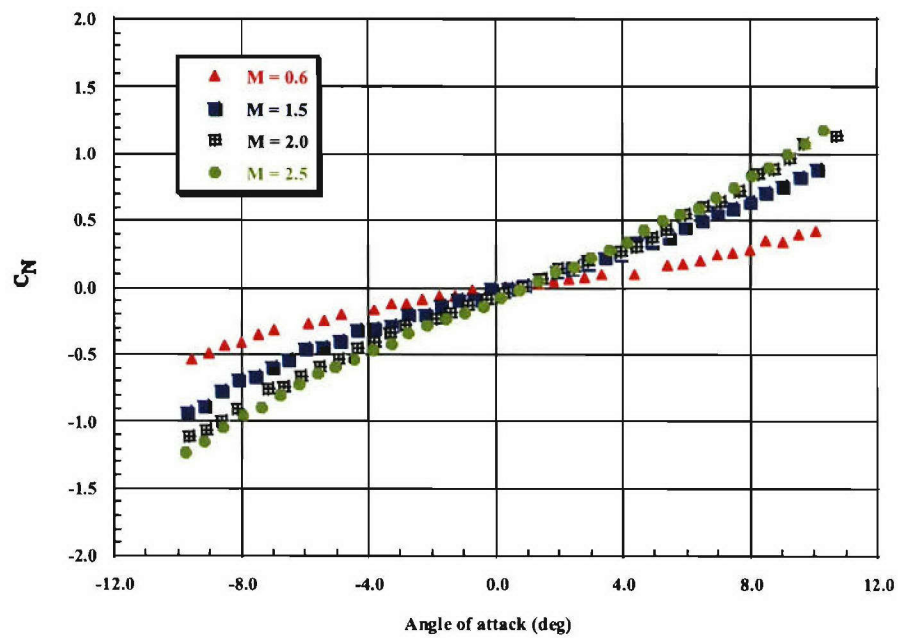
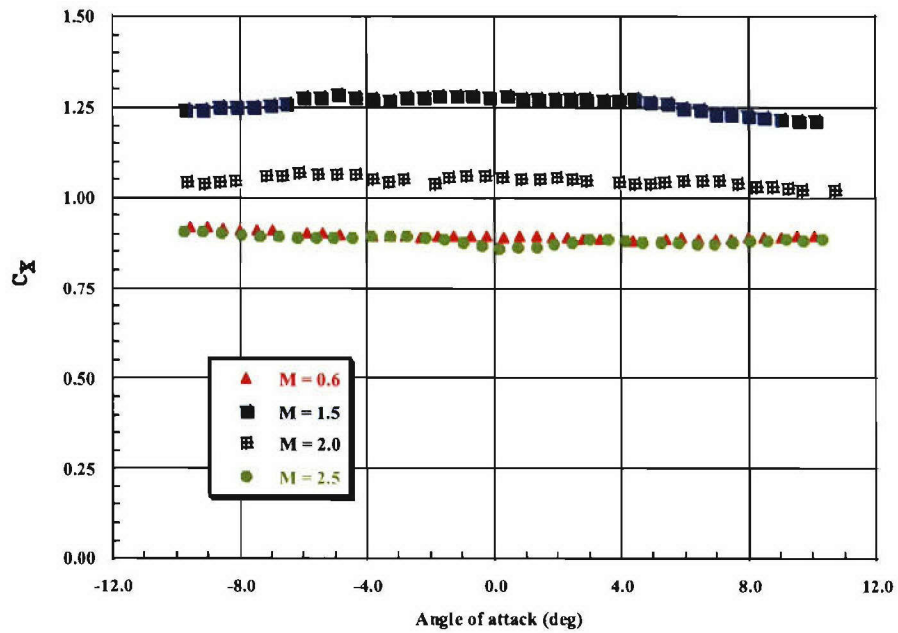
CONFIGURATION: A3\_8 ;  $\phi = 0.0^\circ$



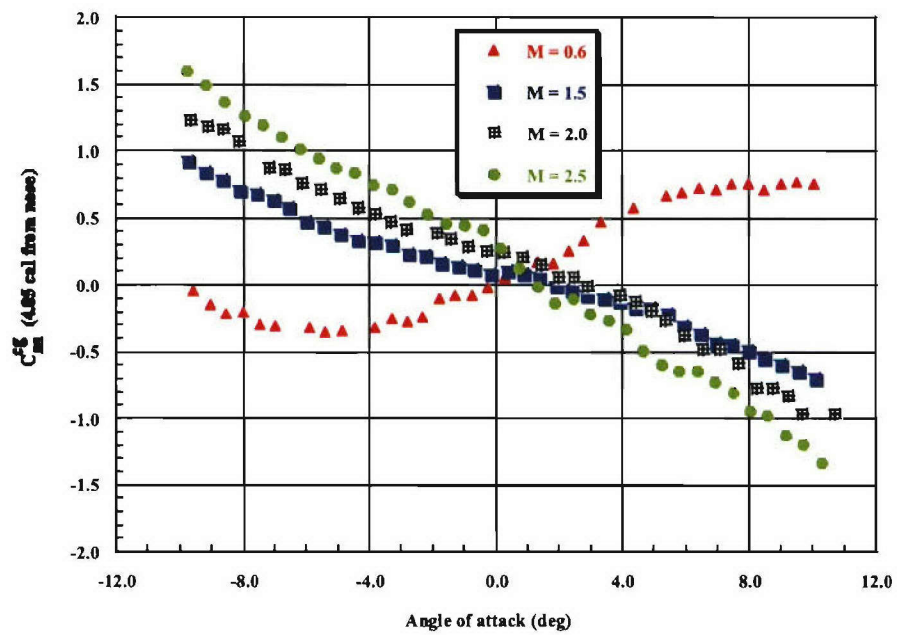
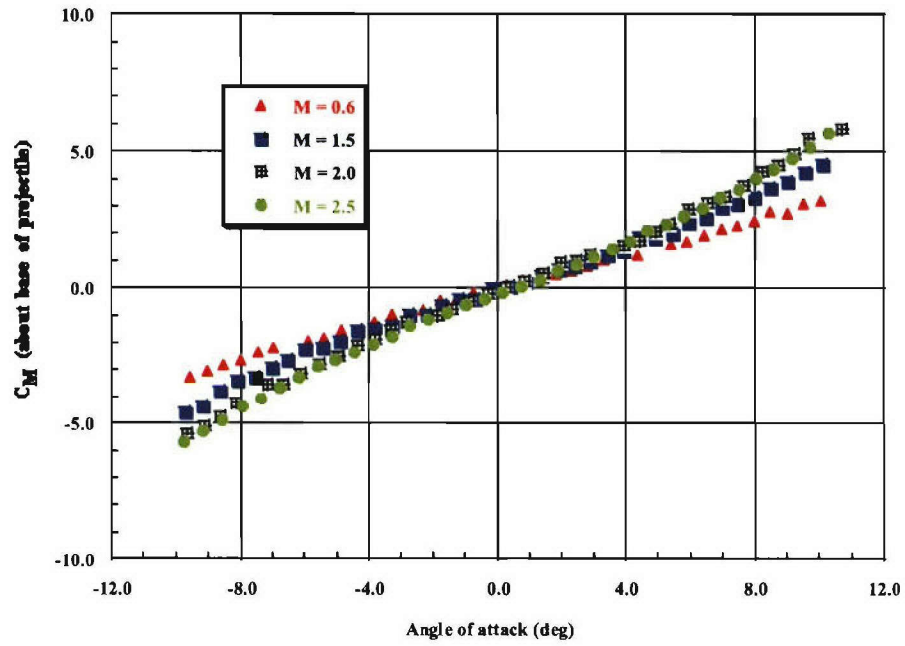
CONFIGURATION: A3\_8 ;  $\phi = 0.0^\circ$



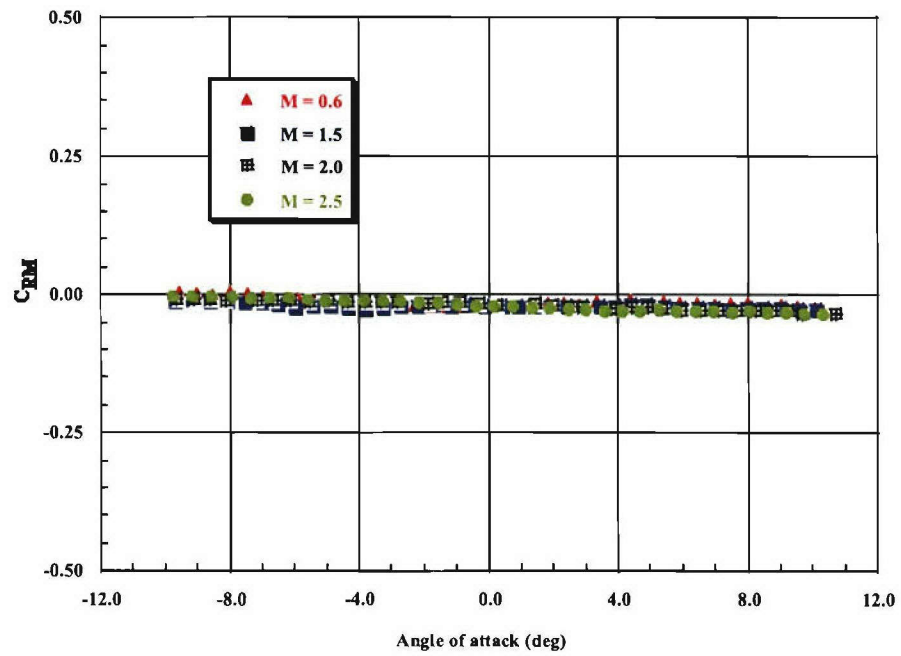
CONFIGURATION: A3\_8 ;  $\phi = 45.0^\circ$



CONFIGURATION: A3\_8 ;  $\phi = 45.0^\circ$

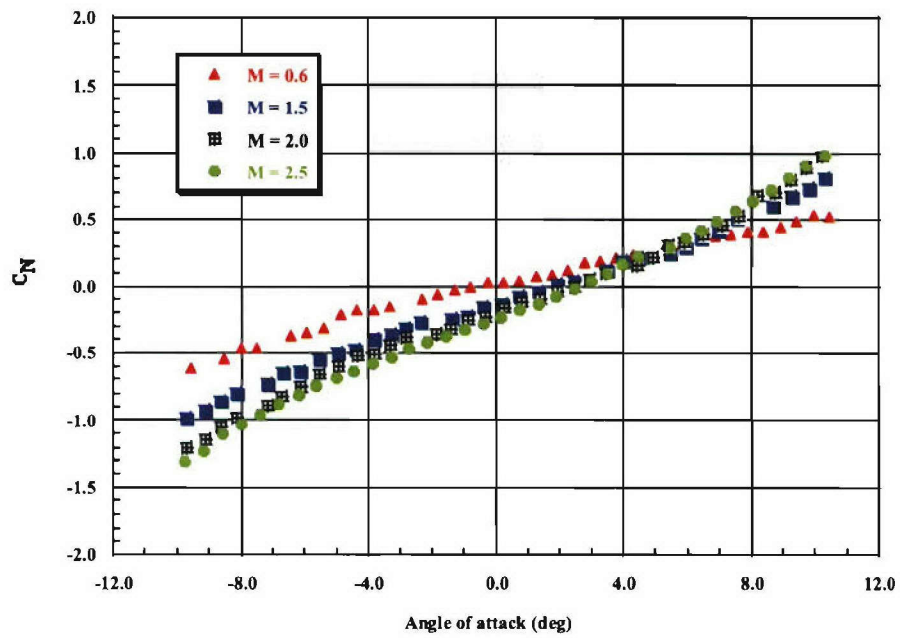
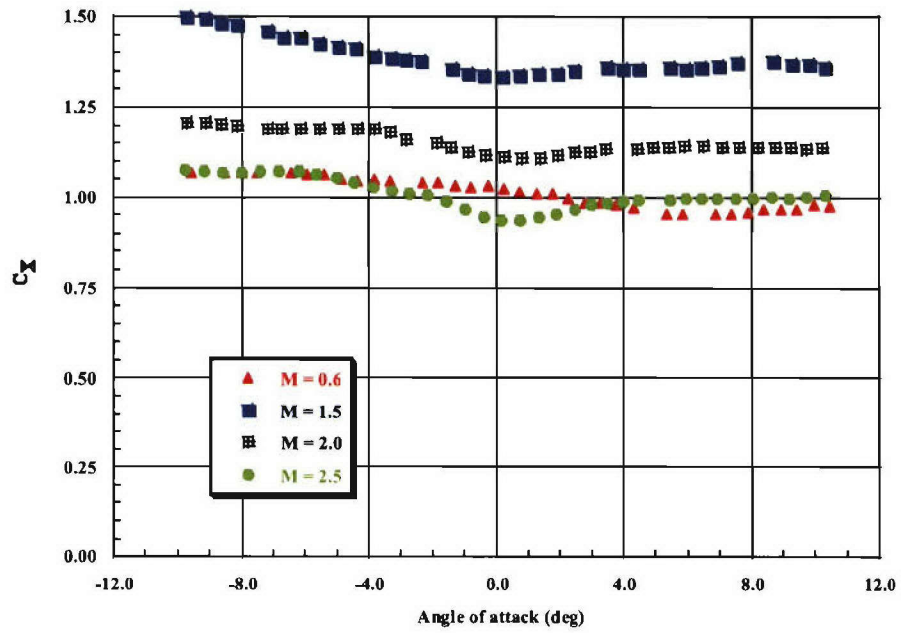


CONFIGURATION: A3\_8 ;  $\phi = 45.0^\circ$

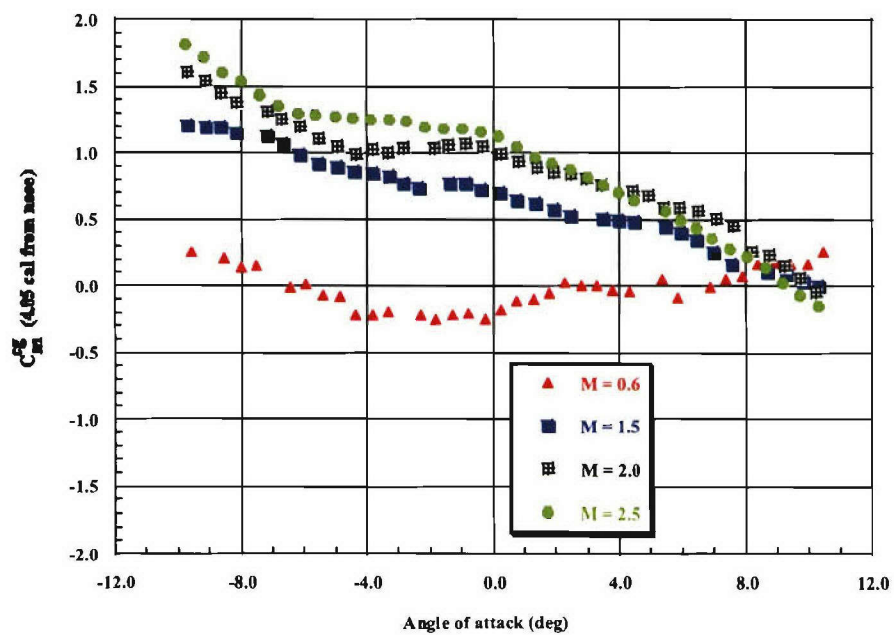
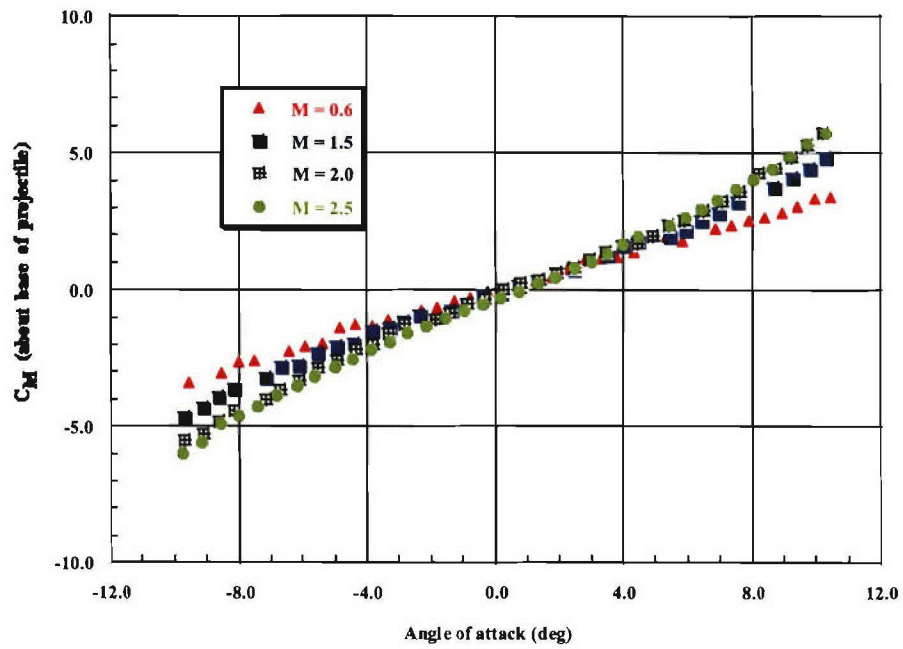




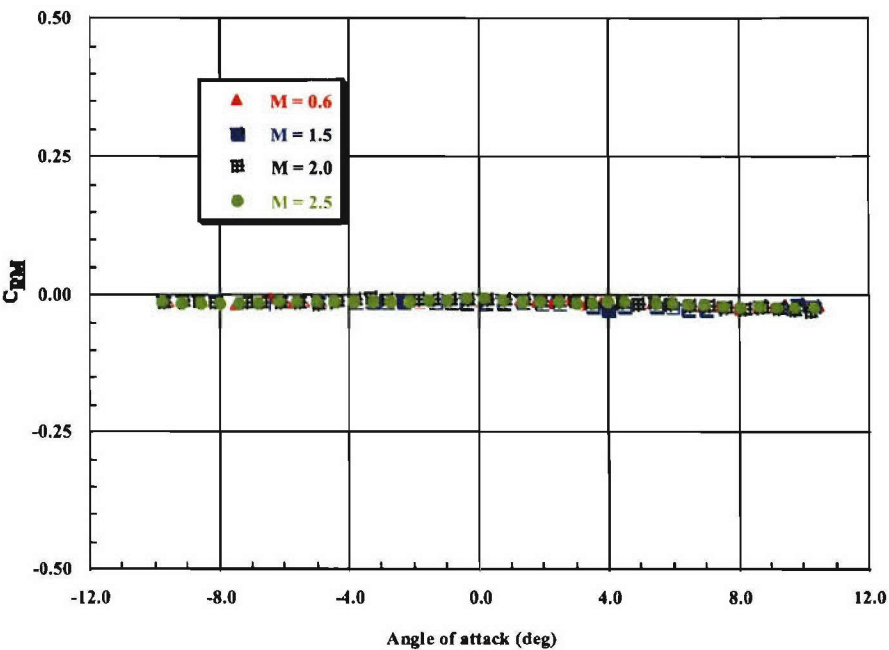
CONFIGURATION: A3\_10 ;  $\phi = 0.0^\circ$



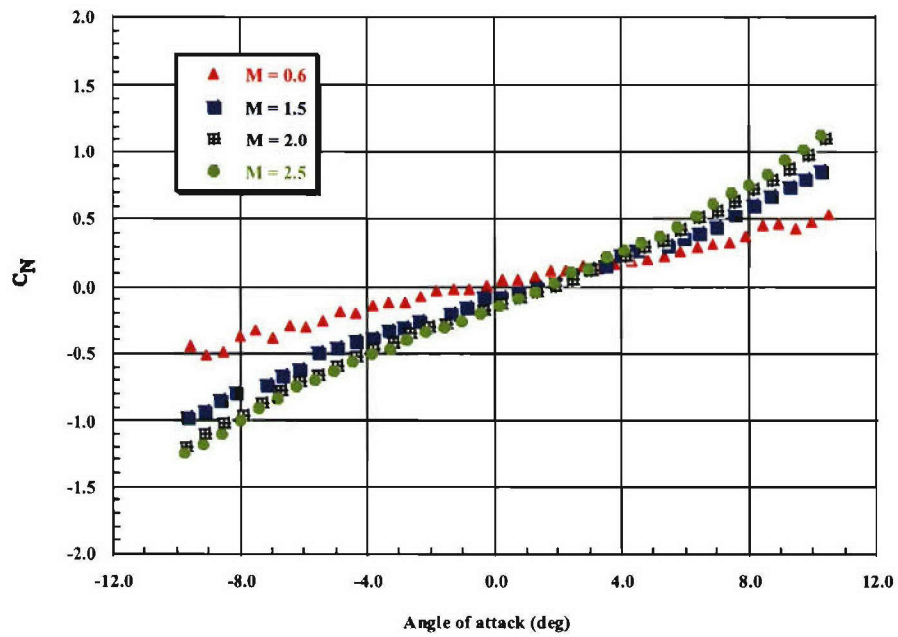
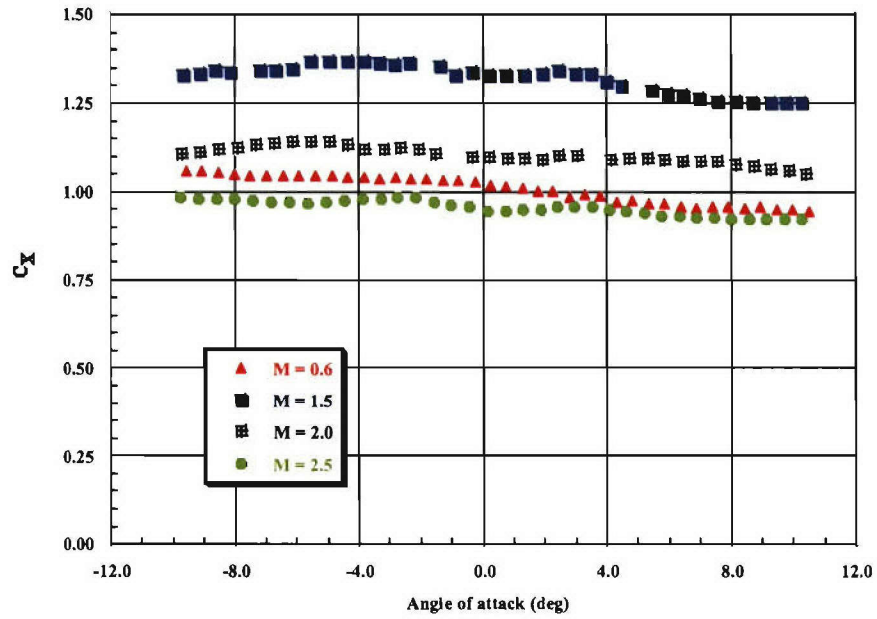
CONFIGURATION: A3\_10 ;  $\phi = 0.0^\circ$



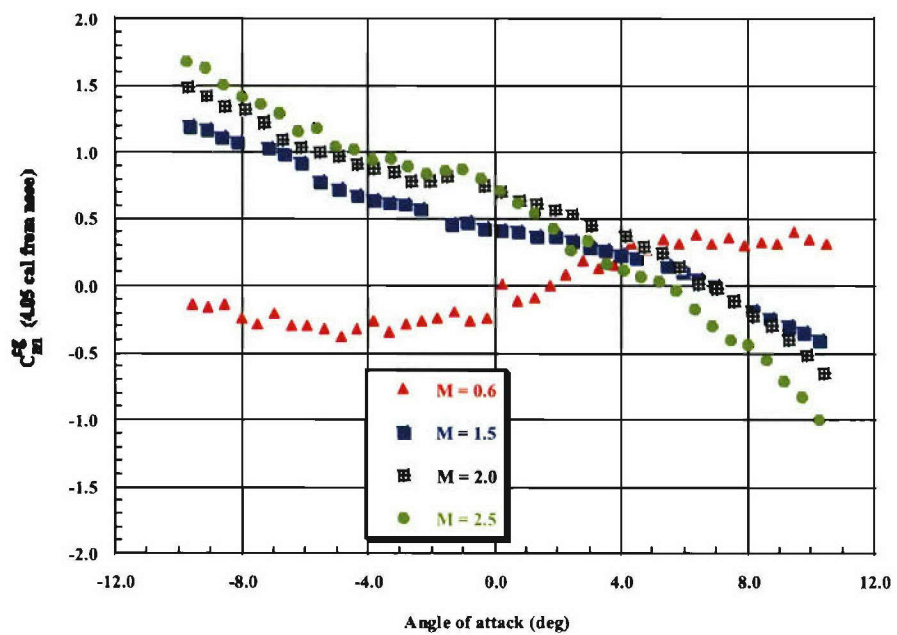
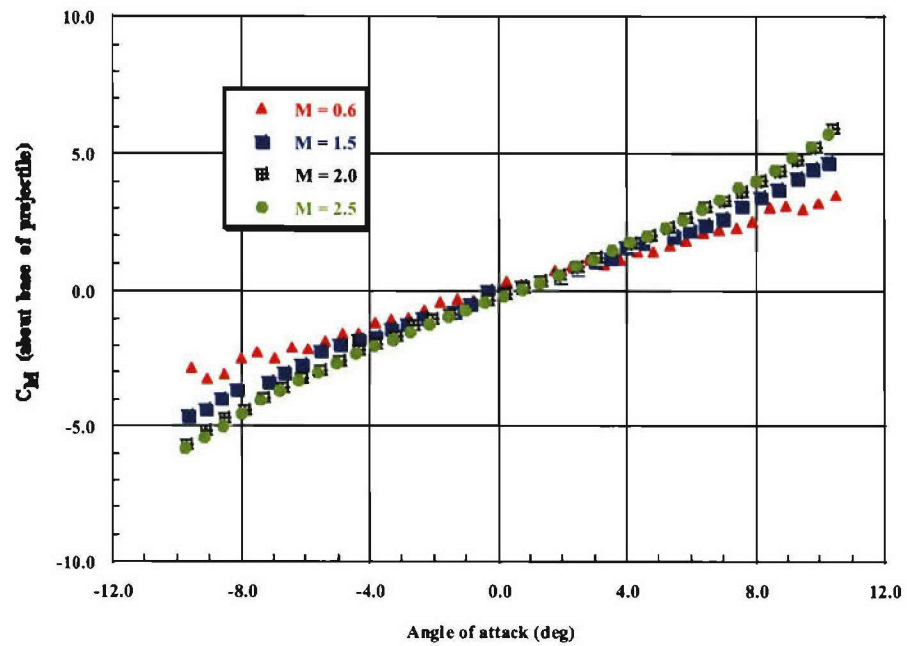
CONFIGURATION: A3\_10 ;  $\phi = 0.0^\circ$



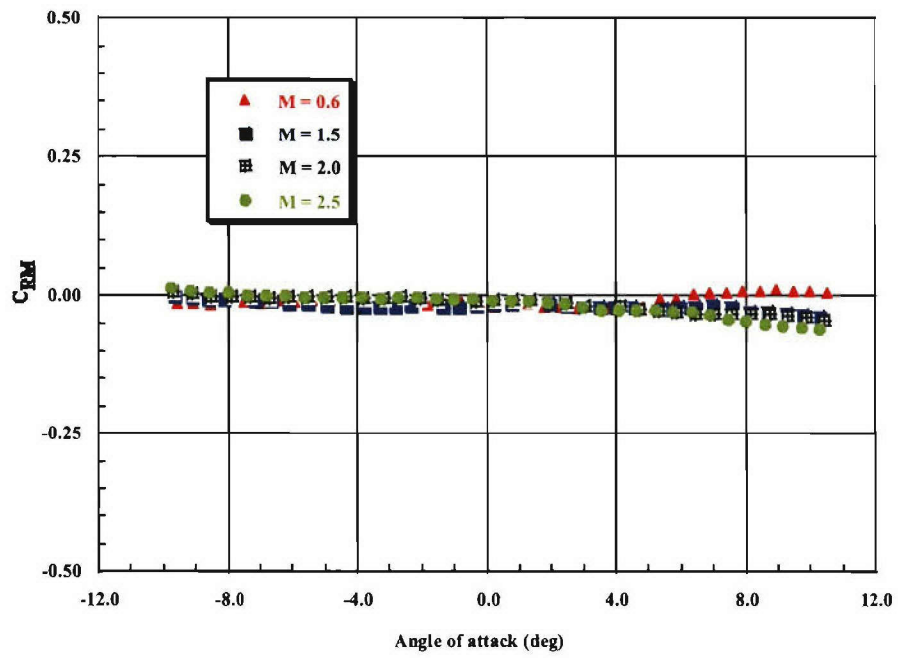
CONFIGURATION: A3\_10 ;  $\phi = 45.0^\circ$



CONFIGURATION: A3\_10 ;  $\phi = 45.0^\circ$



CONFIGURATION: A3\_10 ;  $\phi = 45.0^\circ$



## Annexe B – Tabulated Wind Tunnel Aerodynamic Coefficients vs. Mach Number for A3

Table B1 – Configuration A3\_1 ;  $\phi = 0.0^\circ$

Mach	$C_{X0}$	$C_{N\alpha}$	$C_{M\alpha}^b$	$C_{M\alpha}^{cg}$	$X_{CP0}$ (cal)	$C_{l\delta\delta}$ ( $\alpha = 0.0$ )	Run Number
0.595	0.951	1.74	18.25	7.90	-10.49	-	R7095
0.595	0.939	1.63	17.27	7.59	-10.62	-	R7099
1.487	1.250	4.24	22.32	-2.88	-5.27	-	R7063
1.487	1.251	4.20	22.22	-2.76	-5.29	-	R7064
1.987	1.018	5.10	26.20	-4.15	-5.14	-	R7025
2.487	0.873	6.10	28.26	-8.04	-4.63	-	R7002
2.491	0.876	6.06	27.91	-8.14	-4.61	-	R7003
2.981	0.799	6.88	28.19	-12.72	-4.10	-	R7018
2.983	0.805	6.86	28.09	-12.73	-4.09	-	R7019
3.000	0.944	6.90	30.37	-10.67	-4.40	-	ISL

Table B2 – Configuration A3\_1 ;  $\phi = 45.0^\circ$

Mach	$C_{X0}$	$C_{N\alpha}$	$C_{M\alpha}^b$	$C_{M\alpha}^{cg}$	$X_{CP0}$ (cal)	$C_{l\delta\delta}$ ( $\alpha = 0.0$ )	Run Number
0.595	0.947	1.87	18.16	7.05	-9.73	-	R7097
0.595	0.943	1.83	18.24	7.35	-9.97	-	R7098
1.487	1.255	4.32	22.59	-3.15	-5.22	-	R7065
1.993	1.021	5.27	25.89	-5.45	-4.91	-	R7026
2.491	0.866	5.98	27.26	-8.31	-4.56	-	R7013
2.491	0.864	6.16	27.72	-8.92	-4.50	-	R7014
2.984	0.813	6.65	27.76	-11.83	-4.17	-	R7020
3.000	0.951	7.15	30.42	-12.13	-4.25	-	ISL

**Table B3 – Configuration A3\_2 ;  $\phi = 0.0^\circ$**

Mach	$C_{X0}$	$C_{N\alpha}$	$C_{M\alpha}^b$	$C_{M\alpha}^{cg}$	$X_{CP0}$ (cal)	$C_{l\delta\delta}$ ( $\alpha = 0.0$ )	$C_{l\delta}$ (/rad)	$\frac{C_{l\delta}}{N_{fins}}$	Run Number
0.595	0.948	2.29	18.56	4.95	-8.11	0.033	0.38	0.095	R7100
1.487	1.269	4.18	22.75	-2.09	-5.45	-0.132	-1.51	-0.378	R7060
3.000	0.964	6.74	30.36	-9.74	-4.51	-0.191	-2.19	-0.547	ISL

**Table B4 – Configuration A3\_2 ;  $\phi = 45.0^\circ$**

Mach	$C_{X0}$	$C_{N\alpha}$	$C_{M\alpha}^b$	$C_{M\alpha}^{cg}$	$X_{CP0}$ (cal)	$C_{l\delta\delta}$ ( $\alpha = 0.0$ )	$C_{l\delta}$ (/rad)	$\frac{C_{l\delta}}{N_{fins}}$	Run Number
0.595	0.946	2.26	18.26	4.82	-8.08	0.031	0.36	0.089	R7101
1.487	1.272	4.36	22.85	-3.10	-5.24	-0.131	-1.50	-0.375	R7061
1.487	1.277	4.39	23.04	-3.09	-5.25	-0.132	-1.51	-0.378	R7062
3.000	0.975	6.87	30.23	-10.67	-4.40	-0.191	-2.19	-0.547	ISL

**Table B5 – Configuration A3\_3 ;  $\phi = 0.0^\circ$**

Mach	$C_{X0}$	$C_{N\alpha}$	$C_{M\alpha}^b$	$C_{M\alpha}^{cg}$	$X_{CP0}$ (cal)	$C_{l\delta\delta}$ ( $\alpha = 0.0$ )	$C_{l\delta}$ (/rad)	$\frac{C_{l\delta}}{N_{fins}}$	Run Number
0.595	1.009	3.01	18.29	0.40	-6.08	-0.051	-0.29	-0.073	R7102
1.487	1.359	4.12	22.50	-2.02	-5.46	-0.240	-1.37	-0.344	R7057
3.000	1.043	6.19	29.77	-7.06	-4.81	-0.354	-2.02	-0.507	ISL

**Table B6 – Configuration A3\_3 ;  $\phi = 45.0^\circ$**

Mach	$C_{X0}$	$C_{N\alpha}$	$C_{M\alpha}^b$	$C_{M\alpha}^{cg}$	$X_{CP0}$ (cal)	$C_{l\delta\delta}$ ( $\alpha = 0.0$ )	$C_{l\delta}$ (/rad)	$\frac{C_{l\delta}}{N_{fins}}$	Run Number
0.595	1.006	2.94	18.32	0.80	-6.22	-0.052	-0.30	-0.074	R7103
1.487	1.362	4.23	22.28	-2.87	-5.27	-0.240	-1.38	-0.344	R7058
1.487	1.368	4.29	22.69	-2.82	-5.29	-0.242	-1.39	-0.347	R7059
3.000	1.056	6.39	29.87	-8.12	-4.68	-0.352	-2.02	-0.504	ISL



**Table B7 – Configuration A3\_4 ;  $\phi = 0.0^\circ$**

Mach	$C_{X0}$	$C_{N\alpha}$	$C_{M\alpha}^b$	$C_{M\alpha}^{cg}$	$X_{CP0}$ (cal)	$C_{l\delta\delta}$ ( $\alpha = 0.0$ )	$C_{l\delta}$ (/rad)	$\frac{C_{l\delta}}{N_{fins}}$	Run Number
0.595	1.101	3.57	19.52	-1.70	-5.47	-0.105	-0.40	-0.100	R7104
1.487	1.423	4.19	22.58	-2.37	-5.38	-0.328	-1.25	-0.313	R7055
1.989	1.185	4.59	25.79	-1.49	-5.63	-0.355	-1.36	-0.339	R7027
2.484	1.037	5.08	26.89	-3.34	-5.29	-0.409	-1.56	-0.391	R7004
2.983	0.987	5.41	27.09	-5.07	-5.01	-0.458	-1.75	-0.437	R7021
3.000	1.139	6.00	29.86	-5.84	-4.98	-0.433	-1.65	-0.413	ISL

**Table B8 – Configuration A3\_4 ;  $\phi = 45.0^\circ$**

Mach	$C_{X0}$	$C_{N\alpha}$	$C_{M\alpha}^b$	$C_{M\alpha}^{cg}$	$X_{CP0}$ (cal)	$C_{l\delta\delta}$ ( $\alpha = 0.0$ )	$C_{l\delta}$ (/rad)	$\frac{C_{l\delta}}{N_{fins}}$	Run Number
0.595	1.102	3.50	19.52	-1.30	-5.58	-0.103	-0.39	-0.098	R7105
1.487	1.423	4.36	22.91	-3.06	-5.25	-0.329	-1.26	-0.314	R7056
1.995	1.181	4.85	26.44	-2.40	-5.46	-0.358	-1.37	-0.342	R7028
2.491	1.035	5.20	26.69	-4.23	-5.14	-0.413	-1.58	-0.394	R7015
2.488	1.016	5.27	26.92	-4.41	-5.11	-0.408	-1.56	-0.390	R7016
2.986	0.984	5.47	26.89	-5.68	-4.91	-0.462	-1.76	-0.441	R7022
3.000	1.148	5.89	29.37	-5.69	-4.98	-0.460	-1.76	-0.439	ISL

**Table B9 – Configuration A3\_5 ;  $\phi = 0.0^\circ$**

Mach	$C_{X0}$	$C_{N\alpha}$	$C_{M\alpha}^b$	$C_{M\alpha}^{cg}$	$X_{CP0}$ (cal)	$C_{l\delta\delta}$ ( $\alpha = 0.0$ )	$C_{l\delta}$ (/rad)	$\frac{C_{l\delta}}{N_{fins}}$	Run Number
0.595	0.925	2.05	17.33	5.13	-8.45	0.000	0.00	0.00	R7106
0.595	0.935	2.11	17.65	5.07	-8.35	0.000	0.00	0.00	R7107
1.487	1.260	4.19	22.11	-2.82	-5.28	-0.078	-0.89	-0.447	R7052
1.487	1.256	4.33	22.73	-3.06	-5.24	-0.079	-0.91	-0.453	R7053
3.000	0.945	6.75	30.21	-9.97	-4.47	-0.102	-1.17	-0.584	ISL

**Table B10 – Configuration A3\_5 ;  $\phi = 45.0^\circ$**

Mach	$C_{X0}$	$C_{N\alpha}$	$C_{M\alpha}^b$	$C_{M\alpha}^{cg}$	$X_{CP0}$ (cal)	$C_{l\delta\delta}$ ( $\alpha = 0.0$ )	$C_{l\delta}$ (/rad)	$\frac{C_{l\delta}}{N_{fins}}$	Run Number
0.595	0.939	2.14	18.42	5.68	-8.60	0.000	0.00	0.000	R7108
1.487	1.269	4.46	22.73	-3.83	-5.09	-0.076	-0.87	-0.435	R7054
3.000	0.951	6.97	30.30	-11.15	-4.35	-0.103	-1.18	-0.590	ISL

**Table B11 – Configuration A3\_6 ;  $\phi = 0.0^\circ$**

Mach	$C_{X0}$	$C_{N\alpha}$	$C_{M\alpha}^b$	$C_{M\alpha}^{cg}$	$X_{CP0}$ (cal)	$C_{l\delta\delta}$ ( $\alpha = 0.0$ )	$C_{l\delta}$ (/rad)	$\frac{C_{l\delta}}{N_{fins}}$	Run Number
0.595	0.975	2.81	19.33	2.59	-6.87	-0.029	-0.17	-0.083	R7109
1.487	1.312	4.15	22.77	-1.91	-5.49	-0.128	-0.73	-0.367	R7049
1.487	1.310	4.14	22.65	-1.97	-5.47	-0.128	-0.73	-0.367	R7050
3.000	0.996	6.32	29.94	-7.69	-4.74	-0.187	-1.07	-0.536	ISL

**Table B12 – Configuration A3\_6 ;  $\phi = 45.0^\circ$**

Mach	$C_{X0}$	$C_{N\alpha}$	$C_{M\alpha}^b$	$C_{M\alpha}^{cg}$	$X_{CP0}$ (cal)	$C_{l\delta\delta}$ ( $\alpha = 0.0$ )	$C_{l\delta}$ (/rad)	$\frac{C_{l\delta}}{N_{fins}}$	Run Number
0.595	0.979	2.49	18.78	3.94	-7.53	-0.029	-0.17	-0.083	R7110
1.487	1.319	4.44	23.14	-3.26	-5.22	-0.129	-0.74	-0.370	R7051
3.000	1.007	6.53	29.65	-9.19	-4.54	-0.185	-1.06	-0.530	ISL

**Table B13 – Configuration A3\_7 ;  $\phi = 0.0^\circ$**

Mach	$C_{X0}$	$C_{N\alpha}$	$C_{M\alpha}^b$	$C_{M\alpha}^{cg}$	$X_{CP0}$ (cal)	$C_{l\delta\delta}$ ( $\alpha = 0.0$ )	$C_{l\delta}$ (/rad)	$\frac{C_{l\delta}}{N_{fins}}$	Run Number
0.595	1.016	2.96	18.44	0.80	-6.22	-0.046	-0.18	-0.088	R7111
1.487	1.338	4.13	22.68	-1.87	-5.50	-0.169	-0.65	-0.323	R7047
1.994	1.098	4.68	25.88	-1.97	-5.53	-0.179	-0.68	-0.342	R7029
2.490	0.950	5.27	27.39	-3.95	-5.20	-0.200	-0.76	-0.382	R7005
3.000	1.034	5.86	29.72	-5.13	-5.07	-0.215	-0.82	-0.411	ISL

**Table B14 – Configuration A3\_7 ;  $\phi = 45.0^\circ$**

Mach	$C_{X0}$	$C_{N\alpha}$	$C_{M\alpha}^b$	$C_{M\alpha}^{cg}$	$X_{CP0}$ (cal)	$C_{l\delta\delta}$ ( $\alpha = 0.0$ )	$C_{l\delta}$ (/rad)	$\frac{C_{l\delta}}{N_{fins}}$	Run Number
0.595	1.012	2.69	18.62	2.64	-6.93	-0.053	-0.20	-0.101	R7112
1.487	1.333	4.44	23.30	-3.12	-5.25	-0.167	-0.64	-0.320	R7048
1.993	1.086	4.91	26.21	-3.01	-5.34	-0.179	-0.68	-0.342	R7030
2.491	0.910	5.61	27.71	-5.64	-4.94	-0.203	-0.78	-0.388	R7017
3.000	1.038	6.17	29.37	-7.32	-4.76	-0.219	-0.84	-0.418	ISL

**Table B15 – Configuration A3\_8 ;  $\phi = 0.0^\circ$**

Mach	$C_{X0}$	$C_{N\alpha}$	$C_{M\alpha}^b$	$C_{M\alpha}^{cg}$	$X_{CP0}$ (cal)	$C_{l\delta\delta}$ ( $\alpha = 0.0$ )	Run Number
0.595	0.918	2.20	17.94	4.82	-8.14	-0.025	R7113
1.487	1.283	4.27	22.47	-2.95	-5.26	-0.021	R7045
1.996	1.056	4.96	25.97	-3.55	-5.23	-0.016	R7031
2.492	0.876	5.88	27.92	-7.08	-4.75	-0.020	R7006
2.492	0.869	5.69	27.45	-6.43	-4.82	-0.019	R7007
3.000	0.951	6.81	30.06	-10.48	-4.41	-0.025	ISL

**Table B16 – Configuration A3\_8 ;  $\phi = 45.0^\circ$**

Mach	$C_{X0}$	$C_{N\alpha}$	$C_{M\alpha}^b$	$C_{M\alpha}^{cg}$	$X_{CP0}$ (cal)	$C_{l\delta\delta}$ ( $\alpha = 0.0$ )	Run Number
0.595	0.893	1.94	17.50	5.96	-9.03	-0.020	R7114
0.595	0.930	1.98	17.85	6.05	-9.00	-0.024	R7115
1.479	1.280	4.19	21.71	-3.22	-5.18	-0.019	R7046
1.997	1.060	5.20	26.16	-4.80	-5.03	-0.016	R7032
1.993	1.051	5.14	25.90	-4.66	-5.04	-0.018	R7033
2.479	0.875	5.96	27.05	-8.42	-4.54	-0.019	R7008
3.000	0.961	6.88	29.93	-10.99	-4.35	-0.027	ISL

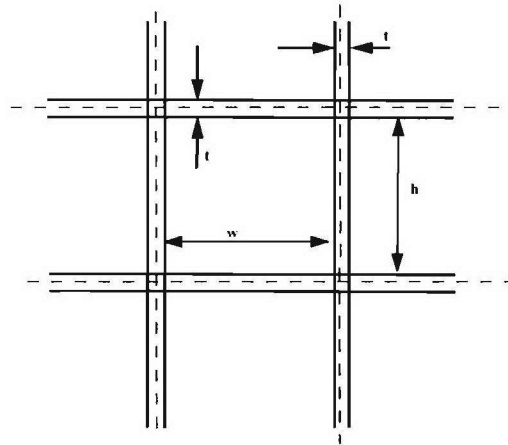
**Table B17 – Configuration A3\_10 ;  $\phi = 0.0^\circ$**

Mach	$C_{X0}$	$C_{N\alpha}$	$C_{M\alpha}^b$	$C_{M\alpha}^{cg}$	$X_{CP0}$ (cal)	$C_{l\delta\delta}$ ( $\alpha = 0.0$ )	Run Number
0.595	1.027	2.89	18.67	1.45	-6.45	-0.013	R7118
1.487	1.346	4.39	23.30	-2.84	-5.30	-0.013	R7039
1.487	1.347	4.22	22.56	-2.53	-5.35	-0.012	R7040
1.996	1.120	4.71	25.68	-2.32	-5.46	-0.008	R7037
2.488	0.956	5.37	27.65	-4.27	-5.15	-0.006	R7011
3.000	1.046	6.15	29.82	-6.78	-4.85	-0.015	ISL

**Table B18 – Configuration A3\_10 ;  $\phi = 45.0^\circ$**

Mach	$C_{X0}$	$C_{N\alpha}$	$C_{M\alpha}^b$	$C_{M\alpha}^{cg}$	$X_{CP0}$ (cal)	$C_{l\delta\delta}$ ( $\alpha = 0.0$ )	Run Number
0.595	1.025	2.41	18.38	4.05	-7.63	-0.017	R7119
1.487	1.345	4.30	22.57	-3.03	-5.25	-0.017	R7041
1.995	1.100	5.05	26.25	-3.79	-5.20	-0.010	R7038
2.490	0.963	5.61	27.10	-6.31	-4.83	-0.008	R7012
3.000	1.045	6.39	29.83	-8.18	-4.67	-0.016	ISL

## Annexe C – Theoretical Choking Mach Number



$$\left(\frac{A}{A^*}\right)^2 = \frac{1}{M^2} \left[ \frac{2}{\gamma+1} \left( 1 + \frac{\gamma-1}{2} M^2 \right) \right]^{\frac{\gamma+1}{\gamma-1}}$$

Fin Type	Nominal cell width (cal)	Nominal cell height (cal)	Web thickness (cal)	Area ratio $\frac{A^*}{A} = \frac{w h}{(w+t)(h+t)}$	$M_{cr}$ (calculated)
Thick Fin	0.124	0.161	0.017	0.795	0.548
Thin Fin	0.140	0.173	0.005	0.938	0.744
Hexagonal	0.135	0.135	0.017	0.789	0.542

## Annexe D – Tabulated Wind Tunnel Aerodynamic Coefficients for Various Lattice Fin Geometries

**Table D1 – Configuration Thick Fin (A3\_1);  $\phi = 0.0^\circ$**

Mach	$C_{X0}$	$C_{N\alpha}$	$C_{M\alpha}^b$	$C_{M\alpha}^{cg}$	$X_{CP0}$	Run Number
0.595	0.951	1.74	18.25	7.90	-10.49	R7095
0.595	0.939	1.63	17.27	7.59	-10.62	R7099
1.487	1.250	4.24	22.32	-2.88	-5.27	R7063
1.487	1.251	4.20	22.22	-2.76	-5.29	R7064
1.987	1.018	5.10	26.20	-4.15	-5.14	R7025
2.487	0.873	6.10	28.26	-8.04	-4.63	R7002
2.491	0.876	6.06	27.91	-8.14	-4.61	R7003
2.981	0.799	6.88	28.19	-12.72	-4.10	R7018
2.983	0.805	6.86	28.09	-12.73	-4.09	R7019

**Table D2 – Configuration Thin Fin;  $\phi = 0.0^\circ$**

Mach	$C_{X0}$	$C_{N\alpha}$	$C_{M\alpha}^b$	$C_{M\alpha}^{cg}$	$X_{CP0}$	Run Number
0.598	0.594	3.42	18.81	-1.56	-5.49	R7956
0.598	0.599	3.38	18.49	-1.61	-5.47	R7951
0.598	0.596	3.31	18.08	-1.59	-5.47	R8008
0.789	0.659	3.50	19.36	-1.45	-5.53	R7957
0.790	0.666	3.66	20.23	-1.57	-5.52	R8007
0.790	0.667	3.44	19.12	-1.32	-5.57	R7950
1.486	0.901	4.76	22.92	-5.42	-4.81	R7979
1.990	0.696	5.37	26.02	-5.91	-4.85	R7986
2.457	0.602	4.78	25.65	-2.82	-5.36	R7994
2.460	0.602	4.84	25.73	-3.06	-5.32	R7992
2.946	0.535	4.90	25.75	-3.40	-5.26	R8001
3.937	0.443	4.61	23.06	-4.39	-5.00	R8012

**Table D3 – Configuration Open Base;  $\phi = 0.0^\circ$**

Mach	$C_{X0}$	$C_{N\alpha}$	$C_{M\alpha}^b$	$C_{M\alpha}^{cg}$	$X_{CP0}$	Run Number
0.598	0.842	1.93	18.38	6.89	-9.52	R7952
0.789	0.972	2.56	18.66	3.46	-7.31	R7953
1.486	1.197	3.79	23.15	0.58	-6.10	R7972
1.990	0.963	4.78	25.73	-2.73	-5.38	R7987
2.462	0.868	5.45	26.45	-5.96	-4.86	R7993
2.947	0.802	6.37	27.32	-10.60	-4.29	R8003
3.936	0.694	5.83	23.14	-11.54	-3.97	R8014

**Table D4 – Configuration Hexagonal;  $\phi = 0.0^\circ$**

Mach	$C_{X0}$	$C_{N\alpha}$	$C_{M\alpha}^b$	$C_{M\alpha}^{cg}$	$X_{CP0}$	Run Number
0.598	0.948	1.81	18.06	7.27	-9.95	R7948
0.790	1.095	2.16	17.56	4.68	-8.11	R7949
1.486	1.268	4.54	23.25	-3.74	-5.12	R7980
1.988	1.011	4.98	26.37	-3.28	-5.29	R7985
2.461	0.902	5.56	26.64	-6.43	-4.79	R7991
2.947	0.853	6.18	27.24	-9.50	-4.41	R8002
3.935	0.749	5.78	23.27	-11.14	-4.02	R8013

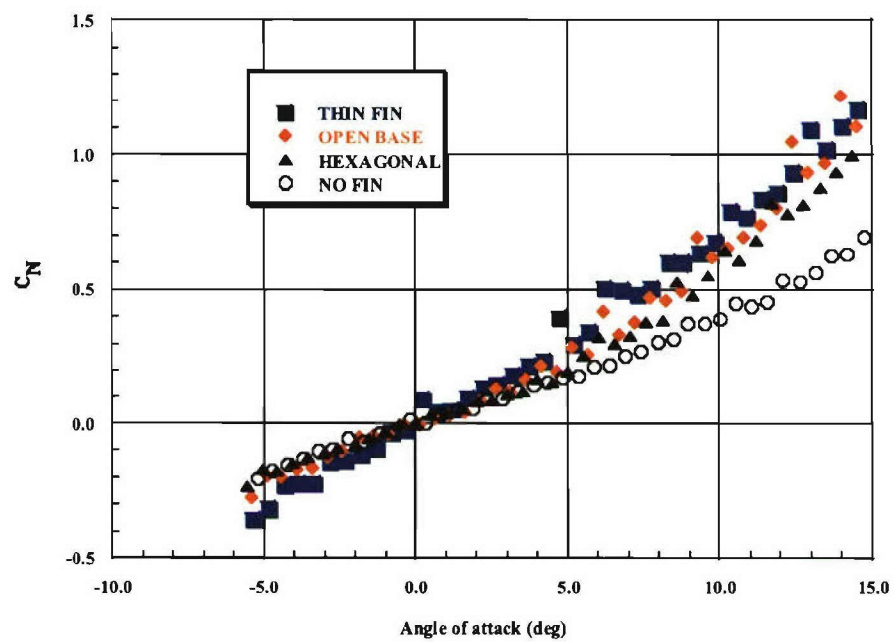
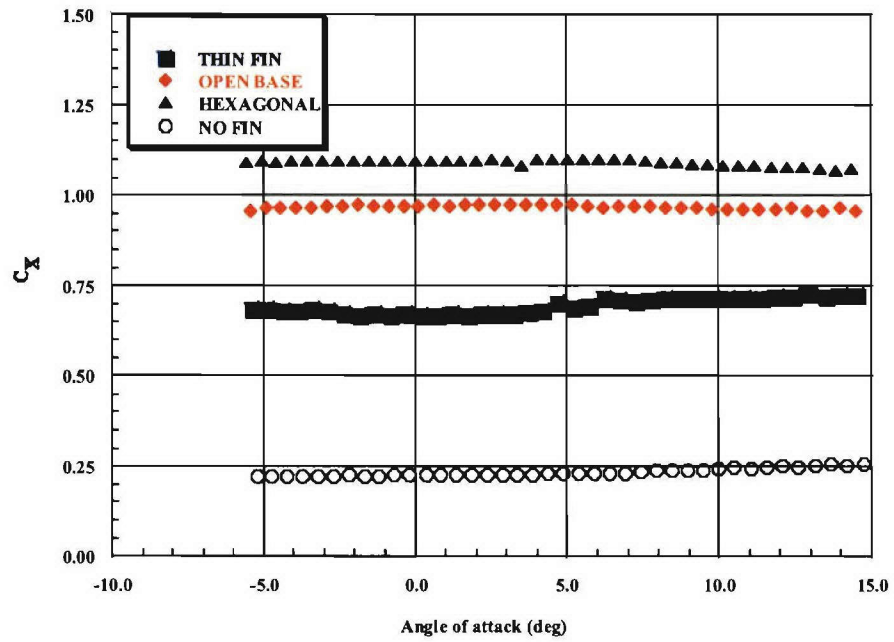
**Table D5 – Configuration No Fin**

Mach	$C_{X0}$	$C_{N\alpha}$	$C_{M\alpha}^b$	$C_{M\alpha}^{cg}$	$X_{CP0}$	Run Number
0.598	0.221	1.93	17.46	5.96	-9.03	R7955
0.598	0.218	1.99	17.94	6.07	-9.00	R7968
0.789	0.224	2.08	18.25	5.89	-8.79	R7954
1.475	0.441	2.20	20.98	7.90	-9.55	R7969
1.986	0.313	2.55	24.41	9.24	-9.57	R7983
2.457	0.241	2.85	24.30	7.34	-8.52	R7990
2.948	0.215	3.25	25.40	6.08	-7.82	R7999

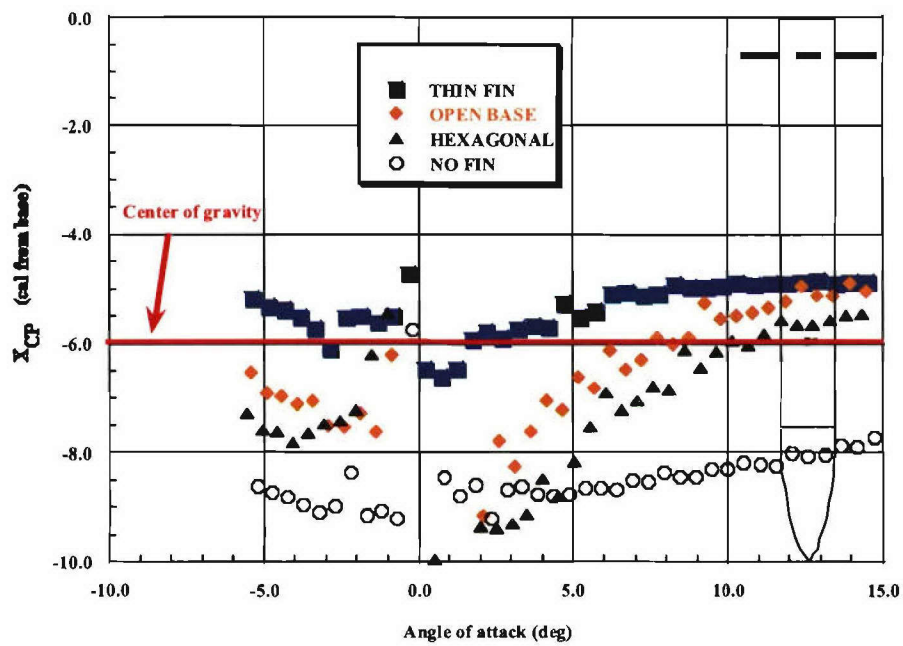
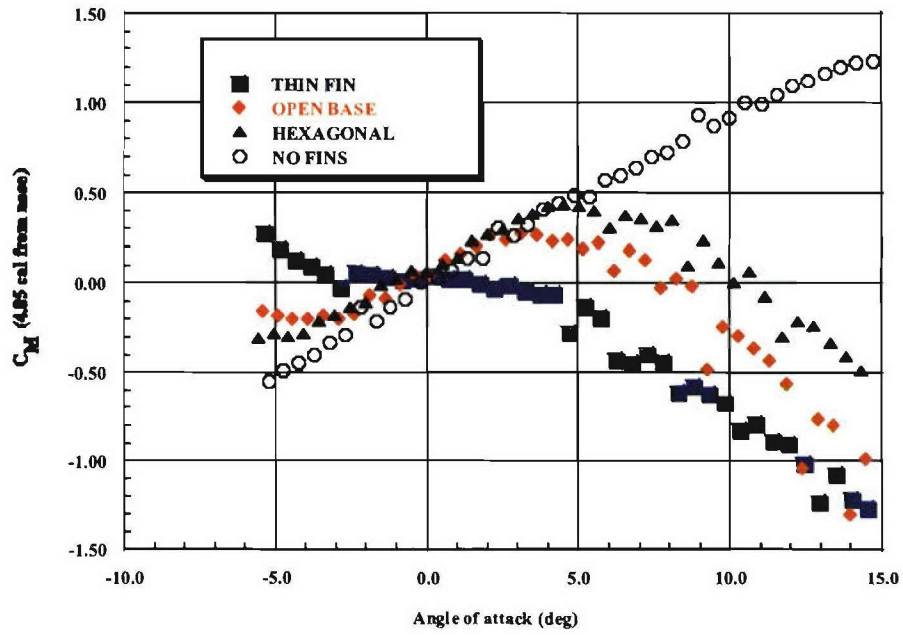
**Annexe E – Plotted Wind Tunnel Aerodynamic  
Coefficients for Various Geometries  
(M = 0.8, 2.0, 2.5 and 4.0)**



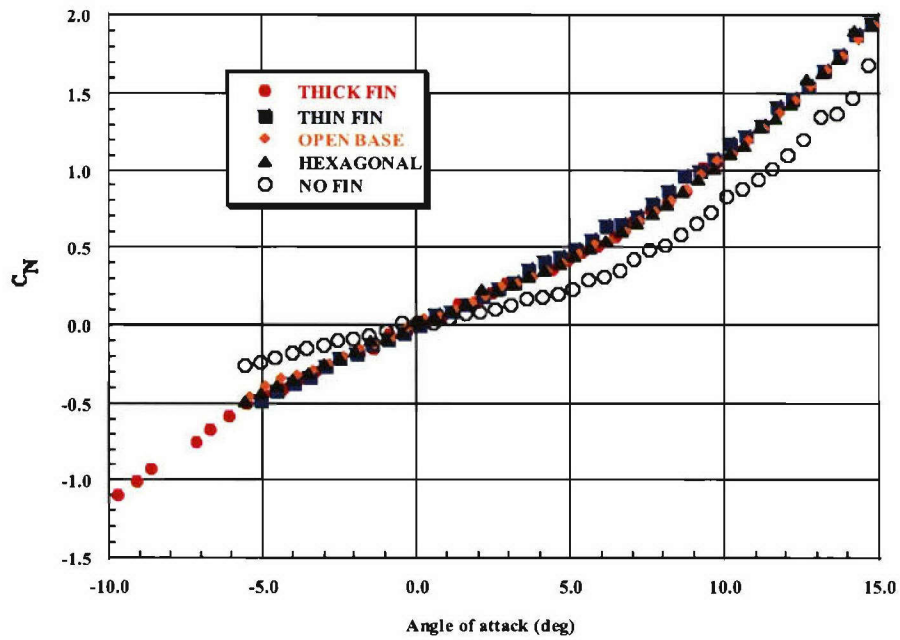
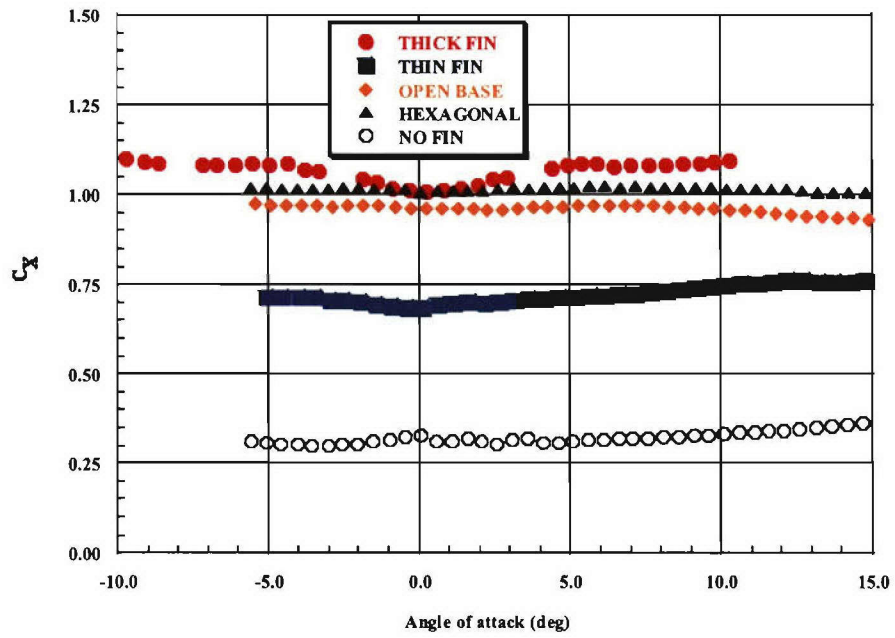
$M = 0.8$



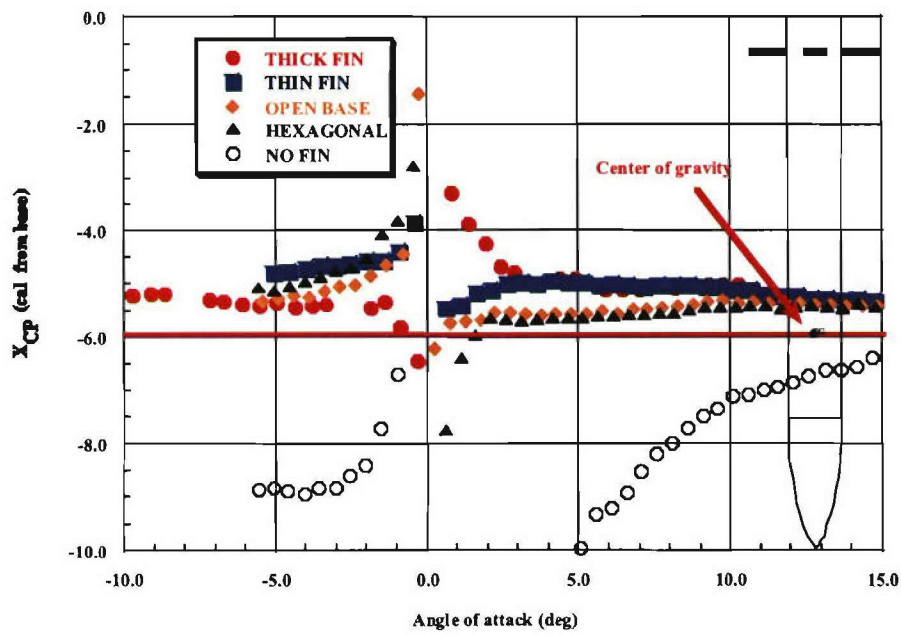
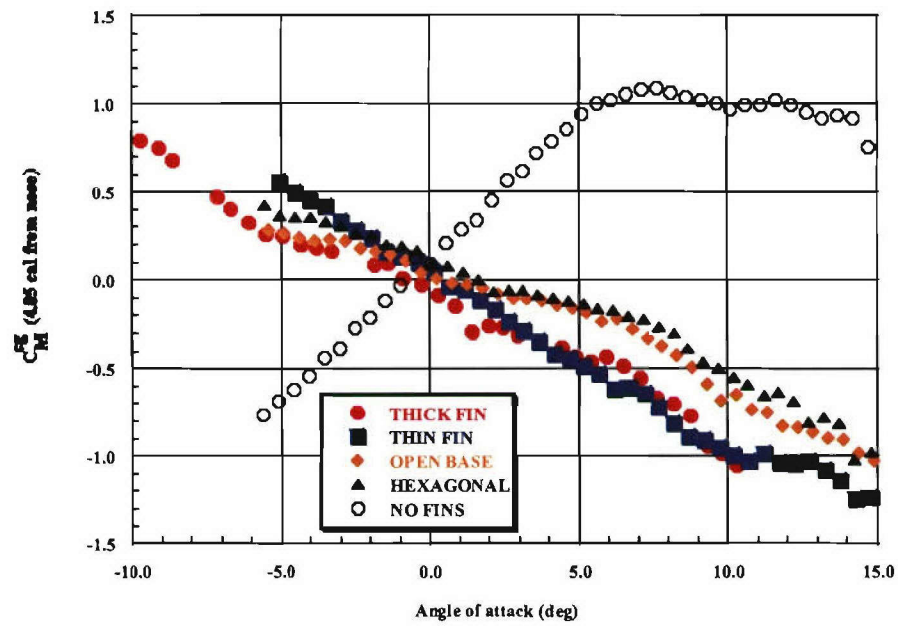
$M = 0.8$



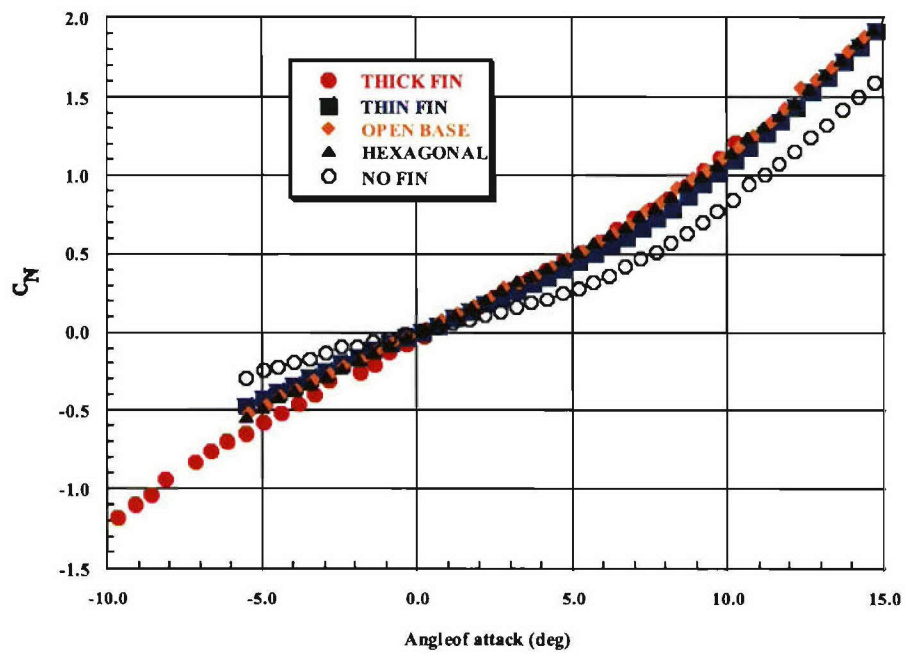
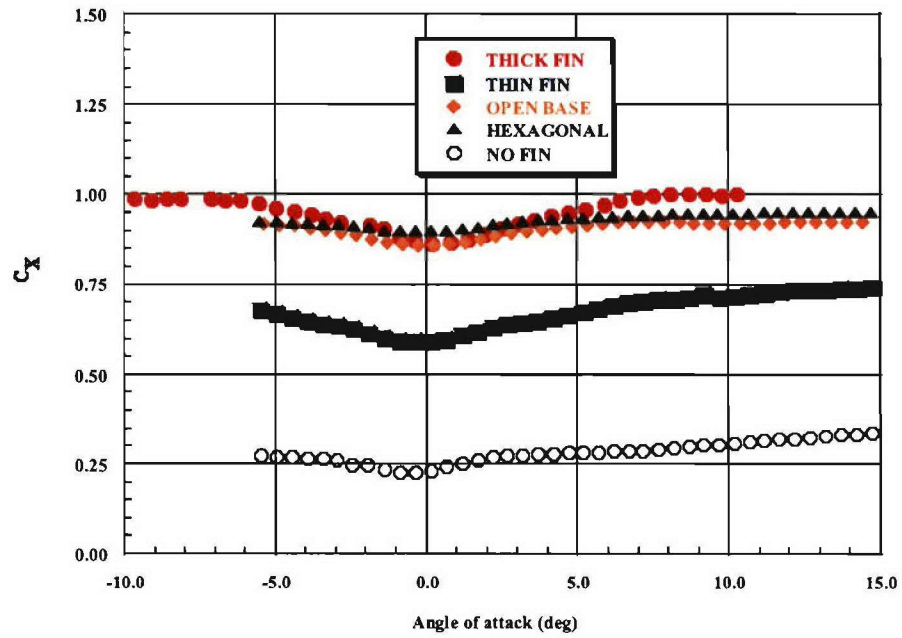
$M = 2.0$



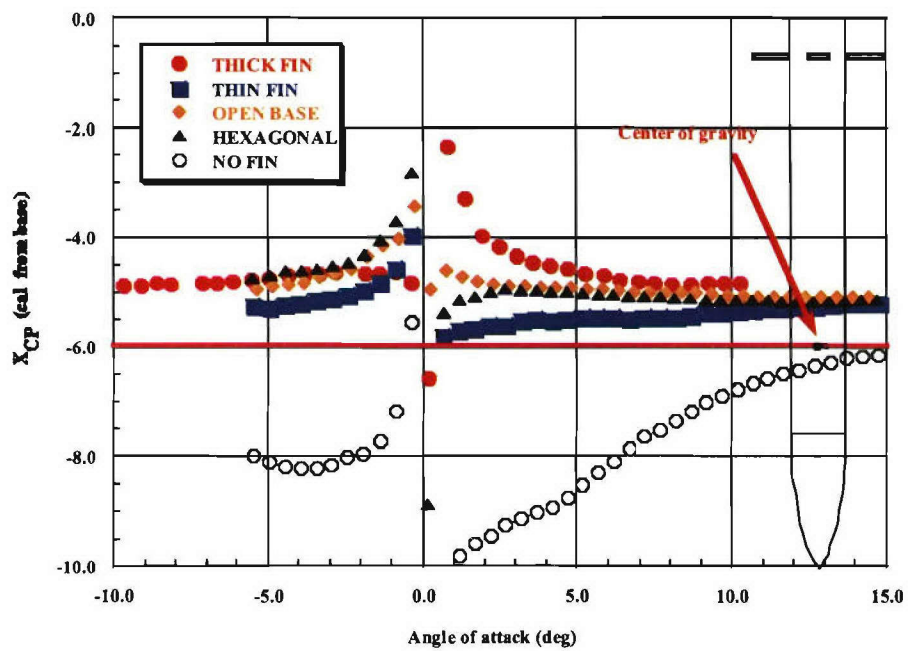
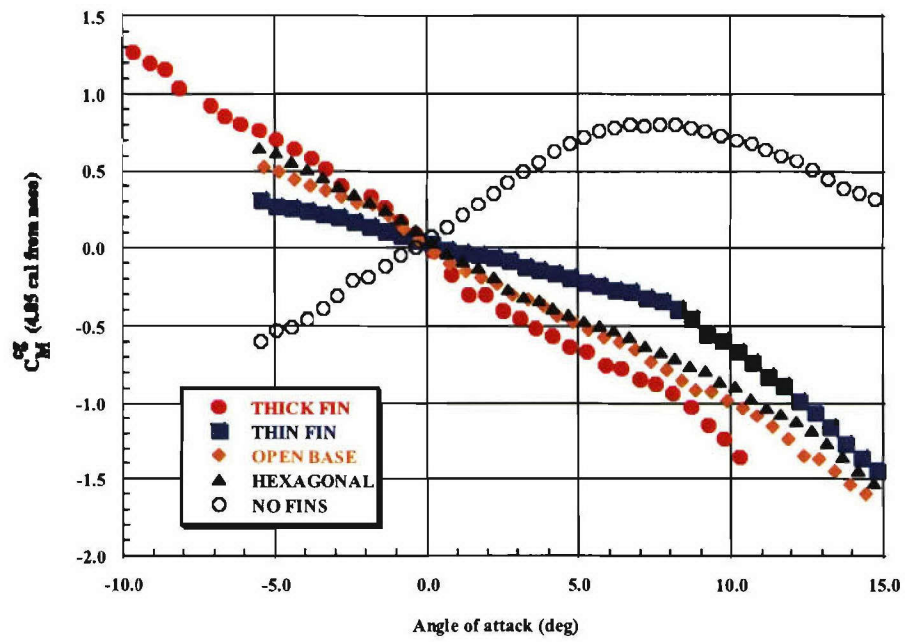
$M = 2.0$



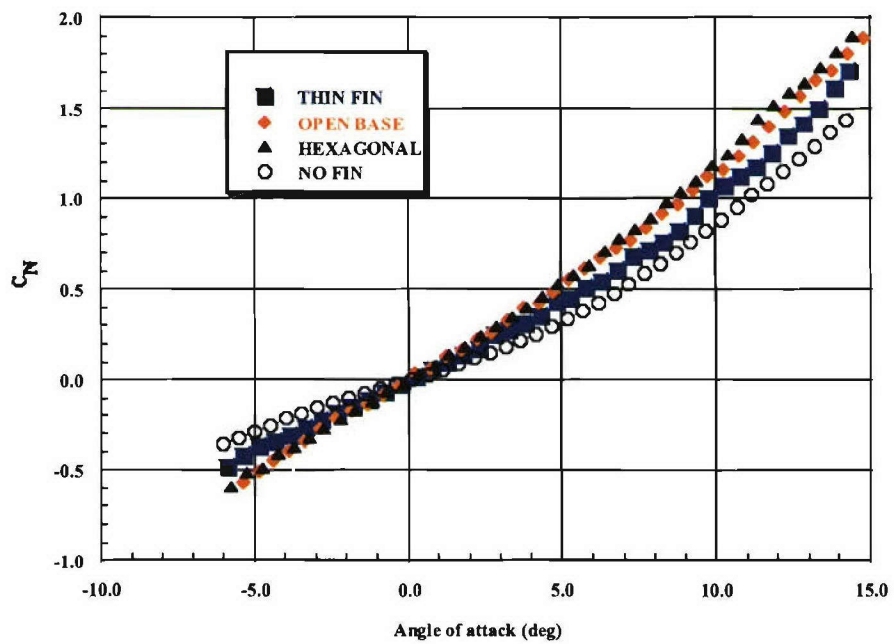
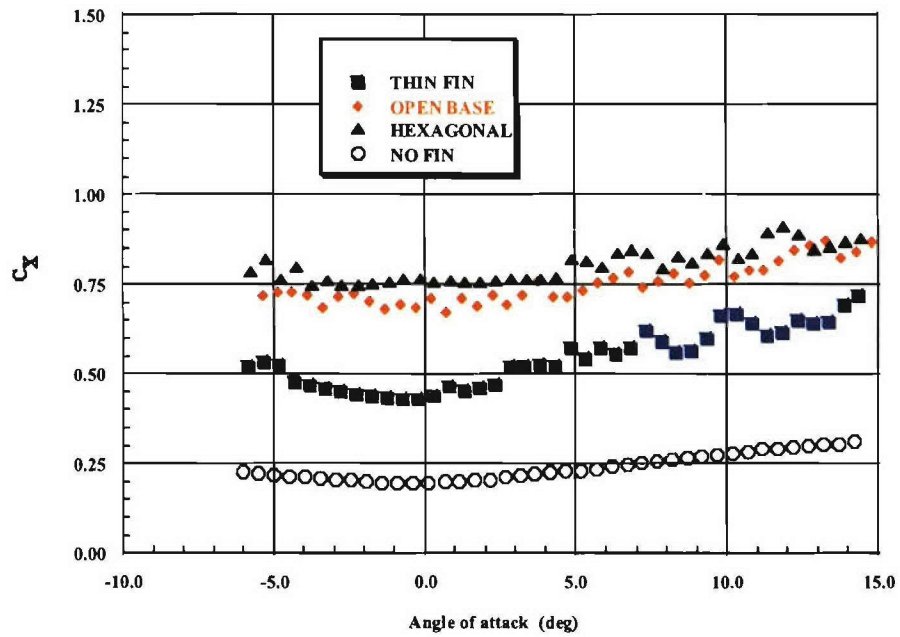
$M = 2.5$



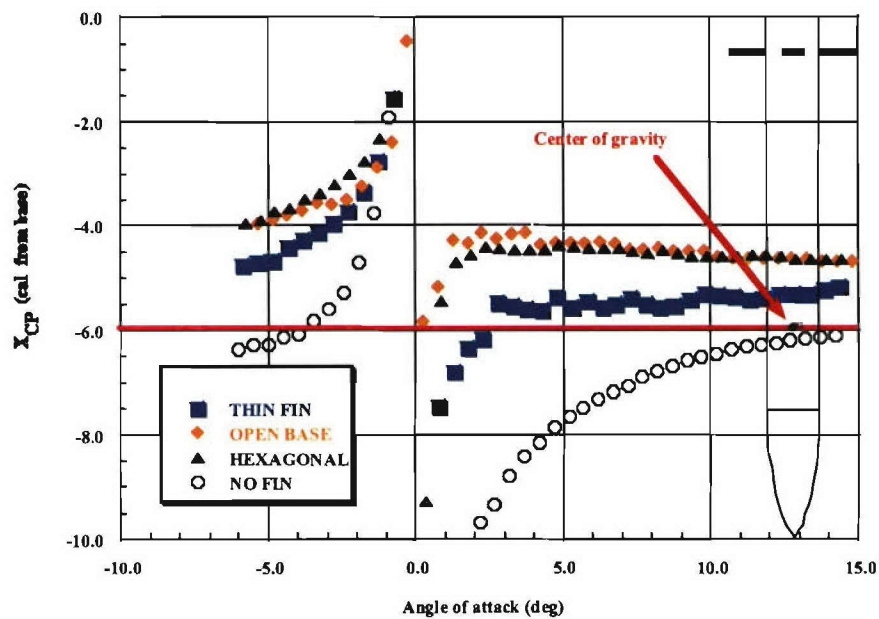
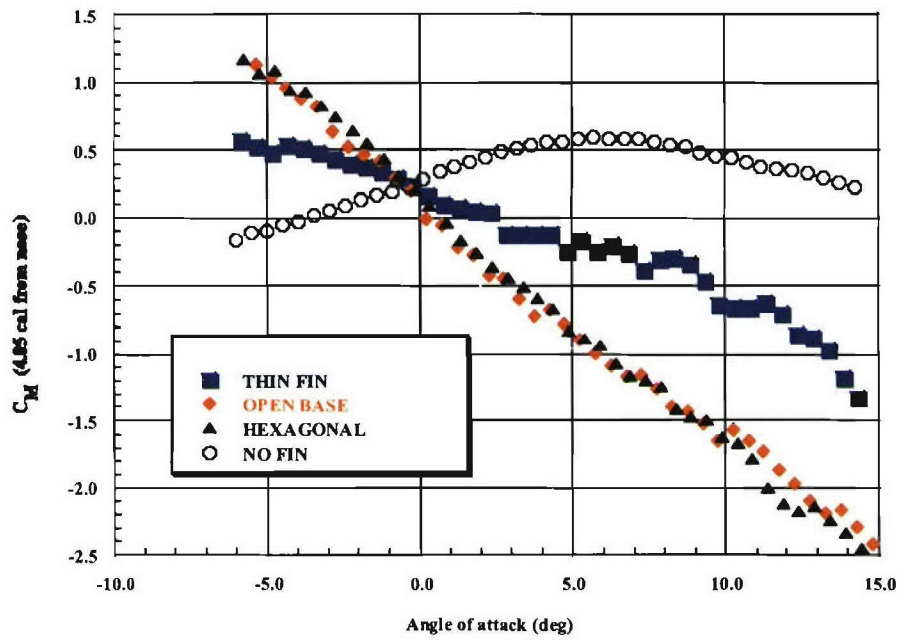
$M = 2.5$



$M = 4.0$

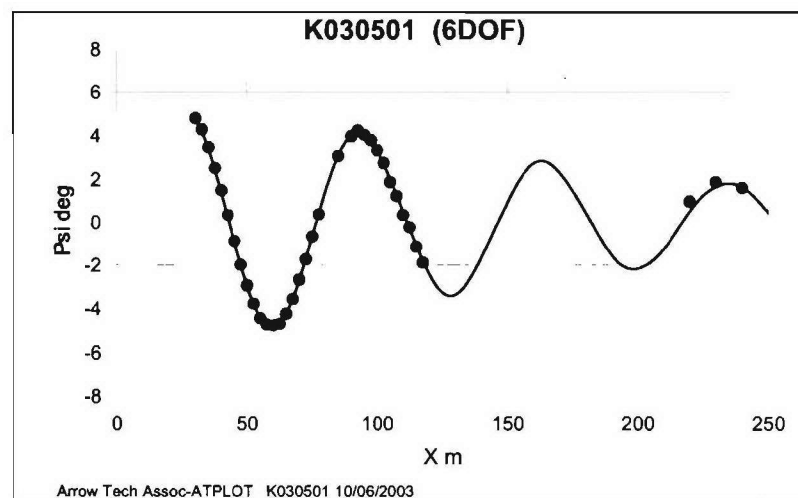
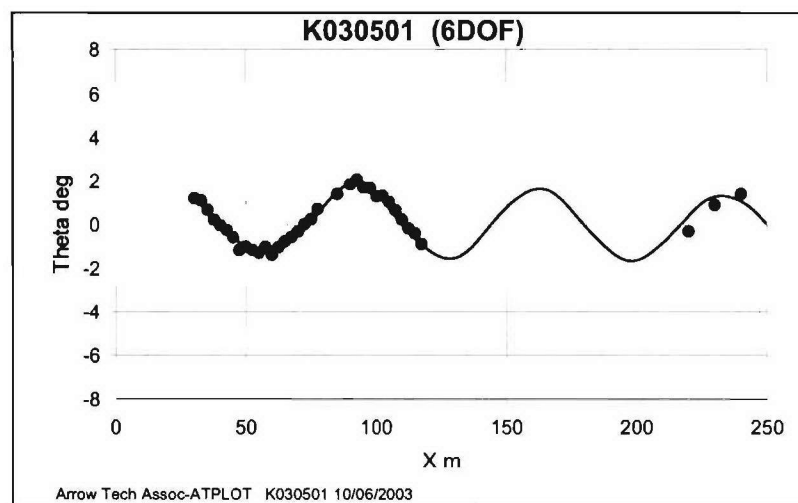
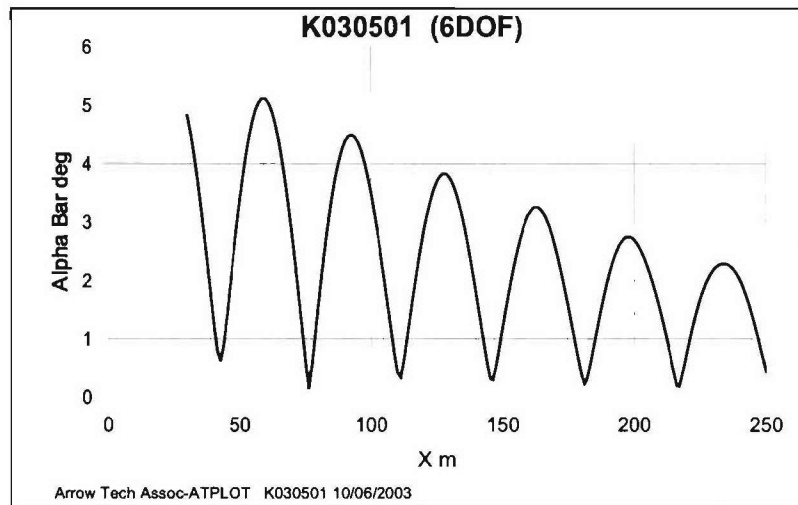


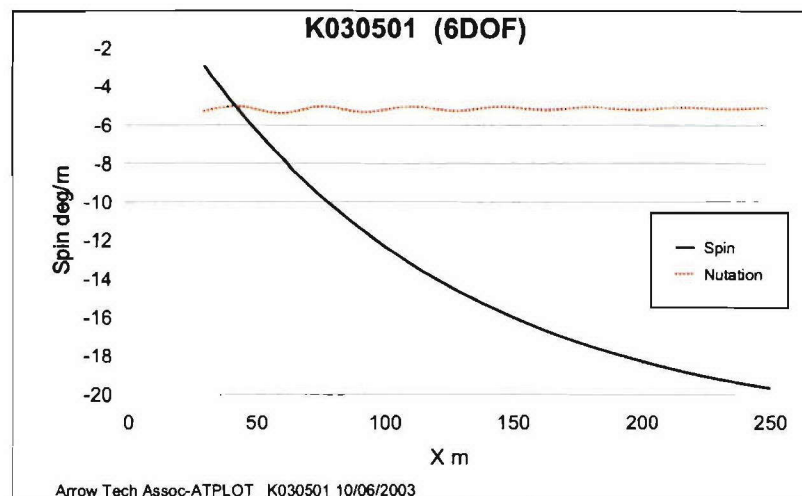
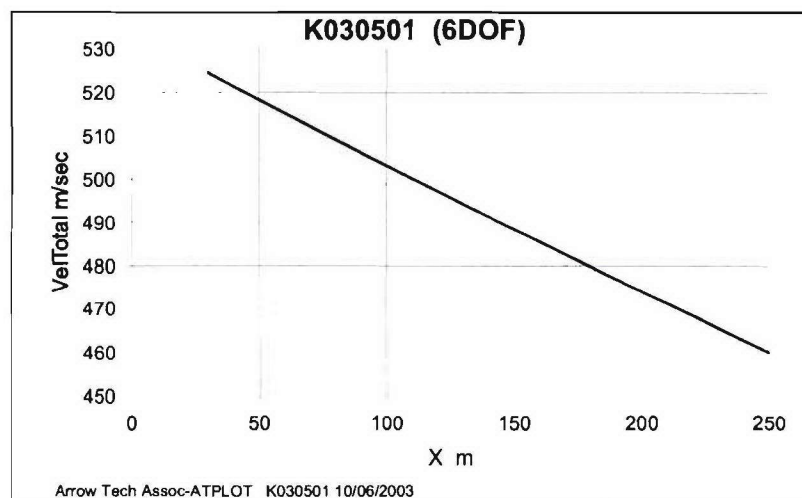
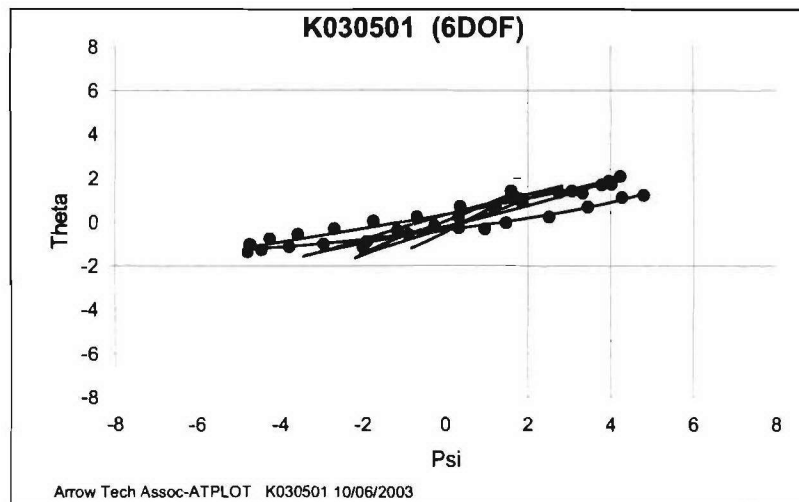
$M = 4.0$

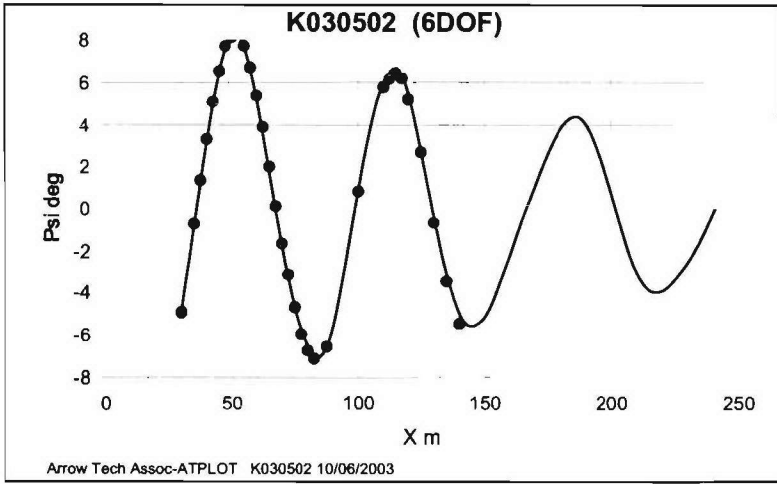
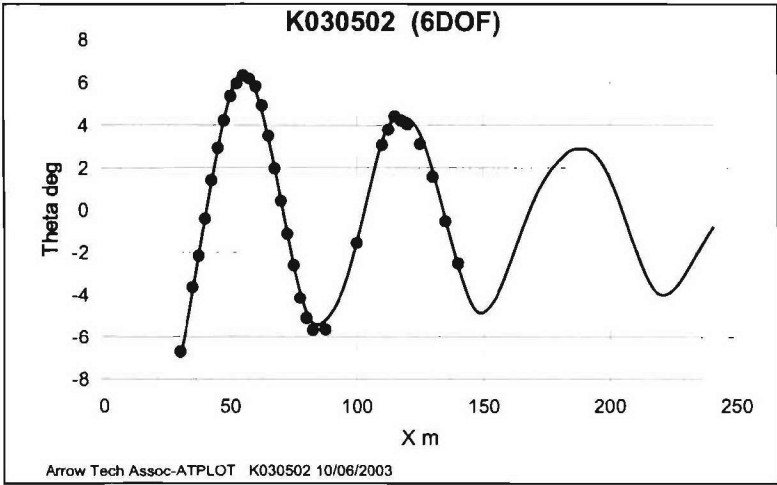
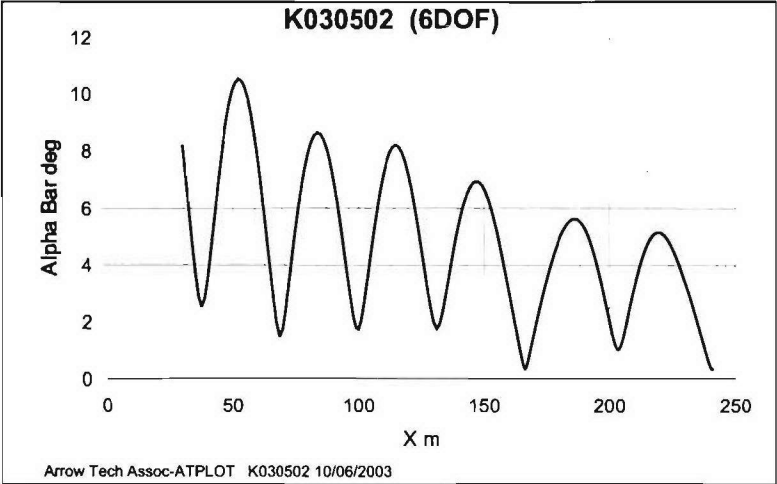


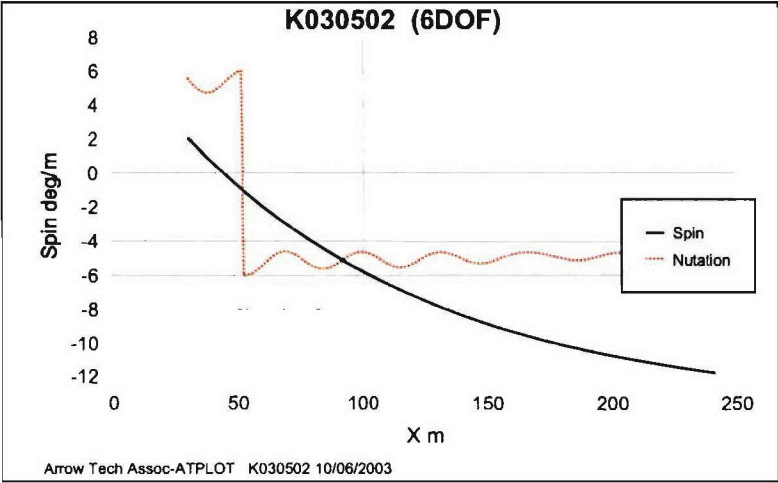
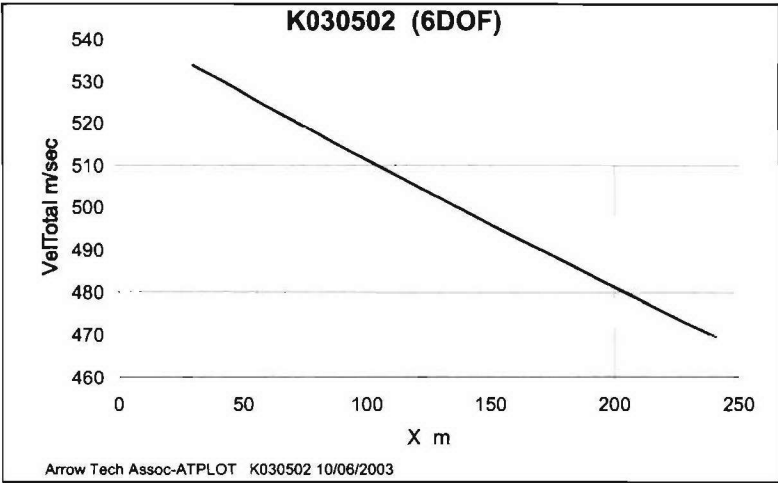
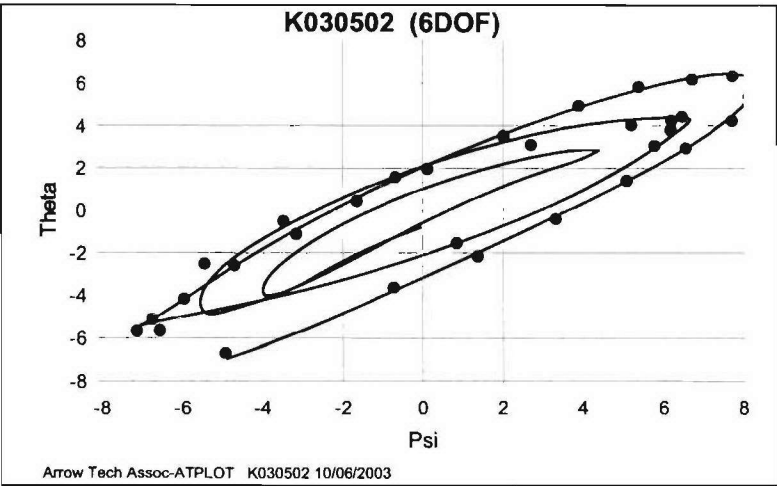


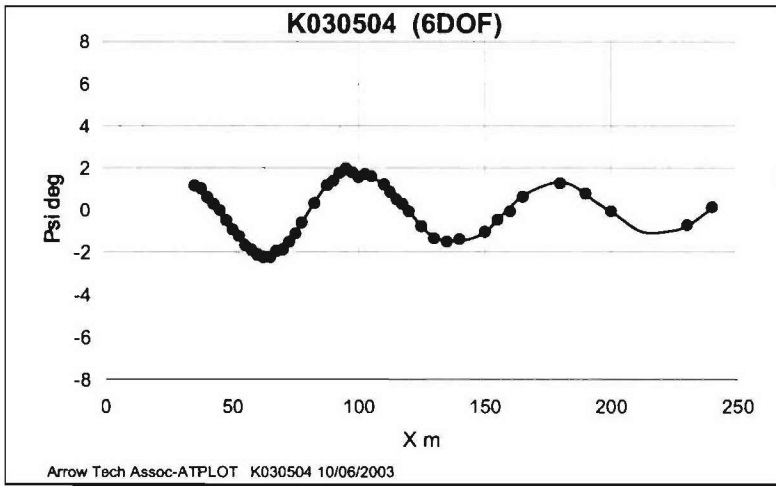
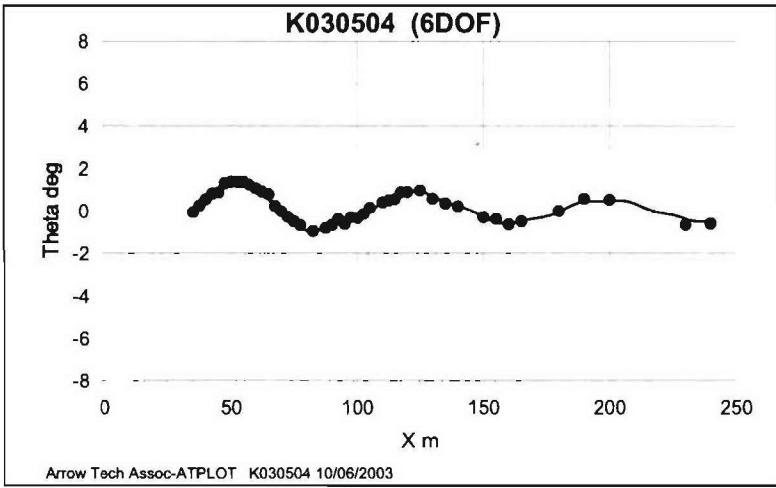
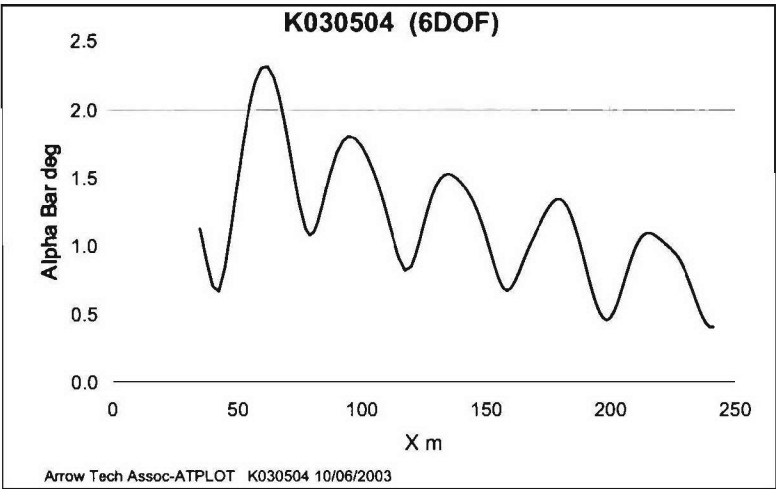
## **Annexe F – Free-Flighth Motion Plots**

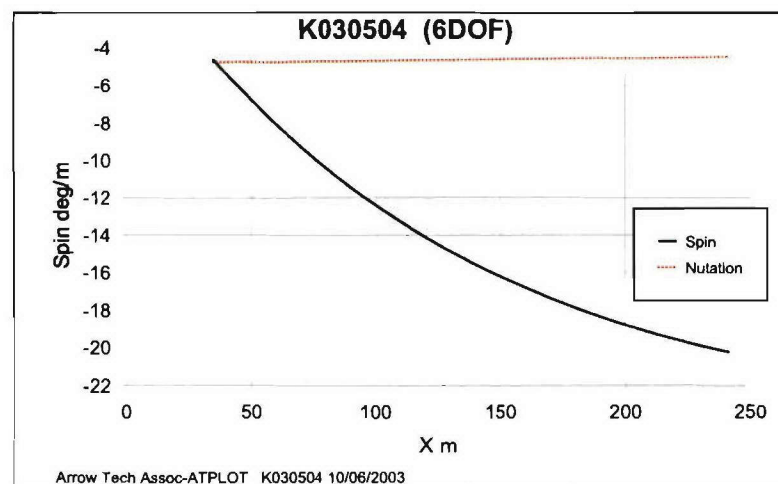
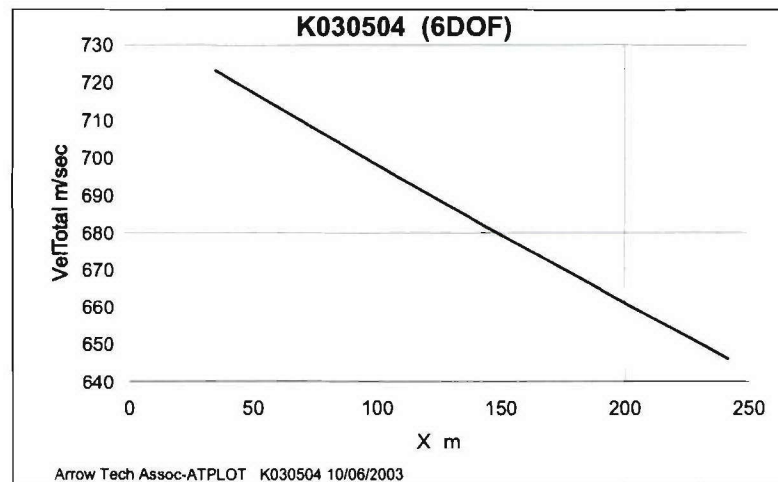
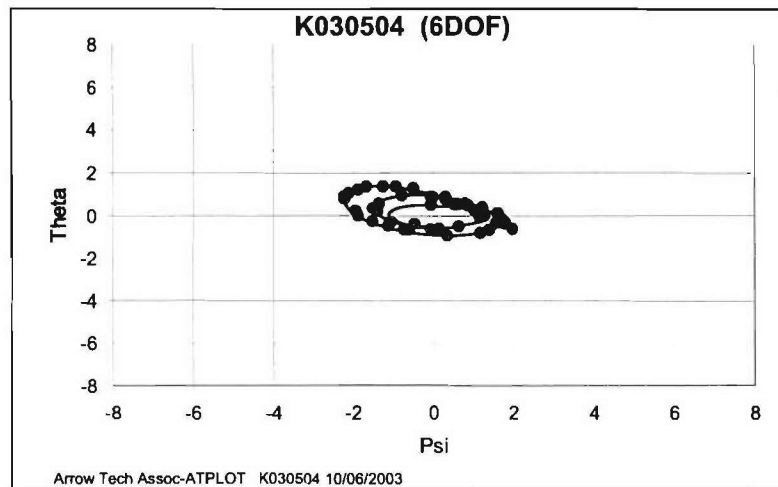


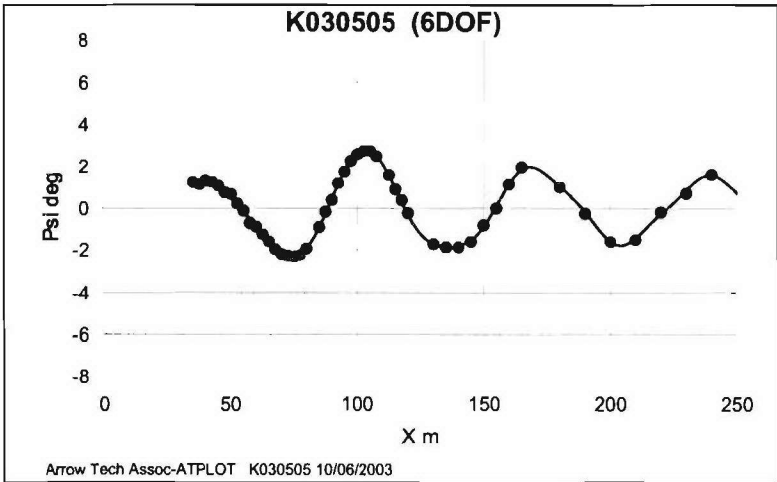
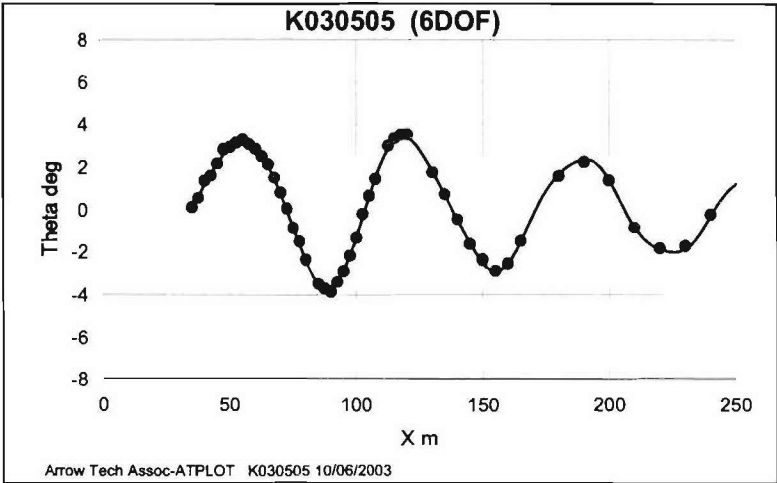
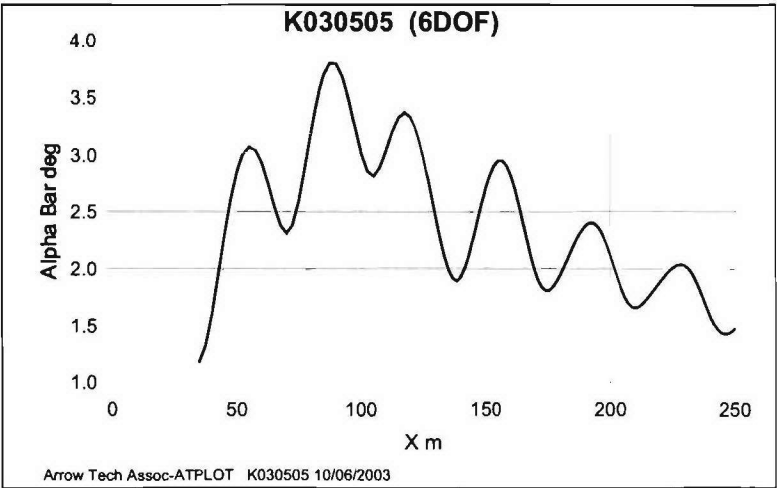




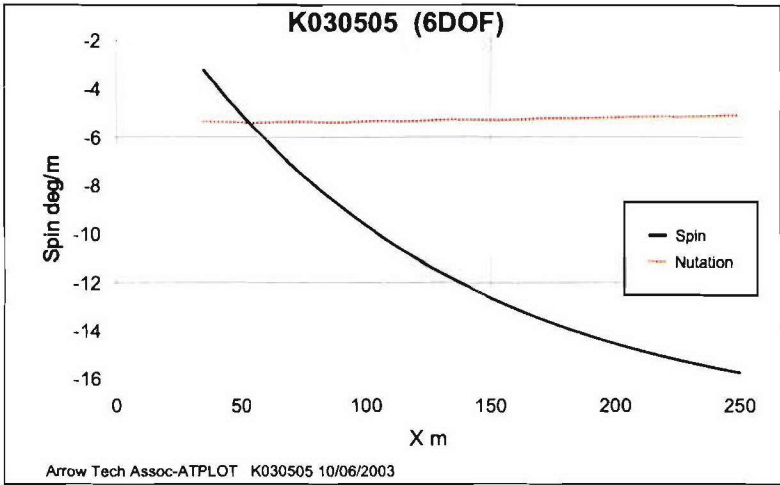
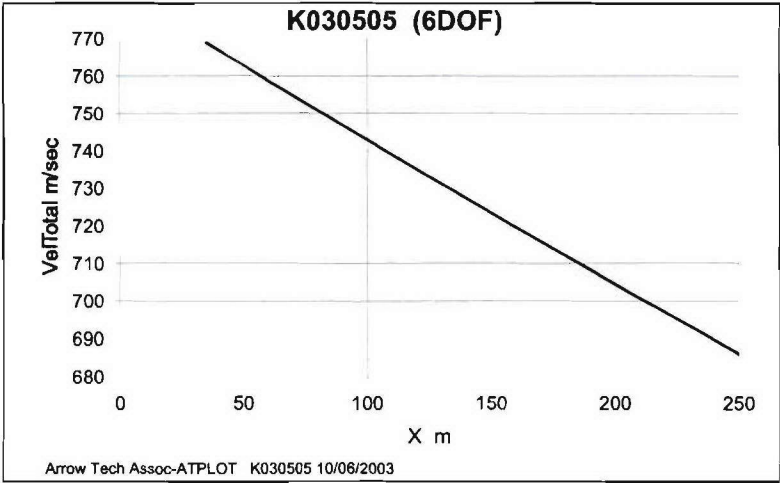
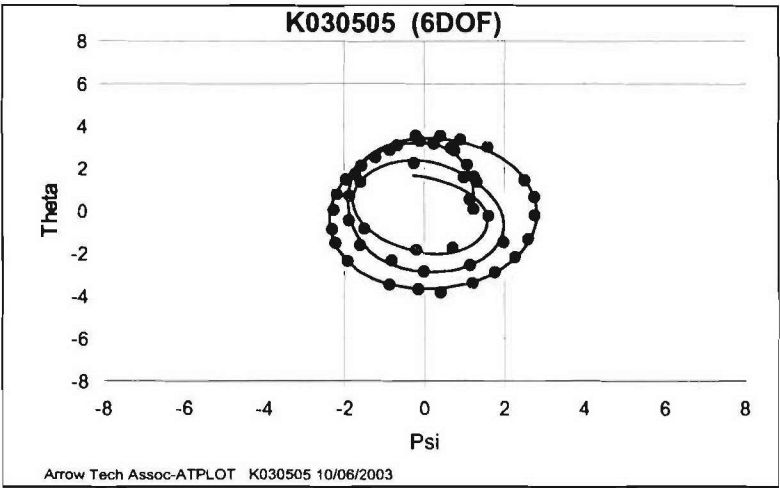


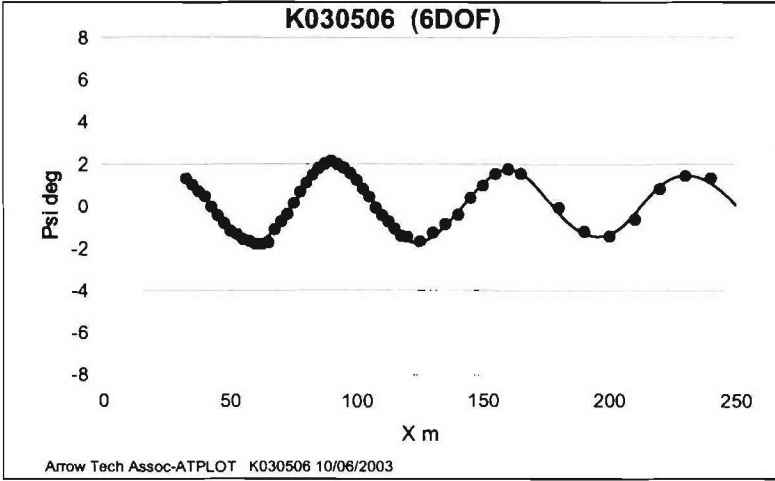
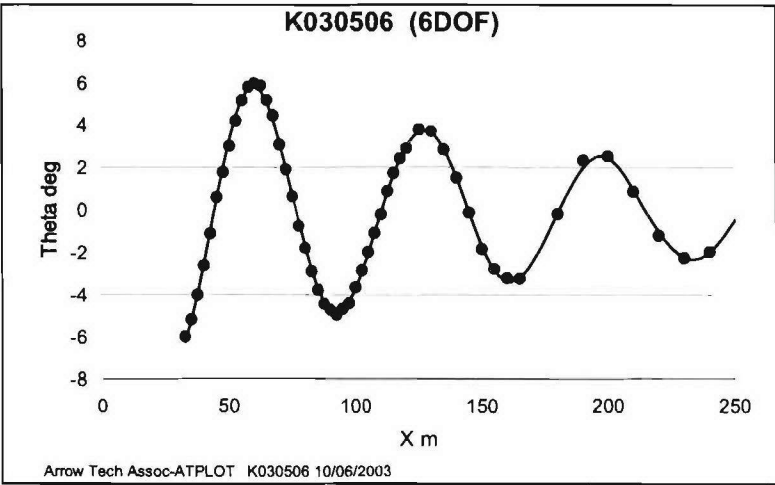
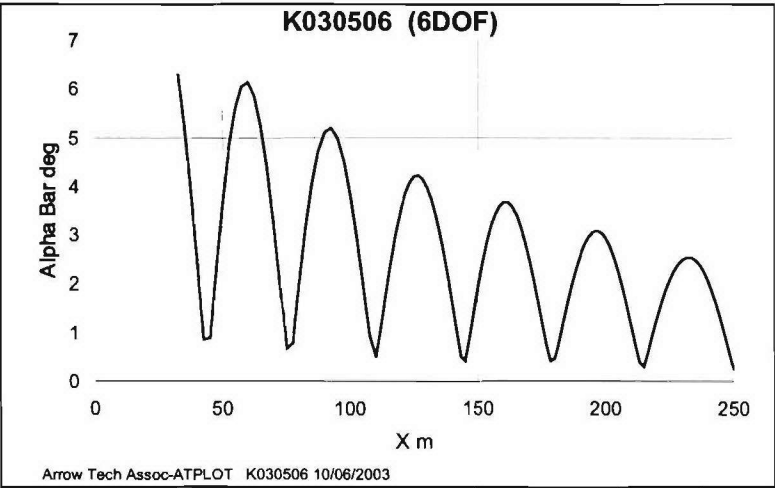


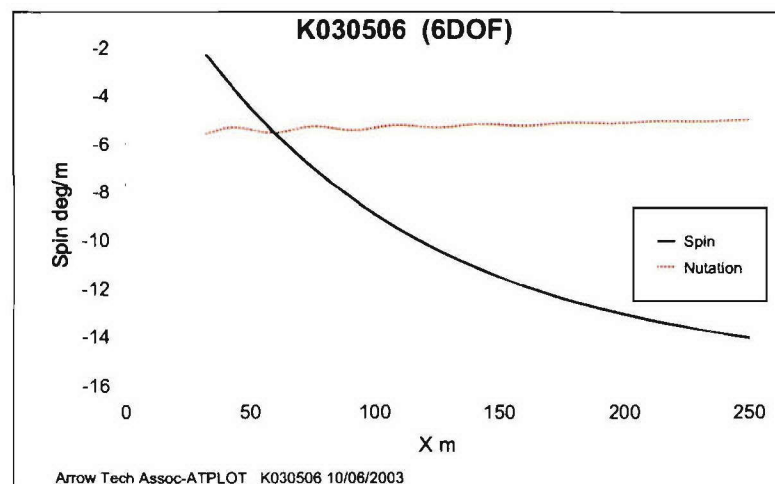
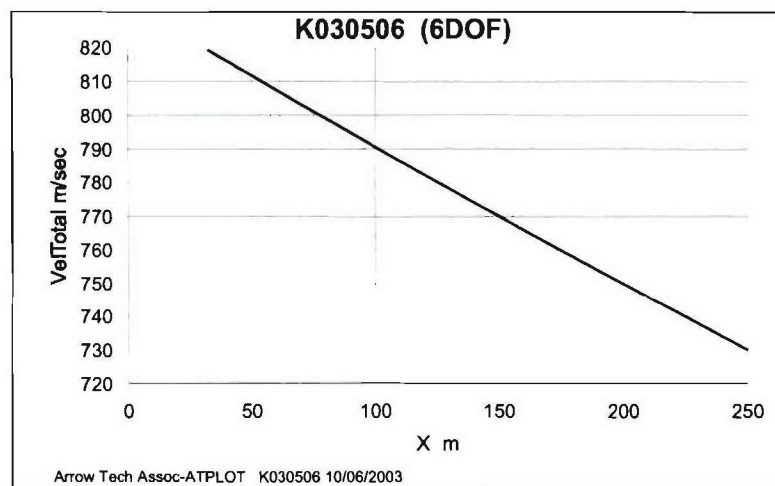
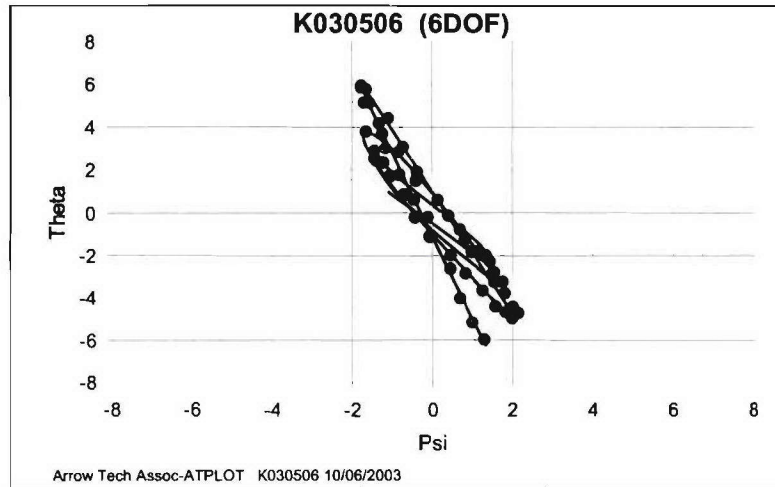


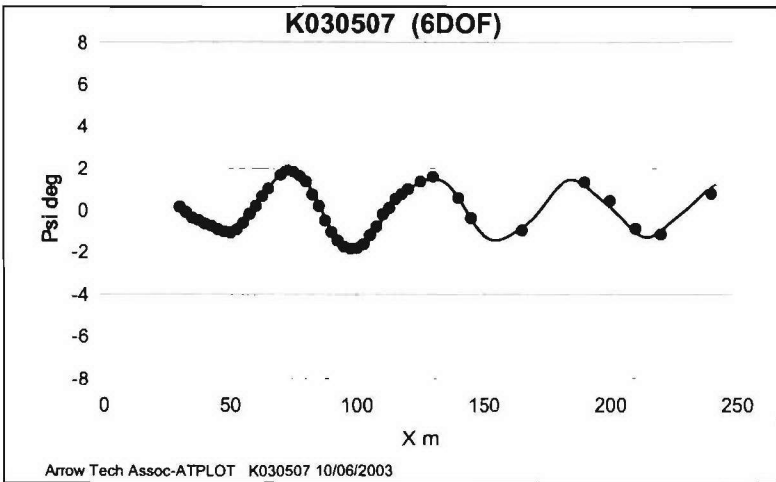
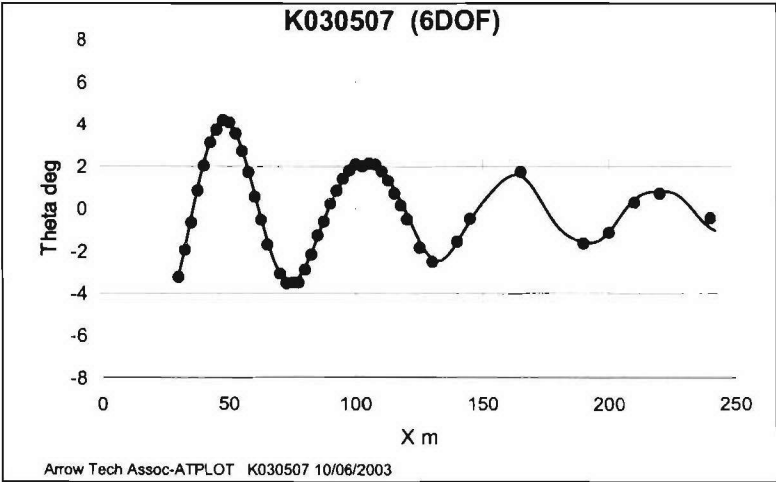
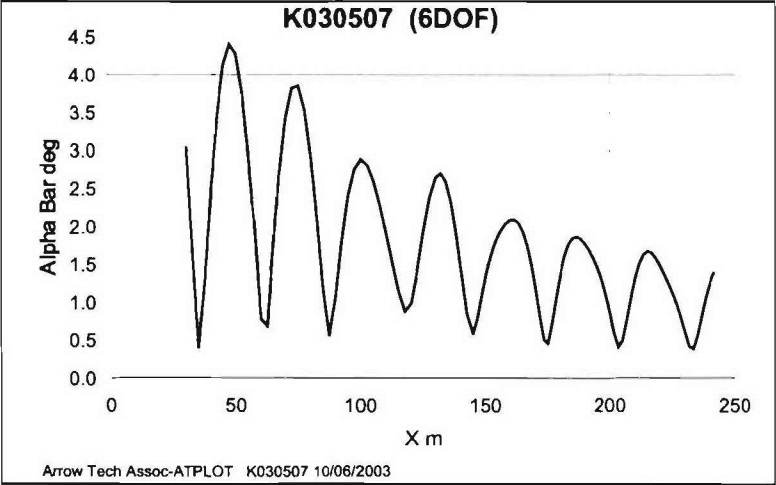


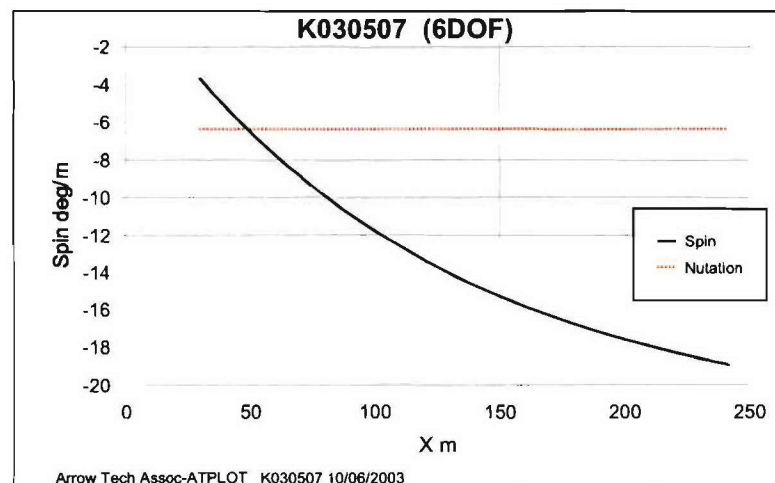
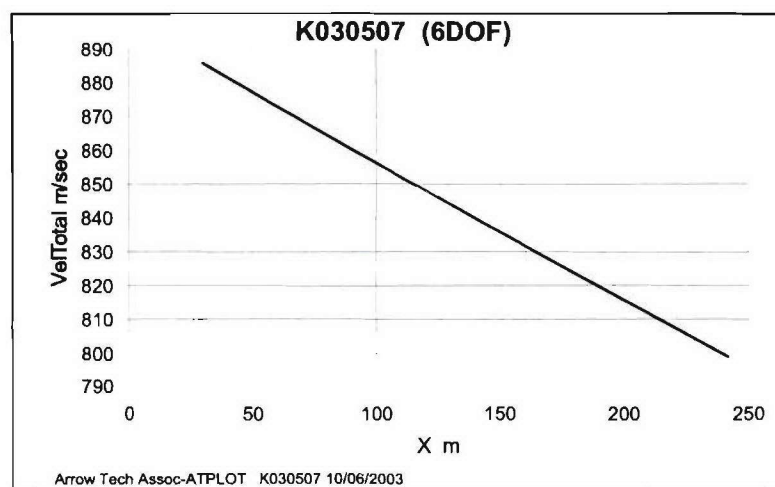
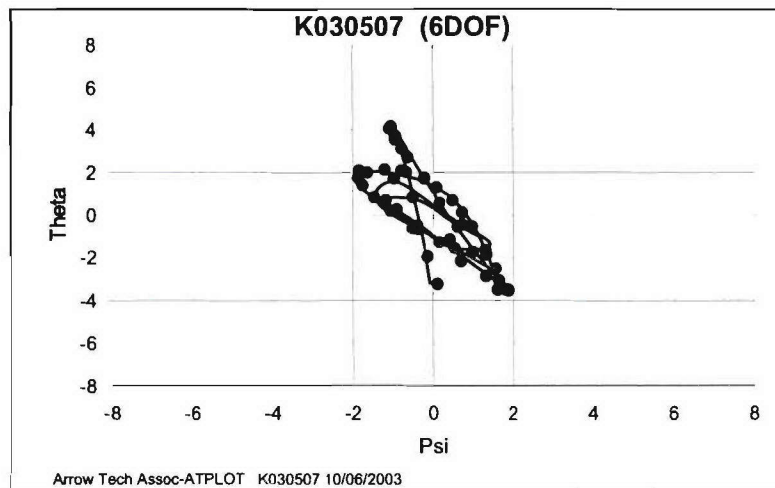


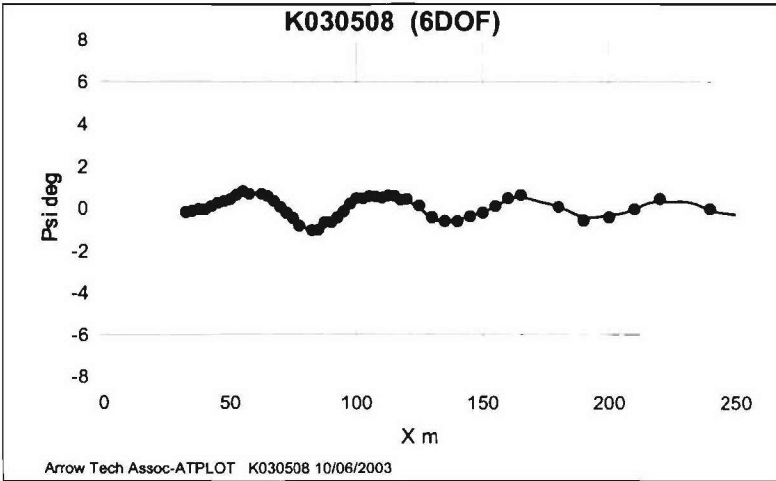
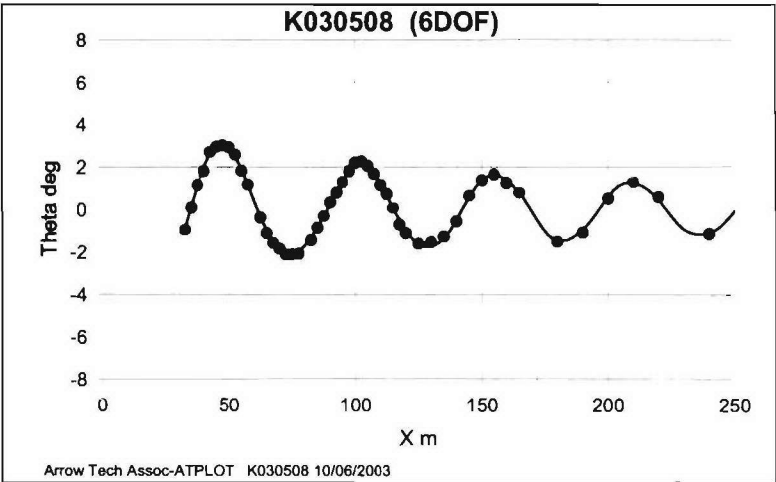
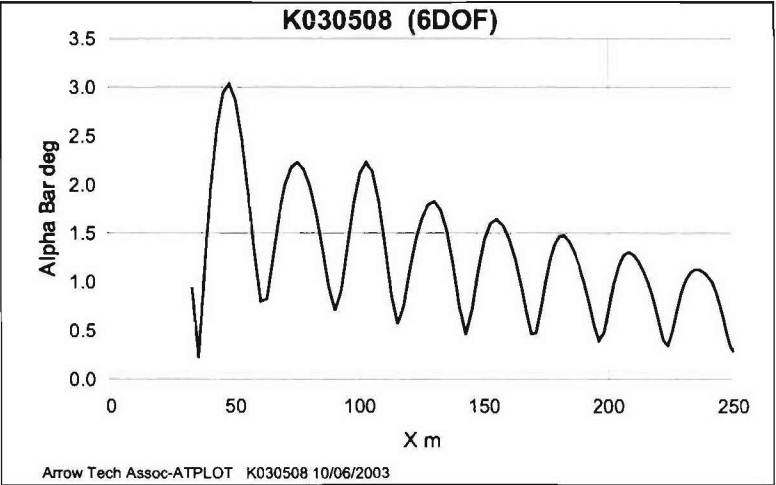


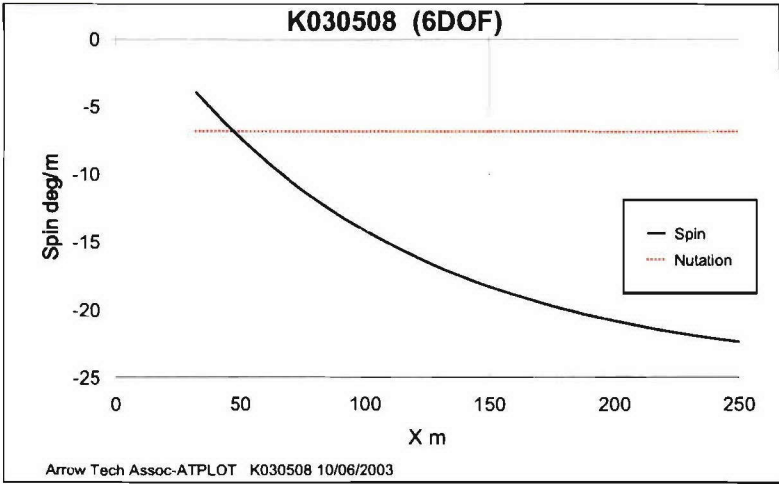
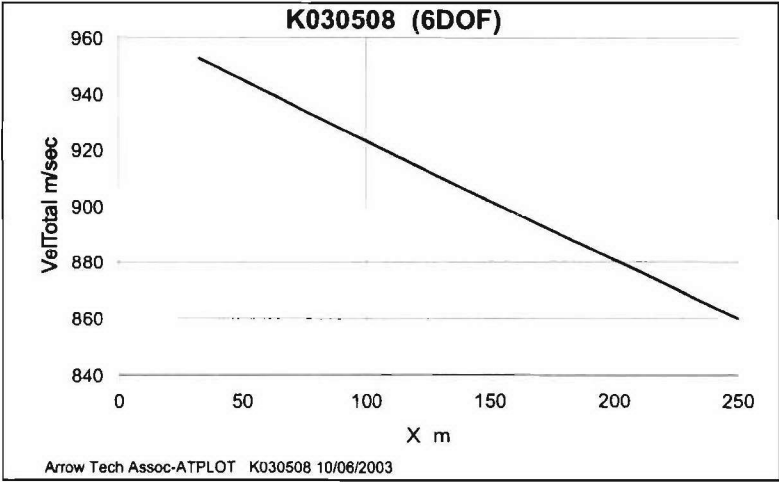
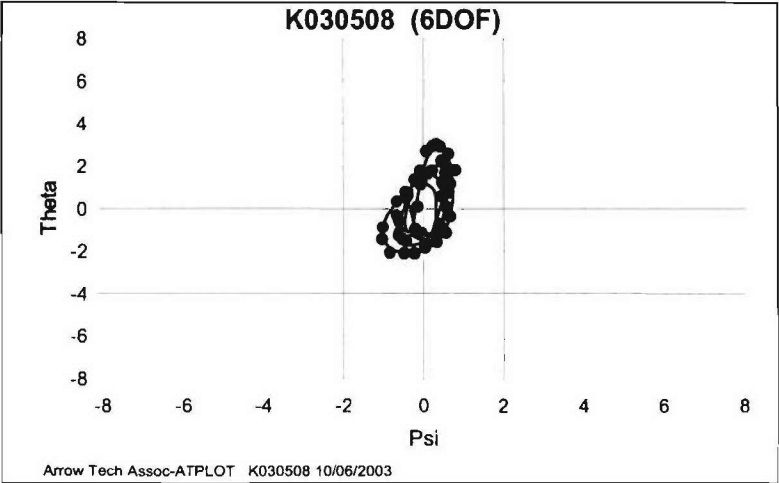


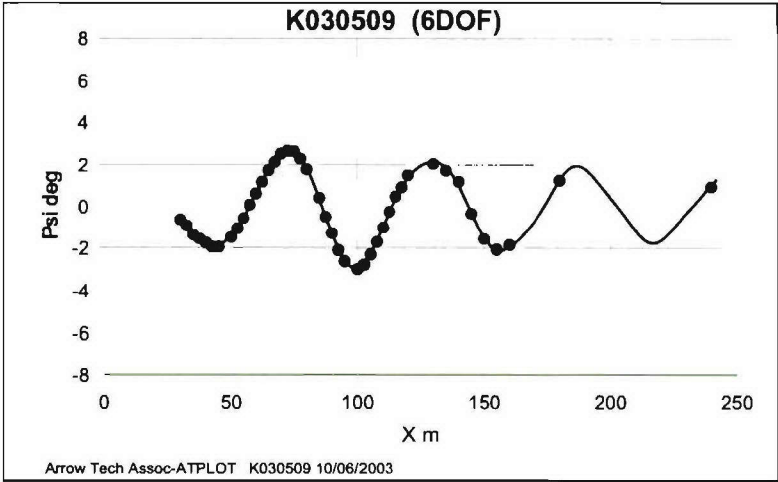
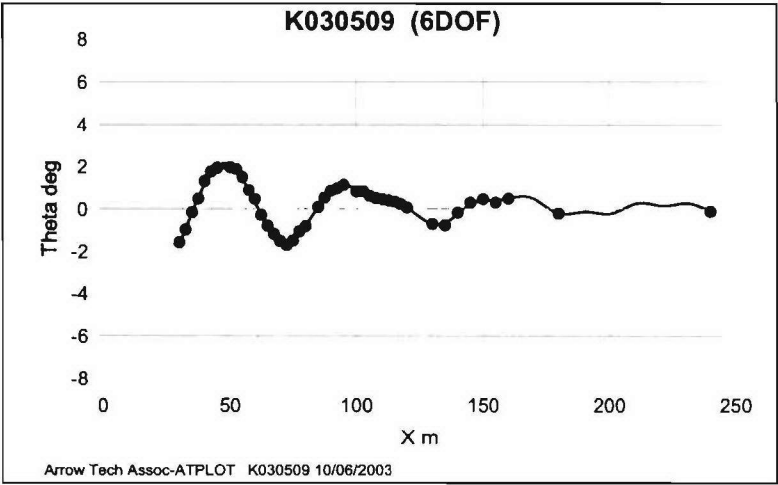
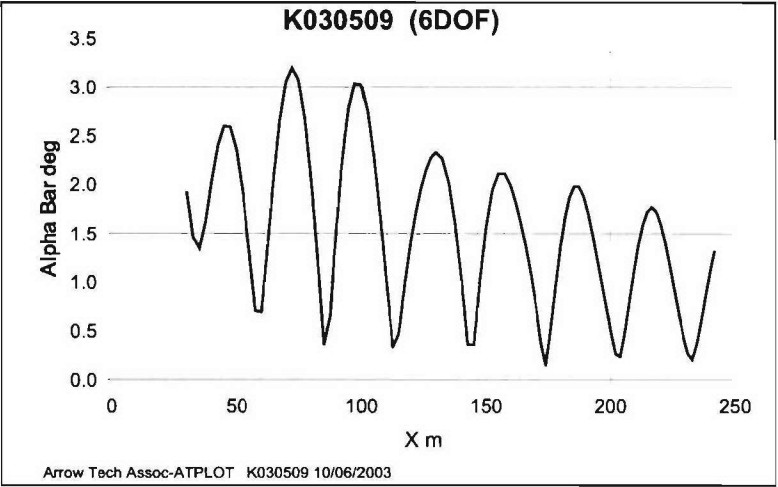




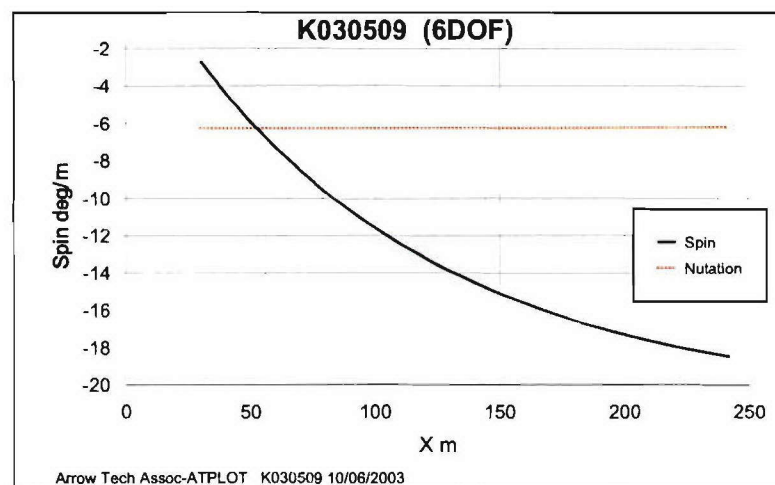
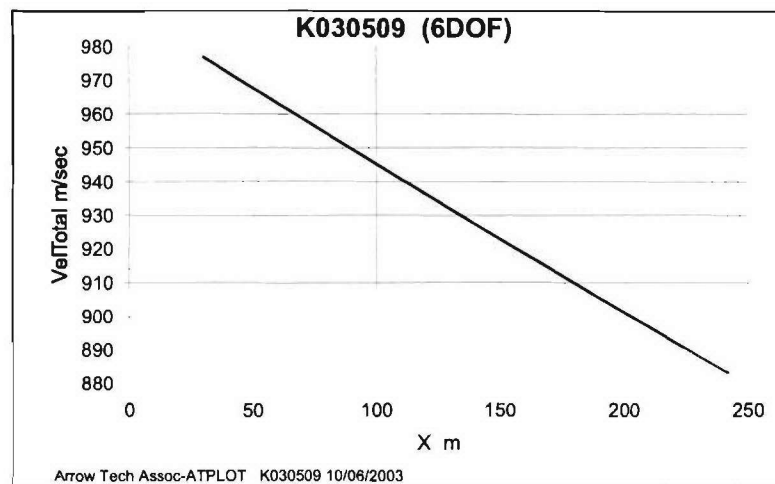
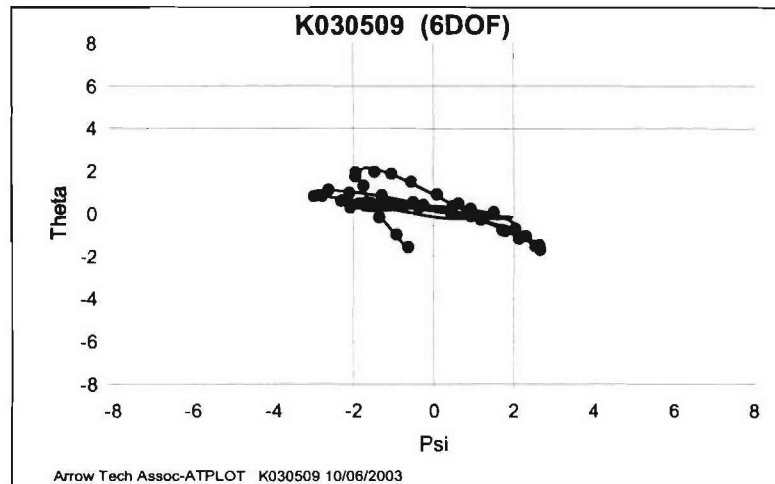


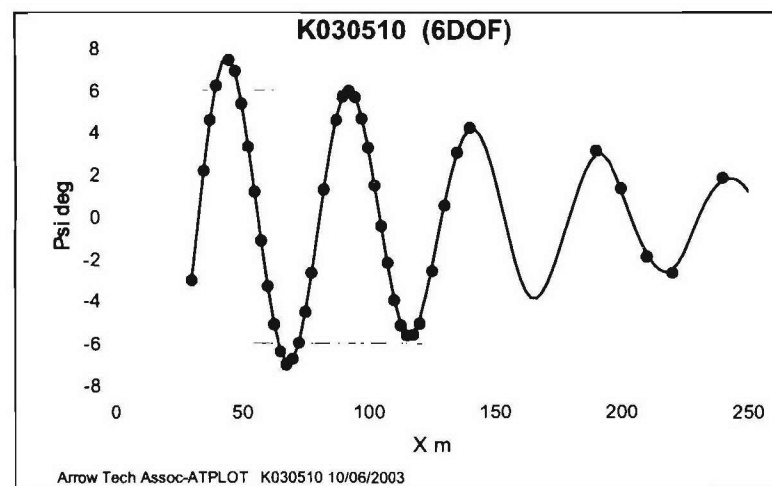
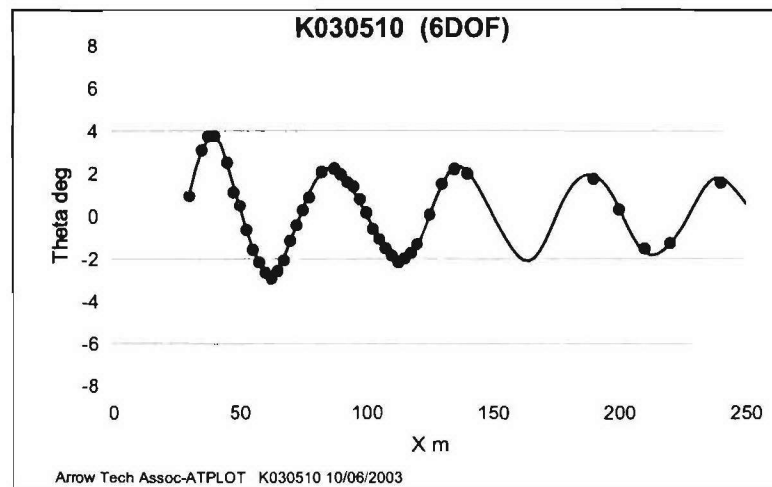
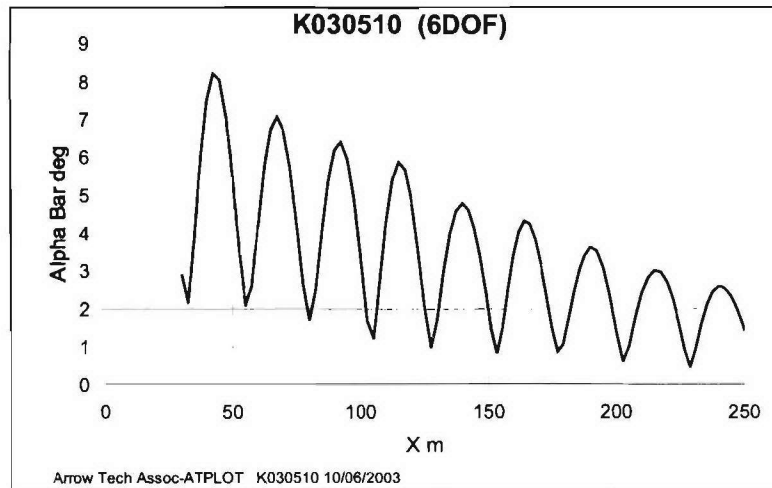


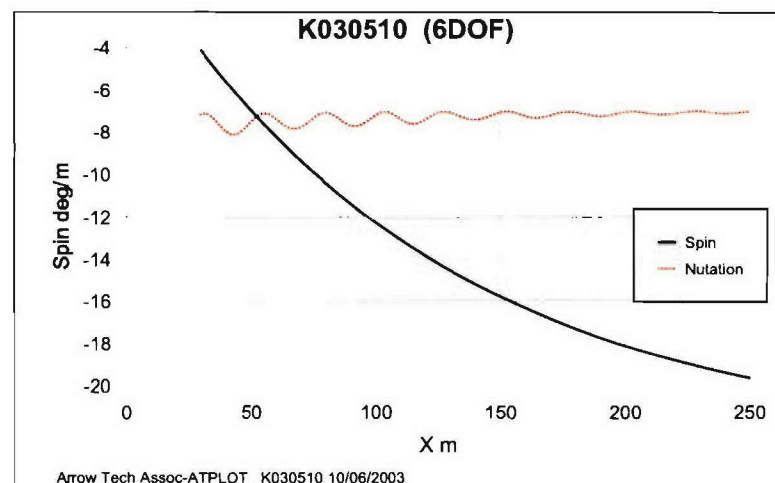
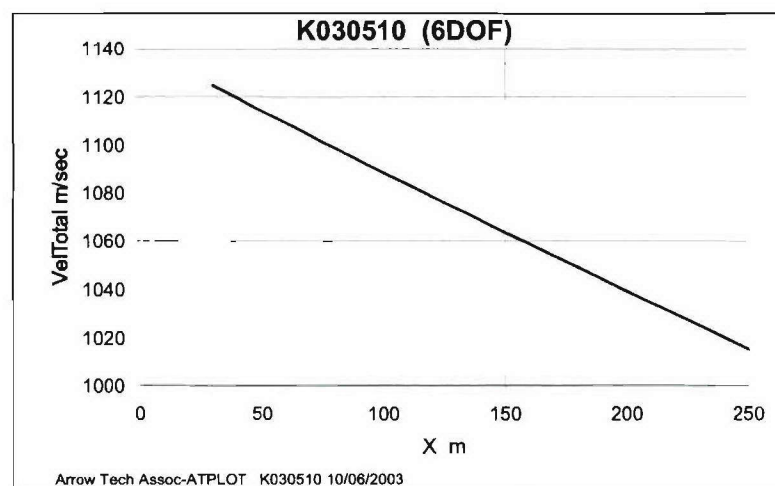
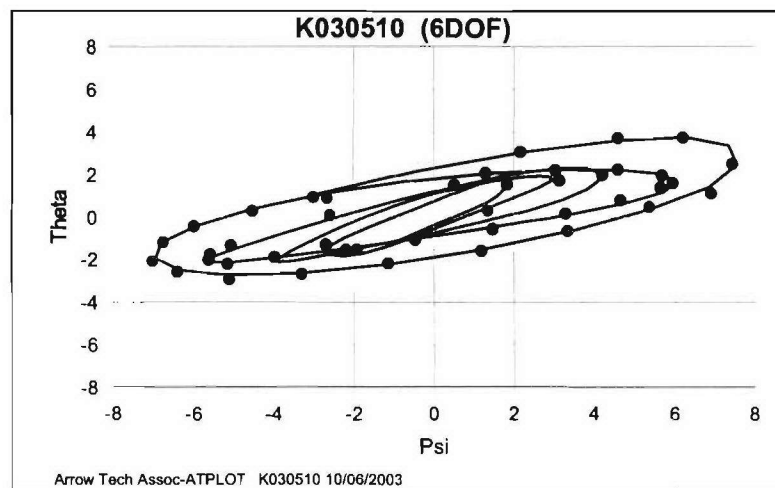


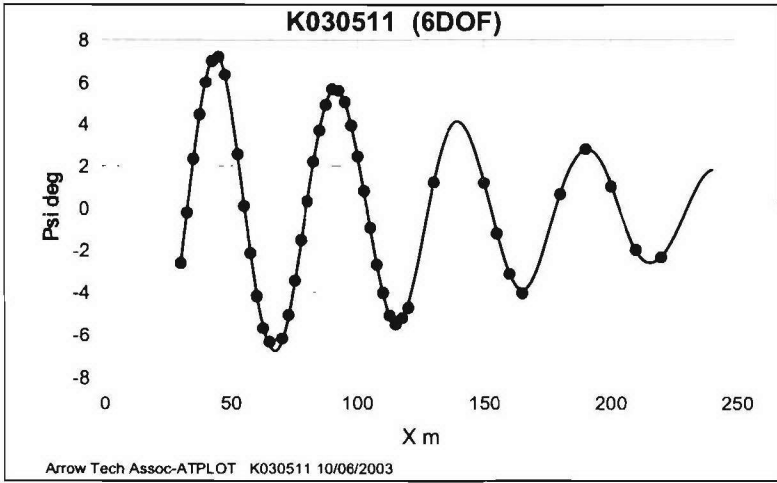
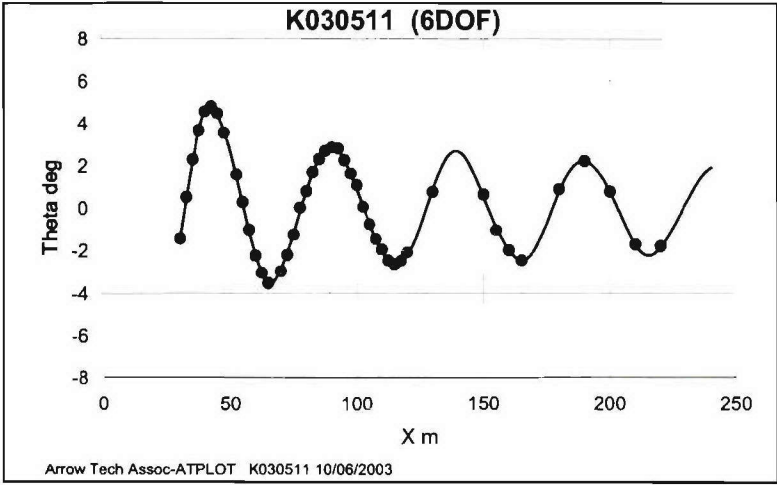
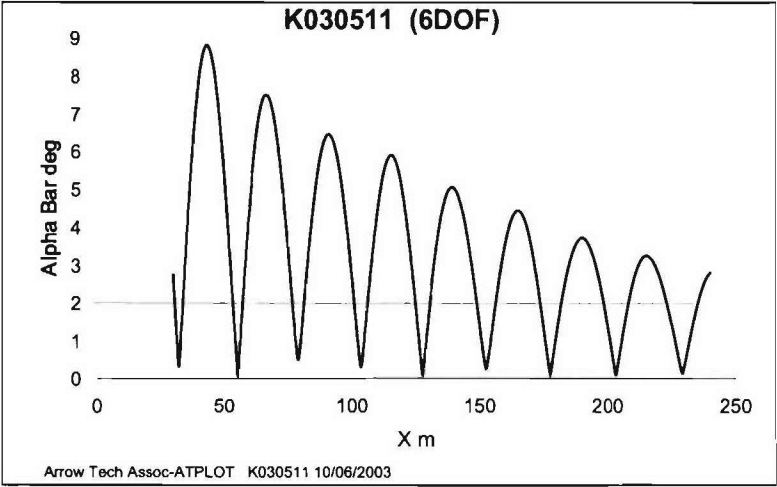


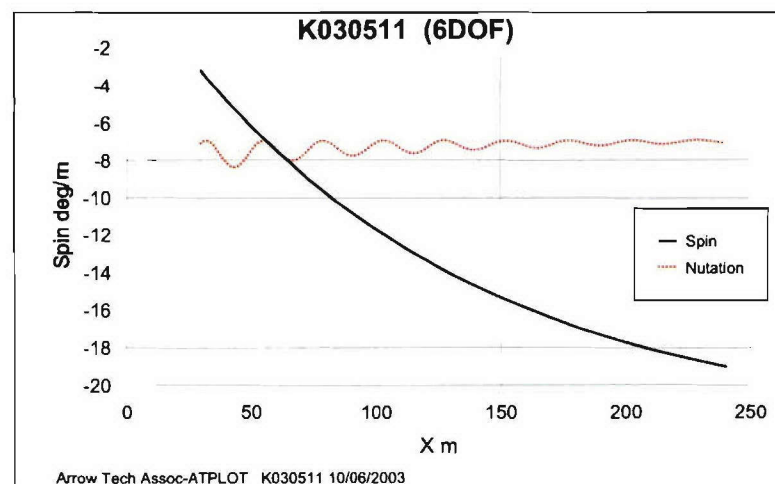
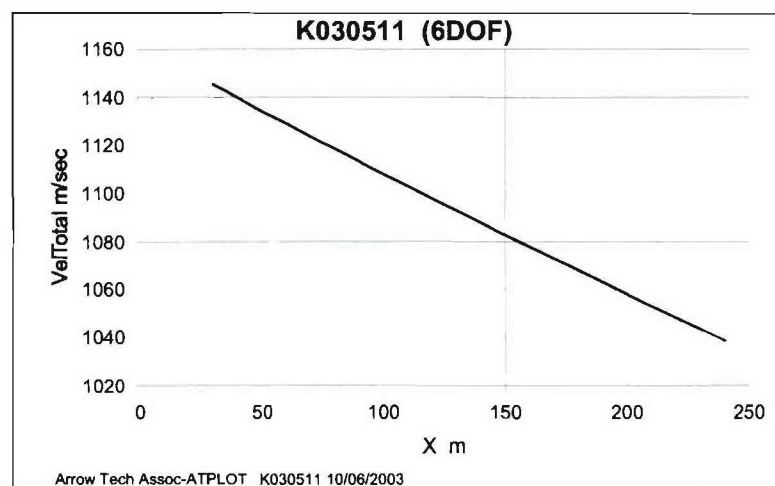
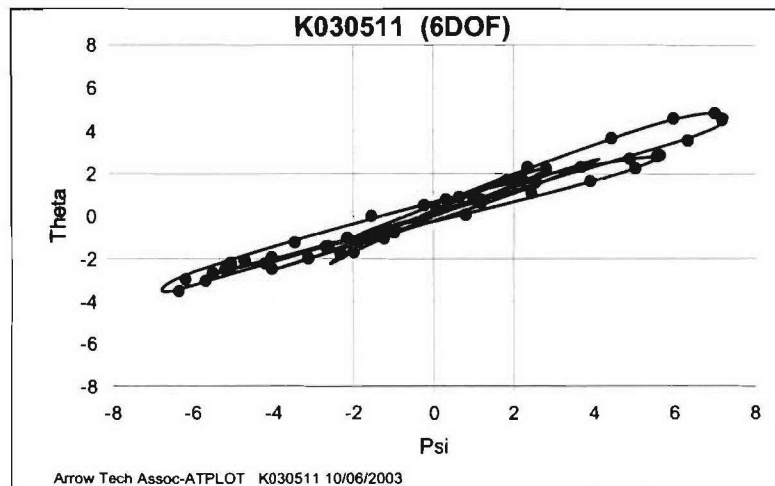


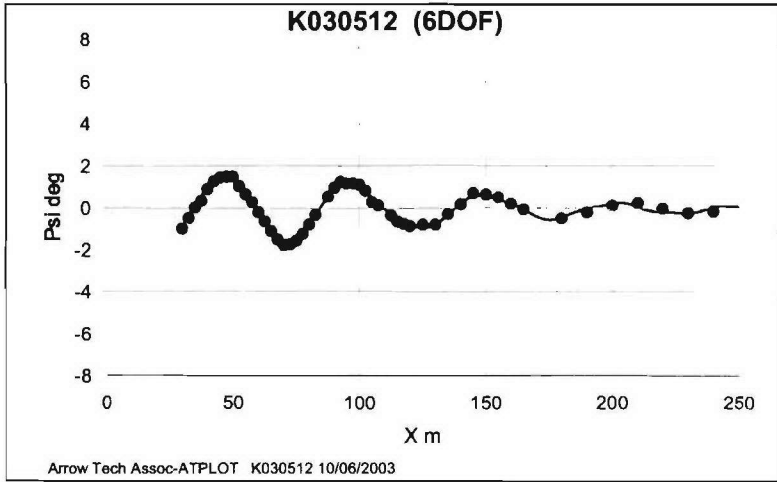
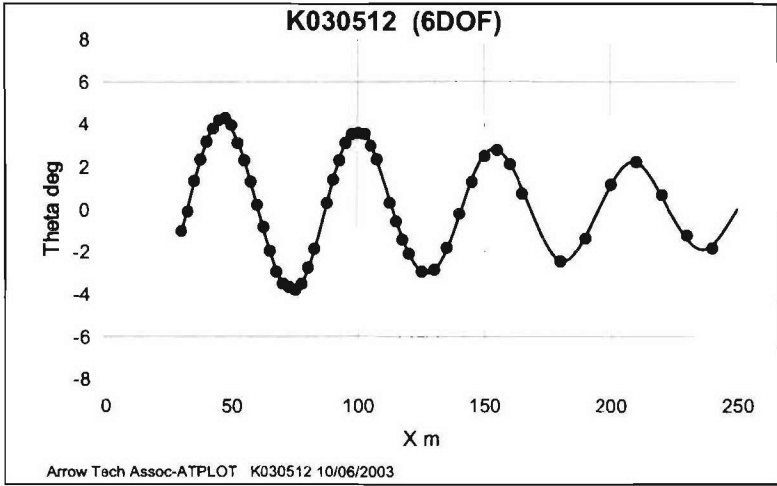
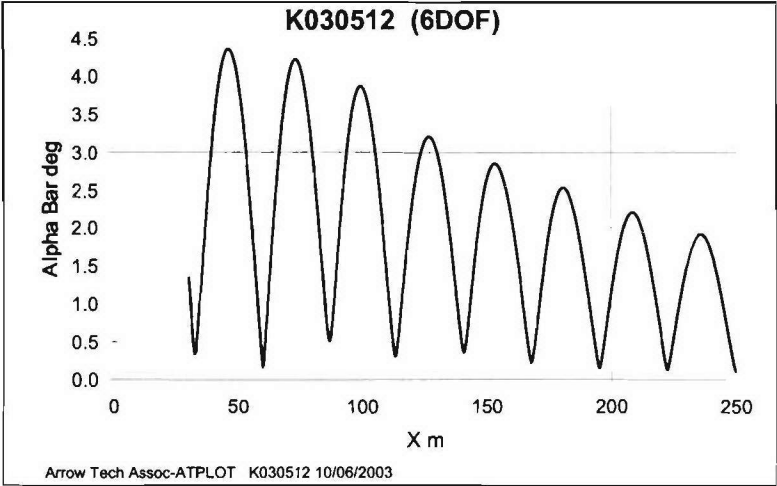


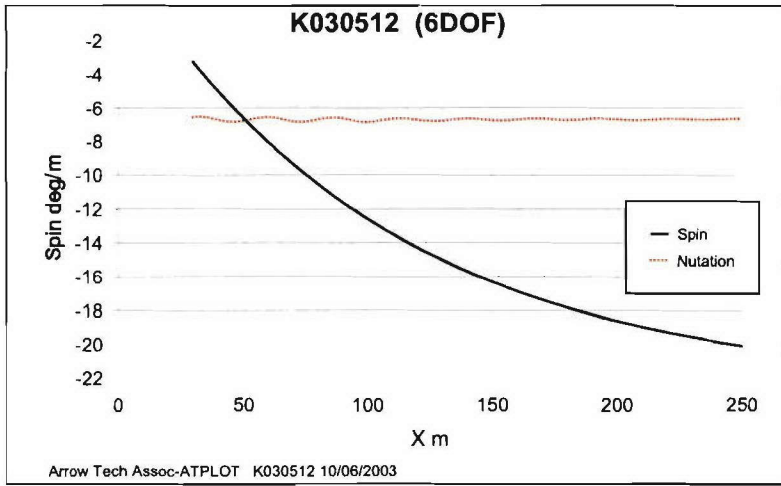
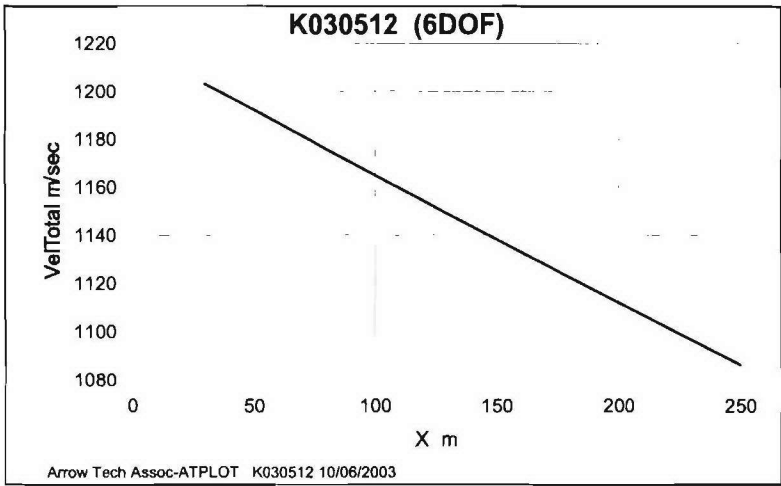
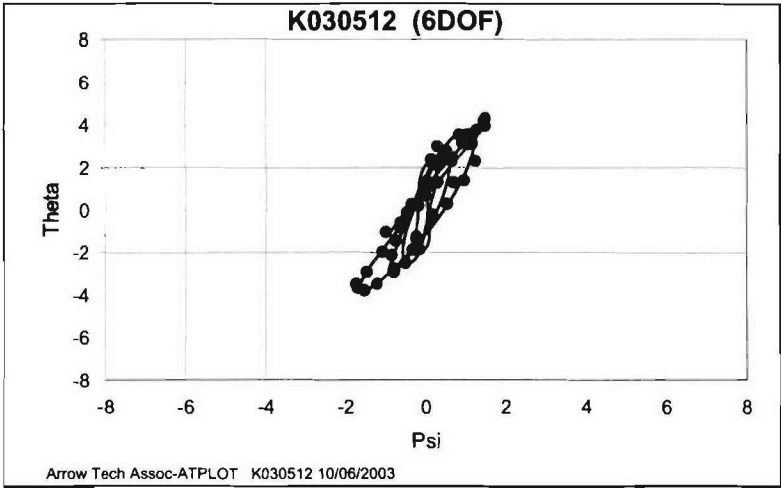












## List of symbols

### Aeroballistic range symbols

<u>Variable</u>	<u>Computer Output</u>	<u>Description</u>
$a_R$		Speed of sound in aeroballistic range
$A$		Cross sectional area of projectile ( $m^2$ )
$d$		Diameter of projectile (mm)
c. g.	CG	Center of gravity (m)
$C_{l_p}$		Roll damping moment coefficient
$C_{l_\delta}$		Roll moment coefficient due to fin cant
$C_{l_\gamma}$	Clg	Induced roll moment coefficient
$C_{n_p}$	Cnp	Magnus moment coefficient
$C_{n_\gamma}$	Cng	Induced yaw moment coefficient
$C_{nsm}$	Cnsm	Side moment coefficient
$C_N$	CN	Normal force coefficient
$C_{N_\delta \delta A}$	CNda	Trim force coefficient component
$C_{N_\delta \delta B}$	CNdB	Trim force coefficient component
$C_M$	Cm	Static pitch moment coefficient
$C_{M_q}$	Cmq	Pitch damping moment coefficient
$C_{M_\delta \delta A}$	Cmda	Trim moment coefficient component
$C_{M_\delta \delta B}$	CmdB	Trim moment coefficient component
$C_{m_\gamma}$	Cmg	Induced pitching moment coefficient
$C_{X0}$	CX0	Axial force coefficient at zero angle of attack
$C_{Y_p}$	CYp	Magnus moment coefficient
$C_{Y_\gamma}$	CYg	Induced normal force coefficient



$C_{Z\gamma}$	CZg	Induced normal force coefficient
$I_x, I_y$	-	Axial and transverse moments of inertia ( $\text{kg m}^2$ )
$l$	-	Length of projectile (m)
$l/d$	-	Length-to-diameter ratio
$m$	-	Mass of projectile (kg)
$M$	Mach	Mach number
$p$	-	Spin rate (rad/s or deg/m)
$P_R$		Atmospheric pressure inside aeroballistic range
$Re_l$	-	Reynolds number based on length of projectile
$u, v, w$	-	Projectile component velocities (m/s)
$V$	-	Total projectile velocity (m/s)
$V_{\text{muz}}$	-	Muzzle velocity (m/s)
$X, Y, Z$	-	Projectile coordinates (m)
$T_R$		Atmospheric temperature inside aeroballistic range ( $^{\circ}\text{C}$ )
$t$	-	Time of flight (s)
$\bar{\alpha}$	$\alpha$	Total angle of attack (deg)
$\bar{\alpha}_{\text{max}}$	AMAX	Maximum angle of attack (deg)
$\lambda_N, \lambda_P$	LN, LP	Nutation and precession damping (1/m)
$\theta, \psi, \phi$	-	Projectile orientation (deg)
$\delta$	-	Fin cant angle (rad or deg)
$\delta_T$	-	Total trim angle (rad or deg)
$\bar{\delta}^2$	DBSQ	Mean squared yaw ( $\text{deg}^2$ )
$\varepsilon$	-	Sine of the total angle of attack, $\sin \bar{\alpha} = \frac{v^2 + w^2}{V^2}$
$\rho$	-	Air density ( $\text{kg/m}^3$ )
6DOF	-	Six degrees of freedom

### Subscripts

$\bar{\alpha}_i$	ai (i)	Derivative with respect to $\epsilon_i$
M	M	Variation with Mach number

### Examples

$C_{M_{\bar{\alpha}}}$	Cma	Pitching moment coefficient slope
$C_{M_{\bar{\alpha}^3}}$	Cma3	Pitching moment coefficient w.r.t. $\epsilon^3$
$C_{M_{q\bar{\alpha}^2}}$	Cmq2	Pitch damping coefficient w.r.t. $\epsilon^2$

### Wind Tunnel Symbols

A	Axial force
a	Distance between the point of application of the balance forward normal force $N_1$ and BRC, m
BRC	Balance reference center, m
b	Distance between the point of application of the balance aft normal force $N_2$ and BRC, m
$B_i$	Polynomial coefficient
c	distance between BRC and aft of model (MRC)
$C_X$	Axial force coefficient
$C_{X0}$	Axial force coefficient (at $\alpha = 0^\circ$ )
$C_M$	Pitching moment coefficient about MRC (in this case of projectile)
$C_{M_{\alpha}}$	Pitching moment coefficient slope (at $\alpha = 0^\circ$ ), $\text{rad}^{-1}$
$C_N$	Normal force coefficient
$C_{N_{\alpha}}$	Normal force coefficient slope (at $\alpha = 0^\circ$ ), $\text{rad}^{-1}$
$C_{RM}$	Roll moment coefficient
D, d	Reference or nominal diameter of model, m or cal

$l$	Projectile length, m
$M_{\infty}$	Nominal free stream Mach number
$M_i$	Measured Mach number at the $i^{\text{th}}$ balance reading
MRC	Moment Reference Center, located at the model base
$N$	Total normal force, N
$N_1$	Forward normal force, N
$N_2$	Aft normal force, N
$P_{\infty}$	Free stream static pressure ( $= P_{\text{inf}}$ ), Pa
$P_i$	Pressure measured with the $i^{\text{th}}$ transducer, Pa
$P_s$	Static pressure in the test section, Pa
$P_t$	Average total pressure, Pa
$P_{ti}$	Total pressure measured in the settling chamber at the time of the $i^{\text{th}}$ balance reading, Pa
$P_{vi}$	Test section static pressure measured on wall at the time of the $i^{\text{th}}$ balance reading, Pa
$Q$	Test section dynamic pressure, Pa
$R$	Roll moment, N m
$Re$	Reynolds number per unit length, $\text{m}^{-1}$
$Re_l$	Reynolds number based on model length
$S$	Body cross-sectional area, $= \pi d^2 / 4$ , $\text{m}^2$
$T_a$	Reservoir air temperature, $^{\circ}\text{K}$
$T_v$	Test section temperature, $^{\circ}\text{K}$
$U_{\infty}$	Free stream velocity ( $= U_{\text{inf}}$ ), m/s
$V$	Projectile velocity, m/s
$X_{\text{CP}}$	Position of center of pressure aft of MRC, in caliber
$X_{\text{CPO}}$	Position of center of pressure aft of MRC at $\alpha = 0.0^{\circ}$ , in caliber
$Y$	Total side force, N
$\alpha$	Angle of attack, deg
$\gamma$	Specific heat ratio
$\mu$	Air viscosity in test section, Pa·s

$\rho$  Air density in test section, kg/m<sup>3</sup>  
 $\rho_{\infty}$  Free stream density, kg/m<sup>3</sup>

Superscript

b about base of projectile  
cg about cg of projectile  
BRC about balance reference center  
MRC about moment reference center (= base of projectile)